

## University of Southampton Research Repository ePrints Soton

Copyright © and Moral Rights for this thesis are retained by the author and/or other copyright owners. A copy can be downloaded for personal non-commercial research or study, without prior permission or charge. This thesis cannot be reproduced or quoted extensively from without first obtaining permission in writing from the copyright holder/s. The content must not be changed in any way or sold commercially in any format or medium without the formal permission of the copyright holders.

When referring to this work, full bibliographic details including the author, title, awarding institution and date of the thesis must be given e.g.

AUTHOR (year of submission) "Full thesis title", University of Southampton, name of the University School or Department, PhD Thesis, pagination

**UNIVERSITY OF SOUTHAMPTON**

FACULTY OF PHYSICAL SCIENCES AND ENGINEERING

Electronics and Computer Science

**Two Degree of Freedom Capacitive MEMS Velocity Sensor**

by

**Ali Alshehri**

Thesis for the degree of Doctor of Philosophy

April 2015



UNIVERSITY OF SOUTHAMPTON

**ABSTRACT**

FACULTY OF PHYSICAL AND APPLIED SCIENCES

School of Electronic and Computer Science

Doctor of Philosophy

**Tow Degree of Freedom Capacitive MEMS Velocity Sensor**

Ali Alshehri

This research presents the design and implementation of a novel two-degree-of-freedom (2-DoF) capacitive MEMS velocity sensor for use with structural vibration measurements. The sensor comprises two mass–spring–damper systems that are connected in series. The base principal system is used as the principal sensing element, and the other system functions as the secondary sensing element for the implementation of an internal velocity feedback loop. This loop is aimed at producing damping force on the proof mass of the principal sensing system, so that the frequency response function of the velocity sensor takes on three important properties: (1) At low frequencies below the fundamental resonance of the 2-DoF sensor, the output of the sensor becomes proportional to the velocity of the sensor’s frame. (2) Around the fundamental resonance, the sensor is characterised by a flat amplitude spectrum. (3) Finally, above the fundamental resonance, the sensor is characterised by an amplitude roll-off with only a 90° phase lag. In contrast to standard accelerometer vibration sensors, this sensor produces the desired velocity output within the bandwidth up to the first resonance frequency and generates a filtering effect with a –90° phase lag after the first resonance frequency. A piezoresistive MEMS velocity sensor presented in the literature was explored to confirm the effectiveness of the concept that drives the current 2-DoF velocity sensor. Such technique, however, is susceptible to temperature changes, presents low sensitivity and requires several fabrication steps. To avoid these drawbacks, the sensor proposed in this research was specifically designed with a capacitive transducer and an actuation technique. The sensor interface and the controller are implemented on a printed circuit board. The control loop and closed-loop response were designed by a post-process intended to measure frequency response functions (FRFs) for the displacements of the two proof masses with respect to (i) base acceleration and (ii) the electrostatic actuator applied to the principal proof mass. The comparison of the simulated and measured FRFs indicates that the MEMS sensor dynamically and closely reproduces the desired 2-DoF response. The first prototype sensor was fabricated on a silicon-on-insulator (SOI) wafer with two masks. Below 1 kHz, the measured output signal of the closed-loop sensor is proportional to the velocity of the base. Above the fundamental resonance, the output signal rolls off with a phase lag of –90°. The second prototype sensor is grounded on an innovative design and fabrication process, which enabled the direct measurement of the relative displacement between the two proof masses. The measurement was conducted using a capacitive transducer and mechanical subtraction. The second prototype was fabricated on an SOI wafer with three masks. The post-process of the measured data shows that at low frequencies (between about 300 Hz and 1 kHz), the spectrum of the sensor’s output signal is proportional to the base velocity. Around the fundamental resonance frequency, the characteristic resonance peak flattens and the phase lag decreases to –90°. These three properties are of considerable interest for the implementation of vibration control systems that use feedback loops with a collocated velocity sensor and piezoelectric patch actuator pairs.

# Table of Contents

<b>ABSTRACT</b> .....	<b>i</b>
<b>Table of Contents</b> .....	<b>ii</b>
<b>List of Tables</b> .....	<b>vii</b>
<b>List of Figures</b> .....	<b>ix</b>
<b>DECLARATION OF AUTHORSHIP</b> .....	<b>xvii</b>
<b>Acknowledgements</b> .....	<b>xix</b>
<b>Abbreviations</b> .....	<b>xxi</b>
<b>Symbols</b> ... ..	<b>xxiii</b>
<b>Chapter 1: Introduction</b> .....	<b>1</b>
1.1 Introduction.....	1
1.2 Motivation and Contribution .....	2
1.3 Thesis Structure .....	4
<b>Chapter 2: Fundamental Principles</b> .....	<b>7</b>
2.1 Introduction.....	7
2.2 Vibratory System Modelling .....	7
2.2.1 Single-Degree-of-Freedom System .....	7
2.2.2 Two-Degrees-of-Freedom System.....	9
2.3 The Principle of Capacitive MEMS Sensors .....	16
2.3.1 Capacitive Transduction .....	16
2.3.2 Capacitive Actuation .....	17
2.4 Damping Coefficient Estimation .....	19
2.4.1 Squeeze Film Damping.....	19
2.4.2 Slide Film Damping.....	20
2.5 Spring Constant.....	21
2.6 Vibration Control.....	24
2.7 Summary.....	27
<b>Chapter 3: Literature Review</b> .....	<b>29</b>
3.1 Introduction.....	29
3.2 Vibration Control System Using a Velocity Feedback Loop .....	29
3.2.1 Velocity Measurement Using an Accelerometer .....	29

3.2.2	Velocity Measurement Using a Two-Degree-of-Freedom MEMS Velocity Sensor.....	32
3.2.3	Velocity Measurement Using a Geophone .....	37
3.2.4	Velocity Measurement Using a Laser Doppler Vibrometer .....	38
3.3	Multi-Degree-of-Freedom Capacitive MEMS Devices.....	39
3.3.1	Gyroscope Capacitive MEMS Sensor with Multi-DoF Structure .....	39
3.3.2	Energy Harvesting Capacitive MEMS Devices with Multi-DoF Structure.....	41
3.4	Microfabrication Using Silicon-on-Insulator Technology.....	42
3.4.1	Two-Mask Dry-Release Method .....	43
3.4.2	Dicing-Free Dry-Release Method.....	44
3.5	Electric Isolation of the Device Layer in SOI Wafer.....	44
3.5.1	Electric Isolation Using Handle and SiO <sub>2</sub> Layers.....	45
3.5.2	Electric Isolation Using Silicon Dioxide Deposition.....	46
3.5.3	Electric Isolation Using SU-8 Photoresist .....	47
3.6	Summary .....	48
<b>Chapter 4: Velocity Sensor Theoretical Analysis.....</b>		<b>51</b>
4.1	Introduction.....	51
4.2	Operating Concept of the Velocity Sensor .....	51
4.3	Dynamic Response Functions.....	53
4.4	Velocity Sensor Closed-Loop Transfer Function .....	59
4.5	Control Gain and Feedback Loop Stability .....	61
4.6	Summary .....	68
<b>Chapter 5: Implementation and Measurements for the First Prototype Capacitive MEMS Velocity Sensor .....</b>		<b>71</b>
5.1	Introduction.....	71
5.2	Mechanical Structure of the Sensing Element .....	71
5.3	Fabrication of the First Prototype .....	74
5.4	Interface and Control Electronic Circuit.....	76
5.4.1	Pickoff Circuit .....	77
5.4.2	Control Circuit .....	82
5.5	Experimental Measurement of Dynamic Response Functions .....	84
5.6	Stability and Design of the Velocity Feedback Loop .....	88

5.7	Closed-Loop Response .....	92
5.8	Design Issues of the First Prototype Sensor .....	94
5.9	Summary.....	95
<b>Chapter 6:</b>	<b>Mechanically Coupled and Electrically Isolated Two-Degree-of-Freedom Capacitive MEMS Velocity Sensor.....</b>	<b>97</b>
6.1	Introduction.....	97
6.2	Operation Concept .....	97
6.3	Mechanical Design of the Sensing Element .....	98
6.4	Finite Element Analysis.....	101
6.5	Fabrication .....	102
6.6	Interface and Control Circuit .....	107
6.7	Dynamic Response Functions.....	108
6.8	Measurement of Pickoff Circuit Gain.....	113
6.9	Design of the Internal Velocity Feedback Loop.....	116
6.10	Closed Loop Measurement .....	120
6.11	Electrostatic Spring Softening Effect in Closed Loop Measurement.....	122
6.12	Design Issues of the Second Prototype Sensor.....	124
6.13	Summary.....	125
<b>Chapter 7:</b>	<b>Conclusion and Future Work.....</b>	<b>127</b>
7.1	Conclusion .....	127
7.2	Future Work.....	129
7.2.1	Enhancing the Pickoff Circuit Performance .....	129
7.2.2	Design Consideration of the Sensing Element .....	130
<b>Appendices.....</b>		<b>133</b>
<b>Appendix A.....</b>		<b>133</b>
A.1	Frequency Response Functions of the Input Acceleration and Electrostatic Force .....	133
A.2	MATLAB Code of the Control Gain $g$ With Real Integrator.....	135
A.3	MATLAB Code of the Control Gain $g$ With Real Integrator and 2 <sup>nd</sup> Order Low Pass Filter (LPF).....	137
A.4	Open Loop Control Transfer Function Using Simulated and Measured FRF	140
A.5	Post Process for Closed Loop Prediction Using Simulated and Measured FRF .....	145
<b>Appendix B.....</b>		<b>151</b>
B.1	First Prototype PCB .....	151
B.2	Second Prototype PCB.....	153

<b>Appendix C .....</b>	<b>155</b>
C.1 Lithography.....	155
C.2 SiO <sub>2</sub> Layer Coating Using PECVD.....	157
C.3 Hard Mask SiO <sub>2</sub> Etch Using ICP Etching.....	159
C.4 DRIE of the Device Layer .....	160
C.5 DRIE of the Handle Layer Using Soft Mask.....	161
C.6 DRIE of the Handle Layer Using Hard Mask.....	162
<b>List of References .....</b>	<b>163</b>



## List of Tables

Table 5-1: First prototype capacitive MEMS velocity sensor parameters. ....	73
Table 5-2: Sense capacitors dimensions and capacitance values of the first prototype 2-DoF velocity sensor. ....	74
Table 6-1: Physical geometries of the principal and secondary proof masses, and sense and actuator capacitor electrode taken from the mask layout.....	100
Table 6-2: Physical and electronic parameters of the 2-DoF capacitive MEMS velocity sensor. ....	101



## List of Figures

Figure 2-1: Basic mass-spring-damper model for the S-DoF system. ....	7
Figure 2-2: Bode plot of the transfer function in equation 2-4 with the S-DoF parameters: $m = 1 \text{ mg}$ , $b = 1 \text{ mN.s/m}$ , and $k = \{10, 50, 100\} \text{ N/m}$ . The resonance frequency increases proportionally with the spring constant, while the DC sensitivity decreases. ....	9
Figure 2-3: Two-degrees-of-freedom system block diagram. ....	10
Figure 2-4: Two-degrees-of-freedom system free-body diagram. ....	11
Figure 2-5: A differential parallel plate capacitor used in inertial MEMS sensors. ....	16
Figure 2-6: Capacitive actuation mechanism with proof mass. ....	17
Figure 2-7: A differential lateral comb capacitor used in inertial MEMS sensors. ....	18
Figure 2-8: Squeeze film air flow: (a) squeezed air flow if plates are moving towards each other; (b) drawn air flow if plates are moving away from each other (reproduced from [42]). ....	19
Figure 2-9: Slide film air flow (reproduced from [42]). ....	21
Figure 2-10: Fixed-guided single-beam structure in inertial MEMS sensors. ....	21
Figure 2-11: Fixed-guided single-beam structure in inertial MEMS sensors with trapezoidal cross section due to fabrication imperfection. ....	23
Figure 2-12: Fixed-guided folded beam. ....	23
Figure 2-13: Active vibration control topology; (a) feed-forward control for periodic vibration source and (b) feedback control for random vibration source (reproduced from [24]). ....	25
Figure 2-14: Different feedback loop vibration controllers with their open-loop control function frequency responses; (a) direct velocity feedback that synthesises active damping control, (b) displacement feedback that synthesises active stiffness control and (c) acceleration feedback that synthesises active mass control (reproduced from [24]). ....	26
Figure 3-1: (a) Simple block diagram of a single-unit vibration control system using an accelerometer and patch actuator (reproduced from [24]). (b) Smart panel with multiple decentralised velocity feedback control units (reproduced from [25]). ....	30
Figure 3-2: Smart panel applications using a velocity feedback control loop for an active damping control system; (a) the back side of the panel shows 16 piezoceramic patch actuators and (b) the top side of the panel shows 16 accelerometer sensors (reproduced from [21]). ....	30

Figure 3-3: Simulated open-loop frequency response function of the sensor/actuator pair (reproduced from [17]).....	31
Figure 3-4: First prototype micro-scale velocity sensor, which comprises two beam-proof masses connected in series and an induction coil actuator for the implementation of an internal velocity feedback loop; (a) block diagram of the velocity sensor and (b) implementation (reproduced from [60]).....	33
Figure 3-5: The micro-scale 2-DoF velocity sensor generates a frequency response function of up to 5 kHz, which was derived from the transfer function between the velocity sensor output and the velocity of sensor base value. The thin solid line represents the open-loop response, and the thick solid line denotes the closed-loop response (reproduced from [60]).....	34
Figure 3-6: Schematic of the 2-DoF MEMS piezoresistive velocity sensor (reproduced from [26]). .....	35
Figure 3-7: (Left) Detailed top view of the fabricated velocity sensor and (right) the 2-DoF MEMS piezoresistive velocity sensor in ceramic packaging (reproduced from [26]).	35
Figure 3-8: The measured frequency response of the 2-DoF MEMS velocity shows the relationship between principal sensor output $V_a$ and the velocity of the sensor's frame ( $j\omega v$ ). The blue line represents the open-loop sensor, and the red line denotes the closed-loop sensor (reproduced from [26]).	36
Figure 3-9: Geophone GS-200DX frequency response with a voltage output per input velocity (inch/sec), showing a natural frequency around the 10 Hz and flat response afterward (reproduced from [65]).....	38
Figure 3-10: 3-DoF MEMS gyroscope; (a) 3-DoF gyroscope lumped model, (b) SEM of the gyroscope (reproduced from [75]).	40
Figure 3-11: (a) Experimental measurement of the sense mode of the two resonance frequencies and the drive-mode of the single resonance frequency; the overlap area between the two modes determines the sensor's bandwidth. (b) Experimental evaluation to the sense mode, which shows immunity to pressure changes in the flat region (reproduced from [75]).....	41
Figure 3-12: (a) 3-DoF lumped model and (b) system structure depicted using finite-element-method (FEM) software and SEM for the suspension (reproduced from [79]).....	42
Figure 3-13: Frequency response of the 3-DoF system showing three resonance frequencies (reproduced from [79]).....	42
Figure 3-14: SOI fabrication process with no release holes on proof mass (reproduced from [87]). .....	43

Figure 3-15: Fabrication process of the full wafer dicing-free dry-release. a) Back side etching process, b) front side etching process (device feature, release holes), c) HF vapour phase etching process and d) device, handle wafer and wafer grid separation (reproduced from [83]).	44
Figure 3-16: Sub-micro-gravity capacitive SOI micro accelerometer, (left) schematic diagram of the accelerometer, and (right) SEM photo of the back side of the proof mass (reproduced from [89]).	45
Figure 3-17: Micro-mirror plate microfabrication steps. (a-c) front-side DIRE, (d-g) preservation of the back side of the mirror and DRIE, (h and h') micro-mirror release using wet etching and (i) Cr/Au coating. (Copied from [90])	46
Figure 3-18: A cross-section SEM. (Left) the silicon wall array 30 $\mu\text{m}$ deep using electrochemical etching and (right) the thick $\text{SiO}_2$ layer deposited using thermal oxidation process (a, b, c and d) show a closer view of the deposited $\text{SiO}_2$ (reproduced from [92]).	47
Figure 3-19: Trapped air after spinning the SU-8.	48
Figure 4-1: Two-DoF velocity sensor block diagram.	52
Figure 4-2: Two-DoF velocity sensor free-body diagram.	53
Figure 4-3: Simulink model of the 2-DoF sensing element represented with equations 4-4 (a, b).	55
Figure 4-4: Simulated FRFs of principal system output $Y$ (blue/dashed line), secondary system output $Z$ (red/solid line), and secondary system output $X$ (green/dashed-dotted line) with respect to the input acceleration $Acc$ .	57
Figure 4-5: Simulated FRFs of principal system output $Y$ (blue/dashed line), secondary system output $Z$ (red/solid line), and secondary system output $X$ (green/dashed-dotted line) with respect to the input electrostatic force $F_s$ applied to the principal sensor.	57
Figure 4-6: Bode plot of the integrator function in equation 4-13 with a $K_{int} = 1$ and a cut-off frequency at 10 Hz.	60
Figure 4-7: Control gain frequency-dependent function. Because the maximum control gain is at 1.8k, the control gain values from the blue line will not be valid for stable and causal closed-loop systems.	63
Figure 4-8: Bode plot of the open-loop control transfer function using an integrator function with $K_{int} = 1$ and cut-off frequency at 10 Hz; the maximum control gain is 65.5 dB.	64
Figure 4-9: Bode plot of the second-order low-pass filter with a cut-off frequency at 2 kHz.	65
Figure 4-10: Bode plot of the open-loop control transfer function with second-order low-pass filter. The maximum control gain is 104 dB.	65

Figure 4-11: Control gain frequency-dependent function with a second-order low-pass filter. The control gain values from the blue line are only valid for stable and causal closed-loop systems, which is also well below the maximum control gain at 165k... 66

Figure 4-12: Open (red line) and closed (blue line) loop velocity sensor frequency response, using the control gain  $g=73k$ , an integrator with cut-off frequency at 10 Hz and a second-order low-pass filter with a cut-off frequency at 2 kHz..... 67

Figure 5-1: A conceptual design of the first prototype sensor shows the principal proof mass  $m_p$  is anchored to the frame with four straight beams, and the secondary proof mass  $m_s$  suspended within the principal proof mass with four folded-beam springs. The device layer thickness is  $50 \times 10^{-6}$  m. .... 72

Figure 5-2: Measurement of the average dimensions of the trapezoidal cross section of (a) the principal system straight beams and (b) secondary system folded-beam..... 73

Figure 5-3: SOI wafer fabrication process for the first prototype velocity sensor. .... 75

Figure 5-4: (a) SEM photo of the 2-DoF capacitive MEMS sensing block, showing proof masses  $m_p$  and  $m_s$ , sense capacitors  $C_{sp}$  and  $C_{ss}$  and actuation capacitor  $C_{ap}$ ; (b) enlarged SEM photo of the lower left part of the sensing block, showing folded spring  $k_s$ ; and (c) upper right part of the sensing element, showing the parallel plates and lateral comb capacitor  $C_{ssl}$  and  $C_{apl}$ , respectively. .... 76

Figure 5-5: Diagram of the velocity sensor interface and control circuit block. .... 77

Figure 5-6: Schematic of the pickoff circuit showing the differential sense capacitor with parasitic capacitors, charge integrator, diode AM demodulation, and instrumentation amplifier. .... 78

Figure 5-7: Pickoff circuit simulated measurement using PSpice, showing (a) the proof mass displacement, (b) a charge integrator AM signal with 1-MHz frequency and (c) the instrumentation amplifier of the differential output signal..... 79

Figure 5-8: Charge integrator measured Bode plot of the principal sensor (blue line) and the secondary sensor (red line), both responses have  $-180^\circ$  phase in the region between overlapping in the 1.5MHz – 1.7MHz. .... 80

Figure 5-9: Differential line subtraction circuit for measuring the relative displacement  $x$  of the secondary proof mass with respect to the principal proof mass..... 81

Figure 5-10: Top view of the interface and control circuit of the 2-DoF velocity sensor. .... 81

Figure 5-11: Integration circuit..... 82

Figure 5-12: Electrostatic feedback force circuit..... 83

Figure 5-13: Experimental setup used to measure the FRFs of the 2-DoF velocity sensor using (a) the Agilent signal analyser (35670A); the FRFs of the principal and secondary sensors were measured for output signals  $y$  and  $z$  with respect to (b) the

electrostatic force applied to the principal sensor and (c) the external input acceleration.....	84
Figure 5-14: Simulated (dashed blue line) and measured (solid red line) (a) $G_{Y,Acc}$ and (b) $G_{Z,Acc}$ .....	85
Figure 5-15: Simulated (dashed blue line) and measured (solid red line) (a) $G_{Y,Fs}$ and (b) $G_{Z,Fs}$ .....	86
Figure 5-16: Simulated (dashed blue line) and measured (solid red line) FRFs of relative displacement $x$ , (a) $G_{X,Acc}$ and (b) $G_{X,Fs}$ .....	88
Figure 5-17: Bode plot of the measured (solid red lines) and simulated (dashed blue lines) FRFs of control open-loop function $G_{ol,x,fs}(\omega)$ . The plot shows the $-180^\circ$ phase crossover frequency at the second resonance frequency. Accordingly, the maximum stable feedback gain is about 66 dB. ....	89
Figure 5-18: The blue line represents the simulated frequency-dependent control gain that eliminates the imaginary part of the closed-loop transfer function. The dashed red line is the maximum gain for the stable feedback loop. ....	90
Figure 5-19: Bode plot of the measured (solid red lines) and simulated (dashed blue lines) FRFs of the control open-loop function $G_{ol,x,fs}(\omega)$ with a second-order low-pass filter. The maximum stable feedback gain is about 104 dB. ....	91
Figure 5-20: The solid blue line is the simulated frequency-dependent control gain that eliminates the imaginary part of the closed-loop transfer function with a compensator. The dashed red line represents the maximum stable gain of the feedback loop with a compensator. ....	92
Figure 5-21: Simulated (a) and measured (b) frequency responses of the output signal $y$ from the sensor per unit sensor's frame velocity with internal open (dashed blue lines) and closed (solid red lines) feedback loops. ....	93
Figure 6-1: Schematic of the 2-DoF velocity sensor. ....	98
Figure 6-2: Simplified mechanical design of the 2-DoF capacitive MEMS sensor showing the electric isolation trenches, the principal sensor with a proof mass $m_p$ , top and bottom sense capacitor $C_{ps\_top,bot}$ for measuring the displacement $y$ of proof mass $m_p$ , the secondary sensor with a proof mass $m_s$ and top and bottom sense capacitor $C_{ss\_top,bot}$ for measuring displacement $x$ .....	99
Figure 6-3: Geometries of the (a) folded-flexure beam of the principal sensor, (b) double-folded beam of the principal sensor, and (c) folded beam of the secondary sensor..	100
Figure 6-4: Finite element analysis of the 2-DoF sensing element using CoventorWare. It shows that the (a) 1st mode or first resonance frequency is at 1.2 kHz, the (b) 2nd mode or resonance frequency is at 3.9 kHz, the (c) 3rd mode is at 6.74 kHz and the (d) 4th mode is at 10.8 kHz. ....	102

Figure 6-5: SOI microfabrication steps for the proposed 2-DoF velocity sensor. (a) Device and handle layer hard and soft masks, (b) DRIE handle layer using a soft mask, (c) DRIE device layer using a hard mask (d) DRIE handle layer using hard mask, (e) dry-release step using an HF vapour phase etcher. The areas A and B of the proof masses are electrically isolated. The handle layer support structure holds the fragmented proof mass. .... 104

Figure 6-6: SEM image of a development wafer for the two DRIE processes for the handle layer. Given the insufficient fluorine ion etching agents, the trenches narrow at the end and the grass effect occurs. The grassing occurs at the bottom of the trench and on the edges of the support structure. .... 105

Figure 6-7: HF vapour phase etch step of the first successful fabrication batch, (a) shows the thermal chuck that carries the released devices on the carrier wafer with some released unwanted handle layer pieces, (b) the SOI wafer after the release process, it shows some of the unreleased devices because of the handle layer was not completely processed, and it also shows the alignment marks used during the lithography processes. .... 105

Figure 6-8: Front-side SEM images of the 2-DoF sensing element; (left) full view of the sensor showing the secondary proof mass anchored onto the principal proof mass and the principal proof mass anchored onto the frame; (right) close view of the sensor showing the electric isolation trenches and the principal and secondary top sense electrodes. .... 106

Figure 6-9: Back-side SEM images of the 2-DoF sensing element; (left) full view of the sensor showing the handle layer support structure under the principal and secondary proof masses; (right) close view of the sensor showing the electric isolation trenches and the handle layer support structure. .... 106

Figure 6-10: Block diagram of the interface and control electronic circuit of the second prototype velocity sensor. .... 107

Figure 6-11: Interface and control circuit of the second prototype velocity sensor under test. The accelerometer reference sensor is closely aligned to 2-DoF MEMS sensing element during the acceleration response measurement using shaker table. .. 108

Figure 6-12: Simulated (blue/dashed line) and measured (red/solid line) FRFs of the acceleration input (a)  $G_{Y,Acc}$  and (b)  $G_{X,Acc}$ . .... 110

Figure 6-13: Simulated (blue/dashed line) and measured (red/solid line) FRFs of the electrostatic force input applied to the principal sensor (a)  $G_{Y,F_s}$  and (b)  $G_{X,F_s}$ . .... 111

Figure 6-14: Simulink model of the second prototype 2-DoF velocity sensor for the analysis of the pickoff noise generated by the secondary sensor. .... 112

Figure 6-15: Simulated power spectral density of the secondary sensor transfer function $G_{X,Fs}$ including pickoff noise. ....	112
Figure 6-16: Experimental measurement of power spectral density for the electronic noise of the secondary sensor pickoff circuit. The measurement was conducted using Agilent 35670A signal analyser. The electronic noise is around $150 \mu V/\sqrt{Hz}$ for the bandwidth below the first resonance frequency of the 2-DoF. ....	113
Figure 6-17: Experimental measurements of the pickoff circuit of the principal sensor; (a) the output voltage of the pickoff is 4.63 Vpp and (b) the peak-to-peak MSA400 optical measurement of the principal proof mass displacement is 2.85 $\mu m$ . .	115
Figure 6-18: Experimental measurements of the pickoff circuit of the secondary sensor; (a) the output voltage of the pickoff is 7.1 Vpp and (b) the peak-to-peak MSA400 optical measurement of the secondary proof mass displacement 2.17 $\mu m$ . ...	115
Figure 6-19: Simulated frequency-dependent control gain values (blue/solid line). For stable feedback loop, only g values under 103 dB are valid for applying the required damping force on the principal sensor. ....	117
Figure 6-20: Simulated control open loop transfer function $G_{ol-X-Fs}$ shows the $-180^\circ$ phase crossover at the second resonance, which determines the maximum stable control gain of 103 dB. ....	118
Figure 6-21: Simulated bode plots of control open loop transfer function $G_{ol-X-Fs}$ with low-pass filter addition; the image shows the $-180^\circ$ phase crossover at the second resonance, which determines the maximum stable control gain of 112 dB...	119
Figure 6-22: Simulated frequency-dependent control gain values (blue/solid line) with the low-pass. Dashed/red line is the maximum gain is 112 dB. ....	120
Figure 6-23: Simulated open-loop (solid/blue line) and closed-loop (dashed/red line) Bode plots using transfer function $G_Y(s)$ , where the open loop response of the sensor using $g=0$ , and closed loop response using $g=110.37$ dB at 500 Hz. ....	121
Figure 6-24: Open and closed loop measurement of the velocity sensor output Y per unit of the velocity of the sensor's frame. The blue/dotted line is the measured open loop response, red/solid line is the measured closed loop response, and green/dashed line is the simulated closed loop respons. ....	122
Figure 6-25: Simulated (blue/dashed line) and experimental (red/solid line) closed loop measurement of the velocity sensor output Y per unit of the velocity of the sensor's frame. The simulation measurement includes the spring softening effect; for both measurements, the phase around the resonant frequency shows a change from $-180^\circ$ to $180^\circ$ . ....	123



# DECLARATION OF AUTHORSHIP

I, **Ali Alshehri**, declare that the thesis entitled “**Two Degree of Freedom Capacitate MEMS Velocity Sensor**” and the work presented in it are my own and has been generated by me as the result of my own original research. I confirm that:

1. This work was done wholly or mainly while in candidature for a research degree at this University;
2. Where any part of this thesis has previously been submitted for a degree or any other qualification at this University or any other institution, this has been clearly stated;
3. Where I have consulted the published work of others, this is always clearly attributed;
4. Where I have quoted from the work of others, the source is always given. With the exception of such quotations, this thesis is entirely my own work;
5. I have acknowledged all main sources of help;
6. Where the thesis is based on work done by myself jointly with others, I have made clear exactly what was done by others and what I have contributed myself;
7. Parts of this work have been published as:

1- Alshehri, A., Almutairi, B., Gardonio, P., Kraft, M., “*Design, fabrication and implementation of a capacitive MEMS velocity sensor based on mechanically coupled and electrically isolated two-degree-of-freedom systems*” (submitted to J-MEMS – under review).

2- Alshehri, A., Almutairi, B., Gardonio, P., Kraft, M., “*Two-degree of freedom capacitive MEMS velocity sensor with two coupled electrically isolated mass-spring-damper systems*”, *IEEE Sensors 2014*, pp. 1603-1606, 2-5 Nov. 2014.

3- Alshehri, A, Kraft, M., Gardonio, P., “*Two-mass MEMS velocity sensor: Internal feedback loop design*”, *IEEE Sensors Journal*, vol.13, no.3, pp.1003-1011, March 2013

4- Alshehri, A, Kraft, M., Gardonio, P., Elliott, S., Zilletti, M., “*Two-mass MEMS velocity sensor feedback control loop design*”, *IEEE Sensors 2011*, pp.153-156, 28-31 Oct. 2011

5- Alshehri, A., Gardonio, P., Elliott, S., Zilletti, M., Kraft, M., “*Experimental evaluation of a two degree of freedom capacitive MEMS sensor for velocity measurements*”, *Procedia Engineering*, Vol. 25, pp 619-622, 4-7 Sept. 2011

6- Alshehri, A., Kraft, M., Gardonio, P., “*Two-degree-of-freedom capacitive MEMS velocity sensor: Initial test measurements*”, *MME2010 Workshop*, pp.269-272, 26-29 Sept. 2010

Signed:.....

Date: .....

## Acknowledgements

First of all, I would like to express my gratitude to my supervisor, Professor Michael Kraft, for the great opportunity that he offered me to do my PhD research with him. He gave me invaluable support, assistance and guidance during my research.

I would also like to thank Professor Paolo Gardonio for his guidance during my research and the valuable time he spent discussing fundamental details of the theoretical and practical work.

Furthermore, I would like to thank my brother-in-law, Bader Almutairi, for all the help and support he offered me with my PhD research. Also, I would like to thank my colleagues Ioannis, Owain, Reuben, Pajwaak, Tess and Michele for their advice and friendship.

Moreover, I am grateful to my warm-hearted mother, who has devoted her life to us. I would like to thank my brothers, Abdulhakim, Murad, Moayyad, Mohammad, Abdulrahman, Faisal and Bader, and my two beloved sisters for their support along my PhD journey.

I deeply grateful to my faithful wife for her priceless encouragement, support, and endless patience at all times with our beautiful kids, Abdullah and Wateen.

I am eternally grateful to my father, who supported me throughout my studies until the last day of his life, 1 March 2013; may Allah grant him the highest place in Jannah.

Last, but not least, I am thankful to the King Abdulaziz City for Science and Technology (KACST<sup>1</sup>) for the scholarship and support that allowed me to pursue my PhD degree at the University of Southampton.

---

<sup>1</sup> [www.kacst.edu.sa](http://www.kacst.edu.sa), Riyadh – Saudi Arabia



## Abbreviations

AM	amplitude modulation
ASIC	application-specific integrated circuit
BOX	buried oxide layer in SOI wafer
C-V	capacitance to voltage
CDS	correlated double sampling
CVC	capacitance-to-voltage converter
CVD	chemical vapour deposition
DC	direct current
DI water	deionized water
DoF	degree-of-freedom
DRIE	deep reactive ion etching
EMI	electromagnetic field interference
FEM	finite element method
FRF	frequency response function
HF	hydrofluoric acid
ICP	inductively coupled plasma
LDV	laser Doppler vibrometer
LPF	low pass filter
LPF2	second order low pass filter
MEMS	micro-electro-mechanical systems
MSA	micro system analyser
Op-amp	operational amplifier

PECVD	plasma-enhanced chemical vapour deposition
PCB	printed circuit board
PR	photoresist
PSD	power spectral density
RIE	reactive ion etching
rpm	rotation per minute
S-DoF	single-degree-of-freedom
SC	switched capacitor pickoff circuit
SEM	scanning electron microscope
Si	Silicon
SiO <sub>2</sub>	silicon dioxide
SMD	surface mount device
SOI	silicon-on-insulator

## Symbols

$a, Acc$	acceleration signal in Laplace domain
$A$	area ( $m^2$ )
$b$	damping coefficient
$bp$	principal sensor damping coefficient
$bs$	secondary sensor damping coefficient
$C$	capacitance (F)
$C_{ap}$	actuation capacitor of the principal sensor
$C_f$	Charge integrator feedback capacitor
$C_{fi}$	Feedback capacitor of the integration circuit
$C_{sp}$	sense capacitor of the principal sensor
$C_{ss}$	sense capacitor of the secondary sensor
$d_0$	nominal gap between capacitor electrodes
$\epsilon$	air gap between capacitor electrodes permittivity
$E$	Young's modulus, which is $169 \times 10^9 \text{ N/m}^2$
$f_c$	cut-off frequency (Hz)
$f_{np}$	principal sensor natural frequency
$f_{ns}$	secondary sensor natural frequency
$f_s, Fs$	electrostatic force applied on the principal proof mass
$F_{1,2}$	first, second resonance frequency of the 2-DoF sensor
$g$	feedback loop control gain
$G_{ol,X,Fs}$	open-loop control transfer function

$G_{X,Acc}$	frequency response function of the secondary sensor output X due acceleration input
$G_{X,Fs}$	frequency response function of the secondary sensor output X due electrostatic force input
$G_{Y,Acc}$	frequency response function of the principal sensor output Y due acceleration input
$G_{Y,CL}$	closed loop frequency response function of the velocity sensor
$G_{Y,Fs}$	frequency response function of the principal sensor output Y due electrostatic force input
$G_{Z,Acc}$	frequency response function of the secondary sensor output Z due acceleration input
$G_{Z,Fs}$	frequency response function of the secondary sensor output Z due electrostatic force input
H	height (m)
L	length (m)
$k_e$	electrostatic spring
k	spring constant
$K_{int}$	integrator circuit gain
$k_p$	principal sensor spring constant
$K_{pp}$	pickoff gain of the principal sensor
$K_{ps}$	pickoff gain of the secondary sensor
$k_s$	secondary sensor spring constant
Mag.	magnitude of the Bode plot
m	proof mass
$m_p$	principal sensor proof mass

$m_s$  secondary sensor proof mass  
 $Q$  quality factor  
 $R_f$  charge integrator feedback resistor  
 $R_{fa}$  input resistor of the gain circuit  
 $R_{fb}$  feedback resistor of the gain circuit  
 $R_{ff}$  feedback resistor of the feedback circuit  
 $R_{fi}$  feedback resistor of the integration circuit  
 $R_{f1,2}$  input resistor of the feedback circuit  
 $R_{ini}$  input resistor of the integration circuit  
 $s$  Laplace parameter  
 $\tau$  time constant (sec)  
 $V_{el}$  Velocity (m/sec)  
 $V_b$  bias voltage  
 $V_{bot\_ele}$  Voltage signal applied to the bottom actuator  
 $V_{fb}$  feedback signal voltage  
 $V_c$  charge integrator output voltage  
 $V_i$  output voltage signal of the integration circuit  
 $V_{pp}$  peak-to-peak voltage  
 $V_r$  carrier signal  
 $V_{top\_ele}$  Voltage signal applied to the top actuator  
 $V_x$  output signal of the subtraction circuit  $V_x = V_z - V_y$  (secondary proof mass relative displacement with respect to the principal proof mass)  
 $V_y$  pickoff circuit output voltage of the principal sensor

$V_z$  pickoff circuit output voltage of the secondary sensor (first prototype PCB)  
 $\omega$  frequency (rad/sec)  
 $W$  width (m)  
 $w_c$  Cut-off frequency of the second order low pass filter (rad/sec)  
 $w_1$  sensor's frame displacement  
 $w_2$  principal proof mass displacement  
 $w_3$  secondary proof mass displacement  
 $w'_1$  sensor's frame velocity  
 $w'_2$  principal proof mass velocity  
 $w'_3$  secondary proof mass velocity  
 $w''_1$  sensor's frame acceleration  
 $w''_2$  principal sensor acceleration  
 $w''_3$  secondary sensor acceleration  
 $x$  secondary proof mass relative displacement with respect to the principal proof mass  
 $x'$  secondary proof mass relative velocity with respect to the principal proof mass  
 $x''$  secondary proof mass relative acceleration with respect to the principal proof mass  
 $y$  principal proof mass relative displacement with respect sensor's frame  
 $y'$  principal proof mass relative velocity with respect sensor's frame  
 $y''$  principal proof mass relative acceleration with respect sensor's frame  
 $z$  secondary proof mass relative displacement with respect sensor's frame  
 $z'$  secondary proof mass relative velocity with respect sensor's frame  
 $z''$  secondary proof mass relative acceleration with respect sensor's frame

بِسْمِ اللَّهِ الرَّحْمَنِ الرَّحِيمِ

In the name of Allah, the most gracious, the most merciful



# Chapter 1: **Introduction**

## **1.1 Introduction**

The micromachining technology employed by semiconductor manufacturers is used to fabricate miniature mechanical sensors, known as micro-electro-mechanical systems (MEMS). This well-established micromachining technology endows MEMS with the expansive ability to perform functions at excellent operation and accuracy whilst maintaining low cost [1–3]. The most common MEMS devices are inertial accelerometer and gyroscope sensors, which are used to determine the physical quantity of motion of a dynamic object by measuring its acceleration or angular velocity [4–6].

Noise and vibration control is becoming increasingly important for the ground and air transportation industries [7–10], which normally employ passive stiffness, damping and mass treatments to reduce vibration transmission and sound radiation problems [11]. During the past two decades, increasing interest has been directed towards active vibration control systems, with some applications already installed in surface and air transportation vehicles [12] [13]. Velocity feedback control is a preferred approach to generating structural active damping [14] because it guarantees unconditional stability when a collocated and dual sensor/actuator pair is used [15] [16].

Of particular interest is the concept of structural vibration control, wherein a velocity sensor is used to detect structural vibration in the low audio frequency range [17]. Such sensors can be coupled with an actuator to form a lightweight and compact control unit that implements active vibration control via a negative velocity feedback loop [18]. When this control unit is bonded on a flexible thin structure, such as a plate or a shell, it produces active damping force, which effectively absorbs vibration energy and reduces the response of the structure around the resonance frequencies of low-order structural modes [19]. When an array of these control units is bonded on a flexible structure, both vibration and sound radiation control are achieved at low audio frequencies [20-22].

## **1.2 Motivation and Contribution**

This research focuses on the design and implementation of a two-degree-of-freedom (2-DoF) capacitive MEMS velocity sensor. It is realised for application in a particular concept of smart panels, in which sensors and actuators are embedded on thin plates or shells to enable the implementation of an active vibration control system for velocity feedback loops.

A velocity feedback loop controller is typically implemented using an under-damped accelerometer followed by an integrator electronic circuit [23–25]. However, this type of configuration presents two problems: First, at high frequencies, the output of an under-damped accelerometer is characterised by a resonance frequency of a sharp peak and a phase lag of  $-180^\circ$ . Therefore, velocity measurement around the resonance frequency is proportional to velocity, but such measurement has a negative polarity. Consequently, a large positive feedback control signal drives the actuator, thereby causing control spillover and potentially leading to system instability [24]. The resonance peak of the accelerometer can be solved by using an over-damped accelerometer or a low-pass filter. In either case, however, the  $-180^\circ$  phase is distributed around the resonance frequency, thus reducing the bandwidth of velocity measurement. Nevertheless, the  $-180^\circ$  phase is still encountered at high frequency, where in practical implementation, additional phase lag is commonly introduced due to the actuator and the electronic circuit, which could lead to instability. The second problem is that the configuration does not provide direct velocity measurements, thus giving rise to the need for a real integrator that always exhibits a cut-off at low frequencies. This causes the velocity control loop to encounter  $+180^\circ$  phase before the cut-off frequency of the real integrator, again, this could lead to instability.

By contrast, the frequency response of a 2-DoF velocity sensor has three important properties. First, velocity is directly measured. Second, around its fundamental resonance, the sensor is characterised by a flat amplitude spectrum. Finally, above the fundamental resonance, it is characterised by an amplitude roll-off with only a  $90^\circ$  phase lag. The sensor therefore produces the desired velocity output up to the cut-off frequency set by its fundamental resonance frequency, after which it generates a filtering effect with only a  $90^\circ$  phase lag. With these functions, the sensor can prevent the instability and control

spillover encountered with a velocity feedback loop that employs an accelerometer sensor [17] [24].

Little research has been devoted to the use of 2-DoF MEMS sensors to measure the velocity of structures, even as this approach shows potential for overcoming the aforementioned problems. The only previously developed device in this regard is the MEMS piezoresistive demonstrator in [26]. It was fabricated using surface micromachining technology [27], which resulted in a relatively small proof mass and susceptibility to mechanical (Brownian) noise [28]. The fabrication required nine masks and 145 steps, which caused the sensor to be prone to fabrication tolerance, also resulting in a lengthy and costly fabrication process. Moreover, the piezoresistive technology used to measure proof mass displacement is prone to temperature changes and nonlinear effects and has relatively low sensitivity [28–30].

This research addresses the design and implementation of a 2-DoF capacitive MEMS velocity sensor. The sensor is designed to overcome the aforementioned problems encountered with the velocity sensor employing an accelerometer with an integrator and the piezoresistive velocity sensor. The fabrication of the sensor is based on silicon-on-insulator (SOI) wafer technology, which requires only a few fabrication masks and entails a minimal number of steps. The sensor employs capacitive transduction and actuation techniques, which improve a transducer's linearity, sensitivity and stability. The new sensor also benefits from a large proof mass, which reduces mechanical Brownian noise.

The 2-DoF capacitive MEMS velocity sensor comprises two mass–spring–damper systems that are mechanically connected in series. The first system is the principal sensor, which is used as the primary inertial sensing system for measuring velocity. The second mass–spring–damper system is used as a secondary sensor for the implementation of an internal velocity feedback loop via the capacitive actuator of the principal system. This feedback loop produces damping force on the principal proof mass. When the 2-DoF sensor is operated in closed-loop mode, the output of the sensor takes on three main features: It becomes proportional to the base velocity; the first resonance peak flattens; and after the first resonance frequency, the amplitude decreases with a  $-90^\circ$  phase lag. These three features of the proposed sensor are of considerable importance in the construction of a stable velocity feedback loop control that is used for the active vibration control of distributed flexible structures.

As part of this research, two prototypes of the 2-DoF capacitive MEMS velocity sensor were reported in [31-35]. The first prototype is fabricated with SOI technology that uses only two masks. To construct the internal velocity feedback loop of the sensor, the relative displacement between the two proof masses is indirectly obtained by electrically subtracting the two mass displacements with respect to the frame. The design of the second prototype sensor is based on an innovative method for directly measuring the relative displacement between the two proof masses by means of mechanical subtraction. This method entails the mechanical coupling and electrical isolation of the two mass–spring–damper systems. The sensor is fabricated using SOI wafer technology, for which the process requires only three masks. For each prototype, theoretical and simulation analyses are carried out, and interface and control circuits are implemented on a printed board circuit (PCB) using surface mount devices (SMD). The experimental measurements closely agree with the theoretical ones—an agreement that confirms the effectiveness of the concept that underlies the 2-DoF capacitive MEMS velocity sensor.

### **1.3 Thesis Structure**

The thesis is dedicated on the research of the new 2-DoF capacitive MEMS velocity sensor. It is structured into seven chapters.

Chapter 2 discusses some of the fundamental principles of the capacitive MEMS sensors. It addresses the system level modelling of the single-degree-of-freedom (S-DoF) and the 2-DoF system. The capacitive transducer and actuation technique are briefly discussed. The lumped parameters (i.e. proof mass, spring constant, and damper coefficients) are the core of the system model. Therefore, the damping coefficient and spring constant estimations are presented. A brief discussion about the vibration control is presented, to address some of the important aspects that are related to the velocity sensor.

Chapter 3 presents a literature review which explores several areas related to the 2-DoF capacitive MEMS velocity sensor, such as: the multi-DoF MEMS sensors, the possible methods to measure the velocity of a structure including the 2-DoF velocity sensor, and SOI technology fabrication methods that are adopted in the new fabrication process of the second prototype velocity sensor.

Chapter 4 illustrates the velocity sensor modelling and theoretical analysis. It starts with explanation of the concept of velocity sensor operation. The dynamic response functions

of the 2-DoF velocity sensor are derived with respect to the input acceleration and the electrostatic force applied to the principal mass–spring–damper system. Then, the control loop design and stability are discussed, and finally, the closed-loop mode of the velocity sensor is presented.

Chapter 5 expounds on the hardware implementation and the experimental measurements for the first prototype 2-DoF capacitive MEMS velocity sensor. SOI fabrication and the mechanical structure of the sensor are explained, after which the electronic interface and control circuit are presented. The dynamic response functions of the sensor are also measured. The design and stability of the control loop are discussed, and accordingly, the closed-loop response is presented. Finally, the design and implementation issues of the first prototype are explained.

Chapter 6 addresses the design and implementation of the second prototype 2-DoF velocity sensor, which is aimed at solving the problems encountered with the first prototype. The chapter describes the mechanical design of the sensor and then presents the finite element analysis. The developed SOI technology fabrication for the second prototype sensor is also provided, after which the new electronic circuit of the sensor is discussed. The chapter also expounds on the measured dynamic response functions and the control loop design and stability. Finally, the closed-loop response of the second prototype is discussed.

Finally, chapter 7 presents the research conclusion and addresses the future work that can be carried out on the capacitive MEMS velocity sensor.



## Chapter 2: Fundamental Principles

### 2.1 Introduction

This chapter presents the fundamental principles of the capacitive MEMS sensor, which are necessary for the design and implementation of the 2-DoF capacitive MEMS velocity sensor. The mass-spring-damper system modelling is discussed for S-DoF and a 2-DoF systems, along with the transfer functions that are used to analyse the dynamic response of both systems. The capacitive transduction and actuation techniques are briefly discussed, followed by a short explanation of the damping estimation and spring constant calculation. Finally, the vibration control is introduced, with an emphasis on the velocity feedback loop vibration control.

### 2.2 Vibratory System Modelling

#### 2.2.1 Single-Degree-of-Freedom System

The single-degree-of-freedom (S-DoF) system can be represented with a basic mass-spring-damper model, as shown in Figure 2-1. It comprises a proof mass  $m$  attached to the system base with an elastic element of a spring constant  $k$ , along with a dashpot symbol of damping coefficient  $b$ .

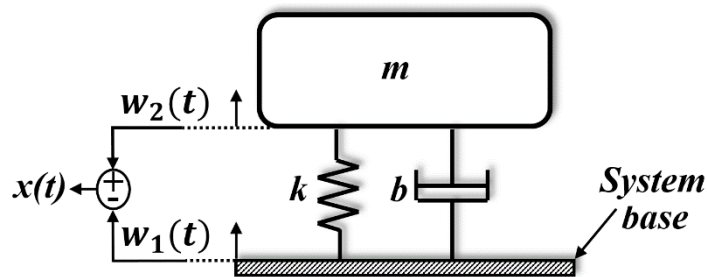


Figure 2-1: Basic mass-spring-damper model for the S-DoF system.

The relative displacement  $x$  is equal to the difference between the displacement of the base  $w_1$  and the displacement of the proof mass  $w_2$ , thus:

$$x = w_2 - w_1 \quad 2-1$$

## Chapter 2: Fundamental Principles

---

If the proof mass acceleration is denoted by  $\ddot{w}_2$ , the base and the proof mass velocity are denoted by  $\dot{w}_1$  and  $\dot{w}_2$ , respectively, then the time domain equation of motion of the mass-spring-damper model in Figure 2-1 can be derived by applying Newton's second law as follows:

$$m\ddot{w}_2(t) = b[\dot{w}_2(t) - \dot{w}_1(t)] + k[w_2(t) - w_1(t)] \quad 2-2$$

If the base acceleration ( $\ddot{w}_1$ ) is denoted by  $a$ , and the proof mass relative acceleration and velocity are  $\ddot{x}$  and  $\dot{x}$ , respectively, equation 2-2 can be represented as follows:

$$ma = m\ddot{x} + b\dot{x} + kx \quad 2-3$$

By applying the Laplace transform for equation 2-3, the transfer function of the S-DoF is given by:

$$\frac{x(s)}{a(s)} = \frac{1}{s^2 + \frac{b}{m}s + \frac{k}{m}} \quad 2-4$$

where  $s$  is the Laplace parameter.

The natural frequency of the S-DoF system is given by the following [36]:

$$\omega_0 = \sqrt{\frac{k}{m}} \quad 2-5$$

For constant acceleration (i.e.  $s=0$ ), the static sensitivity of the S-DoF system is equal to:

$$\text{Sensitivity} = \left. \frac{x(s)}{a(s)} \right|_{s=0} = \frac{m}{k} \quad 2-6$$

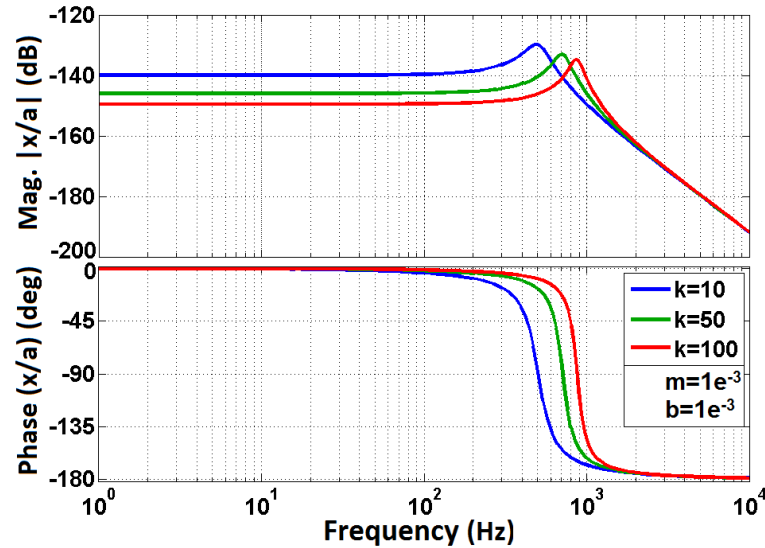


Figure 2-2: Bode plot of the transfer function in equation 2-4 with the S-DoF parameters:  $m = 1 \text{ mg}$ ,  $b = 1 \text{ mN.s/m}$ , and  $k = \{10, 50, 100\} \text{ N/m}$ . The resonance frequency increases proportionally with the spring constant, while the DC sensitivity decreases.

The frequency response of the S-DoF system with input acceleration (equation 2-4) is shown in Figure 2-2. In the frequency band below the resonance frequency, the displacement  $x$  is proportional to the base acceleration  $a$  with  $0^\circ$  phase, whereas the magnitude decreases with a phase lag of  $-180^\circ$  above the resonance frequency. This is a typical inertial accelerometer frequency response, where the bandwidth is determined by the resonance peak. As shown in Figure 2-2 and according to equation 2-5, the accelerometer bandwidth is proportional to the spring constant and to the inverse of the proof mass. On the other hand, as can be seen in Figure 2-2 and according to equation 2-6, the static sensitivity increases with a larger proof mass, and it decreases by increasing the spring constant. Therefore, the design of the accelerometer comes across as a trade-off between the bandwidth and the static sensitivity, which needs to be considered based on the application requirements.

### 2.2.2 Two-Degrees-of-Freedom System

A multi-degrees-of-freedom system (M-DoF) is more complex than the S-DoF system. As shown in the previous section, the S-DoF has only a single motion coordinate. The M-DoF system is different in that this type of system can be modelled as a combination of mass-spring-damper systems with a finite number of natural frequencies equal to the number of degrees of freedom.

The  $n$ -DoF system has  $n$  number of motion equations; each shows the relationship of the  $i^{\text{th}}$  ( $i=1$  to  $n$ ) mass with other mass-spring-damper systems parameters [37]. If the response of these motion equations are assumed linear, then each mass displacement can be modelled as the superposition of the effect produced by the external forces [24].

The 2-DoF system, as shown in Figure 2-3, can be represented with two motion coordinates,  $x_1$  and  $x_2$ , to define the displacements of mass  $m_1$  and  $m_2$ , respectively. These two displacements are taken with respect to the base of the 2-DoF system. Thus, the 2-DoF system has two motions of equations associated with each degree of freedom or, in other words, each mass. These two motion equations are mechanically coupled, where the motion of one mass will be influenced by the other.

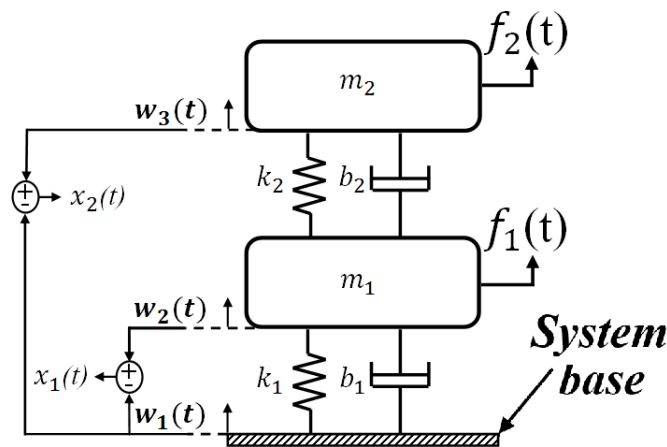


Figure 2-3: Two-degrees-of-freedom system block diagram.

Figure 2-3 shows the lower degrees-of-freedom mass  $m_1$  that is attached to the base with a dashpot of a damping coefficient  $b_1$  and with an elastic mount of a spring constant  $k_1$ . The mass  $m_2$  is stacked on top of mass  $m_1$  and attached with a dashpot of a damping coefficient  $b_2$  and an elastic mount with a spring constant  $k_2$ . The figure shows two external forces  $f_1$  and  $f_2$  applied to the mass  $m_1$  and  $m_2$ , respectively.

Deriving the motion equations is easier using the free-body diagram in Figure 2-4, which shows the different forces applied to the two masses with their directions. The base,  $m_1$  and  $m_2$  displacements are denoted as  $w_1$ ,  $w_2$  and  $w_3$ , respectively.

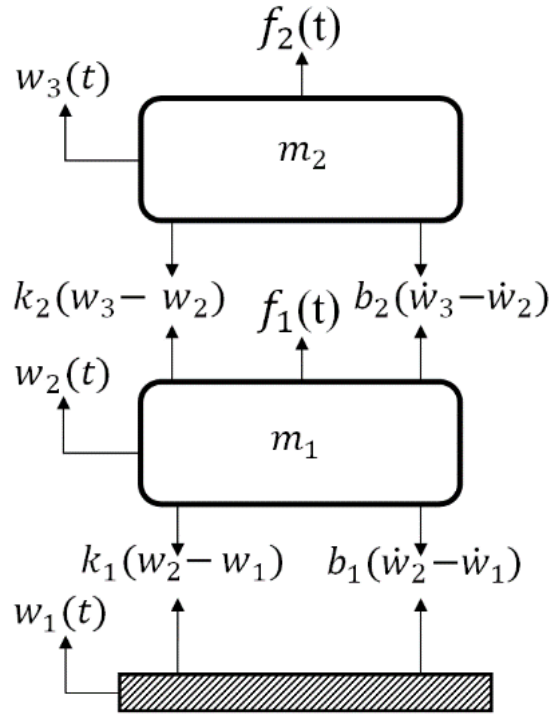


Figure 2-4: Two-degrees-of-freedom system free-body diagram.

If the velocity is given by the time derivative of the displacement, then  $w_1$ ,  $w_2$  and  $w_3$  are the velocities of the base,  $m_1$  and  $m_2$ , respectively. The same concept applies to the acceleration, which is the second derivative of the displacement, i.e.  $\ddot{w}_1$ ,  $\ddot{w}_2$  and  $\ddot{w}_3$ , respectively. The motion equations of the 2-DoF system, for the free-body diagram in Figure 2-4, can be derived by applying Newton's second law, as follows [38]:

$$\begin{aligned} m_1 \ddot{w}_2 &= -b_1(\dot{w}_2 - \dot{w}_1) - k_1(w_2 - w_1) + b_2(\dot{w}_3 - \dot{w}_2) + k_2(w_3 - w_2) + f_1 \\ m_2 \ddot{w}_3 &= -b_2(\dot{w}_3 - \dot{w}_2) - k_2(w_3 - w_2) + f_2 \end{aligned} \quad 2-7$$

If the relative displacement to the base of the two masses  $x_1$  and  $x_2$  are defined as

$$\begin{aligned} x_1 &= w_2 - w_1 \\ x_2 &= w_3 - w_1 \\ x_2 - x_1 &= w_3 - w_2 \end{aligned} \quad 2-8$$

and if the first time derivative of the relative displacement  $x_1$  and  $x_2$  gives the relative velocity  $\dot{x}_1$  and  $\dot{x}_2$ , and the second time derivative of the relative displacement gives the relative acceleration  $\ddot{x}_1$  and  $\ddot{x}_2$ , then the motion equations of the 2-DoF system in equation 2-7 can be rewritten as follows:

$$\begin{aligned} m_1\ddot{w}_1 &= -m_1\ddot{x}_1 - (b_1 + b_2)\dot{x}_1 - (k_1 + k_2)x_1 + b_2\dot{x}_2 + k_2x_2 + f_1 \\ m_2\ddot{w}_1 &= b_2\dot{x}_1 + k_2x_1 - m_2\ddot{x}_2 - b_2\dot{x}_2 - k_2x_2 + f_2 \end{aligned} \quad 2-9$$

The motion equation of the mass  $m_1$  in equation 2-9 includes terms involving the relative displacement of the mass  $m_2$ ; the equation of  $m_2$  in equation 2-9 also contains terms belonging to the relative displacement of mass  $m_1$ . This indicates the mechanical coupling, where the motion of either mass will be influenced by the other.

The following discussion is for the forced vibration analysis, where equation 2-9 can be written in the form of matrix differential equation as:

$$\begin{aligned} \begin{bmatrix} m_1 \\ m_2 \end{bmatrix} \ddot{w}_{c1} - \begin{bmatrix} f_1 \\ f_2 \end{bmatrix} &= \begin{bmatrix} -m_1 & 0 \\ 0 & -m_2 \end{bmatrix} \begin{bmatrix} \ddot{x}_1 \\ \ddot{x}_2 \end{bmatrix} + \begin{bmatrix} -b_1 - b_2 & b_2 \\ b_2 & -b_2 \end{bmatrix} \begin{bmatrix} \dot{x}_1 \\ \dot{x}_2 \end{bmatrix} + \\ &\begin{bmatrix} -k_1 - k_2 & k_2 \\ k_2 & -k_2 \end{bmatrix} \begin{bmatrix} x_1 \\ x_2 \end{bmatrix} \end{aligned} \quad 2-10$$

$$M_i \ddot{w}_{c1}(t) - F(t) = M \ddot{x}(t) + B \dot{x}(t) + Kx(t)$$

where  $M$ ,  $B$  and  $K$  are the mass, damping and spring-constant matrices of the 2-DoF system, respectively;  $M_i$  is the mass matrix;  $\ddot{x}(t)$ ,  $\dot{x}(t)$  and  $x(t)$  are the relative mass acceleration, velocity and displacement vectors, respectively; and  $F(t)$  is the external force vector.

The analysis of motion for forced vibration can be presented in the Laplace domain for the matrix equation 2-10. The forced vibration can be the acceleration input force applied to the 2-DoF system (i.e.  $m * \ddot{w}_1 = m * a$ ), and/or the external force applied to the 2-DoF system (i.e.  $f_1$  and  $f_2$ ). The following is the Laplace transform of equation 2-10:

$$\begin{aligned} & \begin{bmatrix} m_1 \\ m_2 \end{bmatrix} a(s) - \begin{bmatrix} F_1(s) \\ F_2(s) \end{bmatrix} \\ &= \begin{bmatrix} -s^2 m_1 - s(b_1 + b_2) - (k_1 + k_2) & sb_2 + k_2 \\ sb_2 + k_2 & -s^2 m_2 - sb_2 - k_2 \end{bmatrix} \begin{bmatrix} X_1(s) \\ X_2(s) \end{bmatrix} \end{aligned} \quad 2-11$$

$$M_i a(s) - F(s) = [s^2 M + sB + K]X(s)$$

The frequency response analysis of the two mass displacements can be examined for the following cases:

- 1- The system is under acceleration, and no force is applied ( $F_1 = F_2 = 0$ ). The transfer function between the mass relative displacement ( $X_{1,2}$ ) and applied acceleration  $a$  can be derived from equation 2-11, as follows:

$$G_{X_1 Acc}(s) = \left. \frac{X_1(s)}{a(s)} \right|_{F(s)=0} = \begin{bmatrix} 1 \\ 0 \end{bmatrix} \frac{M_i}{[s^2 M + sB + K]} \quad 2-12$$

$$G_{X_2 Acc}(s) = \left. \frac{X_2(s)}{a(s)} \right|_{F(s)=0} = \begin{bmatrix} 0 \\ 1 \end{bmatrix} \frac{M_i}{[s^2 M + sB + K]}$$

- 2- The system is excited by either external forces  $F_1$  or  $F_2$ , and no acceleration is applied to the 2-DoF system ( $a(s)=0$ ). Thus, the transfer function between the mass relative displacement ( $X_{1,2}$ ) and applied force  $F$  can be derived from equation 2-11, as follows:

$$G_{X_1 F}(s) = \left. \frac{X_1(s)}{F(s)} \right|_{a(s)=0} = - \begin{bmatrix} 1 \\ 0 \end{bmatrix} \frac{1}{[s^2 M + sB + K]} \quad 2-13$$

$$G_{X_2 F}(s) = \left. \frac{X_2(s)}{F(s)} \right|_{a(s)=0} = - \begin{bmatrix} 0 \\ 1 \end{bmatrix} \frac{1}{[s^2 M + sB + K]}$$

If the 2-DoF system motion in equation 2-11 is assumed linear, the full analysis of motion for the forced vibration (i.e. the 2-Dof is excited with acceleration and external force) can be obtained by applying super-position, as follows [24]:

$$\begin{aligned}
 X_1(s) &= G_{X_1Acc}(s) * a(s) + G_{X_1F_1}(s) * F_1(s) + G_{X_1F_2}(s) * F_2(s) \\
 X_2(s) &= G_{X_2Acc}(s) * a(s) + G_{X_2F_1}(s) * F_1(s) + G_{X_2F_2}(s) * F_2(s)
 \end{aligned}
 \tag{2-14}$$

If the external forces  $f_1$  and  $f_2$  are not applied (i.e.  $f_1=f_2=0$ ), and the damping coefficients are neglected ( $b_1=b_2=0$ ), then the equations of motion (in equation 2-9) of the 2-DoF system are rewritten as follows:

$$\begin{aligned}
 m_1\ddot{x}_1 &= -k_1x_1 + k_2(x_2 - x_1) & (a) \\
 m_2\ddot{x}_2 &= -k_2(x_2 - x_1) & (b)
 \end{aligned}
 \tag{2-15}$$

If we assume that the displacements  $x_1$  and  $x_2$  of the two masses are harmonic, with similar frequency  $\omega$  and phase  $\varphi$ , then  $x_1$  and  $x_2$  can be given as:

$$\begin{aligned}
 x_1 &= X_1 \cos(\omega t + \varphi) \\
 x_2 &= X_2 \cos(\omega t + \varphi)
 \end{aligned}
 \tag{2-16}$$

where  $X_1$  and  $X_2$  are the constant amplitudes of  $x_1$  and  $x_2$ , respectively, and the acceleration is given by the second-order time derivatives of  $x_1$  and  $x_2$ :

$$\begin{aligned}
 \ddot{x}_1 &= -\omega^2 X_1 \cos(\omega t + \varphi) \\
 \ddot{x}_2 &= -\omega^2 X_2 \cos(\omega t + \varphi)
 \end{aligned}
 \tag{2-17}$$

By substituting equations 2-16 and 2-17 in equation 2-15 (a, b), and dividing by  $\cos(\omega t + \varphi)$ , equation 2-15 takes the following form:

$$\begin{aligned}
 [-m_1\omega^2 + (k_1 + k_2)]X_1 - k_2X_2 &= 0 & (a) \\
 -k_2X_1 + [-m_2\omega^2 + k_2]X_2 &= 0 & (b)
 \end{aligned}
 \tag{2-18}$$

Equations 2-18 (a, b) can be rewritten in a matrix form, as follows:

$$\begin{bmatrix} -m_1\omega^2 + (k_1 + k_2) & -k_2 \\ -k_2 & -m_2\omega^2 + k_2 \end{bmatrix} \begin{bmatrix} X_1 \\ X_2 \end{bmatrix} = 0 \quad 2-19$$

Equation 2-19 shows the matrix representation of the two unknowns  $X_1$  and  $X_2$ . The trivial solution of these equations is  $X_1 = X_2 = 0$ , which means no displacement. The nontrivial solution of the constants  $X_1$  and  $X_2$  is obtained by equating the determinant to zero [38]:

$$\begin{vmatrix} -m_1\omega^2 + (k_1 + k_2) & -k_2 \\ -k_2 & -m_2\omega^2 + k_2 \end{vmatrix} = 0 \quad 2-20$$

The determinant solution gives a fourth-order polynomial equation, which is also referred to as the 2-DoF frequency equation:

$$\omega^4 - \left( \frac{k_1 + k_2}{m_1} + \frac{k_2}{m_2} \right) \omega^2 + \frac{k_1}{m_1 m_2} = 0 \quad 2-21$$

Thus, the roots of equation 2-21 are obtained if the quadratic formula is used, as follows:

$$\omega_{1,2}^2 = \frac{1}{2} \left( \frac{k_1 + k_2}{m_1} + \frac{k_2}{m_2} \right) \mp \frac{1}{2} \sqrt{\left( \frac{k_1 + k_2}{m_1} + \frac{k_2}{m_2} \right)^2 - 4 \frac{k_1}{m_1 m_2}} \quad 2-22$$

The two solutions  $\omega_{1,2}$  are the two *natural frequencies* of the undamped 2-DoF system. The nontrivial solutions of  $X_1$  and  $X_2$  in equation 2-18 are possible when either of the natural frequencies  $\omega_1$  or  $\omega_2$  is substituted.

These 2-DoF derived equations are essential for modelling, theoretical analyses and design of the 2-DoF velocity sensor in Chapter 4.

## 2.3 The Principle of Capacitive MEMS Sensors

### 2.3.1 Capacitive Transduction

Inertial MEMS sensors with capacitive transducers transform the proof mass deflection, due to inertial force, into a capacitance change. One common capacitor configuration is the differential parallel capacitor, as shown in Figure 2-5. When the proof mass approaches one electrode (e.g. top electrode) of these differential capacitors, the capacitance value increases at this side and decreases at the other electrode (e.g. bottom electrode).

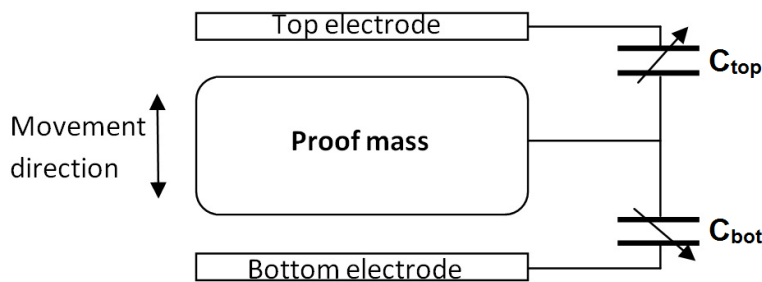


Figure 2-5: A differential parallel plate capacitor used in inertial MEMS sensors.

The capacitance ( $C$ ) between the two moving parallel plates is given by [28]:

$$C = \frac{\epsilon_0 A}{(d_0 \pm x)} \quad 2-23$$

The differential capacitance is given by [28]:

$$C_d = C_{top} - C_{bot} = \epsilon_0 A \left( \frac{1}{d_0 - x} - \frac{1}{d_0 + x} \right) \quad 2-24$$

where  $C_{top}$  and  $C_{bot}$  are the top and bottom capacitors,  $\epsilon_0$  is the permittivity of the air or the material between the two plates,  $A$  is the electrode overlap area,  $d_0$  is the nominal gap distance between the two plates and  $x$  is the displacement of the proof mass.

Equation 2-24 shows a nonlinear relationship between the change in capacitance and the proof mass displacement. If the proof mass deflection is very small compared to the

nominal gap ( $x^2 \ll d_0^2$ ) [28] [30] [39], the change in capacitance can be assumed linear. Thus, equation 2-24 can be rewritten as follows [28]:

$$C_d = C_{top} - C_{bot} \approx \epsilon_0 A \left( \frac{2x}{d_0^2} \right) \quad 2-25$$

### 2.3.2 Capacitive Actuation

The capacitive actuation mechanism can be employed to control the proof mass deflection by means of applying an electrostatic force to return the proof mass to its nominal position. Therefore, when the capacitive MEMS sensor is operated in closed-loop mode, the proof mass will be relatively small ( $x^2 \ll d_0^2$ ), and the linearity assumption of the differential sense capacitor can be practically achieved [28] [40] [41].

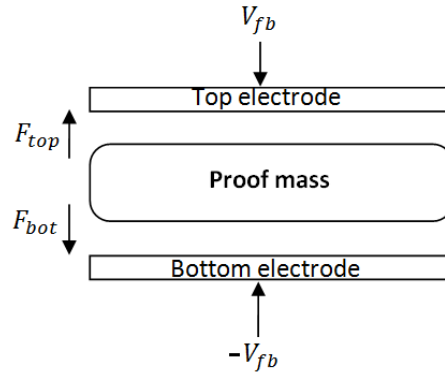


Figure 2-6: Capacitive actuation mechanism with proof mass.

The differential parallel capacitor is one way to apply electrostatic force on the proof mass, as shown in Figure 2-6. The net electrostatic force  $F_t$  applied to the proof mass is given by the following [28]:

$$F_t = F_{top} - F_{bot} = \frac{1}{2} \epsilon_0 A \left[ \frac{(V_{fb})^2}{(d_0 - x)^2} - \frac{(V_{fb})^2}{(d_0 + x)^2} \right] \quad 2-26$$

As can be seen, in equation 2-26, the generated force is nonlinear with respect to the displacement  $x$  and the applied voltage  $V_{fb}$  [39]. If the proof mass displacement is very small, the electrostatic force  $F_t$  can be assumed linear with respect to displacement  $x$ . In

addition, the electrostatic force with respect to the applied voltage  $V_{fb}$  can be assumed linear if the balanced actuation technique is employed [30]. This can be achieved by adding a bias voltage  $V_b$  such that the top electrode is energised by  $V_b+V_{fb}$ , while the bottom electrode is energised by  $V_b-V_{fb}$ . Therefore, equation 2-26 can be presented with a linearized electrostatic force as follows [28]:

$$F_t = F_{top} - F_{bottom} \approx 2\varepsilon_0 A \left[ \frac{V_b V_{fb}}{d_0^2} \right] \quad 2-27$$

The electrostatic force generated by the parallel plate actuator works against the mechanical spring [42], and as a result a spring softening effect occurs. The electrostatic spring  $k_e$  is given by:

$$k_e = \frac{d}{dx} (F_{top} - F_{bot}) = \varepsilon_0 A \left[ \frac{(V_{fb})^2}{(d_0 - x)^3} - \frac{(V_{fb})^2}{(d_0 + x)^3} \right] \approx \varepsilon_0 A \frac{V_{fb}^2}{d_0^3} \quad 2-28$$

Another capacitive actuation technique is the lateral comb capacitance as shown in Figure 2-7. This technique offers linear electrostatic force; however, it requires high excitation voltage compared to the parallel plate capacitor.

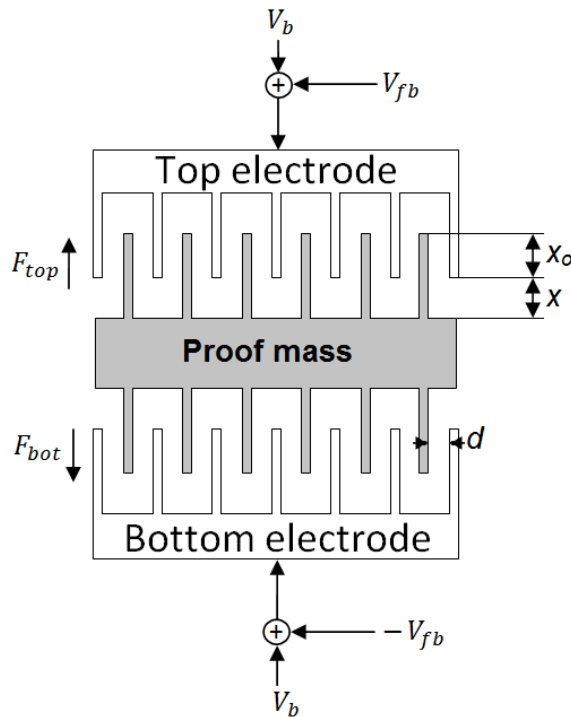


Figure 2-7: A differential lateral comb capacitor used in inertial MEMS sensors.

The electrostatic force generated with lateral comb capacitors is independent of the displacement  $x$  and the nominal overlap width  $x_o$ . If the balanced actuation technique is used such that the top electrode is energized by  $V_b+V_{fb}$ , and the bottom electrode is energized by  $V_b-V_{fb}$ , the balanced electrostatic force of the lateral comb capacitor is given by the following [30]:

$$F_t = F_{top} - F_{bot} = 4N\epsilon_0t \left[ \frac{V_b V_{fb}}{d} \right] \quad 2-29$$

## 2.4 Damping Coefficient Estimation

The gas trapped between two moving plates of a micro scale has a major influence on the entire MEMS sensor measurement as the flow of gas molecules affects the dynamics of the capacitive MEMS inertial sensors. In general, two types of air damping phenomena are of concern in capacitive MEMS: squeeze film damping and slide film damping [16].

### 2.4.1 Squeeze Film Damping

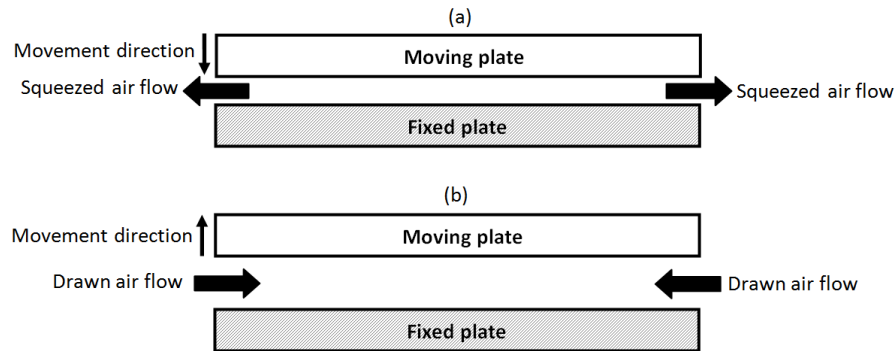


Figure 2-8: Squeeze film air flow: (a) squeezed air flow if plates are moving towards each other; (b) drawn air flow if plates are moving away from each other (reproduced from [42]).

The effect of squeeze film damping is depicted in Figure 2-8. The case where two parallel plates are moving towards each other is shown in Figure 2-8(a). Here, the air pressure between the two plates increases, and the air is squeezed out. If the parallel plates move away from each other, as shown in Figure 2-8(b), the air pressure decreases, and the air is drawn inside. The drag force, initiated by the air flow, causes a damping force, which

works against the plates' surfaces. The squeeze film damping is given by the following [42]:

$$b(\omega) = \left( \frac{64}{\pi^6} * \frac{P_a}{h_o} * \frac{A * \sigma}{\omega} \right) \times \left( \sum_{m=1,3,5...} \left( \sum_{n=1,3,5...} \frac{m^2 + (n/\eta)^2}{(mn)^2 \{ [m^2 + (n/\eta)^2]^2 + [\sigma^2/\pi^4] \}} \right) \right) \quad 2-30$$

$$\sigma = 12\mu_{\text{eff}} \left( \frac{b}{h_o} \right)^2 \left( \frac{\omega}{P_a} \right) \quad 2-31$$

$$\mu_{\text{eff}} = \frac{\mu}{(1 + 9.638K_n^{1.159})} \quad 2-32$$

$$K_n = \lambda/h_o \quad 2-33$$

where,  $\omega$  is the frequency in rad/sec,  $b(\omega)$  is the frequency dependant damping coefficient,  $a$  and  $b$  are the plate length and width ( $a > b$ ), respectively,  $\lambda$  is the mean free path (63nm),  $h_o$  is the mean gap between plates,  $K_n$  is the Knudsen number,  $m$  and  $n$  are the indices' odd numbers,  $A$  is the area of the plate ( $a \times b$ ),  $\sigma$  is the squeeze number,  $\eta$  is the ratio of  $a/b$ .  $\mu_{\text{eff}}$  is the effective viscosity,  $P_a$  is the ambient pressure (101.325 kPa),  $\mu$  is the air viscosity ( $18.27 \times 10^{-6}$  Pa.sec), and  $k_{eq}(\omega)$  is the equivalent damping spring constant.

The damping estimation cut-off frequency is given by [43]:

$$\omega_c = \frac{\pi^2}{12} * \frac{Ph^2}{\mu} * \left( \frac{1}{a^2} + \frac{1}{b^2} \right) \quad 2-34$$

The output of equation 2-30 represents the damping value between two parallel rectangular plates with respect to the frequency  $\omega$ . The damping coefficient before cut-off  $\omega_c$  is almost constant, thus, the squeeze film damping can be assumed linear. After the cut-off frequency  $\omega_c$ , the damping coefficient decreases and can be neglected [43] [44].

### **2.4.2 Slide Film Damping**

Of the two plates shown in Figure 2-9, the top plate is moving in parallel with the bottom fixed plate with a velocity  $V_p$ . Due to this movement, the friction between the plate surfaces and gas produces a shear force  $\sigma$  that causes the gas to flow with different velocities  $V_{gas}$  [42].

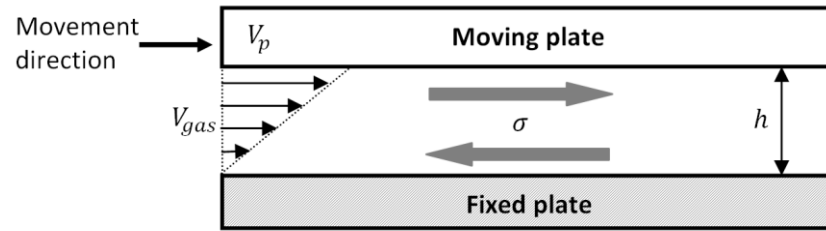


Figure 2-9: Slide film air flow (reproduced from [42]).

If the following assumptions are considered, where the distance between the two plates is constant, and the plate movement is linear, the slide film damping between two parallel plates can be given by [42]:

$$b_{slide} = \frac{\mu_{eff} * A}{h} \quad 2-35$$

where  $b_{slide}$  is the slide film damping between two surfaces,  $A$  is the area between the two slide films,  $\mu_{eff}$  is the effective viscosity and  $h$  is the gap between the plates.

## 2.5 Spring Constant

The elastic beam or spring in inertial MEMS sensors has to be compliant to excitation in one direction (e.g. y-axis), perpendicular to the spring axis, and has to have high stiffness to other directions (e.g. x- and z-axis). Beam elasticity behaviour is nonlinear with large deflections, but with a small deflection, linear elasticity can be assumed [45].

The single-beam type shown in Figure 2-10 is fixed to the anchor from one end and guided from the other end.

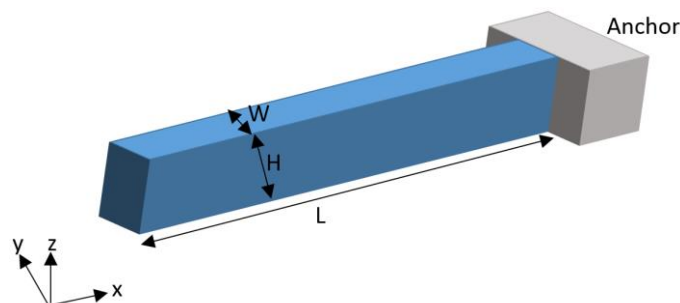


Figure 2-10: Fixed-guided single-beam structure in inertial MEMS sensors.

## Chapter 2: Fundamental Principles

---

If the elastic beam has a rectangular cross section, and the geometries are  $L$  (length),  $H$  (height) and  $W$  (width), then the moment of inertia  $I$  for the three axes  $x$ ,  $y$  and  $z$  are given by the following [42]:

$$I_x = \frac{HL^3}{12} \quad I_y = \frac{HW^3}{12} \quad I_z = \frac{WH^3}{12} \quad 2-36$$

If the beam is designed with  $L > H > W$ , then the lowest moment of inertia is  $I_y$ , followed by  $I_z$  and then  $I_x$ . Thus, the beam is constrained to move along the  $y$ -axis. The spring constant of the beam along the  $y$ -axis is given by [42]

$$k = \frac{12EI_y}{L^3} = \frac{EHW^3}{L^3} \quad 2-37$$

where  $E$  is Young's modulus, which is  $169 \text{ GN/m}^2$ .

The microfabrication of the MEMS sensor usually come across an inevitable degree of imperfection, such as over-etching the bottom end of the beam. Thus, the beam cross section becomes trapezoidal, as shown in Figure 2-11. Therefore, the moment of inertia  $I_y$  becomes:

$$I_y = \frac{H(a+b)(a^2 + b^2)}{48} \quad 2-38$$

Using similar concept, when  $L > H > b$  and  $a$ , then the beam is constrained to move along the  $y$ -axis, therefore, by substituting equation 2-38 in equation 2-37, the spring constant of the trapezoidal cross section beam is equal [46]:

$$k = \frac{EH(a+b)(a^2 + b^2)}{4L^3} \quad 2-39$$

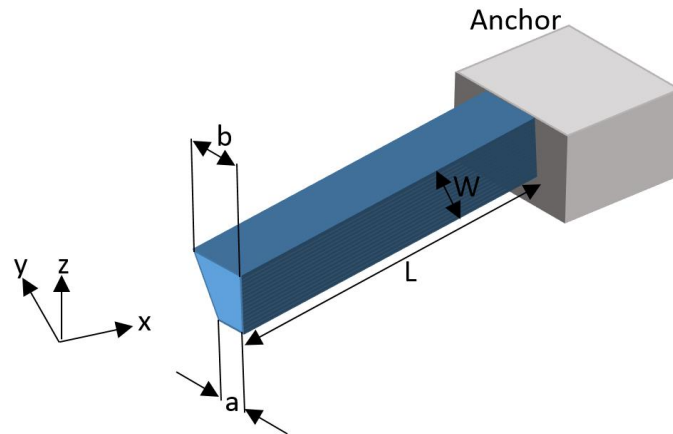


Figure 2-11: Fixed-guided single-beam structure in inertial MEMS sensors with trapezoidal cross section due to fabrication imperfection.

For large displacement, the single-beam structure is susceptible to the axial force, which results in a nonlinear effect between the applied force and displacement [47]. The folded beam is another type of spring structure, as shown in Figure 2-12. The axial force has less effect, and the nonlinearity decreases for large displacements [30].

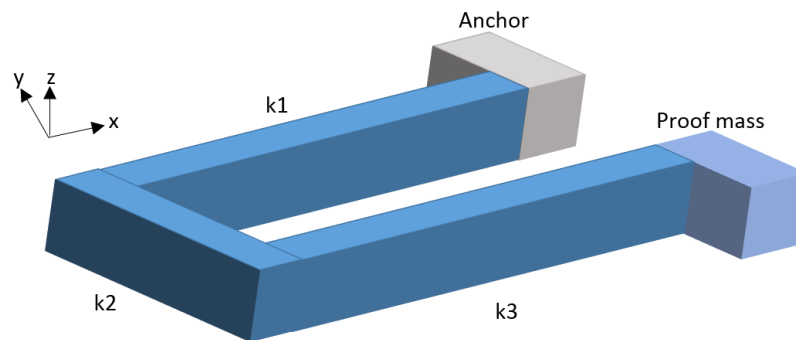


Figure 2-12: Fixed-guided folded beam.

The total spring constant of the folded beam shown in Figure 2-12 can be treated as parallel single beams [42]:

$$\frac{1}{k_{eq}} = \frac{1}{k_1} + \frac{1}{k_2} + \frac{1}{k_3} \quad 2-40$$

If the proof mass is moving in the y-axis, as shown in Figure 2-12, the spring constant  $k_2$  is much larger than  $k_1$  and  $k_3$ , and if the length L of  $k_1$  and  $k_3$  are equal, equation 2-40 can be rewritten as follows:

$$k_{eq} = \frac{k_1 + k_3}{k_1 k_3} = \frac{EHW^3}{2L^3} \quad 2-41$$

The aforementioned spring constant equations will be referred to when discussing the design of the 2-DoF velocity sensor in chapter 5 and 6.

## **2.6 Vibration Control**

The unwanted vibration encountered in equipment or structures causes undesirable motions that may lead to structural damage or excessive sound/noise. Structural vibration can be eliminated or reduced by applying passive isolation or active vibration control [48] [49]. Passive isolation is achieved by isolating a vibration source from a structure with the use of flexible couplings, mounts or damping elements. These elements isolate vibration in the middle and high audio frequency ranges [50].

By contrast, an active vibration controller modifies the dynamic characteristics of a vibrated structure and improves the efficiency of vibration isolators. An active vibration controller consists of three key components: (1) a control system, (2) a sensing system that provides the controller with an input measurement that represents a vibration signal and (3) an actuation system that converts controller output into a force that counteracts structural vibration. The active vibration control is effective at a frequency range below the resonance of the controller equipment (i.e. low audio frequency range) [50].

Active vibration control can be implemented with feed-forward or feedback approaches, as shown in Figure 2-13(a) and (b), respectively. Feed-forward control is achieved by measuring input vibration/noise sufficiently in advance to enable the controller to generate a control signal that overcomes vibration. In principle, this approach is effective with periodic vibration signals [49], which are usually generated by rotating machines [24]. For random vibration signals, however, feedback control is a more favourable option. Feedback control aims to modify the response of a fixable structure by introducing vibration force at a direction opposite that of a disturbance vibration signal. In the design process, a feedback active controller requires a considerably high feedback gain. Hence, stability studies on the control loop are crucial. Additional attention should be paid to system parameter variations, such as loads applied on flexible structures, temperature changes or nonlinear effects associated with sensor and actuator elements [24]. The stability of the feedback approach can be maximised if the physical placements of an error

sensor and a controlling actuator are accurately aligned on the same sense and actuation axis (i.e. a collocated actuator/sensor pair) [49]. The subsequent discussion focuses on active vibration control via the feedback approach, which is the application that benefits the most from the 2-DoF velocity sensor proposed in this research.

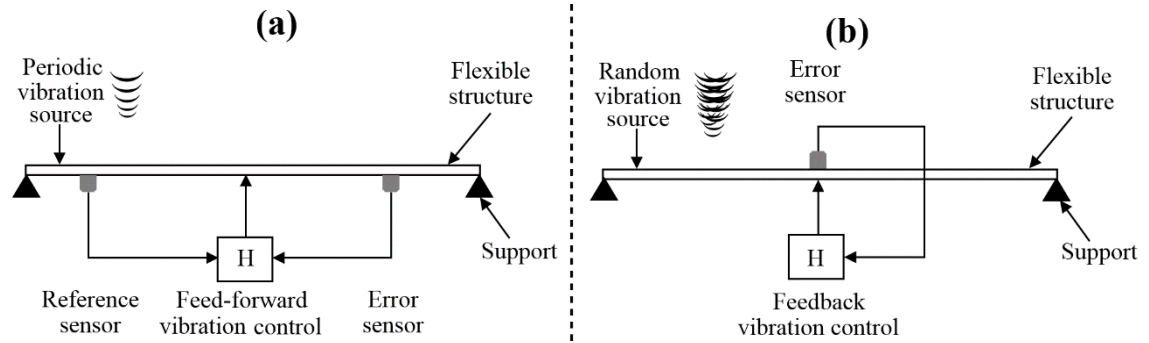


Figure 2-13: Active vibration control topology; (a) feed-forward control for periodic vibration source and (b) feedback control for random vibration source (reproduced from [24]).

According to classical control theory [51], active vibration control via the feedback approach can be implemented with proportional, integral or derivative control [24]. By constructing a feedback loop with a collocated pair that comprises the velocity sensor of an output  $v_e(\omega)$  and the actuator of an output force  $F(\omega)$ , a proportional controller employs a velocity feedback loop that synthesises active damping (Figure 2-14(a)); an integral controller ( $1/j\omega$ ) employs a displacement feedback loop that synthesises active stiffness (Figure 2-14(b)); and a derivative controller ( $j\omega$ ) employs an acceleration feedback loop that synthesises active mass (Figure 2-14(c)). Open-loop control function  $F(\omega)/v_e(\omega)$  is used to examine feedback loop stability for the above-mentioned controllers [24]. The FRFs of the integral and the derivative feedback loop (Figure 2-14(c) and 2-2(b), respectively) show a sequence of resonance and anti-resonance peaks that are associated with a sequence of phase changes between  $0^\circ$  and  $180^\circ$ . Although, this indicates that both control loops are unconditionally stable, as the phase does not cross the  $180^\circ$ , the phase and gain margin are considered tight so that small variation in the response function can lead to instability. In practice, an additional phase is usually introduced to the feedback loop by the sensor/actuator pair and the electronic circuit. Such introduction strongly affects the stability of a feedback loop. Active vibration control with an integral or derivative feedback loop can therefore be considered conditionally stable [24]. Contrastingly, the proportional function in Figure 2-14(a) shows that the phase is

confined between the  $90^\circ$  and  $-90^\circ$ ; in principle, therefore, a direct velocity feedback loop is unconditionally stable with any control gain value [15] [16] [52].

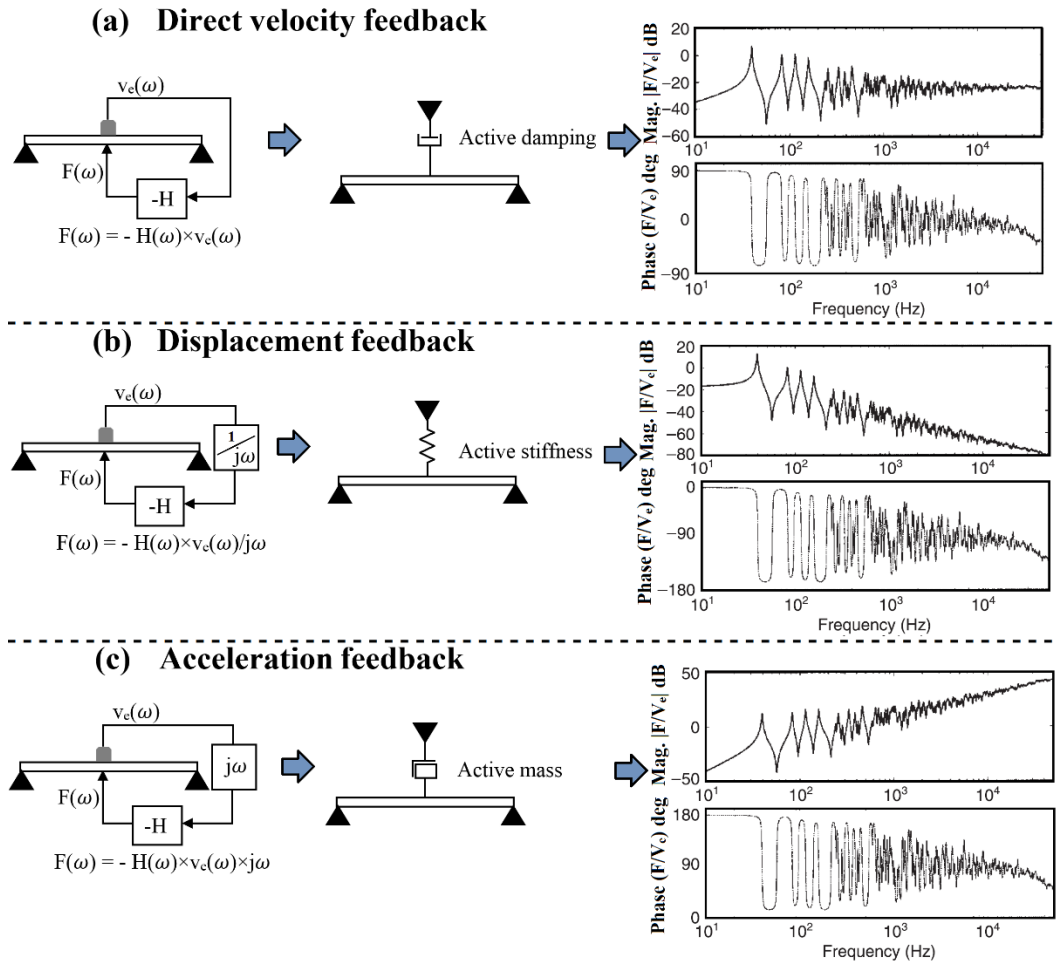


Figure 2-14: Different feedback loop vibration controllers with their open-loop control function frequency responses; (a) direct velocity feedback that synthesises active damping control, (b) displacement feedback that synthesises active stiffness control and (c) acceleration feedback that synthesises active mass control (reproduced from [24]).

The 2-DoF velocity sensor presented in this research is conceived in relation to vibration control for direct velocity feedback. Of particular interest is the concept of smart structures, wherein sensor and actuator transducers are embedded on thin plates or shells to implement single- or multiple-channel control systems that reduce vibration and sound radiation. This concept is discussed in Section 3.3.

## **2.7 Summary**

This chapter discussed some of the background subjects necessary to design the 2-DoF MEMS velocity sensor. Because the capacitive MEMS inertial sensor can be modelled with a mass-spring-damper system, the modelling approach of the S-DoF and 2-DoF systems was briefly addressed. The transfer function of each system was obtained to analyse the dynamic response. The capacitive transduction and actuation were also considered. Two different capacitor types are usually employed: varying gap and varying overlap area capacitors. The former can be constructed with parallel plates moving towards each other, and the latter can be constructed with interdigitated fingers that move towards each other. Each type was addressed with the associated capacitance functions, which are required in the velocity sensor design. The damping coefficient estimation and spring constant calculation were discussed as well. The final section of this chapter briefly discusses vibration control, with specific focus on feed-forward and feedback loop vibration control. For random vibration noise, feedback loop vibration control is more effective than the feed-forward approach. The former is implemented with a proportional, integral or derivative function in the feedback loop. Amongst these implementations, the proportional function synthesises a direct velocity feedback loop and is unconditionally stable for any feedback control gain value.



## Chapter 3: Literature Review

### 3.1 Introduction

This chapter addresses the latest developments in research on 2-DoF MEMS velocity sensors. First, vibration control using a velocity feedback loop is presented, which will cover the velocity measurement using 1-DoF accelerometer, geo-phone and laser Doppler vibrometer. Followed by, a discussion about the 2-DoF piezoresistive MEMS velocity sensor design and development. Then, a discussion of other applications of M-DoF capacitive MEMS. Finally, silicon-on-insulator (SOI) wafer microfabrication is presented, along with an investigation of various methods used to electrically isolate two blocks within a proof mass.

### 3.2 Vibration Control System Using a Velocity Feedback Loop

As discussed in Section 2.6, active vibration control with a velocity feedback loop is unconditionally stable. Such a control system consists of three main elements: (1) a control system, (2) an actuator element and (3) a velocity sensor. This section discusses possible methods of measuring velocity to enable active vibration control with a velocity feedback loop.

#### 3.2.1 Velocity Measurement Using an Accelerometer

The conventional method of measuring velocity involves the acquisition of a vibrated structure's acceleration by using an accelerometer, followed by the application of the time-integration process to the acceleration output signal to obtain the velocity signal [53-56]. Figure 3-1(a) shows a block diagram of the velocity feedback loop vibration control. This type of control unit is typically composed of a small piezoelectric patch actuator with an under-damped accelerometer sensor at its centre, hence, the sensor implements a velocity feedback loop [57-59]. When an array of these control units is bonded on thin plate or shell structures to construct the smart panel application [24] [25] (as shown in Figure 3-1(b)), active vibration control is implemented, thereby reducing vibration and sound radiation at low audio frequencies.

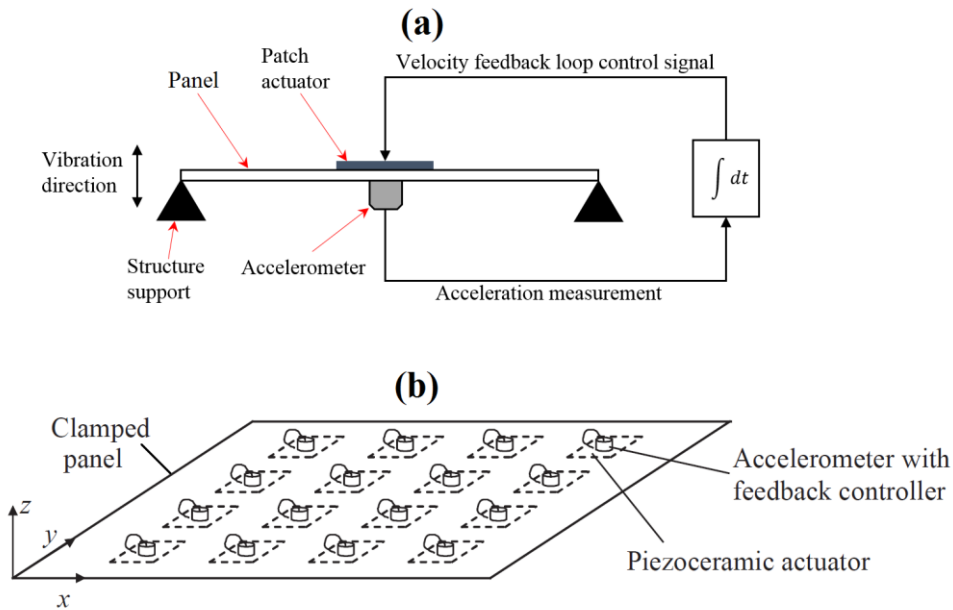


Figure 3-1: (a) Simple block diagram of a single-unit vibration control system using an accelerometer and patch actuator (reproduced from [24]). (b) Smart panel with multiple decentralised velocity feedback control units (reproduced from [25]).

An experimental smart panel configuration [18] [21] is shown in Figure 3-2. The accelerometers and piezoceramic patch actuators are collocated. To apply a negative velocity feedback loop, the output signal from each accelerometer is electronically integrated, inverted and fed back to an actuator.

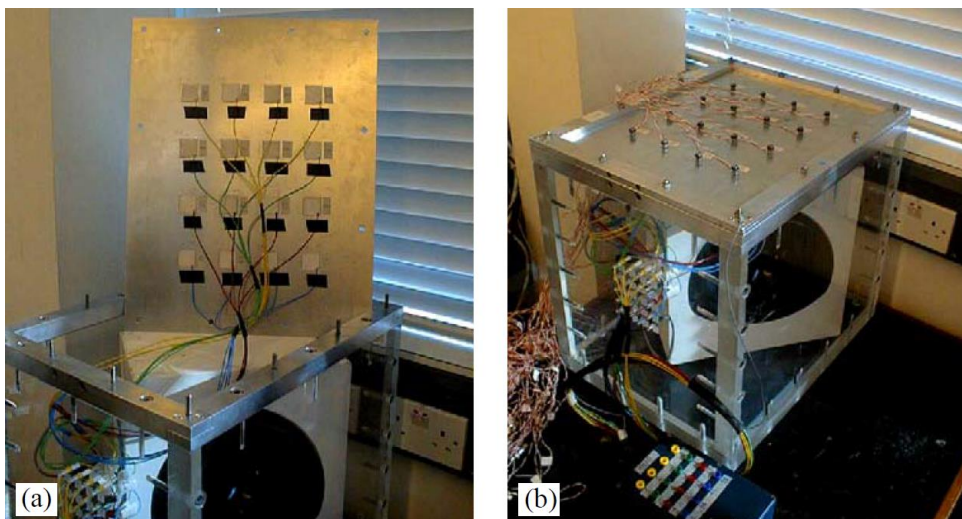


Figure 3-2: Smart panel applications using a velocity feedback control loop for an active damping control system; (a) the back side of the panel shows 16 piezoceramic patch actuators and (b) the top side of the panel shows 16 accelerometer sensors (reproduced from [21]).

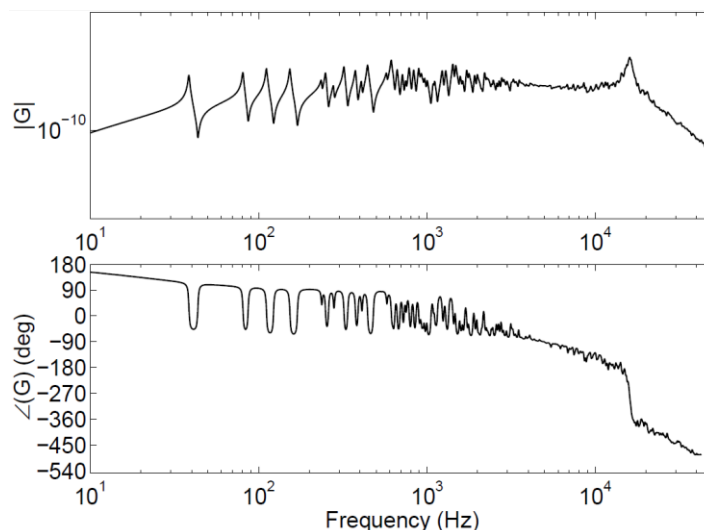


Figure 3-3: Simulated open-loop frequency response function of the sensor/actuator pair (reproduced from [17]).

Such configuration presents two stability issues: First, because the accelerometer does not provide a direct velocity output, an integrator is required. In practice, real integrator always has a low-frequency integration cut-off, which causes the open-loop sensor/actuator FRF to encounter a  $+180^\circ$  phase before the real integrator's cut-off frequency, as illustrated in Figure 3-3. This can cause instability in practical implementation. The second issue is that the open-loop sensor/actuator FRF exhibits a peak at the resonance frequency accompanied with a  $-180^\circ$  phase lag, as indicated in Figure 3-3. This peak produces positive velocity feedback with high control signals, thereby causing spillover, and potentially, system instability. The system is thus conditionally stable with a limited feedback loop gain margin [17] [19].

In principle, the second problem can be solved using a low-pass filter or an over-damped accelerometer. The low-pass filter can be used to attenuate the amplitude of the sensor output signal at high frequencies and thus improve the stability of the feedback loop. However, this solution is not as straightforward to implement as it may seem. The filter should guarantee two concurrent requirements [19] [56]. First, it should have a cut-off frequency close to the fundamental resonance frequency of the accelerometer to maintain the wide frequency band of operation of the feedback loop. Second, it should guarantee a relatively large amplitude roll-off with little phase lag starting from the filter cut-off frequency to avoid instability. In practice, these requirements cannot be simultaneously satisfied. Under such situation, a designer should identify a compromise between the

frequency bandwidth of feedback loop operation and the maximum stable gain that can be implemented. Such compromise determines the maximum control effect that can be produced.

When an over-damped accelerometer is employed, the stability problem is less pronounced around the resonance frequency. Nevertheless, the frequency band of interest of the accelerometer decreases, in which the  $180^\circ$  phase lag around the resonance is spread over the low-frequency band. Therefore, the velocity measurement obtained from the over-damped accelerometer and the integrator is effective only over a narrow low-frequency band [24]. Furthermore, the  $180^\circ$  phase shift is still encountered at low frequencies because of the use of a real integrator and at high frequencies caused by the dynamics of the sensor. These problems further reduce operational bandwidth and potentially cause instability.

### **3.2.2 Velocity Measurement Using a Two-Degree-of-Freedom MEMS Velocity Sensor**

As discussed at the end of section 3.2.1, the conventional method of measuring velocity is achieved by using a S-DoF under-damped accelerometer followed by an integrator. It was noted that with respect to the resonance frequency of the accelerometer, the velocity feedback loop could become unstable due to the high amplitude peak and the  $180^\circ$  phase shift. If an over-damped accelerometer is used, the resonance frequency peak will be lowered; thus, the stability issue regarding the resonance frequency could become less pronounced. However, the  $180^\circ$  phase shift will stretch around the resonance frequency and, accordingly, the effective velocity measurement will be reduced. This is because the damping coefficient is imposed on the accelerometer with reference to the relative velocity of the proof mass to the sensor's frame, which constrains the proof mass from movement relative to the sensor's frame [17].

The 2-DoF velocity sensor works based on the idea of applying absolute damping on the proof mass rather than relative damping. In this case, the resonance frequency of the accelerometer can be reduced, the phase will not stretch around the resonance frequency and the proof mass displacement will not be heavily constrained to move relative to the frame [17]. The application of the 2-DoF MEMS in velocity measurement is relatively unexplored. To confirm the effectiveness of the concept, Gardonio et al. [60] proposed a

2-DoF micro-scale velocity sensor. Figure 3-4(a) shows the block diagram of the sensor and Figure 3-4(b) illustrates the implementation of the prototype. The sensor was made by a pair of cantilever beams with a tip block mass connected in series. The principal sensor outputs velocity measurement. The other cantilever-mass element serves as a control sensing system for the implementation of an internal feedback loop, so that the output of the sensor becomes proportional to the base velocity rather than to the base acceleration. The 2-DoF sensor was designed in such a way that the first resonance frequency occurs at 569 Hz and the second occurs at 2.383 kHz.

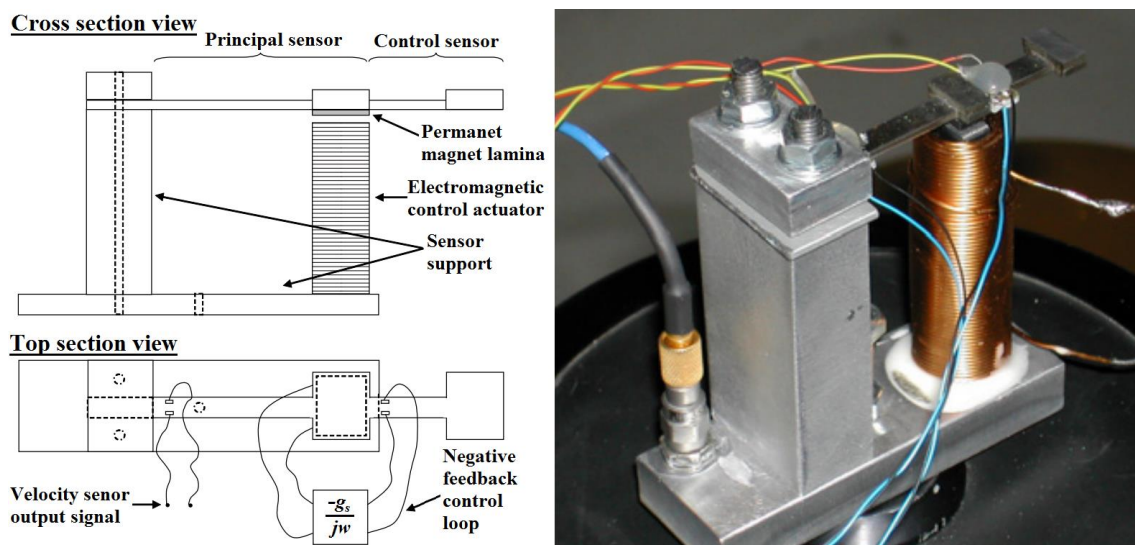


Figure 3-4: First prototype micro-scale velocity sensor, which comprises two beam-proof masses connected in series and an induction coil actuator for the implementation of an internal velocity feedback loop; (a) block diagram of the velocity sensor and (b) implementation (reproduced from [60]).

This micro-scale prototype was designed with a piezoresistive strain gauge to measure block mass displacement. It was further equipped with an electromagnetic control actuator to implement an internal feedback loop. As schematically shown in Figure 3-4(a), the signal proportional to the relative displacement of the control mass with respect to the principal mass was fed to the electronic control circuit, which was then time integrated and amplified by control gain  $g_s$ . This approach meant that at frequencies below the second resonance frequency, a control signal proportional to the absolute velocity of the principal sensing system was fed back to the reactive actuator of the principal system. Thus, the feedback loop produces the desired active damping effect on the mass of the principal system.

Figure 3-5 shows the FRF between the principal sensor output and the velocity at the sensor frame. The thin solid line represents the open-loop response (i.e.  $g_s = 0$ ) of the velocity sensor, which has a rising amplitude and a  $-90^\circ$  phase lag. The output signal is proportional to the acceleration of the sensor frame. Conversely, at a closed feedback loop, the sensor output is proportional to the velocity of the base at low frequencies of up to 200 Hz. The sensor response function is also characterised by a flat amplitude with a  $90^\circ$  phase lag around the first resonance frequency. These three features of the proposed sensor validates the feasibility of employing a 2-DoF sensor as a velocity sensor.

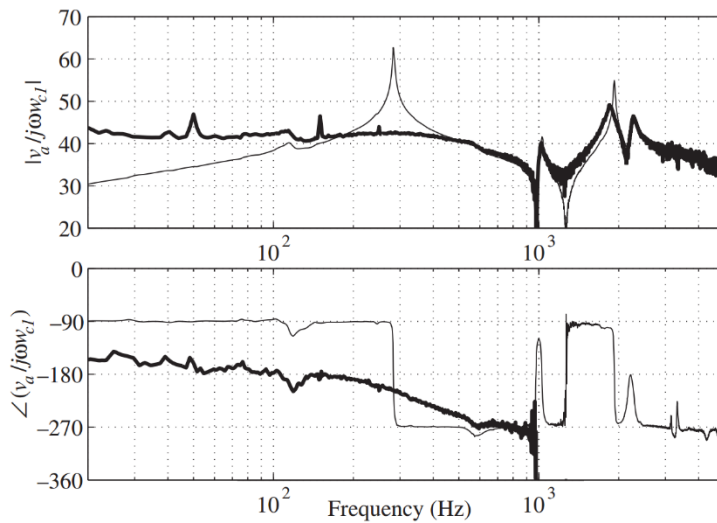


Figure 3-5: The micro-scale 2-DoF velocity sensor generates a frequency response function of up to 5 kHz, which was derived from the transfer function between the velocity sensor output and the velocity of sensor base value. The thin solid line represents the open-loop response, and the thick solid line denotes the closed-loop response (reproduced from [60]).

Gardonio et al. [26] reported a similarly designed 2-DoF velocity sensor, but their device was fabricated with piezoresistive MEMS technology. Figure 3-6 shows the block diagram of the 2-DoF piezoresistive velocity sensor developed in the aforementioned study. The mechanical structure and operation are the same as those of the micro-scale prototype. The first resonance frequency occurs at 2.2 kHz and the second occurs at 13.2 kHz. The sensor employs a piezoresistive technique to detect proof mass displacement and an electrostatic actuator to execute feedback loop control. A detailed top view of the fabricated sensor with ceramic packaging is shown in Figure 3-7.

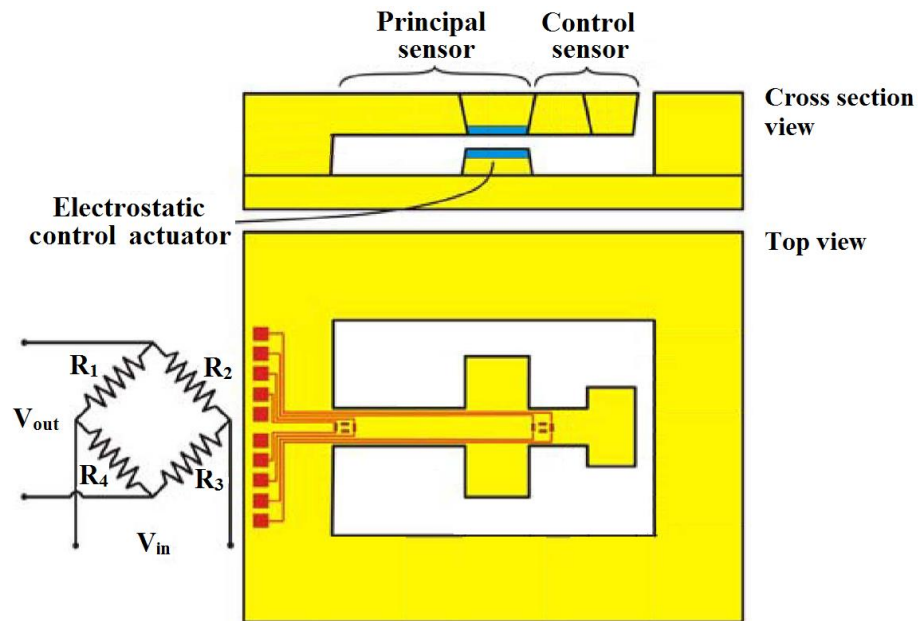


Figure 3-6: Schematic of the 2-DoF MEMS piezoresistive velocity sensor (reproduced from [26]).

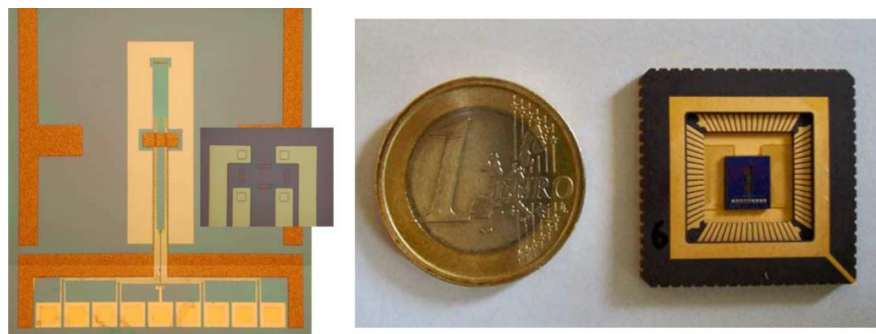


Figure 3-7: (Left) Detailed top view of the fabricated velocity sensor and (right) the 2-DoF MEMS piezoresistive velocity sensor in ceramic packaging (reproduced from [26]).

The 2-DoF piezoresistive MEMS sensor was experimentally tested by mounting the sensor on a shaker table. The output of the principal sensor was measured with respect to the velocity measurement of the base by using a laser vibrometer. The measured FRF of the sensor is shown in Figure 3-8. The blue line shows the open-loop response. The red line shows the feedback loop response, which indicates that the sensor outputs a velocity measurement of up to the first resonance at 2.2 kHz; the first resonance frequency is attenuated; and the phase shift after the first resonance frequency is  $-90^\circ$  instead of  $180^\circ$  encountered with a standard accelerometer method. These three features therefore validate the concept of a velocity sensor at MEMS scale. Thus, the sensor can be effectively used to implement a negative velocity feedback control system without the

control spillover and stability problems generated by the sharp resonance peak and the  $-180^\circ$  phase encountered in the standard accelerometer discussed in the previous section.

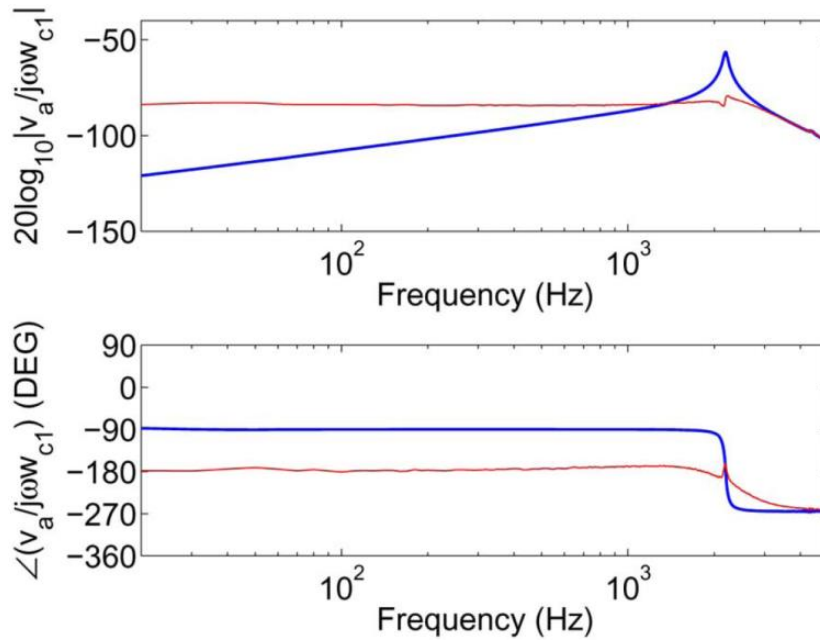


Figure 3-8: The measured frequency response of the 2-DoF MEMS velocity shows the relationship between principal sensor output  $V_a$  and the velocity of the sensor's frame ( $j\omega_{c1}$ ). The blue line represents the open-loop sensor, and the red line denotes the closed-loop sensor (reproduced from [26]).

The 2-DoF piezoresistive MEMS sensor was fabricated with surface micromachining technology that involves the use of nine masks and 145 steps [27]. Such fabrication process is costly and time consuming, furthermore, this technology produces relatively small proof mass, thus, the mechanical Brownian noise has considerable influence on the sensor's performance. Moreover, the numerous fabrication steps involved in the surface micromachining introduces high susceptibility to fabrication tolerance. Despite the potential of the proposed sensor and concept, the use of piezoresistive technology imposes performance limitations. Such problems include the susceptibility of the sensor to temperature changes, nonlinear effects and relatively low sensitivity [28-30].

Capacitive technology is less sensitive to temperature changes, exhibits better linearity and sensitivity and is characterised by better accuracy than piezoresistive transduction techniques [28-30], yet the implementation of 2-DoF velocity sensors with capacitive transduction and actuation technology has not been explored. The capacitive MEMS

velocity sensor presented in this research is similar at system level to the aforementioned piezoelectric MEMS velocity sensor [17]. The capacitive technology requires the design and implementation of such sensors are discussed in the succeeding chapters. These sensors are expected to overcome the problems encountered with a piezoresistive device whilst retaining similar operational properties. Moreover, 2-DoF velocity sensors designed with capacitive technology require only a few fabrication masks and steps under SOI fabrication technology, attributes that reduce time and cost. It also encounters less fabrication imperfections when compared to the lengthy fabrication process of the piezoresistive sensor. Finally, 2-DoF velocity sensors with capacitive technology benefits from relatively large proof mass, which reduces mechanical Brownian noise and increases sensitivity.

### **3.2.3 Velocity Measurement Using a Geophone**

The S-DoF velocity sensor is indeed the optimum option for obtaining velocity measurement for the purpose of active vibration control with a velocity feedback loop. In this section, a discussion of the geophone as an example of the S-DoF and the feasibility of using such a device with an active vibration control system will be presented.

Geophone sensors are commonly used for data acquisition of seismic reflection during oil and mineral exploration and in oceanography applications [61-63]. The structure of a geophone is based on a coil that surrounds a suspended magnetic proof mass. Due to vibration, the proof mass oscillates inside the coil, which results in a change in the magnetic field [64]. The output voltage of the coil is proportional to the velocity of the base. The geophone can be modelled as an S-DoF system with a proof mass, damping coefficient and spring constant. Figure 3-9 shows the frequency response of a commercial geophone used for detecting earth vibrations. The flat frequency response after the resonant frequency (typically at 10 Hz) determines the bandwidth of the velocity measurement.

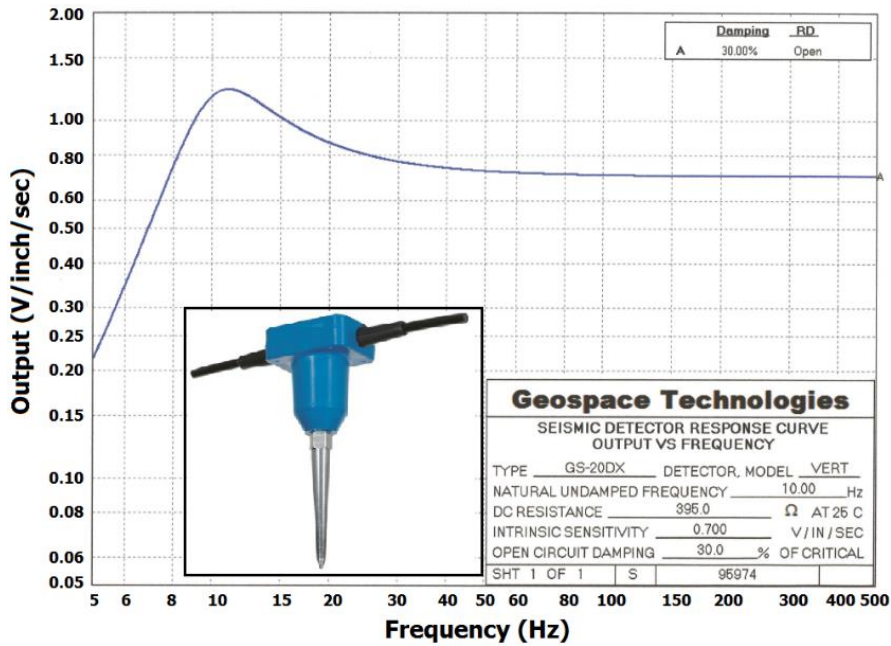


Figure 3-9: Geophone GS-200DX frequency response with a voltage output per input velocity (inch/sec), showing a natural frequency around the 10 Hz and flat response afterward (reproduced from [65]).

Modern geophones have been developed and have become smaller, more rugged, inexpensive and self-powered. However, in the interest of active vibration control in the low audio frequency band, geophones are not an option because of their nonlinear response and inability to measure velocity below the resonant frequency, which is typically around 10 Hz [66-68].

### 3.2.4 Velocity Measurement Using a Laser Doppler Vibrometer

The velocity of a structure can also be measured by applying a laser Doppler vibrometer (LDV) whilst ensuring no contact with the structure [64]. This method is based on detecting the Doppler shift of a laser beam reflected by structural movement. The process is accomplished by targeting a laser beam onto a moving structure and then detecting changes in amplitude and frequency between the original and reflected laser beams. The Doppler shift is linearly proportional to the velocity of a structure.

In active damping control, this method is used mainly for preliminary investigations and for examining the passive influence of an accelerometer on a flexible structure [19] [69]. Velocity measurement that uses the LVD system is more expensive and complex than that achieved with standard accelerometers.

### **3.3 Multi-Degree-of-Freedom Capacitive MEMS Devices**

This section explores some of the MEMS applications with the M-DoF structure, which share some features with the 2-DoF capacitive MEMS velocity sensor in terms of mechanical structure and design criteria.

MEMS devices with the M-DoF structure have proven their ability to transfer the complexity within the electronic control system to the mechanical domain of the MEMS. For example, in a conventional Coriolis vibratory MEMS gyroscope, due to microfabrication imperfections, the gyroscope design requires precise mode-matching within a narrow operational region, involving complex control circuitry. In contrast, 2-DoF MEMS gyroscopes shift the complexity from the electronic control to the mechanical design of the gyroscope, which insures inherent robustness against structural and environmental parameter variations [70]. In a similar fashion, the 2-DoF capacitive MEMS velocity sensor can reduce the complexity of the active vibration control circuit and offer robust velocity feedback loop stability (discussed in Section 3.2.2).

The design of MEMS devices with M-DoF relies on resonance frequency placement, which involves the careful selection of proof masses and spring constant values. The frequency response of the M-DoF structure is characterized by a sequence of resonance peaks separated by anti-resonance peaks [14]. The separation between the resonance frequencies depends on the application. For example, the energy-harvesting MEMS with the M-DoF structure relies on designing a system with multiple and adjacent resonance frequency peaks in order to densely harvest the ambient vibration kinetic energy and change it into electrical energy. In the 2-DoF MEMS gyroscope, the mode-matching is determined by the flat region between the two resonance frequencies. In the 2-DoF velocity sensor, the second resonance frequency should be well above (more than double) the first resonance frequency to ensure good separation and stability, as will be discussed in Chapter 4.

#### **3.3.1 Gyroscope Capacitive MEMS Sensor with Multi-DoF Structure**

The conventional Coriolis vibratory MEMS gyroscope operates based on the energy transfer between the drive and sense modes when an angular rotation is applied [70]. Both drive and sense modes are implemented with an independent and symmetrical S-DoF system. When the two resonance frequencies of each mode are matched, the output of the

sense mode will be in high resolution. However, due to microfabrication imperfections, the design requires precise mode-matching for a narrow operational region involving complex control circuitry. In contrast, M-DoF vibratory rate MEMS gyroscopes in [70-77] are designed to 1) eliminate the mode-matching requirement, 2) produce structural parameter vibrations having less effect on the performance of the sensor and 3) render the gyroscope less sensitive to mechanical coupling and environment changes, such as changes in pressure and temperature. The 3-DoF gyroscope in [75] is one such example; it is depicted with the 3-DoF lumped model shown in Figure 3-10 (a). The sensor is fabricated using a bulk-micromachining process. It has a 2-DoF system for the sense mode and a 1-DoF system for the drive mode. The scanning electron microscope (SEM) image in Figure 3-10 (b) shows the folded beam interconnection between the two proof masses, where  $m_1$  and  $m_2$  are constrained together as 1-DoF in the drive mode and 2-DoF in the sense mode. In Figure 3-11(a), the 2-DoF sense-mode oscillator is characterized by two resonance frequencies and a flat region between the two peaks. The sensor output is taken within the flat region (i.e., the overlap area between the flat region and the resonance frequency of the 1-DoF drive-mode oscillator). The output gain of the sense mode in the bandwidth of interest is less sensitive to the structural and thermal parameter variations, as shown in Figure 3-11(b), and the flat region remains constant at various pressure values.

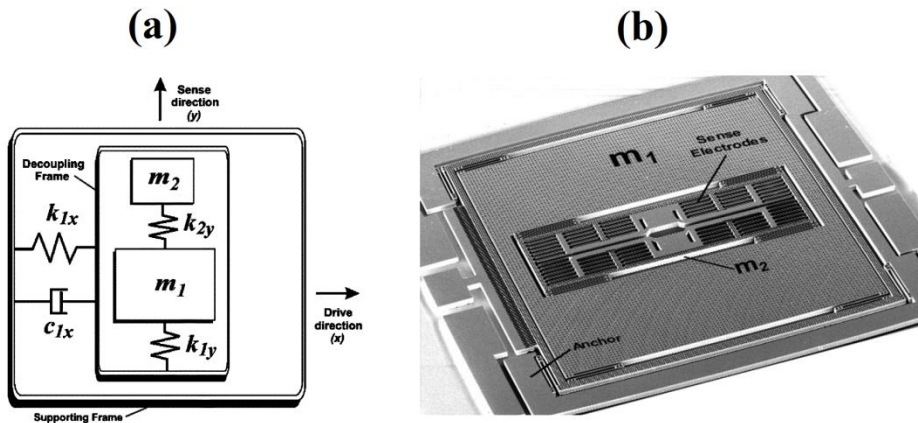


Figure 3-10: 3-DoF MEMS gyroscope; (a) 3-DoF gyroscope lumped model, (b) SEM of the gyroscope (reproduced from [75]).

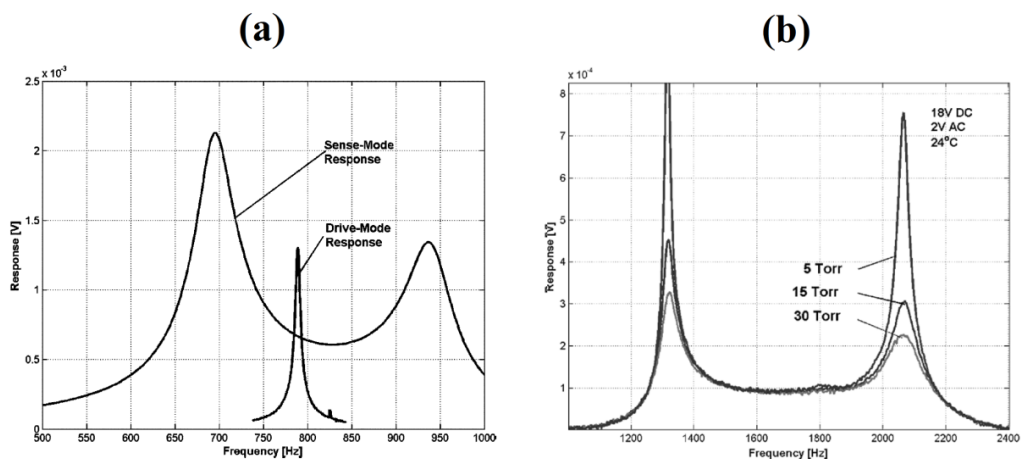


Figure 3-11: (a) Experimental measurement of the sense mode of the two resonance frequencies and the drive-mode of the single resonance frequency; the overlap area between the two modes determines the sensor's bandwidth. (b) Experimental evaluation to the sense mode, which shows immunity to pressure changes in the flat region (reproduced from [75]).

### 3.3.2 Energy Harvesting Capacitive MEMS Devices with Multi-DoF Structure

The mass-spring-damper MEMS systems can be utilized to transduce (harvest) kinetic energy and turn it into electrical energy. The maximum electrical energy obtained is at the resonance frequency; therefore, the operation bandwidth is determined by the resonance frequency [78]. Energy-harvester MEMS with multi-DoF that are designed to increase the harvesting bandwidth by introducing multiple resonance frequencies have been reported [79-82]. The electrostatic 3-DoF MEMS power harvester in [79] is fabricated using SOI technology. It is composed of three mass-spring-damper systems, as shown in Figure 3-12 (a and b), and the frequency response of the three proof masses are shown in Figure 3-13. If the system is designed with a small spacing between the resonance frequencies, a wider harvesting bandwidth is yielded.

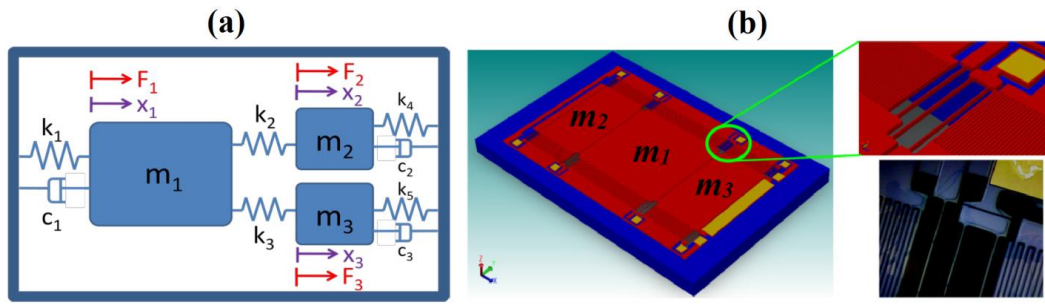


Figure 3-12: (a) 3-DoF lumped model and (b) system structure depicted using finite-element-method (FEM) software and SEM for the suspension (reproduced from [79]).

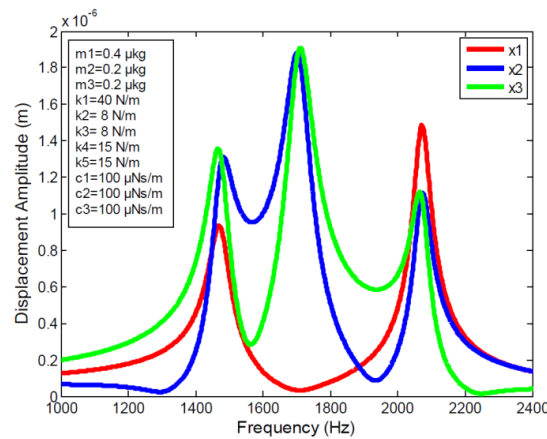


Figure 3-13: Frequency response of the 3-DoF system showing three resonance frequencies (reproduced from [79]).

### 3.4 Microfabrication Using Silicon-on-Insulator Technology

The microfabrication process of the 2-DoF capacitive MEMS velocity sensors is a significant part of the research. Therefore, this section discusses the SOI fabrication methods that can be adopted to fabricate the first and second prototypes of the 2-DoF capacitive MEMS velocity sensor.

One of the design aims of the 2-DoF capacitive MEMS velocity sensor is to employ two large proof masses, which will enhance the sensitivity (as seen in equation 2-6) and also minimize the effect of the mechanical Brownian noise. The SOI fabrication of a sensor with a large proof mass requires a back-etching process to remove the handle layer under the proof mass in order to prevent them from sticking to each other. There are two possible scenarios in which this stiction can occur [83] [84]: First, following the release process, the suspended proof mass is subject to potential stress, which can cause the proof mass to

bend and/or tilt. Accordingly, it may become stuck to the handle layer. Second, the hydrofluoric acid (HF) vapour phase etching process involves a chemical reaction between the silicon dioxide ( $\text{SiO}_2$ ) and the HF vapour. The reaction result includes water ( $\text{H}_2\text{O}$ ) in the form of a gas [85] [86]. However, during the release process, this water can condense in between the proof mass and the handle layer. Thus, permanent stiction to the handle layer can occur.

The following sections discuss two recently developed SOI fabrication processes involving the dry release method. Both processes include removing the handle layer under the proof mass.

### 3.4.1 Two-Mask Dry-Release Method

An SOI fabrication process for a micro-gravity capacitive accelerometer has been reported [87]. The fabrication process is shown in Figure 3-14: the handle wafer under the proof mass is removed via the deep reactive ion etching (DRIE) process down to the buried oxide (BOX) layer. Then, the BOX layer is removed via the dry etching process in inductively coupled plasma (ICP). Finally, the front side of the SOI wafer is etched completely to create the accelerometer's final structure. Because the BOX layer is completely removed before the front-side etching process, no release holes are required. Thus, the sensor proof mass increases.

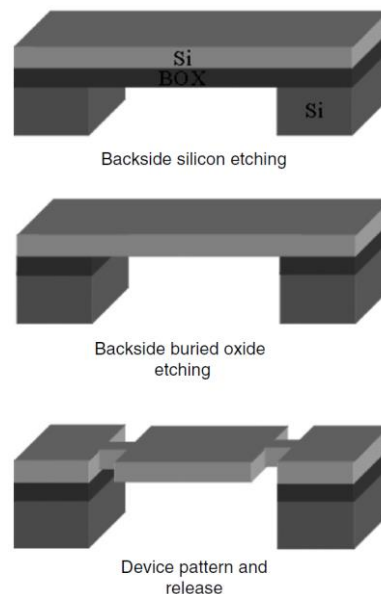


Figure 3-14: SOI fabrication process with no release holes on proof mass (reproduced from [87]).

The fabrication process of the first prototype of the 2-DoF velocity sensor was inspired by the above method, which is discussed in section 5.3.

### 3.4.2 Dicing-Free Dry-Release Method

The fabrication process reported in [83] [88] introduces a full-wafer dicing-free method with dry release using the HF vapour phase. The fabrication steps are shown in Figure 3-15. The process begins with backside DRIE process, which creates deep trenches to allow the releasing agent (HF acid vapour) to etch the BOX layer from the back side. Another DRIE process is then performed on the front side, where the device features, the proof-mass release holes, and the front trenches are created. The trenches on the front side and back side are designed so that they do not overlap to avoid damaging the SiO<sub>2</sub> layer through exposure to two different pressure levels during the DRIE process.

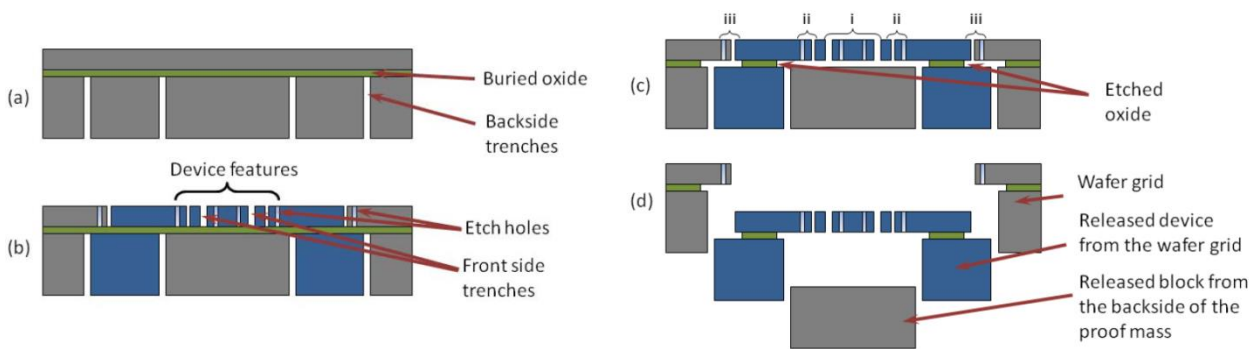


Figure 3-15: Fabrication process of the full wafer dicing-free dry-release. a) Back side etching process, b) front side etching process (device feature, release holes), c) HF vapour phase etching process and d) device, handle wafer and wafer grid separation (reproduced from [83]).

This fabrication process was developed and used for the second 2-DoF sensor prototype, which will be discussed in section 6.5.

### 3.5 Electric Isolation of the Device Layer in SOI Wafer

The design of the second prototype velocity sensor involves an electric isolation between two silicon blocks within the principal proof mass, which is discussed in section 6.5. There are three possible fabrication methods that can be used to electrically isolate two blocks created in the device layer of an SOI wafer, which can be tailored to the design of

the second prototype 2-DoF sensor: 1) The two blocks can be separated by a deep trench reaching down to the BOX layer in such a way that part of the handle layer holds the two blocks together, 2) the dielectric  $\text{SiO}_2$  can be deposited between the two released blocks or 3) an SU-8 photoresist can be deposited between the two blocks.

### 3.5.1 Electric Isolation Using Handle and $\text{SiO}_2$ Layers

This electric isolation technique is inspired by the fabrication process reported in [89] [90], in which part of the handle layer under the proof mass is not removed. Figure 3-16 shows the schematic block and the SEM of a micro-g accelerometer [89] in which part of the handle layer under the proof mass is not removed. Figure 3-17 shows the fabrication process that is performed on the MEMS micro-mirror using an SOI wafer device layer of  $12\ \mu\text{m}$ , a  $0.5\ \mu\text{m}$  BOX layer and a  $290\ \mu\text{m}$  handle layer [90]. First, a DRIE process is carried out on the front side of the SOI wafer (steps a–c). On the back side, a preservation photoresist layer is applied to the handle layer just under the mirror, and DRIE is used to create  $52\text{--}57\ \mu\text{m}$  trenches (steps d–f). The photoresist on the back side is then stripped, and a DRIE is used on the exposed handle layer (g). Next, the  $\text{SiO}_2$  layer is wet etched (step h). The final thickness of the micro-mirror is  $35\ \mu\text{m}$ . Finally, a Cr/Au coat is applied to create the thin, reflective film (step-i).

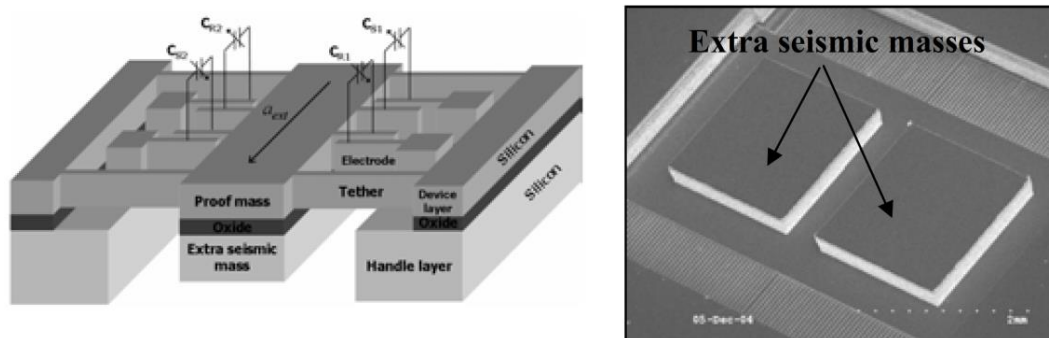


Figure 3-16: Sub-micro-gravity capacitive SOI micro accelerometer, (left) schematic diagram of the accelerometer, and (right) SEM photo of the back side of the proof mass (reproduced from [89]).

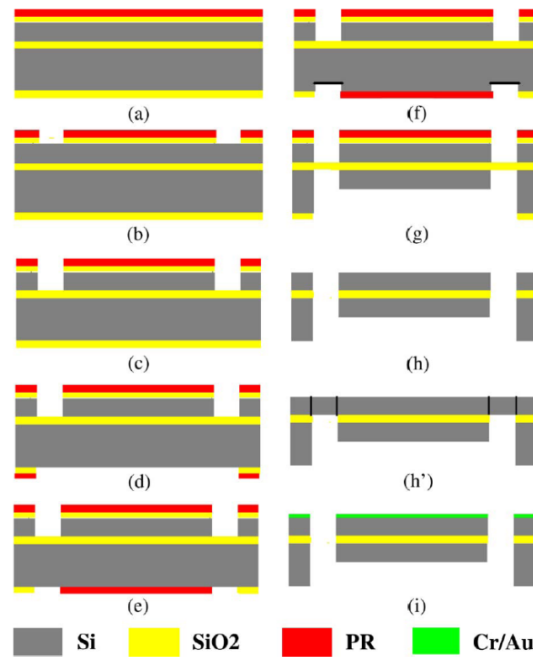


Figure 3-17: Micro-mirror plate microfabrication steps. (a-c) front-side DIRE, (d-g) preservation of the back side of the mirror and DRIE, (h and h') micro-mirror release using wet etching and (i) Cr/Au coating. (Copied from [90])

In the fabrication process illustrated in Figure 3-17, if the proof mass of the sensor is divided into two blocks with a deep trench reaching down to the SiO<sub>2</sub> layer, the two blocks will be securely attached by the handle layer.

### 3.5.2 Electric Isolation Using Silicon Dioxide Deposition

Thick layers and deep blocks of SiO<sub>2</sub> can be made within the silicon substrate to create an electrically isolated area [91-94]. The process involves the creation of silicon pillars or wall arrays using the DRIE process, as shown in Figure 3-18 (left). The trenches are then filled with SiO<sub>2</sub>, as shown in Figure 3-18 (right). Several techniques to obtain a layer of SiO<sub>2</sub> are listed in the literature [84], such as sputtering, thermal oxidation and chemical vapour deposition (CVD). This approach is not preferable in the fabrication process for the second 2-DoF sensor prototype for a number of reasons. First, achieving a thick block of SiO<sub>2</sub> in the range of a 100 μm device layer requires a long deposition process. Second, during the deposition process, the top and bottom surfaces of the SOI wafer will be covered with SiO<sub>2</sub>; hence, an additional etching process is required to remove the unwanted SiO<sub>2</sub>. Third, the SiO<sub>2</sub> block used for electric isolation will be severely affected during the release phase, which is performed using HF vapour phase etching process.

Finally, the silicon layer may exhibit surface tension due to the  $\text{SiO}_2$  deposition process, which could introduce the unwanted modes within the bandwidth of interest [84].

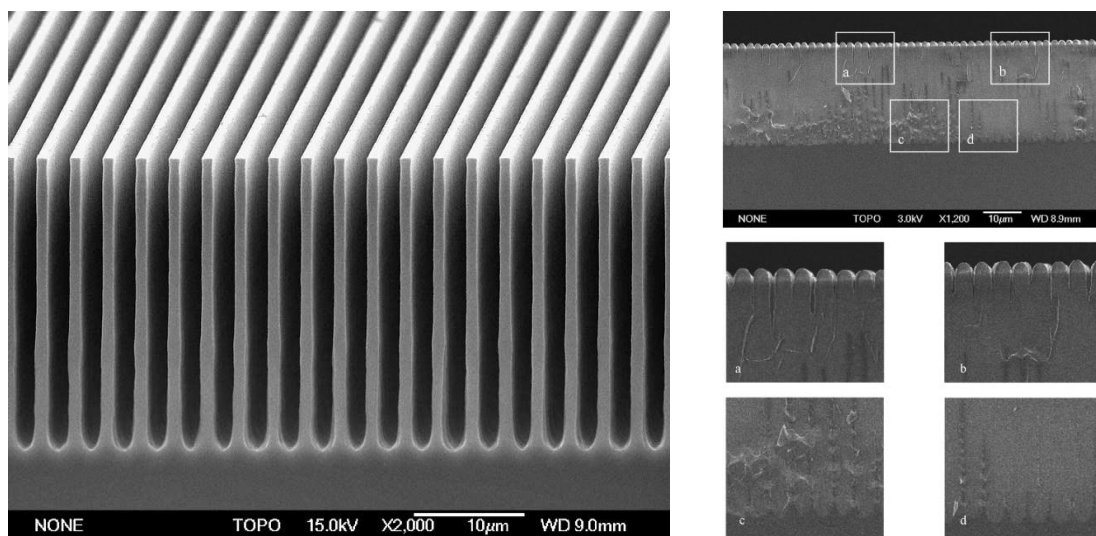


Figure 3-18: A cross-section SEM. (Left) the silicon wall array 30  $\mu\text{m}$  deep using electrochemical etching and (right) the thick  $\text{SiO}_2$  layer deposited using thermal oxidation process (a, b, c and d) show a closer view of the deposited  $\text{SiO}_2$  (reproduced from [92]).

### 3.5.3 Electric Isolation Using SU-8 Photoresist

IBM introduced SU-8 photoresist to the MEMS field in the 1990s. A negative photoresist can produce a thickness of several hundreds of micrometres in a one-spin coating step, and it has excellent adhesion to silicon substrates [95]. Once the SU-8 layer is exposed to ultra violet (UV) light and is post-baked (cured), it reaches its maximum stiffness and acid resistance, which renders it very difficult to remove. Therefore, SU-8 is generally considered to be a functional material in MEMS [96-98]. SU-8 is also a dielectric polymer, which would make it useful as an electric isolation material in the second 2-DoF sensor prototype [99]. To attain successful results, the correct timing of the pre-bake, exposure, post-bake and development must be ensured [100].

SU-8 comes in different viscosities (e.g., SU-8/2 has the lowest viscosity, while SU-8/5 is thicker, SU-8/25 is much thicker and so on [99]). A lower-viscosity material produces a thinner SU-8 layer and vice versa. Even with low-viscosity SU-8, it is important to consider the surface tension because this characteristic creates a phenomenon wherein SU-8 fails to penetrate the trenches of the wafer and leaves a trapped air gap, as shown Figure 3-19. If low-viscosity SU-8 is used, the effect of surface tension can be reduced,

but multiple coats are then required to increase the thickness. Solutions include using a syringe or pipette to inject SU-8 into the trenches before spinning and deflating the trapped air.

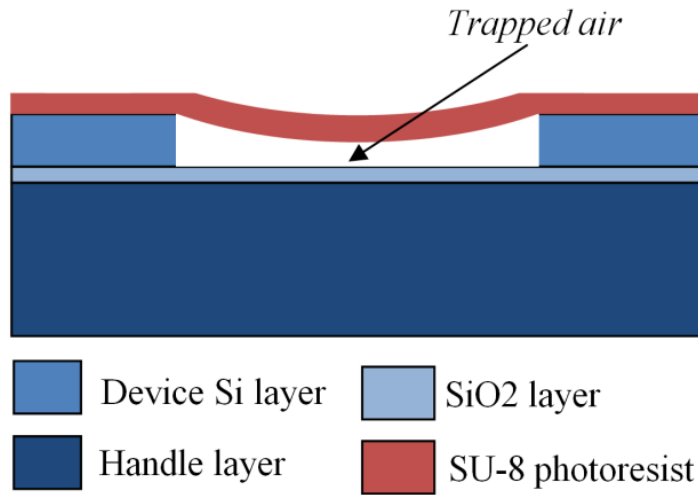


Figure 3-19: Trapped air after spinning the SU-8.

Several problems with the use of SU-8 are presented in [101]. First, air bubbles are observed before and after spinning. This problem can be reduced by allowing the SU-8 to relax for 1–2 hours on the substrate before spinning; if bubbles remain trapped, a sharp needle can be used. Extra time is also essential to allow the SU-8 to planarize on the wafer. Second, if the wafer is not well-cleaned, poor adhesion can occur, leading to SU-8 peeling after development [102]. Third, the SU-8 processes (spinning, pre-baking, exposure, post-baking and development) all require different temperatures. If these processes are not carried out in succession, a thermal mismatch can arise between the SU-8 and the wafer, thereby potentially leading to SU-8 surface cracking. This method was not used in the velocity sensor design, because of the aforementioned problems and the complexity involved.

### 3.6 Summary

This chapter presented some of the topics relevant to research on 2-DoF MEMS velocity sensors. It addressed some of the capacitive MEMS applications with an M-DoF structure, such as the gyroscope and power-harvesting devices. Such applications can reduce electronic circuit complexity and improve performance. These devices share some

features with the 2-DoF capacitive MEMS velocity sensor in terms of mechanical structure and design criteria.

Next, some methods used to measure velocity for the purpose of applying velocity feedback loop vibration control were discussed. One method includes using an accelerometer and applying a time-integration process on the output signal to obtain the velocity. However, due to the use of the real integrator and due to the dynamic response of the accelerometer, this method can lead to instability in terms of the velocity feedback vibration control. The second method is non-contact velocity measurement using a laser Doppler vibrometer. This approach is mainly used to study and analyse the performance of the velocity feedback vibration control. Finally, the 2-DoF piezoresistive MEMS velocity sensor was addressed. It was shown that this sensor can be feasibly employed within a vibration control that is capable of measuring the velocity of the vibrated structure and is able to overcome the problems encountered in the accelerometer method. However, the fabrication process of this velocity sensor was costly and time-consuming. The numerous fabrication steps involved in the surface micromachining introduce a high level of susceptibility to fabrication tolerance. Despite the potential of the proposed sensor and concept, the use of piezoresistive technology imposes performance limitations. Such problems include the susceptibility of the sensor to temperature changes, nonlinear effects and relatively low sensitivity.

Two SOI fabrication methods were also presented. The first was the two-mask dry-release fabrication method, and the second was the dicing-free dry-release method. Both methods remove the handle layer under the proof mass to avoid the possibility of proof mass stiction.

Finally, three potential fabrication methods that could electrically isolate two silicon blocks within the proof mass were discussed. One method includes separating two silicon blocks in the device layer with a deep trench reaching down to the BOX layer and then keeping a part of the handle layer underneath the trench in order to hold these two blocks in place. Other methods include filling the trench with SiO<sub>2</sub> or using an SU8 resist. The second velocity sensor prototype used the first method, which will be discussed in Chapter 6.



## Chapter 4: Velocity Sensor Theoretical Analysis

### 4.1 Introduction

This chapter provides a discussion about the operation concept of the capacitive MEMS velocity sensor, followed by the theoretical analysis of the 2-DoF velocity sensor and the design of a stable velocity feedback loop. Finally, the analysis of the open- and closed-loop velocity sensor is discussed, including the advantages that the velocity sensor can offer to velocity feedback loop vibration control applications.

### 4.2 Operating Concept of the Velocity Sensor

The velocity sensor is formed by a 2-DoF sensing element, which consists of two mass-spring-damper systems and a velocity feedback loop control, as shown in Figure 4-1. The sensing element consists of a bottom mass-spring-damper system, also referred to as the principal sensor because it provides the velocity output signal. The function of the top mass-spring-damper system, also referred to as the secondary sensor, is to implement a negative velocity feedback loop on the proof mass of the principal sensor. The principal system has a proof mass  $m_p$  anchored onto the sensor's frame via a spring  $k_p$ . The secondary system has a proof mass  $m_s$  anchored onto the mass of the principal system via a spring  $k_s$ . The damping effects in the 2-DoF system are modelled with dashpot elements with a damping coefficient  $b_p$  for the principal system and with  $b_{s1}$  and  $b_{s2}$  for the secondary sensors.

The sensing element is designed so that the first resonance is determined by the natural frequency of the principal sensor, while the second resonance is determined by the natural frequency of the secondary sensor. The overall performance of the velocity sensor is determined by the 2-DoF resonance frequencies such that the first resonance indicates the upper limit of the velocity sensor bandwidth, and the amplitude of the second resonance determines the feedback loop stability, as will be discussed in section 4.5.

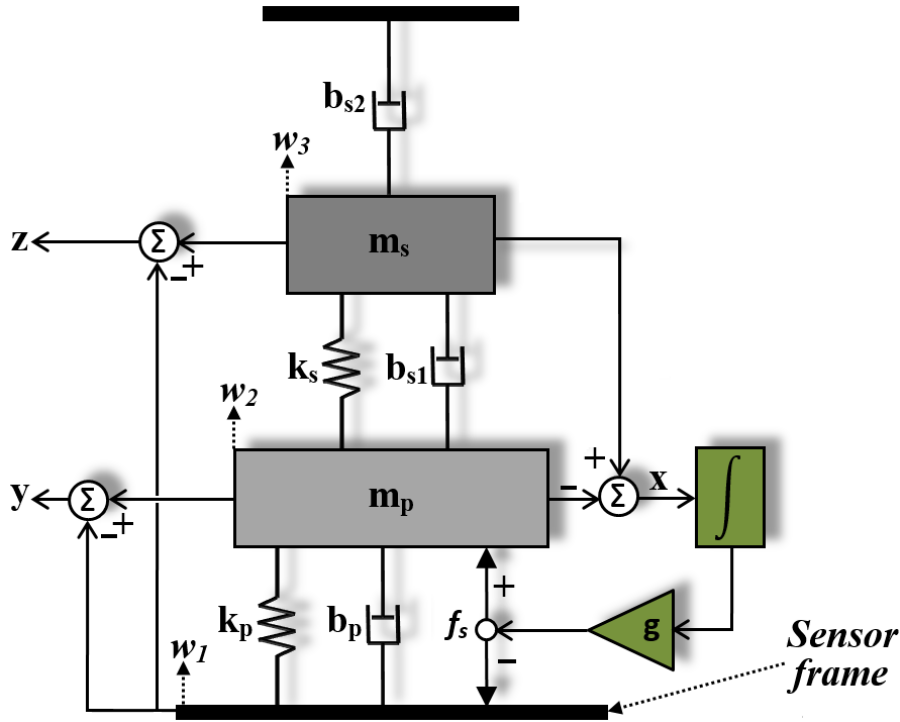


Figure 4-1: Two-DoF velocity sensor block diagram.

As discussed in section 2.2.2 (equation 2-8), if the sensor's frame, the proof mass  $m_p$  and the proof mass  $m_s$  displacements are denoted as  $w_1$ ,  $w_2$  and  $w_3$ , respectively, then the relative displacement of the principal proof mass with respect to the frame ( $y$ ), the relative displacement of the secondary mass with respect to the frame ( $z$ ) and the relative displacement of the secondary mass with respect to the principal mass ( $x$ ) are given by the following:

$$y = w_2 - w_1 \quad (a)$$

$$z = w_3 - w_1 \quad (b) \quad 4-1$$

$$x = z - y = w_3 - w_2 \quad (c)$$

The output signal  $x$  of the secondary proof mass is proportional to the acceleration of the principal proof mass. Therefore, the velocity measurement of the principal proof mass is obtained by time integrating the displacement  $x$  (i.e.  $\int x dt$ ). To construct a negative velocity feedback loop, the velocity measurement is amplified with a control gain  $g$ , after which the control unit outputs an electrostatic force  $f_s$  applied on the principal system. When the control gain  $g$  is correctly tuned and the loop is closed, a damping force effect

is applied, and the frequency response function (FRF) of output signal  $y$  exhibits the three main features as follows:

- 1- Below the first resonance, the output signal  $y$  of the principal sensor is proportional to the velocity of the sensor's frame, rather than acceleration.
- 2- The first resonance peak flattens.
- 3- Above the first resonance, the output signal of the principal sensor declines monotonically with a phase of  $-90^\circ$  instead of  $-180^\circ$ .

These three features of the velocity sensor are of considerable importance in the construction of a stable velocity feedback loop control that is used for the active vibration control of distributed flexible structures.

### 4.3 Dynamic Response Functions

The analytical derivations of the dynamic response functions of the 2-DoF system were discussed in section 2.2.2. The same approach can be applied to determine the dynamic response functions for the principal and secondary sensors with respect to the two possible inputs: first, with sensor input acceleration  $\ddot{w}_1$  and second with the force  $f_s$  applied to the principal sensor.

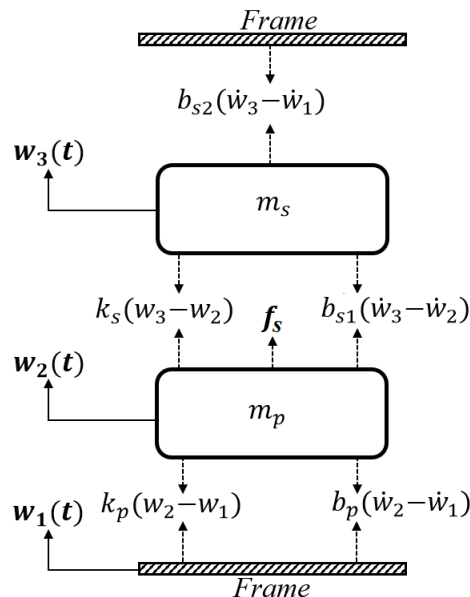


Figure 4-2: Two-DoF velocity sensor free-body diagram.

The block diagram of the 2-DoF velocity sensor in Figure 4-1 is represented with the free-body diagram in Figure 4-2. It shows the direction of forces applied to the principal and secondary proof masses when the sensor is excited by input acceleration and/or electrostatic force. When the sensor is excited, the proof mass  $m_p$  and  $m_s$  will experience displacement  $w_2$  and  $w_3$ , respectively, in the same direction of the displacement of the sensor's frame  $w_1$ . Therefore, each proof mass will be under an inertial force and dissipative spring and damping forces. If the first derivative of the displacement ( $w_1$ ,  $w_2$  and  $w_3$ ) gives velocity ( $\dot{w}_1$ ,  $\dot{w}_2$  and  $\dot{w}_3$ ), and the second derivative gives acceleration ( $\ddot{w}_1$ ,  $\ddot{w}_2$  and  $\ddot{w}_3$ ), the equations of motion are obtained by applying Newton's second law for each proof mass, which gives the following:

$$\begin{aligned} m_p \ddot{w}_2 &= -b_p(\dot{w}_2 - \dot{w}_1) - k_p(w_2 - w_1) + f_s + b_{s1}(\dot{w}_3 - \dot{w}_2) + k_s(w_3 - w_2) & (a) \\ m_s \ddot{w}_3 &= -b_{s1}(\dot{w}_3 - \dot{w}_2) - k_s(w_3 - w_2) - b_{s2}(\dot{w}_3 - \dot{w}_1) & (b) \end{aligned} \quad 4-2$$

Equation 4-2 (a, b) can be represented with the relative displacements  $y$  and  $z$  of the principal and the secondary sensors, respectively, as defined in equation 4-1 (a, b). If the first derivative of the relative displacement gives velocity ( $\dot{y}$  and  $\dot{z}$ ), and the second derivative gives acceleration ( $\ddot{y}$  and  $\ddot{z}$ ), the equations of motion will be as follows:

$$\begin{aligned} m_p \ddot{w}_1 &= -m_p \ddot{y} - b_p \dot{y} - k_p y + f_s + b_{s1}(\dot{z} - \dot{y}) + k_s(z - y) & (a) \\ m_s \ddot{w}_1 &= -m_s \ddot{z} - b_{s1}(\dot{z} - \dot{y}) - k_s(z - y) - b_{s2} \dot{z} & (b) \end{aligned} \quad 4-3$$

To study the frequency response of the 2-DoF velocity sensor, the differential equations in 4-3 (a, b) can be represented in the Laplace domain with the parameter  $s$  as follows:

$$\begin{aligned} m_p s^2 W_1 &= -[m_p s^2 + (b_p + b_{s1})s + (k_p + k_s)]Y + F_s + [b_{s1}s + k_s]Z & (a) \\ m_s s^2 W_1 &= -[m_s s^2 + (b_{s1} + b_{s2})s + k_s]Z + [b_{s1}s + k_s]Y & (b) \end{aligned} \quad 4-4$$

The Simulink model in Figure 4-3 is constructed using equation 4-4 (a, b). It shows that the system has two inputs: the acceleration of the sensor frame ( $Acc=s^2W_1$ ) and the input force  $F_s$ . As defined in equation 4-1, the 2-DoF sensor has two output displacement signals  $Y$  and  $Z$ , as well as the relative displacement between the principal and secondary sensors  $X$ .

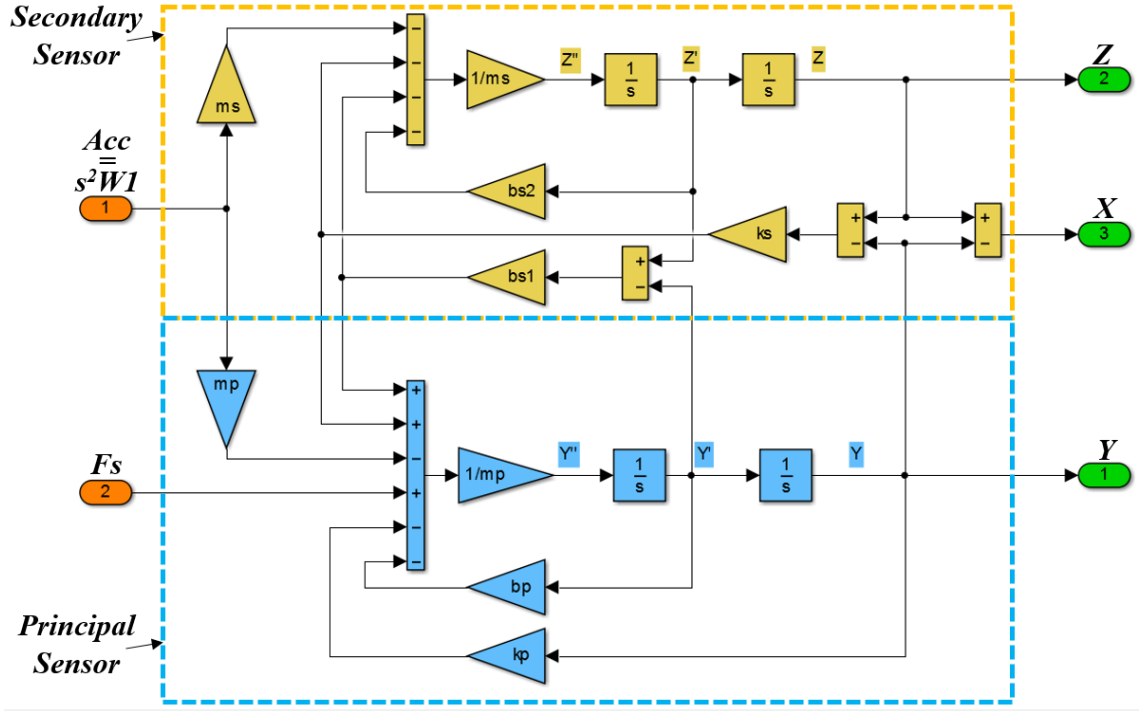


Figure 4-3: Simulink model of the 2-DoF sensing element represented with equations 4-4 (a, b).

In the absence of  $F_s$ , which means no electrostatic force is applied to the principal proof mass, the frequency response functions (FRFs) that give the displacement  $Y$  and  $Z$  per unit input acceleration  $Acc$  can be derived from equation 4-4 (a, b) as

$$G_{Y,Acc} = \frac{Y}{Acc} \Big|_{F_s=0} = \frac{-m_p B_2 - m_s B_1}{A_1 B_2 - A_2 B_1} \quad (a)$$

$$G_{Z,Acc} = \frac{Z}{Acc} \Big|_{F_s=0} = \frac{-m_p A_2 - m_s A_1}{A_1 B_2 - A_2 B_1} \quad (b)$$

4-5

where  $A_1 = m_p s^2 + (b_p + b_{s1})s + (k_p + k_s)$ ,  $A_2 = B_1 = b_{s1}s + k_s$

$$B_2 = m_s s^2 + (b_{s1} + b_{s2})s + k_s$$

In absence of the acceleration input (i.e.  $w_1=0$ ), the two FRFs that give the relative displacement  $Y$  and  $Z$  per unit input electrostatic force  $F_s$  applied to the proof mass  $m_p$  can also be derived from equation 4-4 (a, b) as follows:

$$G_{Y,FS} = \left. \frac{Y}{FS} \right|_{Acc=0} = \frac{B_2}{A_1B_2 - A_2B_1} \quad (a) \quad 4-6$$

$$G_{Z,FS} = \left. \frac{Z}{FS} \right|_{Acc=0} = \frac{A_2}{A_1B_2 - A_2B_1} \quad (b)$$

The 2-DoF velocity sensor is designed with capacitive sense and actuation technology, therefore, if the displacements  $Y$  and  $Z$  of the two proof masses are relatively small compared to the sense capacitor nominal gap, the spring constant, the damping coefficients, the electrostatic feedback force and the pickoff circuit can be assumed linear [103]. Accordingly, the 2-DoF system can be assumed linear. For simplicity the pickoff gain constants are assumed to equal one. Therefore, the displacement signals  $Y$  and  $Z$  can be derived as the superposition of the effects caused by the sensor base acceleration ( $Acc$ ) in equation 4-5 (a, b) and the electrostatic force ( $FS$ ) in equation 4-6 (a, b):

$$Y(s) = G_{Y,Acc} * Acc(s) + G_{Y,FS} * F_S(s) \quad (a)$$

$$Z(s) = G_{Z,Acc} * Acc(s) + G_{Z,FS} * F_S(s) \quad (b) \quad 4-7$$

As shown in equation 4-1 (c), the relative displacement  $x$  between the two proof masses  $m_p$  and  $m_s$ , necessary to implement the internal velocity feedback loop, can be calculated by taking the difference of the two signals for the relative displacements  $y$  and  $z$ ; i.e.  $x=z-y$ . Thus the relative displacement  $x$  can also be expressed in terms of FRFs as follows:

$$X(s) = G_{X,Acc} * Acc(s) + G_{X,FS} * F_S(s) \quad 4-8$$

In this case, the FRFs that give the relative displacement  $X$  per unit sensor's frame acceleration ( $Acc$ ) or per unit applied electrostatic force ( $FS$ ), are reconstructed from the following relations:

$$G_{X,Acc} = G_{Z,Acc} - G_{Y,Acc} = \left. \frac{X}{Acc} \right|_{FS=0} = \frac{(B_1 - A_1)m_s + (B_2 - A_2)m_p}{A_1B_2 - A_2B_1} \quad (a) \quad 4-9$$

$$G_{X,FS} = G_{Z,FS} - G_{Y,FS} = \left. \frac{X}{FS} \right|_{Acc=0} = \frac{A_2 - B_2}{A_1B_2 - A_2B_1} \quad (b)$$

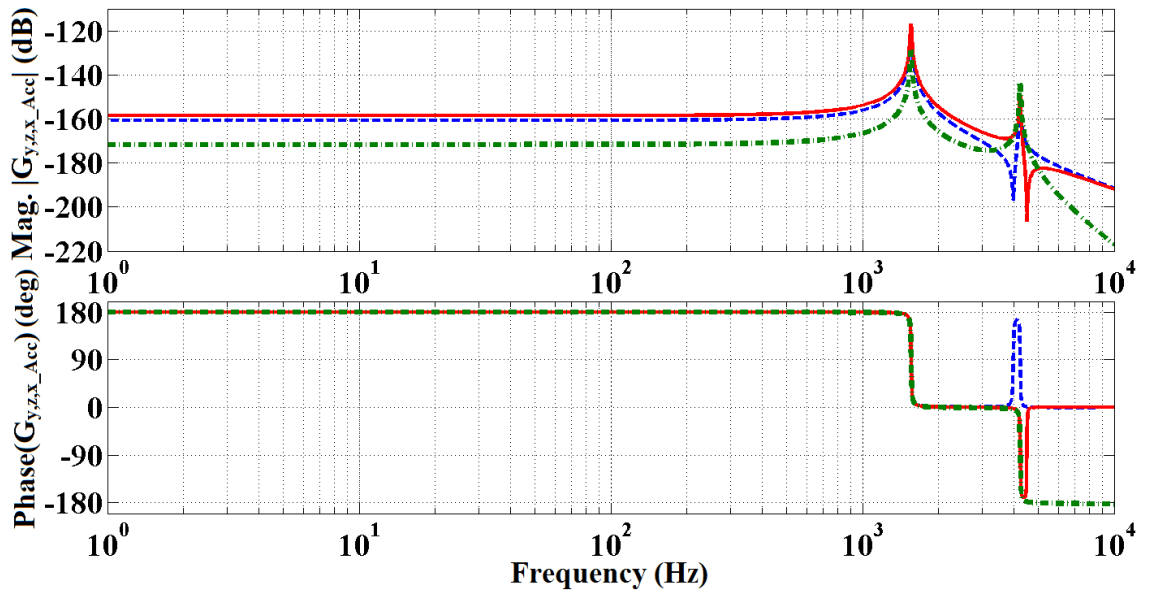


Figure 4-4: Simulated FRFs of principal system output  $Y$  (blue/dashed line), secondary system output  $Z$  (red/solid line), and secondary system output  $X$  (green/dashed-dotted line) with respect to the input acceleration  $Acc$ .

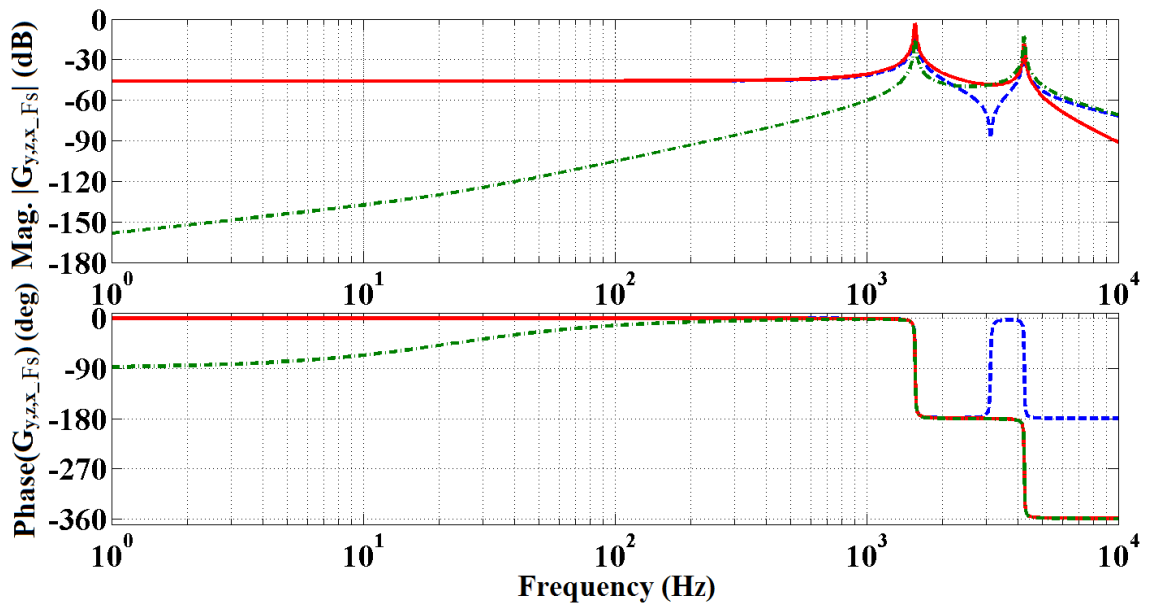


Figure 4-5: Simulated FRFs of principal system output  $Y$  (blue/dashed line), secondary system output  $Z$  (red/solid line), and secondary system output  $X$  (green/dashed-dotted line) with respect to the input electrostatic force  $F_s$  applied to the principal sensor.

The simulated FRFs in equations 4-5 (a, b) and 4-9 (a) of the input acceleration response  $G_{Y,Acc}$  (blue/dashed line),  $G_{Z,Acc}$  (red/solid line) and  $G_{X,Acc}$  (green/dashed-dotted line), respectively, are presented in Figure 4-4 (refer to appendix A.1 for Matlab code). Below the first resonance frequency, all displacements  $Y$ ,  $Z$  and  $X$  show flat amplitude and phase, which is an expected behaviour with respect to input acceleration. At the second resonance frequency, the displacement signal  $Y$  will move out of phase if compared with the displacement signals  $Z$  and  $X$ .

The simulated FRFs in equations 4-6 (a, b) and 4-9 (b) of the input electrostatic force response  $G_{Y,Fs}$  (blue/dashed line),  $G_{Z,Fs}$  (red/solid line) and  $G_{X,Fs}$  (green/dashed-dotted line), respectively, are presented in Figure 4-5 (refer to appendix A.1 for Matlab code). It can be seen that below the first resonance frequency, the displacement  $Y$  and  $Z$  taken with reference to the sensor's frame show flat amplitude and phase, while the amplitude of the displacement  $X$  increases with the frequency, and the phase smoothly increases from  $90^\circ$  to  $0^\circ$ . This indicates that at low frequency, the relative displacement  $X$  of the secondary mass with respect to the principal mass is very low. At the second resonance frequency, the principal proof mass displacement  $Y$  is out phase with respect to the secondary proof mass displacements  $Z$  and  $X$ .

In Figure 4-4 and Figure 4-5, all FRFs are characterized by the two resonances. The principal sensor FRFs  $G_{y,Acc}$  and  $G_{y,Fs}$  (blue/dashed line) are characterized by an antiresonance in between the two main resonance peaks, which are due to the physical collocation feature of the inertial and electrostatic forces that are applied directly to the principal mass [14]. On the other hand, the secondary sensor FRFs  $G_{Z,Acc}$ ,  $G_{X,Acc}$ ,  $G_{Z,Fs}$  and  $G_{X,Fs}$  do not have an antiresonance in between the two resonances because the inertial and electrostatic forces are not physically collocated to this degree of freedom i.e. they are not applied directly to the secondary mass.

The two resonance frequencies of the 2-DoF system can be characterized based on the isolated natural frequency of each degree of freedom. i.e. considering isolated mass-spring systems. By doing so, the design of the 2-DoF natural frequencies will be related to the basic design components of the system, which are comprised of masses and spring constants. If the natural frequencies of the isolated principal ( $\omega_{np}$ ) and secondary ( $\omega_{ns}$ ) mass-spring systems are given by

$$\omega_{np} = \sqrt{\frac{k_p}{m_p}} \quad 4-10$$

$$\omega_{ns} = \sqrt{\frac{k_s}{m_s}}$$

and the mass ratio  $\mu$  is given by

$$\mu = \frac{m_s}{m_p} \quad 4-11$$

then the 2-DoF natural frequencies equation derived in section 2.2.2 can be rewritten as follows:

$$\omega_{n1,2}^2 = \frac{1}{2} \left( (\sqrt{\omega_{np}} + (\mu + 1)\sqrt{\omega_{ns}}) \pm \sqrt{(\sqrt{\omega_{np}} + (\mu + 1)\sqrt{\omega_{ns}})^2 - 4\sqrt{\omega_{np}\omega_{ns}}} \right) \quad 4-12$$

The 2-DoF natural frequencies equation shown in equation 4-12 is a function of the S-DoF system's natural frequencies and masses ratio. This is an important design criterion in the 2-DoF velocity sensor, where the frequency placements of the two resonance frequencies play a very important role in the velocity measurement bandwidth and the internal velocity feedback loop stability.

#### 4.4 Velocity Sensor Closed-Loop Transfer Function

As can be deduced from Figure 4-1, to build a negative velocity feedback loop that produces the desired damping force effect on the principal mass, the displacement  $X$ , which represents the absolute acceleration of the proof mass  $m_p$ , has to be integrated and amplified by a gain  $g$ . Therefore, the feedback loop function  $H(s)$  is given by:

$$H(s) = \frac{Fs(s)}{X(s)} = -g \frac{K_{int}}{1 + \tau s} \quad 4-13$$

where  $K_{int}$  is the DC gain of the integrator circuit, and  $\tau$  is the integration time constant that is equal to the inverse of the cut-off frequency  $f_c$ . Figure 4-6 shows the Bode plot of the integrator function with a  $K_{int} = 1$  and cut-off frequency at 10 Hz.

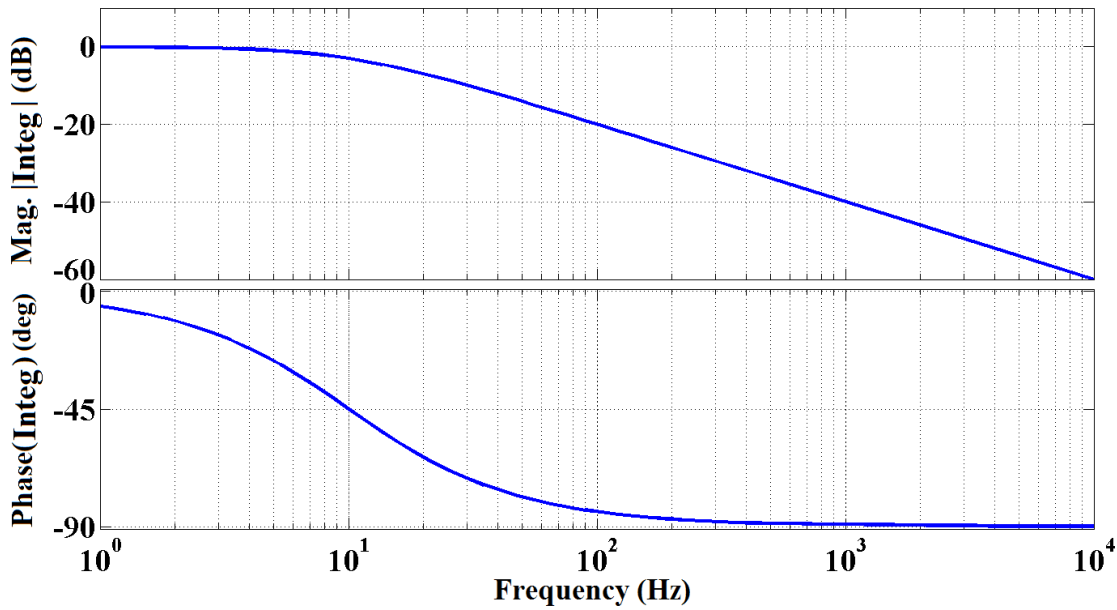


Figure 4-6: Bode plot of the integrator function in equation 4-13 with a  $K_{int} = 1$  and a cut-off frequency at 10 Hz.

Using equations 4-7 (a), 4-8 and 4-13, the closed-loop transfer function  $G_{y,CL}(s)$  of the displacement  $Y$  per input acceleration  $Acc$  of the sensor's frame is given by the following:

$$G_{y,CL}(s) = \frac{Y(s)}{S^2W_1} = G_{Y,Acc}(s) + G_{Y,Fs}(s)G_{X,Acc}(s) \left( \frac{H(s)}{1 - G_{X,Fs}(s)H(s)} \right) \quad 4-14$$

If the FRFs that give the displacement  $Y$ ,  $Z$  and  $X$  per unit input velocity ( $Vel=sW_1$ )  $G_{Y,vel}$ ,  $G_{Z,vel}$  and  $G_{X,vel}$  can be derived from the transfer functions in equations 4-6 and 4-9 as:

$$\begin{aligned} G_{Y,vel}(s) &= \frac{Y}{sW_1} = s * G_{Y,Acc}(s) \\ G_{Z,vel}(s) &= \frac{Z}{sW_1} = s * G_{Z,Acc}(s) \\ G_{X,vel}(s) &= \frac{X}{sW_1} = s * G_{X,Acc}(s) \end{aligned} \quad 4-15$$

then the closed-loop transfer function  $G_{y,CL}(s)$  of the displacement  $Y$  per input velocity  $Vel$  of the sensor's frame is given by the following:

$$G_{y,CL}(s) = \frac{Y(s)}{SW_1} = G_{Y,Vel}(s) + G_{Y,Fs}(s)G_{X,Vel}(s) \left( \frac{H(s)}{1 - G_{X,Fs}(s)H(s)} \right) \quad 4-16$$

The above equation can be used to obtain the open- and closed-loop frequency response of the velocity sensor by using the simulated or measured  $G_{Y,Vel}$ ,  $G_{X,Vel}$ ,  $G_{Y,Fs}$  and  $G_{X,Fs}$  FRFs and by using control function  $H(s)$ , which will be used after studying the internal feedback loop stability in the next section.

## 4.5 Control Gain and Feedback Loop Stability

To apply a control gain  $g$  such that the transfer function  $G_{y,CL}(s)$  of the closed-loop sensor (in equation 4-16) becomes proportional to the velocity of the sensor's frame, the control gain  $g$  can be calculated in the frequency domain ( $j\omega$ ) by expressing the closed-loop transfer function in terms of its real and imaginary parts:

$$G_{Y,CL}(j\omega) = \mathbf{Real}\{G_{Y,CL}(j\omega)\} + \mathbf{Imaginary}\{G_{Y,CL}(j\omega)\} \quad 4-17$$

Then the control gain  $g$  has to be chosen to meet the following conditions:

- i) The imaginary part in the frequency band of interest is eliminated, so the transfer function  $G_{Y,CL}(j\omega)$  becomes proportional to velocity with  $0^\circ$  or  $-180^\circ$  phase.
- ii) The velocity feedback loop remains stable.

Equation 4-17 can be represented with the use of the feedback loop function  $H(s)$  in equation 4-13 as follows:

$$G_{Y,CL}(j\omega) = \frac{\overbrace{(-F_{N2}\omega^2 + F_{N0})}^{\alpha} + j \overbrace{(-F_{N3}\omega^3 + F_{N1}\omega)}^{\beta}}{\underbrace{(F_{D4}\omega^4 - F_{D2}\omega^2 + F_{D0})}_{\gamma} + j \underbrace{(-F_{D3}\omega^3 + F_{D1}\omega)}_{\delta}} \quad 4-18$$

where the parameters of the numerator  $F_{N0}$ ,  $F_{N1}$ ,  $F_{N2}$  and  $F_{N3}$ , and the denominator  $F_{D0}$ ,  $F_{D1}$ ,  $F_{D2}$ ,  $F_{D3}$  and  $F_{D4}$  are listed in appendix A.2.

Multiplying the numerator and denominator in equation 4-18 by the complex conjugate of the denominator gives:

$$G_{Y,CL}(j\omega) = \frac{\alpha + j\beta}{\gamma + j\delta} * \frac{\gamma - j\delta}{\gamma - j\delta} = \frac{(\alpha\gamma + \beta\delta) + \overbrace{j(\beta\gamma - \alpha\delta)}^{\text{imaginary part}}}{\gamma^2 + \delta^2} \quad 4-19$$

The imaginary part in equation 4-19 is solved for  $g$  values that would eliminate it. After lengthy mathematical manipulations (refer to appendix A.2), the control gain  $g(j\omega)$  is a frequency-dependent function in the form of a second-order equation given by the following:

$$\mathbf{Imaginary}\{G_{Y,CL}(j\omega)\} = ag(\omega)^2 + bg(\omega) + c = 0 \quad 4-20$$

where  $a$ ,  $b$  and  $c$  are listed in the MATLAB code appendix A.2.

Since, the control gain  $g$  in equation 4-20 is in the form of a quadratic formula, two solutions are possible for each given frequency:

$$g(\omega) = \frac{-b \pm \sqrt{b^2 - 4ac}}{2a} \quad 4-21$$

The frequency-dependent control gain  $g(j\omega)$  in equation 4-21 can be examined as shown in Figure 4-7 (refer to appendix A.4 for Matlab codeA.2). The control gain  $g$  has two solution and they are indicated as blue and green lines. The feedback loop control function  $H(s)$  in equation 4-13 contains a negative sign, so only positive  $g$  values (from the blue line) is used to apply stable and causal negative velocity feedback loop. Thus, the values of the green line cannot be implemented because the sign of the  $H(s)$  will change, produce a positive feedback force and the control loop will be unstable. In addition, it will make the control system dependent on future inputs; i.e. the frequency response will have a lead phase, which makes the control system noncausal. Therefore, a fixed gain value can be chosen from the blue line so that within the frequency band of interest (bounded by the first resonance), the damping force effect is produced. This result will eliminate the imaginary part in equation 4-19, and the first condition of the control gain  $g$  will be met.

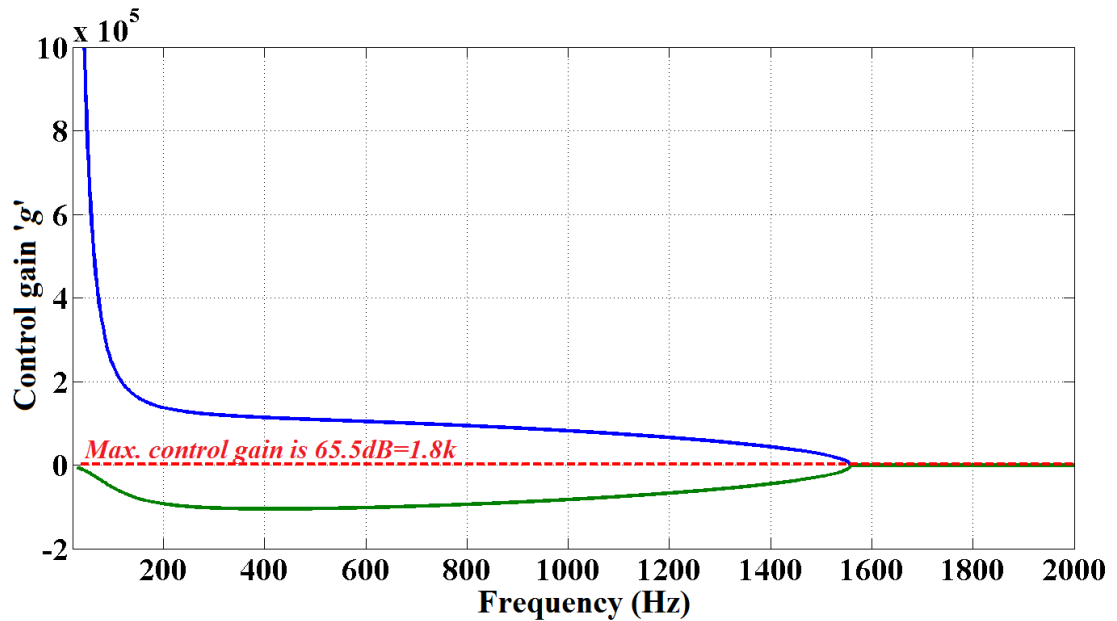


Figure 4-7: Control gain frequency-dependent function. Because the maximum control gain is at 1.8k, the control gain values from the blue line will not be valid for stable and causal closed-loop systems.

The second condition that should be met by the control gain  $g$  is the stability, which can be examined using the open-loop control transfer function with unity gain ( $g=1$ ), which is given by the following expression:

$$G_{ol,X,FS}(s) = H(s) G_{X,FS}(s) \quad 4-22$$

The Bode plot of the open-loop control transfer function in equation 4-22 is presented in Figure 4-8 (refer to appendix A.4 for Matlab code). From classical control theory [51], the phase crossing of the  $-180^\circ$  determines the gain margin. The second resonance frequency peak is below 0 dB, thus, the closed-loop system remains stable as long as the resonance peak does not cross 0 dB. Therefore, the maximum control gain for a stable closed-loop system obtained from the open-loop control transfer function in Figure 4-8 is 65.5 dB ( $\approx 1.8k$ ), however, the control gain in Figure 4-7 that can eliminate the imaginary part is above the maximum gain for a stable closed-loop. Consequently, a control gain that satisfies both conditions (eliminate the imaginary part and stable control system) cannot be achieved due to the low gain margin caused by the high peak of the second resonance.

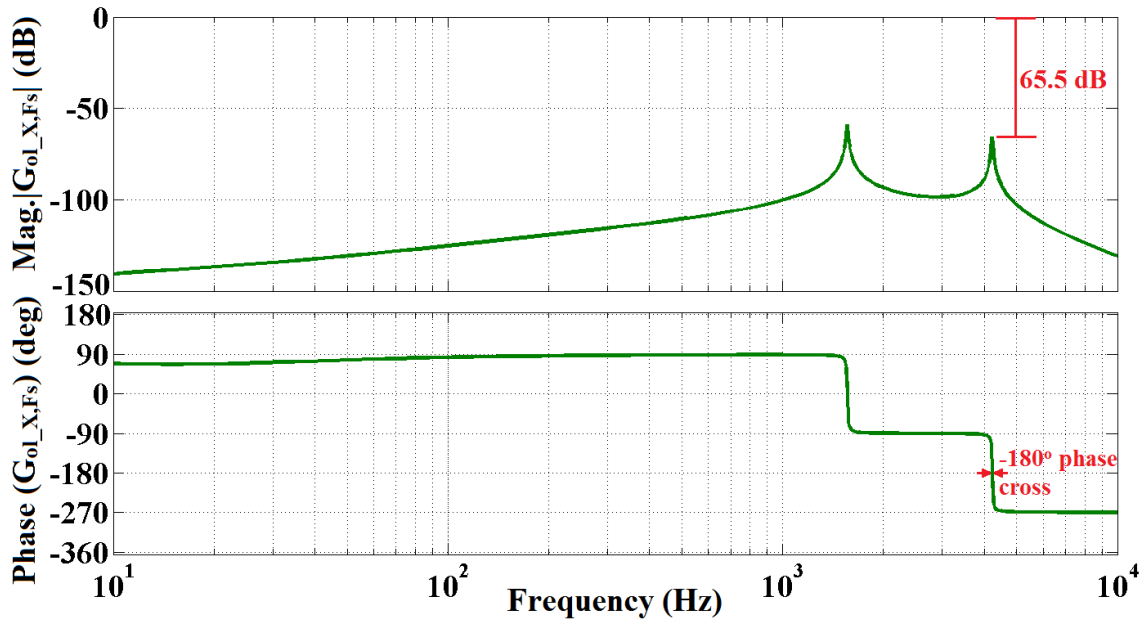


Figure 4-8: Bode plot of the open-loop control transfer function using an integrator function with  $K_{int} = 1$  and cut-off frequency at 10 Hz; the maximum control gain is 65.5 dB.

The gain margin of the open-loop control transfer function can be increased by using a low-pass filter (LPF) in the velocity feedback loop to suppress the second resonance peak. Therefore, the feedback loop function in equation 4-13 is reconstructed with a second-order low-pass filter (LPF2), as follows:

$$H(s) = \frac{Fs(s)}{X(s)} = -g * \frac{K_{int}}{1 + \tau s} * \frac{w_c^2}{s^2 + \frac{w_c}{Q} s + w_c^2} \quad 4-23$$

where  $w_c$  is the cut-off frequency (rad/sec) of the LPF2, which is designed to be in between the two resonance frequencies, and  $Q$  is the quality factor, which is designed to be set at 0.5, i.e. unity gain in the band of interest. Figure 4-9 shows the Bode plot of the LPF2 with a cut-off frequency at 2 kHz, just after the first resonance frequency of the 2-DoF.

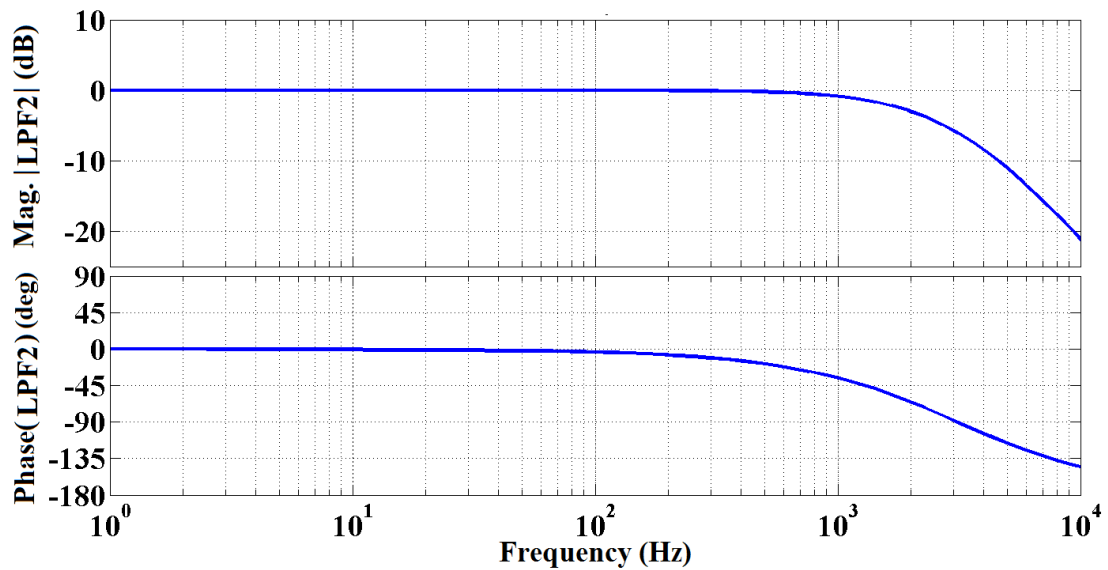


Figure 4-9: Bode plot of the second-order low-pass filter with a cut-off frequency at 2 kHz.

The open-loop control function in equation 4-22 is used in combination with equation 4-23 to investigate the stability. As shown in the Bode plot in Figure 4-10, the introduction of the LPF2 has two main effects: a) The peak of the second resonance frequency is shifted below  $-74$  dB, and b) the  $-180^\circ$  crossover is shifted to be in between the two resonance frequencies, so the control loop has a more relaxed gain margin of 104 dB ( $\approx 165.5k$ ).

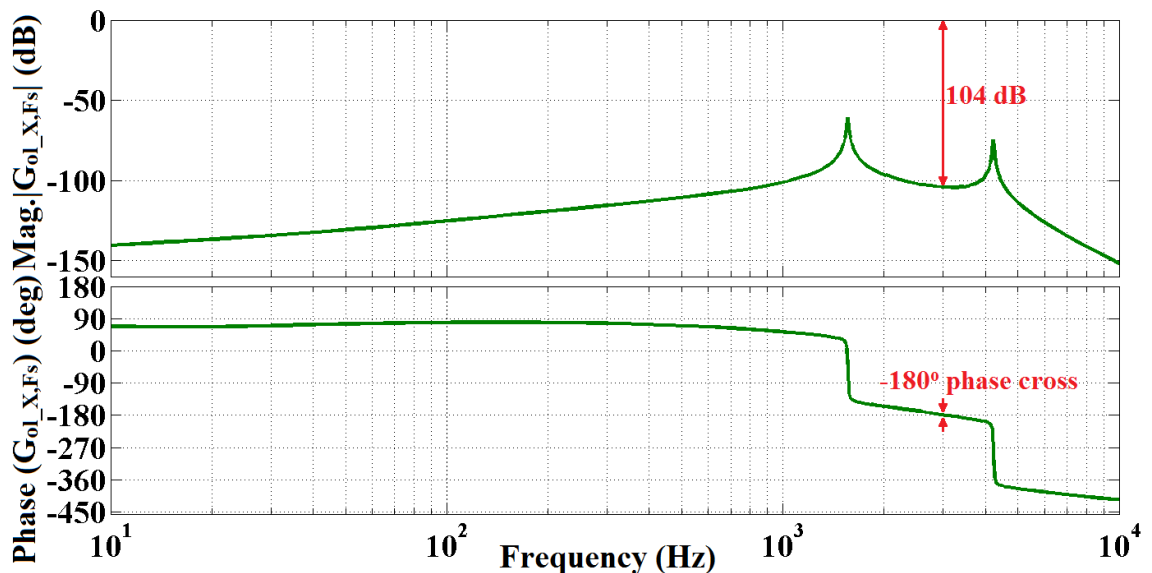


Figure 4-10: Bode plot of the open-loop control transfer function with second-order low-pass filter. The maximum control gain is 104 dB.

The frequency-dependent function of the control gain  $g$  is recalculated, using the same method to calculate the equations from 4-17 to 4-21, including the LPF2 presented within equation 4-23. The quadratic formula parameters  $a$ ,  $b$  and  $c$  are listed in the MATLAB code appendix A.3. Figure 4-11 shows that, with the LPF2, the control gain that guarantees marginal stability (dashed-red line) is above the frequency-dependent control gain that produces the desired velocity output signal. Thus, a velocity feedback control loop can now be implemented by choosing a fixed gain from the blue line, which ensures stability and eliminates the imaginary part of closed loop transfer function  $G_{Y\_CL}$ .

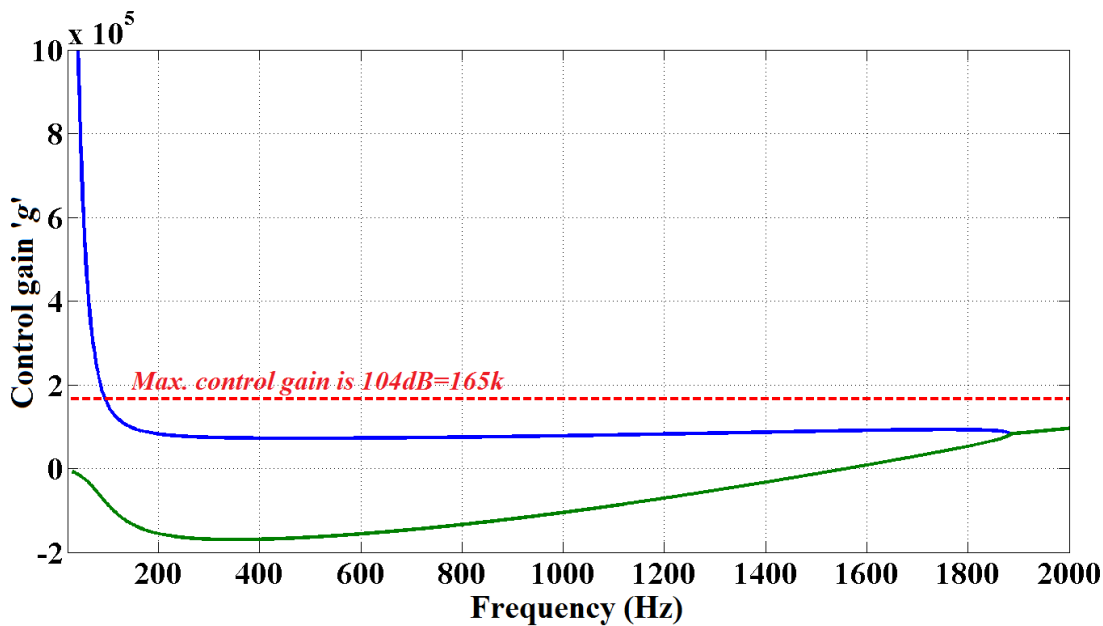


Figure 4-11: Control gain frequency-dependent function with a second-order low-pass filter. The control gain values from the blue line are only valid for stable and causal closed-loop systems, which is also well below the maximum control gain at 165k.

Figure 4-12 shows the bode plot of the open (red line) and closed (blue line) loop output signal  $Y(S)$  per unit of the velocity of the sensor's frame ( $sW_I$ ) simulated using equation 4-16 (refer to appendix A.5 for Matlab code). Considering first the FRF for the open-loop sensor (in red), at frequencies below the first resonance, the magnitude rises proportionally to the frequency, and the phase is fixed at  $90^\circ$ . This is a typical accelerometer behaviour that relates the output displacement  $Y$  of the principal sensor to the input velocity  $sW_I$ . However, when the loop is closed (in blue), the FRF is characterised by the three properties introduced in section 4.2:

- 1- In the frequency range between 100 Hz and 1k Hz, the amplitude of the output signal is proportional to the sensor's frame velocity with  $0^\circ$  phase.
- 2- The first resonance peak is flattened.
- 3- At frequencies higher than the first resonance frequency, the frequency response monotonically decreases and is characterised by a  $-90^\circ$  phase lag.

The control loop function is constructed with an integrator with a cut-off frequency at 10 Hz and LPF2 with a cut-off frequency at 2 kHz. From Figure 4-11, a fixed control gain  $g$  of 73k at 500 Hz is chosen to represent an average value that covers frequency band up to the first resonance.

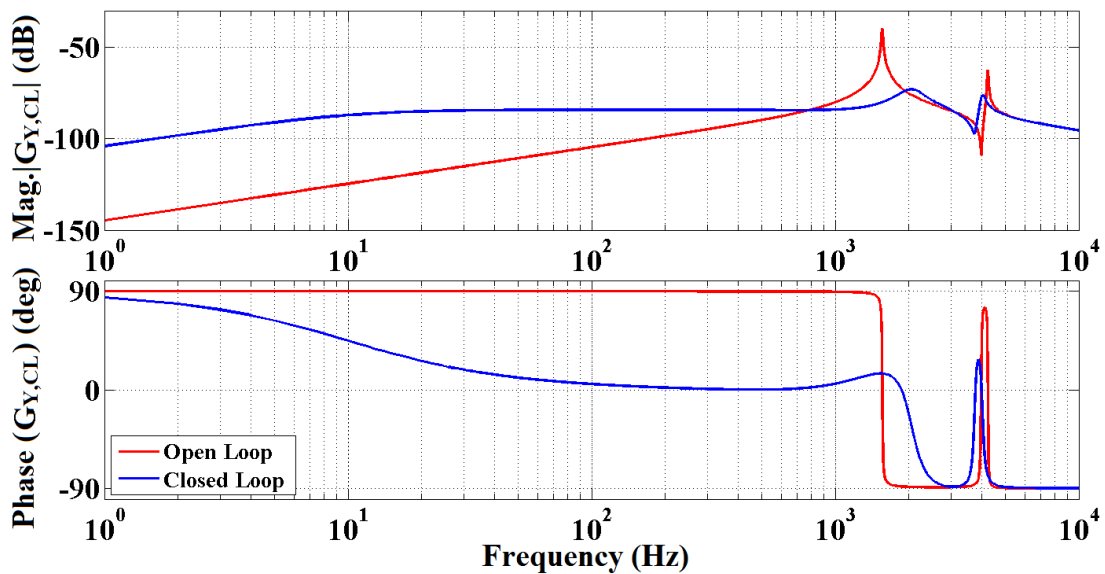


Figure 4-12: Open (red line) and closed (blue line) loop velocity sensor frequency response, using the control gain  $g=73k$ , an integrator with cut-off frequency at 10 Hz and a second-order low-pass filter with a cut-off frequency at 2 kHz.

It can be seen that at low frequency range between 0 – 100 Hz, the closed-loop amplitude increases with frequency and the phase starts from  $90^\circ$  and decreases to  $0^\circ$ . This is due to the real integrator cut-off frequency as shown in Figure 4-6. The integrator effect starts after 100 Hz, which determines the lower frequency limit of the velocity measurement. In contrast to the velocity measurement using standard accelerometer discussed in section 3.3.1, where the real integrator can cause stability problem below its cut-off frequency, the velocity sensor closed loop response in Figure 4-12, shows that the phase is confined between  $+90^\circ$  and  $-90^\circ$  throughout the frequency range, therefore, the stability of the velocity feedback loop vibration control is assured.

As discussed above, the internal velocity feedback loop implemented within the sensor is also prone to instability limitations. Thus, the stability problem described for the velocity feedback loop in vibration control (discussed in section 3.3.1) using the piezoelectric patch actuator and standard accelerometer arises again within the 2-DoF velocity sensor. However the micro-scale dimension of the 2-DoF velocity sensor greatly simplifies the design and implementation of a stable and effective internal feedback loop. In fact, the first and second resonance frequencies of the mechanical structure that form the sensor occur at rather high frequencies. Thus, in the low frequency range where the sensor is designed to operate, its dynamic response is determined by 2-DoF only. As discussed above, the FRF of the open-loop control function can be tailored to maximise the stability limit and control performance. This can be achieved with a proper choice of the mechanical properties of the secondary mass-spring-damper system (resonance frequency and damping ratio) and/or by implementing an LPF compensator. These adjustments can be implemented robustly since the dynamic response of small scale MEMS systems is less sensitive to temperature variations or other exogenous effects and also it is not affected by changes in the controlled structure (for example tensioning effects) when compared with velocity feedback control using standard accelerometers. Moreover, when the 2-DoF capacitive MEMS velocity sensor is used to implement an external feedback loop with a piezoelectric patch actuator, the internal feedback loop implemented within the sensor operates in parallel with the external one, and thus does not introduce time delays in the signal fed back to the piezoelectric patch as normally happens with standard compensators. As a result, the 2-DoF capacitive MEMS velocity sensor can be used to implement a direct velocity feedback loop with piezoelectric patch actuators characterised by a large stability margin.

### **4.6 Summary**

This chapter discussed the 2-DoF capacitive MEMS velocity sensor theoretical analysis. The 2-DoF capacitive MEMS velocity sensor comprises two mass-spring-damper systems connected in series and by an internal velocity feedback loop. The aim of the feedback loop is to produce a damping force on the principal mass. The 2-DoF velocity sensor has three important properties. First, velocity is directly measured. Second, around its fundamental resonance, the sensor is characterised by a flat amplitude spectrum. Finally, above the fundamental resonance, it is characterised by an amplitude roll-off with

only a  $90^\circ$  phase lag. The sensor therefore produces the desired velocity output up to the cut-off frequency set by its first resonance frequency, after which it generates a filtering effect with only a  $90^\circ$  phase lag. With these functions, the sensor can prevent the instability and control spillover encountered with a velocity feedback loop that employs an accelerometer sensor.

The dynamic response functions of the 2-DoF velocity sensor were theoretically derived for the case of input acceleration and the input electrostatic force applied to the principal sensor. The design of the velocity feedback loop and the control gain function were explained. The stability of the 2-DoF velocity sensor was discussed. One way to stabilize the control loop is to introduce a low-pass filter to increase the gain margin. The frequency response of the open- and closed-loop velocity sensor was presented, and the three aforementioned features were verified.



## **Chapter 5: Implementation and Measurements for the First Prototype Capacitive MEMS Velocity Sensor**

### **5.1 Introduction**

This chapter discusses the hardware implementation and measurements of the first prototype in-plane sensor. First, the mechanical structure of the sensor and microfabrication process are presented. Second, the analogue electronic interface and control printed circuit board (PCB) are illustrated. Third, the chapter elucidates the dynamic response functions, which show the measured frequency response functions for the displacements of the principal and secondary proof masses with respect to (i) the base acceleration and (ii) the electrostatic force applied to the principal proof mass. Finally, the stability of the velocity feedback loop is addressed, and the closed-loop velocity sensor is constructed by using the closed-loop transfer function (equation 4-16) and the measured dynamic response functions.

### **5.2 Mechanical Structure of the Sensing Element**

It is desired to design the secondary sensor with a natural frequency well above (more than double) the natural frequency of the principal sensor, so that the two resonance frequencies of the 2-DoF sensor are well separated and are not strongly coupled. This enables the secondary sensor to measure the principal proof mass acceleration, so that the internal feedback loop of the sensor generates the required control signal. Furthermore, as discussed in section 4.5, the maximum feedback loop gain is proportional to the inverse of the amplitude of the second resonance peak. As the resonance frequency increases the resonance peak decreases and the gain margin increases. However, in inertial MEMS sensors, there is a fundamental trade-off between shifting the resonance frequency to higher range and the sensitivity of measuring the base acceleration, which actually decreases as the resonance frequency rises (as discussed in section 2.2.1).

As discussed in section 4.2, the mechanical in-plane structure of the 2-DoF MEMS sensor needs to be designed in such a way that the first resonance is determined by the natural frequency of the principal sensor, whereas the second resonance is determined by the natural frequency of the secondary sensor. Therefore, the natural frequencies of the

**Chapter 5: Implementation and Measurements for the First Prototype Capacitive MEMS Velocity Sensor**

principal and secondary sensors are designed at 2.11 and 3.11 kHz, respectively. Thus, the first and second resonance frequencies of the 2-DoF sensor are at 1.55 and 4.22 kHz, respectively.

A conceptual design of the sensor is shown in Figure 5-1, which shows the proof mass of the principal system ( $m_p$ ) is anchored at the corners with four straight beams of an equivalent spring constant  $k_p$ , whereas the proof mass of the secondary system ( $m_s$ ) is suspended within the principal proof mass with the four folded beams of an equivalent spring constant  $k_s$ . The principal and secondary proof masses are also equipped with parallel plate capacitors  $C_{sp1,2}$  and  $C_{ss1,2}$ , respectively. These capacitors are used to detect the relative displacement  $y$  and  $z$  between the sensor's frame and proof masses  $m_p$  and  $m_s$ , respectively. The principal sensor is further equipped with an interdigitated lateral comb capacitor that is used to generate the reactive electrostatic control force  $f_s$  between the sensor's frame and the proof mass  $m_p$ .

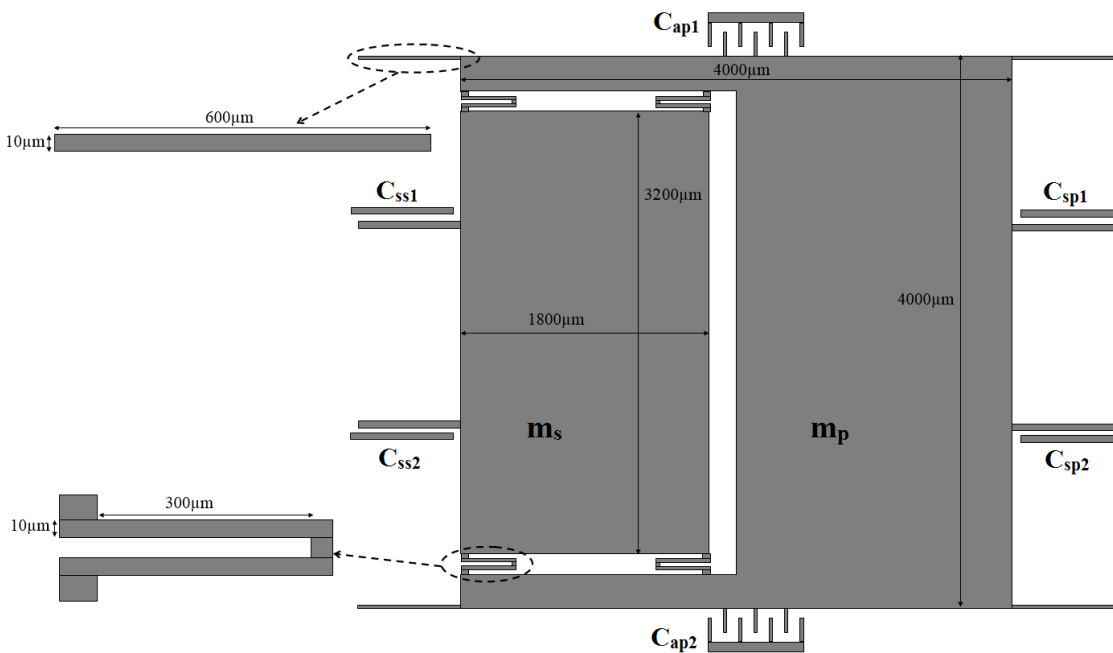


Figure 5-1: A conceptual design of the first prototype sensor shows the principal proof mass  $m_p$  is anchored to the frame with four straight beams, and the secondary proof mass  $m_s$  suspended within the principal proof mass with four folded-beam springs. The device layer thickness is  $50 \times 10^{-6}$  m.

The lumped model parameters of the first prototype 2-DoF capacitive MEMS velocity sensor are summarized in Table 5-1. The proof masses  $m_p$  and  $m_s$  were calculated using

**Chapter 5: Implementation and Measurements for the First Prototype Capacitive MEMS Velocity Sensor**

the dimensions of the mask. Due to the microfabrication imperfections, the straight and folded-beam springs were over-etched from the bottom, thus the beams had a trapezoidal cross section. Figure 5-2 shows the dimensions that were measured under the microscope. The spring constants  $k_p$  and  $k_s$  were calculated using equations 2-39 and 2-41. By using the dimensions of the sense and actuation capacitors in Table 5-2, the damping coefficients  $b_p$  and  $b_{s1}$  were estimated using equation 2-30 for the squeeze-film damping between the sense electrodes, and  $b_{s2}$  was estimated using equation 2-33 for the slide film damping in between the actuator electrodes.

<i>Principal sensor</i>		<i>Control sensor</i>	
$m_p$	$1.103 \times 10^{-6}$ kg	$m_s$	$0.698 \times 10^{-6}$ kg
$b_p$	$0.9 \times 10^{-4}$ N.s/m	$b_{s1}$	$50 \times 10^{-6}$ N.s/m
$k_p$	195 N/m	$b_{s2}$	$0.6 \times 10^{-4}$ N.s/m
		$k_s$	267 N/m
$d_0$		$6 \times 10^{-6}$	m

Table 5-1: First prototype capacitive MEMS velocity sensor parameters.

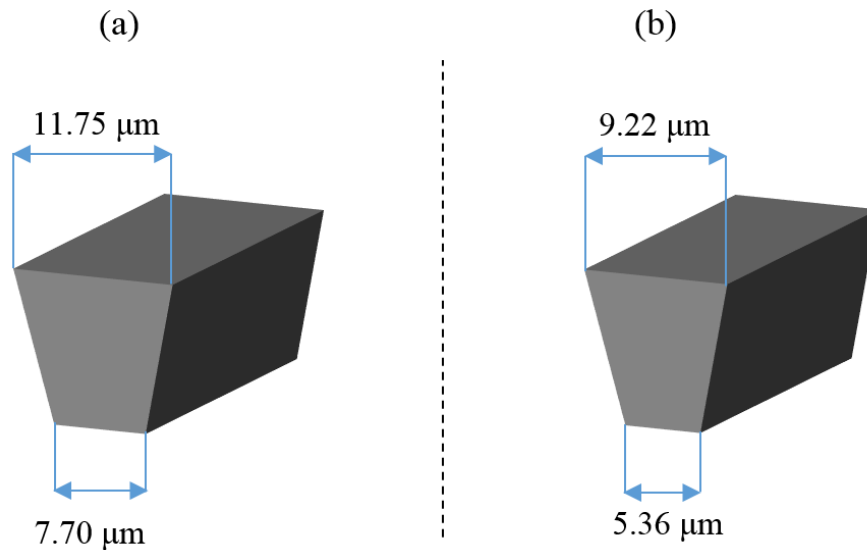


Figure 5-2: Measurement of the average dimensions of the trapezoidal cross section of (a) the principal system straight beams and (b) secondary system folded-beam.

The sense and actuation capacitance of the 2-DoF sensing element are listed in Table 5-2. They were estimated theoretically by using equation 2-23 and the physical dimensions of

## Chapter 5: Implementation and Measurements for the First Prototype Capacitive MEMS Velocity Sensor

the capacitors taken from the mask. The sense capacitors  $C_{sp}$  and  $C_{ss}$  were measured using the Agilent C-V meter 4279A, which included a parasitic capacitance.

	Parameter	Value
<b>Principal sensor</b>	Electrode length of the sense capacitor	$290 \times 10^{-6}$ m
	Electrode width of the sense capacitor	$20 \times 10^{-6}$ m
	Number of sense electrodes top/bottom side	30
	Electrode length of the actuator capacitor	$60 \times 10^{-6}$ m
	Electrode width of the actuator capacitor	$10 \times 10^{-6}$ m
	Number of actuator electrodes top/bottom side	100
	Theoretical estimation of the sense capacitor $C_{sp1,2}$	$640 \times 10^{-15}$ F
	Measured sense capacitance $C_{sp1,2}$ including parasitic capacitance	$36 \times 10^{-12}$ F
<b>Secondary sensor</b>	Electrode length of the sense capacitor	$290 \times 10^{-6}$ m
	Electrode width of the sense capacitor	$20 \times 10^{-6}$ m
	Number of sense electrodes top/bottom side	20
	Theoretical estimation of the sense capacitor $C_{ss1,2}$	$428 \times 10^{-15}$ F
	Measured sense capacitance $C_{ss1,2}$ including parasitic capacitance	$31 \times 10^{-12}$ F
	Device layer thickness (electrode height)	$50 \times 10^{-6}$ m

Table 5-2: Sense capacitors dimensions and capacitance values of the first prototype 2-DoF velocity sensor.

### 5.3 Fabrication of the First Prototype

The first prototype 2-DoF sensing element was fabricated on a 6-inch SOI wafer. The device layer was 50  $\mu\text{m}$  thick, with phosphorous doped n-type silicon of 0.001 to 0.0015  $\Omega\text{cm}$  resistivity. The silicon BOX layer was 2  $\mu\text{m}$  thick and the handle layer was 550  $\mu\text{m}$  thick. The fabrication process required two masks: one for the device layer to define the sensor structure and another for the handle layer to remove the carrier wafer underneath the device area. Using a mask for the handle was to avoid potential stiction of the proof mass to the handle wafer during the release process, as discussed in section 3.4.

The fabrication steps are depicted in Figure 5-3. In step (a), the SOI wafer was prepared by cleaning it with nitric acid to remove any organic residues. In step (b), photolithography was performed to pattern the structural features on the device layer. Step (c) involved DRIE process, which was carried out to etch the 50  $\mu\text{m}$  silicon down to the BOX layer. In step (d), the etched device layer was spin-coated with photoresist, which was used as an adhesive for the carrier wafer. This step is designed to protect the device layer during the subsequent steps and to provide support to the fragile wafer during the second DRIE process. Step (e) entailed the lithographic process of the handle layer,

**Chapter 5: Implementation and Measurements for the First Prototype Capacitive MEMS Velocity Sensor**

which defines the area underneath the proof masses to be removed by the DRIE process in step (f). Afterward, the attached carrier wafer was removed by immersing it in photoresist remover AZ100 at 80° C for 1 hour. Then, the SOI wafer was processed by a plasma asher to ensure that all photoresist residues are removed. At this stage, the sensors were held to the wafer by small bridges, which can be separated from the wafer by breaking them with a pair of tweezers. This method eliminated the use of a dicing saw, which usually leaves some debris. In the final step (step (g)), each device was individually released by using the HF Vapour Phase etching system from Idonus [104]. The SEM images of the sensor is shown in Figure 5-4.

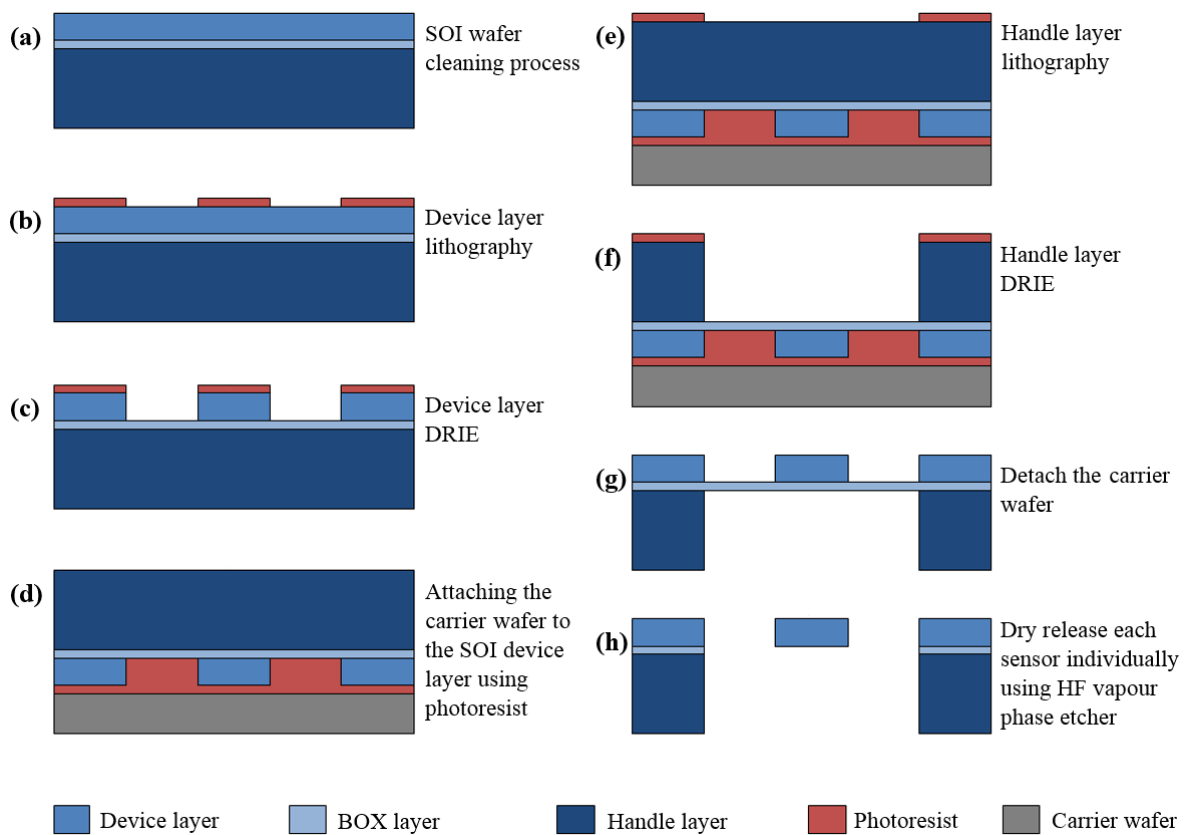


Figure 5-3: SOI wafer fabrication process for the first prototype velocity sensor.

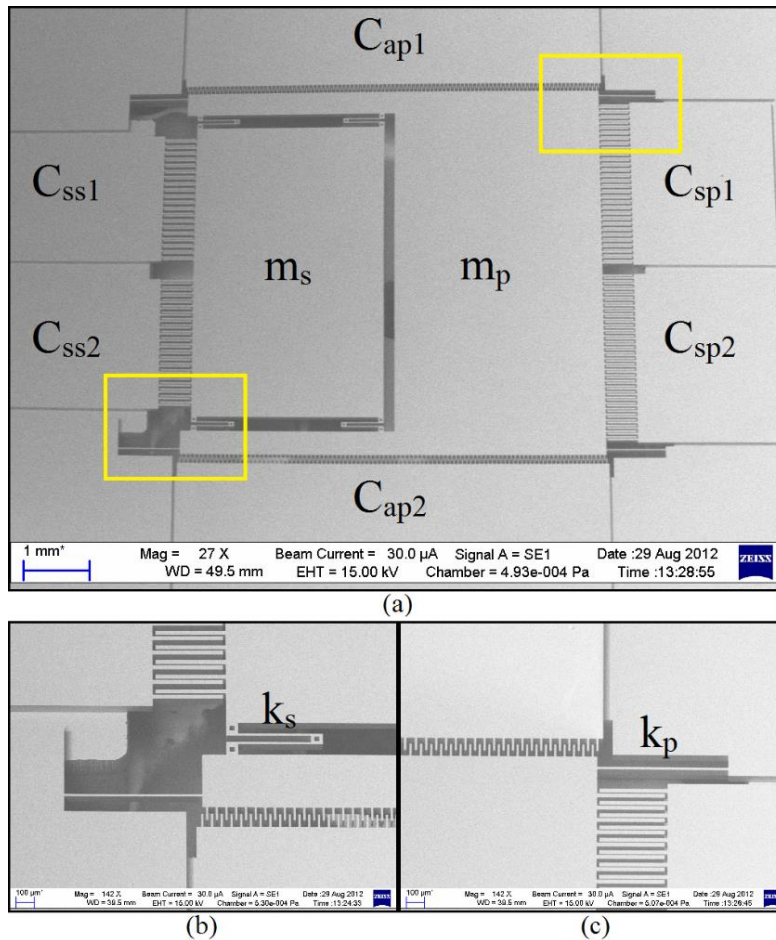


Figure 5-4: (a) SEM photo of the 2-DoF capacitive MEMS sensing block, showing proof masses  $m_p$  and  $m_s$ , sense capacitors  $C_{sp}$  and  $C_{ss}$  and actuation capacitor  $C_{ap}$ ; (b) enlarged SEM photo of the lower left part of the sensing block, showing folded spring  $k_s$ ; and (c) upper right part of the sensing element, showing the parallel plates and lateral comb capacitor  $C_{ss1}$  and  $C_{ap1}$ , respectively.

## 5.4 Interface and Control Electronic Circuit

The block diagram in Figure 5-5 illustrates the interface and control circuit. It is designed to accommodate the first prototype 2-DoF capacitive MEMS sensor with a differential line signal scheme, so that common mode noise is cancelled. The change in capacitance ( $C_{sp}$  and  $C_{ss}$ ) caused by proof mass displacements  $y$  and  $z$  are captured by pickoff circuits and represented with a proportional voltage signal. The relative displacement between the two proof masses  $x$  is then electronically obtained by subtracting the signals of displacements  $z$  and  $y$ , as discussed in equations 4-9. Given that relative displacement  $x$  is proportional to the absolute acceleration of the proof mass of the principal system (with

the opposite sign), the negative velocity feedback loop is constructed with an integration circuit, control gain amplifier  $g$  and feedback voltage circuit. Thus, the output signal of the feedback loop drives the capacitive actuator  $C_{ap}$  to produce a negative velocity feedback on the principal sensor. For the detailed schematic circuit, please refer to appendix B.1.

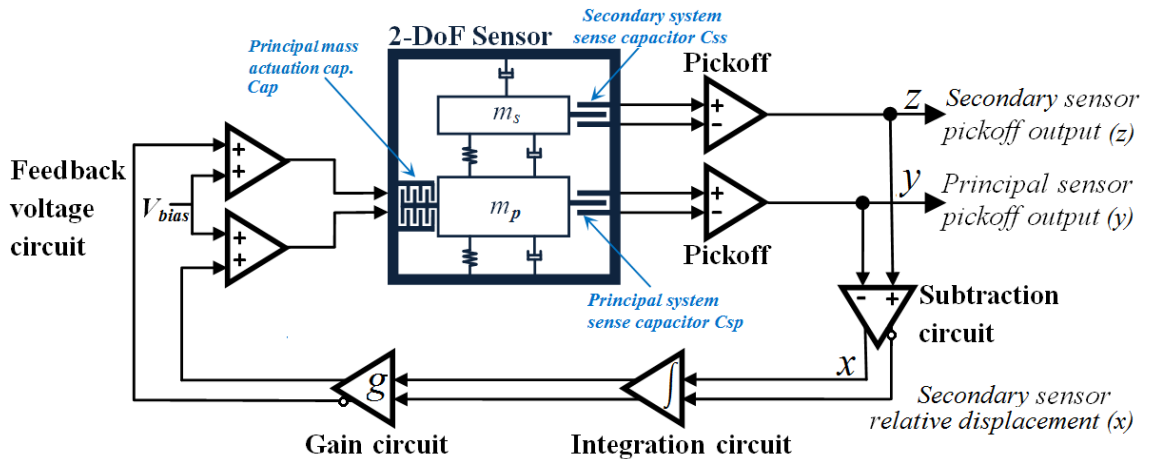


Figure 5-5: Diagram of the velocity sensor interface and control circuit block.

### 5.4.1 Pickoff Circuit

The pickoff circuit plays an important role in the 2-DoF velocity sensor. It captures the change in capacitance in the sense capacitors  $C_{sp}$  and  $C_{ss}$  that is caused by the proof mass displacement and then outputs an electrical signal proportional to the capacitance change. One method to implement the pickoff circuit for both principal and secondary sensors is to employ a capacitance-to-voltage converter (CVC) with continuous-time conversion [105] [106]. This pickoff circuit was chosen because of its simple implementation and because it can be built using discrete components, such as op-amps, resistors and capacitors.

Figure 5-6 shows the electronic schematic of the differential scheme pickoff circuit, where the top and bottom paths are symmetrical in terms of construction and functionality. This symmetry eliminates the common mode noise along the two paths at the output signal. The pickoff circuit is divided into four main sections: (1) a differential sense capacitor configuration, (2) a charge integrator that outputs an amplitude modulation (AM) signal proportional to the proof mass movement, (3) a diode and low-pass filter for AM demodulation and (4) an instrumentation amplifier that combines the

**Chapter 5: Implementation and Measurements for the First Prototype Capacitive MEMS Velocity Sensor**

differential movement of the proof mass and cancels the common mode noise. The differential sense capacitors of the principal and secondary sensors are accompanied in parallel with inevitable parasitic capacitors  $C_{pp}$  and  $C_{sp}$ , which were experimentally measured (Table 5-1). Parasitic capacitance is due to the wire bond, packaging and PCB soldering. The proof mass is connected to a carrier signal of high-frequency  $V_r (\geq 1 \text{ MHz})$ .

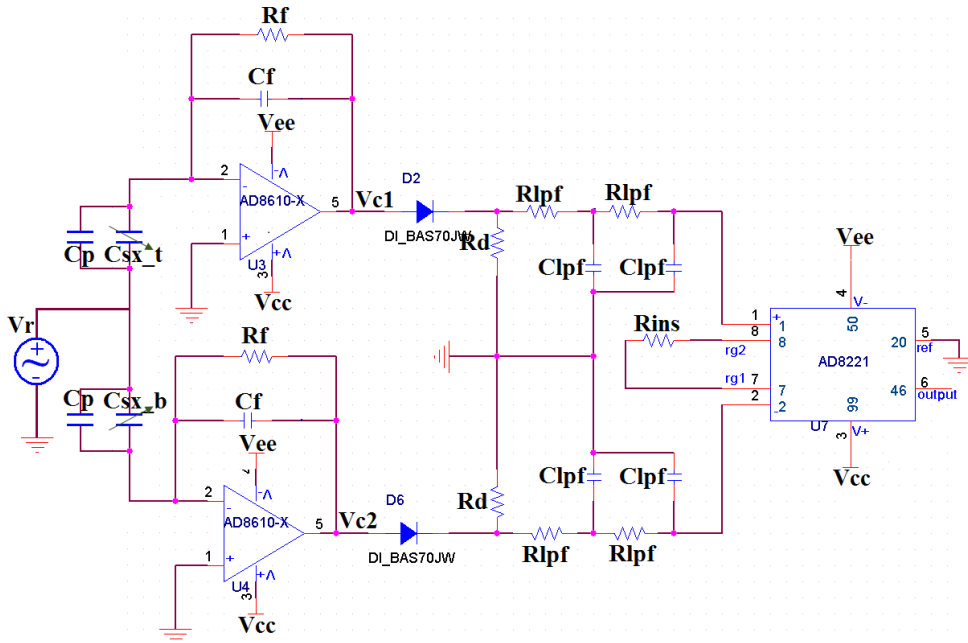


Figure 5-6: Schematic of the pickoff circuit showing the differential sense capacitor with parasitic capacitors, charge integrator, diode AM demodulation, and instrumentation amplifier.

Figure 5-7 shows the PSpice simulation results of the pickoff circuit in Figure 5-6. Because of the proof mass displacement shown in Figure 5-7(a), the charge integrator transforms the change in capacitance into an AM signal of a frequency equal to the carrier signal (Figure 5-7(b)). The demodulation circuit is constructed using a diode and the low-pass filter. It demodulates charge integrator output signal  $V_c$  and outputs a low-frequency signal that is proportional to the change in capacitance. The instrumentation amplifier performs electronic subtraction for the two low-frequency signals and amplifies the difference to output the end-result of the pickoff (Figure 5-7(c)). As can be seen, the output voltage of the pickoff circuit is proportional to the proof mass displacement.

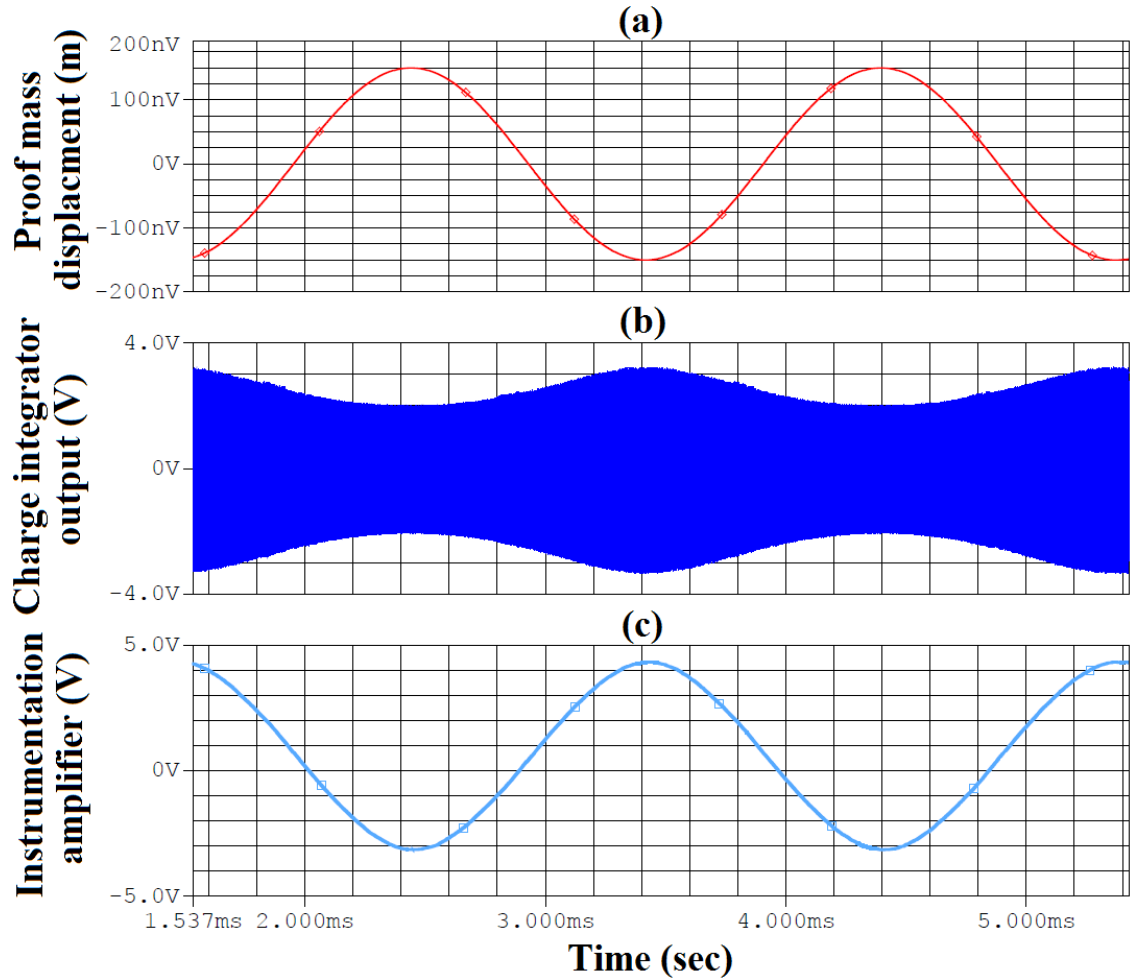


Figure 5-7: Pickoff circuit simulated measurement using PSpice, showing (a) the proof mass displacement, (b) a charge integrator AM signal with 1-MHz frequency and (c) the instrumentation amplifier of the differential output signal.

The frequency response of the charge integrator is given by [106]:

$$\frac{V_c(s)}{V_r(s)} = -\frac{R_f(C_{sx} + C_p)s}{1 + R_f C_f s} \quad 5-1$$

where  $R_f$  and  $C_f$  are the feedback resistor and capacitor of the charge integrator.

Figure 5-8 shows the experimental frequency response measurement of the principal and secondary charge integrators in blue and red lines, respectively. The amplitude of the charge integrators is flat and the phase is  $-180^\circ$  in the frequency range between 1.5 and

1.7 MHz. Within this region, Equation 5-1 can be simplified so that the signal amplification of the charge integrator becomes frequency independent as follows [106]:

$$\frac{V_c(s)}{V_r(s)} = -\frac{C_{sx} + C_p}{C_f} \quad 5-2$$

The gain and phase matching between the two charge integrators reduces the error when the two pickoff signals are subtracted to measure relative displacement  $x$ . However, the matching process is not straightforward because of the discrepancy in the sense capacitor values of the principal and secondary sensors. To solve this problem, the design of each charge integrator is carried out individually, so that both integrators operate at the same carrier signal frequency (1.6 MHz) and have the same amplitude phase ( $-180^\circ$ ).

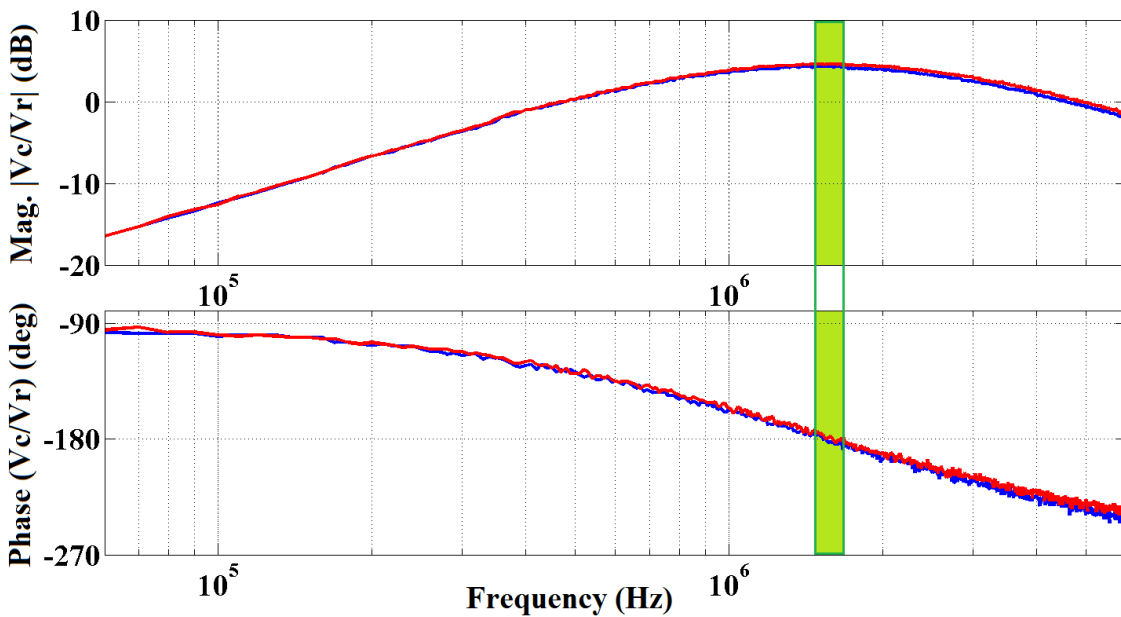


Figure 5-8: Charge integrator measured Bode plot of the principal sensor (blue line) and the secondary sensor (red line), both responses have  $-180^\circ$  phase in the region between overlapping in the 1.5MHz – 1.7MHz.

The velocity feedback loop circuit requires the relative displacement  $x$  of the secondary proof mass with respect to the principal proof mass; thus, the two outputs of pickoff circuits  $V_y$  and  $V_z$  should be electronically subtracted (as discussed in section 4.4). The subtraction is performed using a differential op-amp, as shown in Figure 5-9. The transfer function of the subtraction circuit is given by [107]:

$$V_x = \left(\frac{R_f}{R_{in}}\right) V_z - \left(\frac{R_f}{R_{in}}\right) V_y \quad 5-3$$

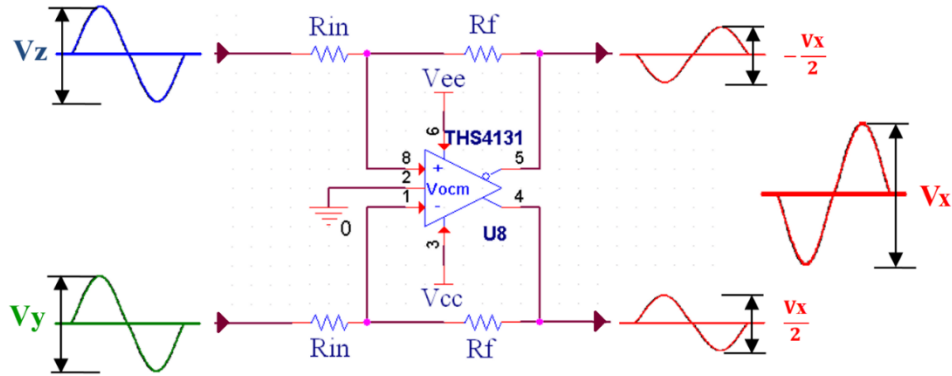


Figure 5-9: Differential line subtraction circuit for measuring the relative displacement  $x$  of the secondary proof mass with respect to the principal proof mass.

Correctly measuring relative displacement  $x$  necessitates that the displacements  $y$  and  $z$  of the principal and secondary sensors be represented with voltage signals  $V_y$  and  $V_z$  with the same pickoff gain. Furthermore, the amplification values of the top and bottom lines of the subtraction circuit should be identical (i.e.  $R_f/R_{in}$ ). Otherwise, the subtraction results will include an error, which degrades the performance of the velocity feedback loop. Figure 5-10 shows the PCB circuit that is designed and implemented using surface mount devices (SMDs). It is designed with the principal and secondary pickoffs on either side of the MEMS sensor, and the subtraction circuit is located between the two pickoffs. The signal path of each circuit is kept to a minimum to decrease the possible external noise that is injected if a longer path is used.

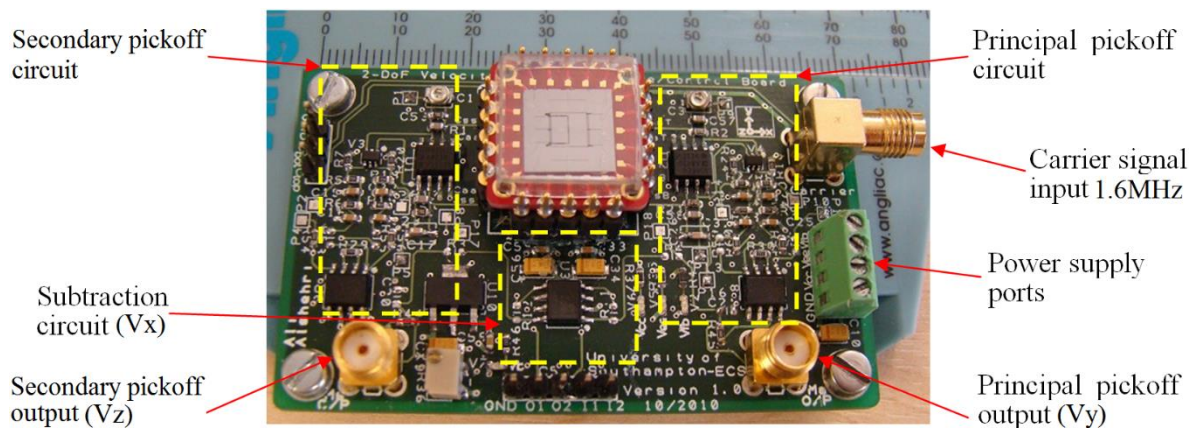


Figure 5-10: Top view of the interface and control circuit of the 2-DoF velocity sensor.

**5.4.2 Control Circuit**

The relative displacement  $x$  of the secondary proof mass, represented with a voltage signal  $V_x$ , is routed to a time integration circuit, so that the output signal  $V_i$  is proportional to the velocity of the principal proof mass. Figure 5-11 shows the integration circuit.

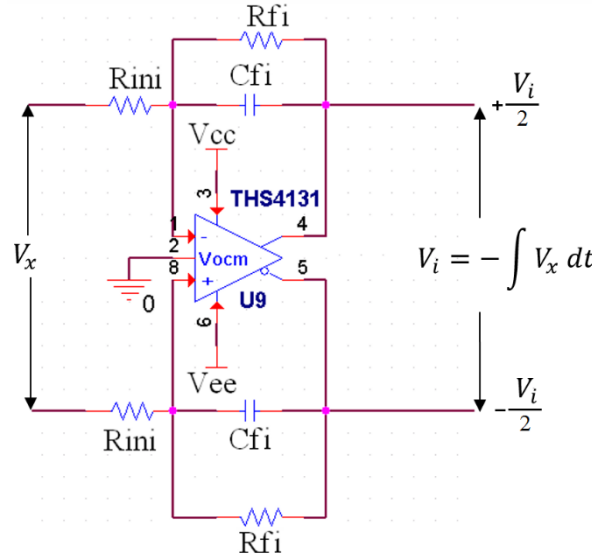


Figure 5-11: Integration circuit.

The output signal  $V_i$  of the integration circuit is given by [108]:

$$V_i = -\frac{R_{fi}/R_{ini}}{1 + R_{fi}C_{fi}s} V_x \tag{5-4}$$

where,  $R_{ini}$  is the input resistor value, and  $R_{fi}$  and  $C_{fi}$  are the feedback resistor and capacitor, respectively.

The integration circuit is designed with three points considered:

- 1- DC gain  $R_{fi}/R_{ini}$ ;
- 2- cut-off frequency  $f_{cutoff} = 1/2\pi R_{fi}C_{fi}$ , which is the point that has a  $-3$  dB frequency from the DC gain and a declining phase towards  $-90^\circ$ ;
- 3- corner frequency  $f_{corner} = 1/2\pi R_{ini}C_{fi}$ , where the magnitude of the frequency response crosses 0 dB.

If any of the two pickoff circuits has an offset, which is due to the mismatch between the differential sense capacitor and the charge integrator, a DC offset will be included in the output signal of the subtraction circuit. Therefore, if a DC offset accompanied the relative displacement signal  $x$ , the integration circuit will integrate this signal and may cause the subsequent differential amplifier to saturate. One way to solve this issue is to implement a high pass filter before the integrator to reject the DC signal.

The final component of the circuit is the voltage feedback circuit (Figure 5-12), which comprises two blocks: First, a differential amplifier is placed just after the integrator; thus, it can be used to add more gain if necessary. The second block consists of the top and bottom adder amplifiers [108]. At any time, the output signals of these two blocks are out-of-phase, with a positive DC offset. Given that the principal sensor is equipped with lateral comb actuators, the voltage required to generate sufficient electrostatic force is considerably high. The top and bottom actuators are therefore connected to an amplifier that can output a signal with a maximum amplitude of 40 V.

$$V_{top\_ele} = \frac{Rf_f}{Rf_1} V_b - \frac{Rf_f}{Rf_2} \left( \frac{Rf_b}{Rf_a} \right) \frac{V_i}{2}$$

$$V_{bot\_ele} = \frac{Rf_f}{Rf_1} V_b + \frac{Rf_f}{Rf_2} \left( \frac{Rf_b}{Rf_a} \right) \frac{V_i}{2}$$

5-5

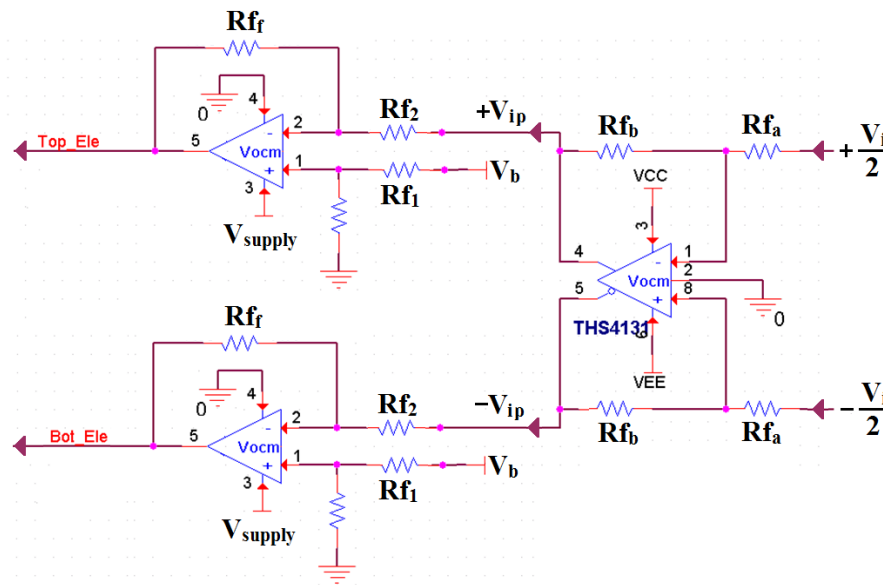


Figure 5-12: Electrostatic feedback force circuit.

### 5.5 Experimental Measurement of Dynamic Response Functions

The FRFs that characterise the dynamic response of the first prototype 2-DoF MEMS velocity sensor were numerically derived using the model presented in section 4.4 and experimentally measured. The FRFs were measured with the setup shown in Figure 5-13.

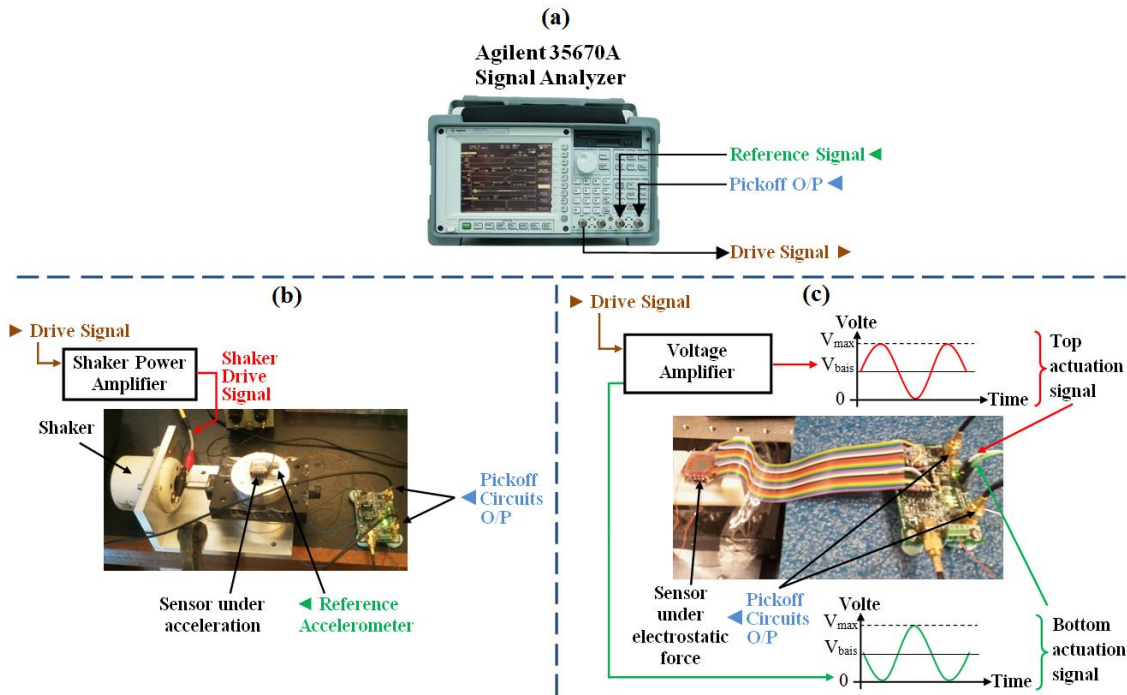


Figure 5-13: Experimental setup used to measure the FRFs of the 2-DoF velocity sensor using (a) the Agilent signal analyser (35670A); the FRFs of the principal and secondary sensors were measured for output signals  $y$  and  $z$  with respect to (b) the electrostatic force applied to the principal sensor and (c) the external input acceleration.

The two FRFs that provide relative displacements  $y$  and  $z$  per unit base acceleration, i.e.  $G_{Y,Acc}$  and  $G_{Z,Acc}$ , were measured with a shaker table (Figure 5-13(b)) that is equipped with a reference accelerometer sensor oriented in the axial direction of motion. The shaker was operated with a white noise drive signal generated by Agilent 35670A signal analyser (Figure 5-13(a)). The MEMS sensor was connected to the pickoff circuits with fine wires to avoid unwanted vibration disturbances during the tests. The outputs of the two pickoff circuits were connected to channel 2 of the signal analyser, whereas the output from the reference accelerometer was connected to channel 1 of the analyser. The two FRFs that provide the relative displacements  $y$  and  $z$  per unit electrostatic force  $F_s$  that is generated by the capacitive actuator of the principal sensor, i.e.  $G_{Y,F_s}$  and  $G_{Z,F_s}$ , were measured with

**Chapter 5: Implementation and Measurements for the First Prototype Capacitive MEMS Velocity Sensor**

a blocked shaker table ( $Acc=0$ ) (Figure 5-13(c)). In this case, the driving white noise signal from the analyser was fed to a voltage amplifier system, which can output a 150 V amplitude signal. The amplified signal was then applied to the capacitive actuator. As with the previous set of measurements, the outputs of the two pickoff circuits were connected to channel 2 of the signal analyser, whereas the output from the actuator driving circuit was connected to channel 1 of the analyser.

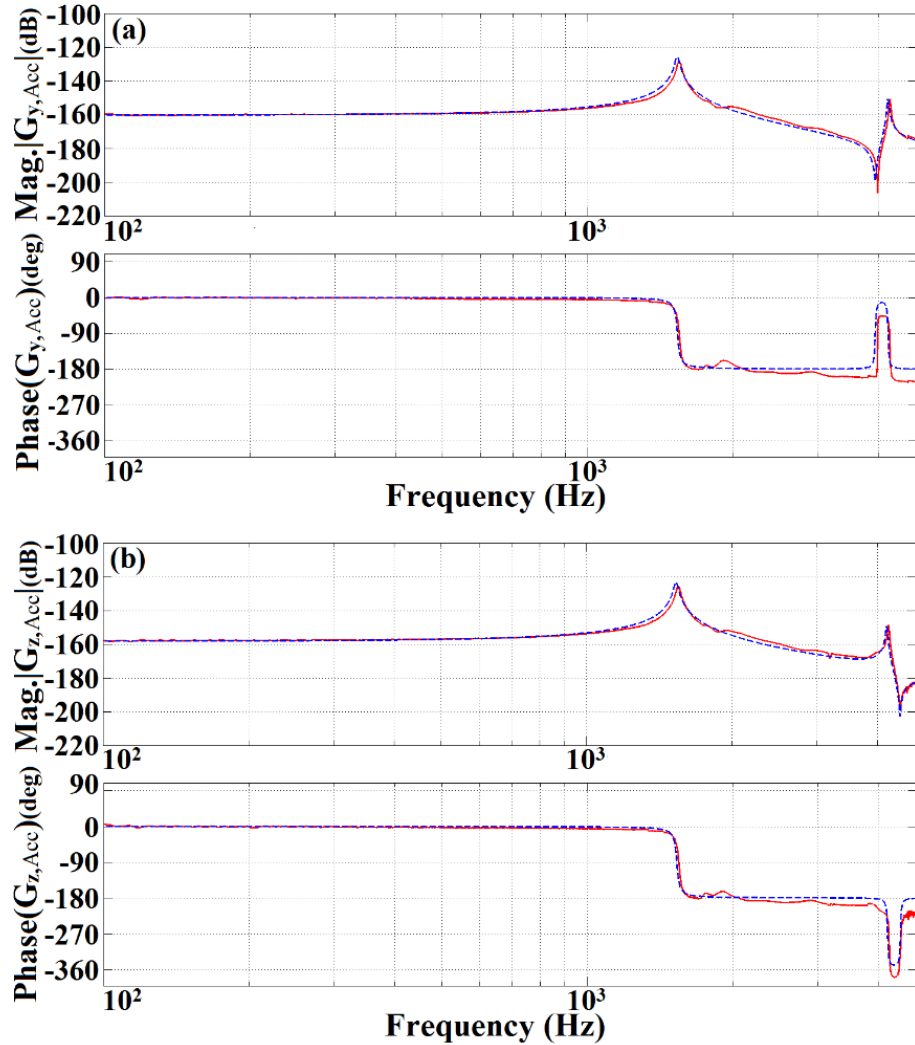


Figure 5-14: Simulated (dashed blue line) and measured (solid red line) (a)  $G_{Y,Acc}$  and (b)  $G_{Z,Acc}$ .

Figure 5-14 shows the simulated (dashed blue line) and measured (solid red line) FRFs in (a)  $G_{Y,Acc}$  and (b)  $G_{Z,Acc}$ . The simulated FRFs were obtained by using the acceleration input response transfer functions in equation 4-5 with the lumped model parameter of the 2-DoF sensor in Table 5-1 (refer to appendix A.1 for Matlab codeA.2).

**Chapter 5: Implementation and Measurements for the First Prototype Capacitive MEMS Velocity Sensor**

Figure 5-15 illustrates the simulated (dashed blue line) and measured (solid red line) FRFs in (a)  $G_{Y,Fs}$  and (b)  $G_{Z,Fs}$ . The simulated FRFs were derived by using the electrostatic force response transfer functions in equation 4-7, all with the lumped model parameter of the 2-DoF sensor in Table 5-1 (refer to appendix A.1 for Matlab codeA.2).

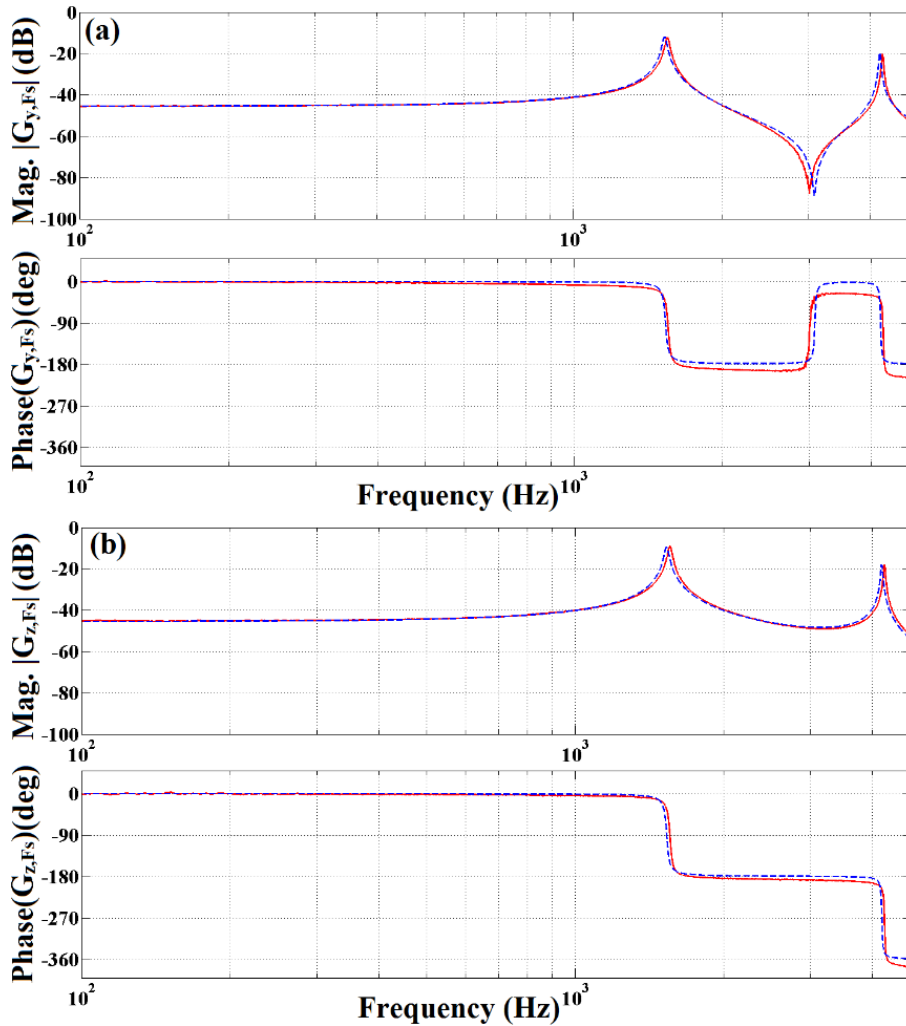


Figure 5-15: Simulated (dashed blue line) and measured (solid red line) (a)  $G_{Y,Fs}$  and (b)  $G_{Z,Fs}$ .

From Figure 5-14 and Figure 5-15, the comparison of the co-respective dashed blue line plots of the simulated FRFs and the solid red line plots of the measured FRFs indicates that the dynamic response of the MEMS sensor closely reproduces the desired 2-DoF response. All the four FRFs are characterised by two resonances at about 1.52 and 4.22 kHz. The  $G_{Y,Acc}$  and  $G_{Y,Fs}$  FRFs are also characterised by an anti-resonance between the two resonances. This anti-resonance is a typical feature of FRFs given by ratios of physically collocated functions, as discussed in section 4.3. By contrast, the  $G_{Z,Acc}$  and

$G_{Z,Fs}$  FRFs do not show this anti-resonance effect. Such absence is also a typical feature of FRFs given by ratios of physically non-located functions.

As discussed in section 4.3, the relative displacement  $x$  between proof masses  $m_p$  and  $m_s$  ( $x$  is necessary to implement the internal feedback loop) is estimated by taking the difference of the two signals for relative displacements  $y$  and  $z$ ; i.e.  $x=z-y$ . In this case, the FRFs that provide relative displacement  $x$  per unit sensor base acceleration ( $Acc$ ) or per unit applied electrostatic force ( $F_s$ ) are reconstructed from the following relations:

$$\begin{aligned} G_{X,Acc} &= G_{Z,Acc} - G_{Y,Acc} \\ G_{X,Fs} &= G_{Z,Fs} - G_{Y,Fs} \end{aligned} \tag{5-6}$$

The two FRFs for  $Acc$  and  $F_s$  are shown in Figure 5-16(a) and 5-15(b), respectively. The results with dashed blue line plots show the  $G_{X,Acc}$  and  $G_{X,Fs}$  FRFs simulated with the lumped parameter model (in Table 5-1). The solid red line plots show the  $G_{X,Acc}$  and  $G_{X,Fs}$  FRFs obtained by subtracting the measured  $G_{Y,Acc}$ ,  $G_{Z,Acc}$ ,  $G_{Y,Fs}$  and  $G_{Z,Fs}$  FRFs, as indicated by Equation 5-6. The simulated data of  $G_{X,Acc}$  agree well with the measured data. Above 500 Hz, the simulated data of  $G_{X,Fs}$  agree with the measured data (solid red lines). The comparison of the simulated and measured data in the low-frequency band below 500 Hz reveals a discrepancy. The measured FRF shows a flat frequency response, whereas the simulated FRF shows a 40 dB/decade increase with frequency. The amplitudes of the  $G_{X,Acc}$  and  $G_{X,Fs}$  FRFs are several orders of magnitude smaller than those of the  $G_{Y,Acc}$ ,  $G_{Z,Acc}$ ,  $G_{Y,Fs}$  and  $G_{Z,Fs}$  FRFs. Thus, the measured data can be easily saturated by noise because of the very low signal levels at low frequencies. This process is therefore prone to influence from exogenous inputs, such as background vibrations of the experimental setup used to measure the FRFs and electrical noise in the pickoff and power circuits. The quality of this signal can be improved by increasing the sensitivity of the capacitive transducer and the electrostatic force output of the actuator.

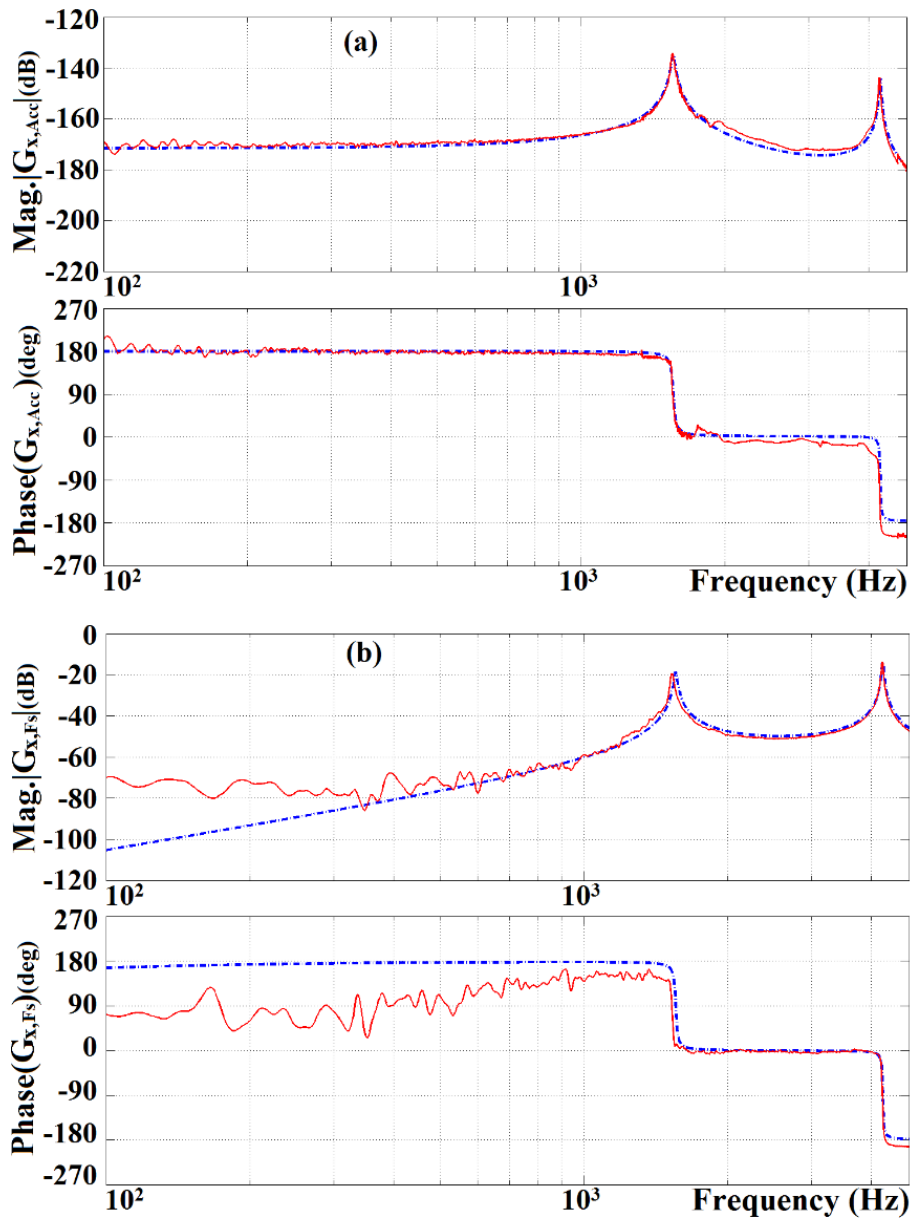


Figure 5-16: Simulated (dashed blue line) and measured (solid red line) FRFs of relative displacement  $x$ , (a)  $G_{X,Acc}$  and (b)  $G_{X,Fs}$ .

## 5.6 Stability and Design of the Velocity Feedback Loop

The implementation of a stable internal feedback loop is discussed in this section. As explained in chapter 4, the open-loop control transfer function is studied to identify the maximum control gain that guarantees system stability. This can be accomplished by recalling equation 4.22:

$$G_{ol_{X,Fs}}(s) = -g \frac{K_{int}}{1 + \tau s} G_{X,Fs}(s)$$

where  $K_{int}$  is the integrator function DC gain, and  $\tau$  denotes the time constant of the integrator function, which is equal to the inverse of the cut-off frequency.

If  $K_{int}$  is set to unity and the cut-off frequency is 10 Hz, the open-loop control transfer function can be investigated using the measured  $G_{X,Fs}$  data, as shown in Figure 5-17 (refer to appendix A.4 for Matlab codeA.2).. The FRF is characterised by two sharp peaks: the first is controlled by the principal system resonance, whereas the second is determined by the secondary system resonance. The phase crosses  $-180^\circ$  at the second resonance frequency, and accordingly, the maximum stable feedback control gain is about 66 dB.

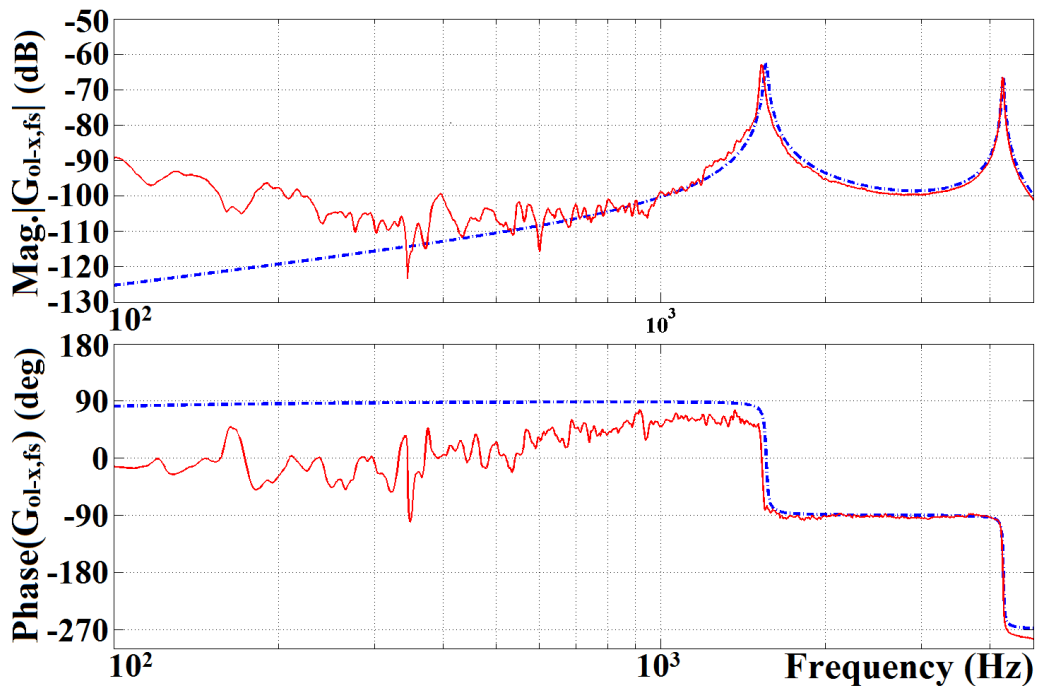


Figure 5-17: Bode plot of the measured (solid red lines) and simulated (dashed blue lines) FRFs of control open-loop function  $G_{ol_{x,fs}}(\omega)$ . The plot shows the  $-180^\circ$  phase crossover frequency at the second resonance frequency. Accordingly, the maximum stable feedback gain is about 66 dB.

As discussed in section 4.5, to generate the control gain  $g$  required for an output signal  $y$  of the closed-loop sensor to be proportional to the velocity of the sensor's frame necessitates the selection of gain  $g$  under the following conditions: (i) The imaginary part

in the frequency band of interest of closed-loop transfer function  $G_{Y\_CL}$  (equation 4-16) should be eliminated, and (ii) the control loop should remain stable.

With equation 4-21, the simulated frequency-dependent control gain with positive sign is only studied, that is, solid blue line in Figure 5-18 (refer to appendix A.2 for Matlab code A.2), which ensures causal closed loop system and eliminates the imaginary part of  $G_{Y\_CL}$ . Thus, even when a maximum control gain (indicated by the dashed red line) is implemented such that the feedback loop is marginally stable, the control effect can be considered negligible, because the feedback loop is below the value necessary to obtain the active damping feedback effect that produces the desired output velocity signal.

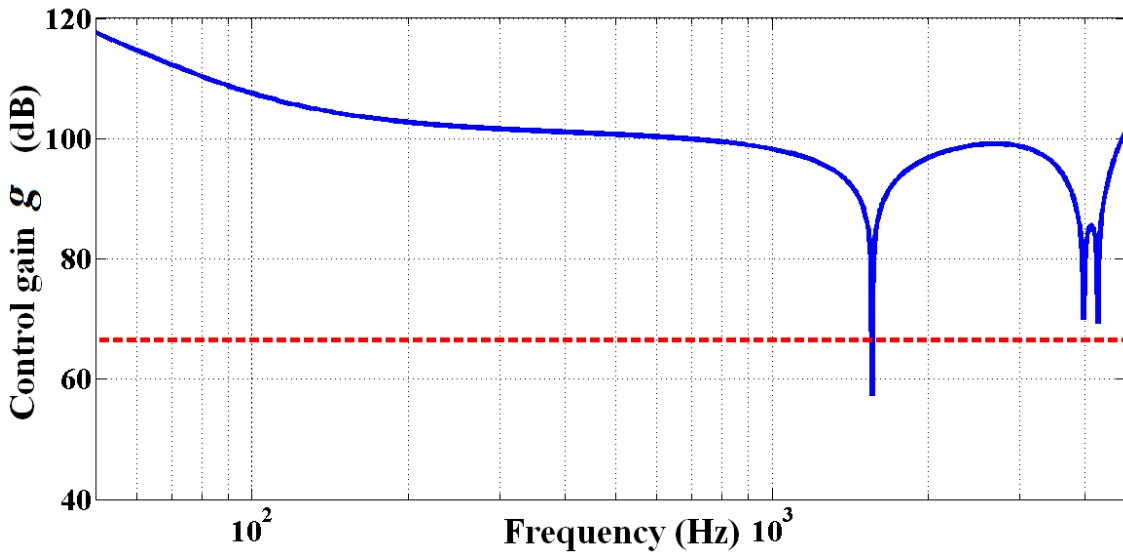


Figure 5-18: The blue line represents the simulated frequency-dependent control gain that eliminates the imaginary part of the closed-loop transfer function. The dashed red line is the maximum gain for the stable feedback loop.

As elaborated in section 4.5, one possible solution to the stability problem is to introduce a compensator, so that the amplitude of the second resonance peak is suppressed. This can be achieved by incorporating a second-order low-pass filter. By recalling the feedback loop function with LPF2 in equation 4-23, we have:

$$H(s) = \frac{Fs(s)}{X(s)} = -g * \frac{K_{int}}{1 + \tau s} * \frac{w_c^2}{s^2 + \frac{w_c}{Q} s + w_c^2} \quad 5-8$$

where  $w_c$  is the cut-off frequency of the second-order low-pass filter (this frequency is set between the two resonance frequencies at 3.1 kHz), and  $Q$  represents the quality factor, which is set to 0.5, i.e. the unity gain in the band of interest.

The open-loop control transfer function in equation 5-7 is used in combination with equation 5-8 to analyse stability. As shown by the Bode plot in Figure 5-19, the introduction of the low-pass filter exerts two main effects: (a) In the Bode plot, the peak of the second resonance frequency shifts to below  $-75$  dB, and (b) the  $-180^\circ$  crossover falls between the two resonance frequencies. Thus, the control loop has a more relaxed gain margin.

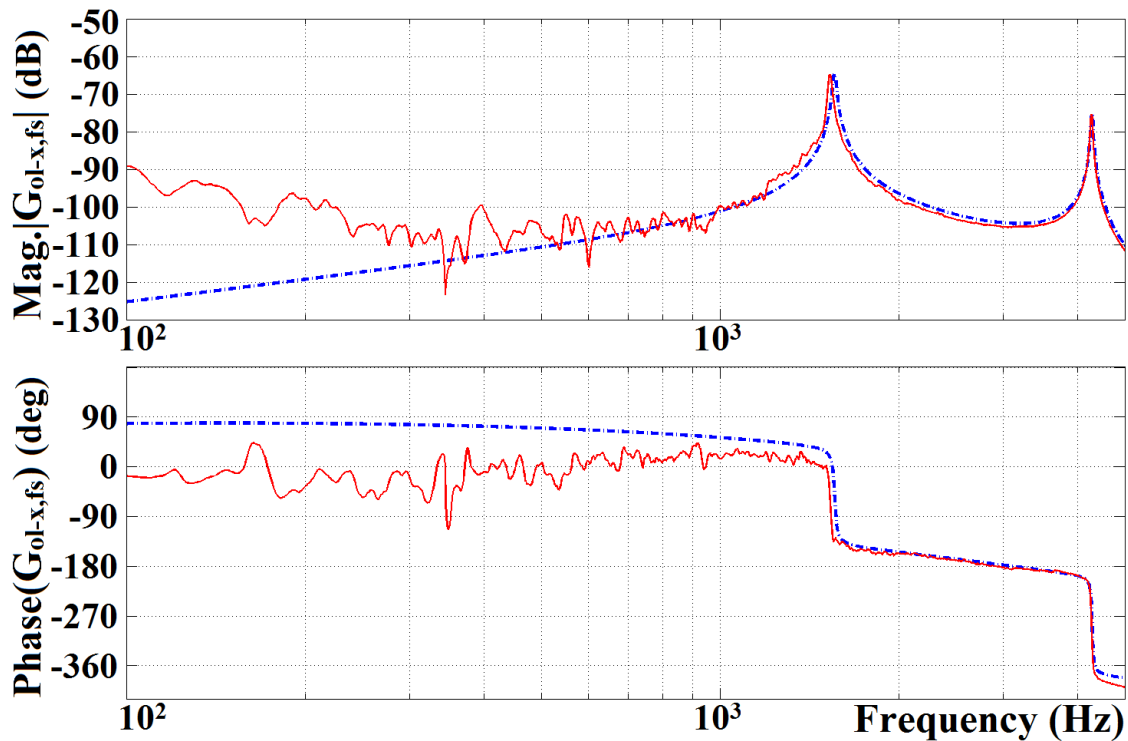


Figure 5-19: Bode plot of the measured (solid red lines) and simulated (dashed blue lines) FRFs of the control open-loop function  $G_{ol-x,fs}(\omega)$  with a second-order low-pass filter. The maximum stable feedback gain is about 104 dB.

The frequency-dependent function of the control gain  $g$  with the second-order low-pass filter presented in appendix A.3 is used. Figure 5-20 shows that with this compensator, the control gain that guarantees marginal stability (dashed red line) is above the frequency-dependent control gain that produces the desired velocity output signal. Thus, a velocity feedback control loop can now be implemented by choosing a fixed gain close

to the average value of the ideal frequency-dependent gain that produces the desired output velocity signal.

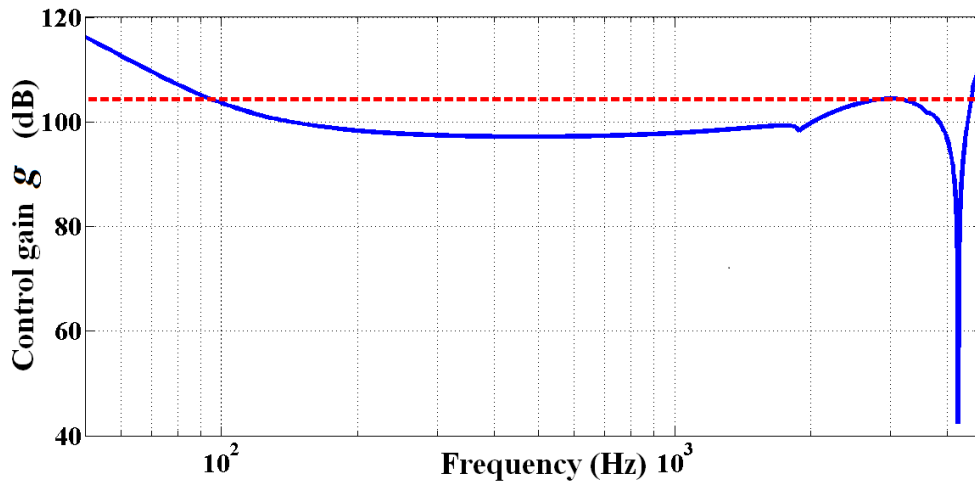


Figure 5-20: The solid blue line is the simulated frequency-dependent control gain that eliminates the imaginary part of the closed-loop transfer function with a compensator. The dashed red line represents the maximum stable gain of the feedback loop with a compensator.

## 5.7 Closed-Loop Response

The open and closed-loop responses of the sensor are derived off-line by using the closed-loop response function  $G_{Y_{CL}}$  in equations 4-16 and 5-8 and by using the measured and simulated  $G_{Y_{Acc}}$ ,  $G_{X_{Acc}}$ ,  $G_{Y_{Fs}}$  and  $G_{X_{Fs}}$  FRFs, discussed in section 4.5 (refer to appendix A.5 for Matlab).

With regard to the simulations based on the theoretical FRFs, Figure 5-21(a) shows that when the internal feedback loop is left open (dashed blue line), the output  $y$  per unit sensor's frame velocity grows proportionally with frequency at frequencies below the first resonance frequency of the 2-DoF MEMS sensor. As expected, therefore, the output signal is proportional to the base acceleration. However, when the feedback loop is closed, with the fixed control gain chosen from Figure 5-20 being  $g=97$  dB, the sensor output per unit sensor frame velocity remains constant (solid red line) at frequencies below the first resonance frequency of the 2-DoF MEMS sensor. That is, the output signal is proportional to the base velocity. Moreover, the sharp peak of the first resonance

flattens. At frequencies above the first resonance, the sensor output per unit sensor's frame velocity tends to roll-off with a phase lag of  $-90^\circ$ .

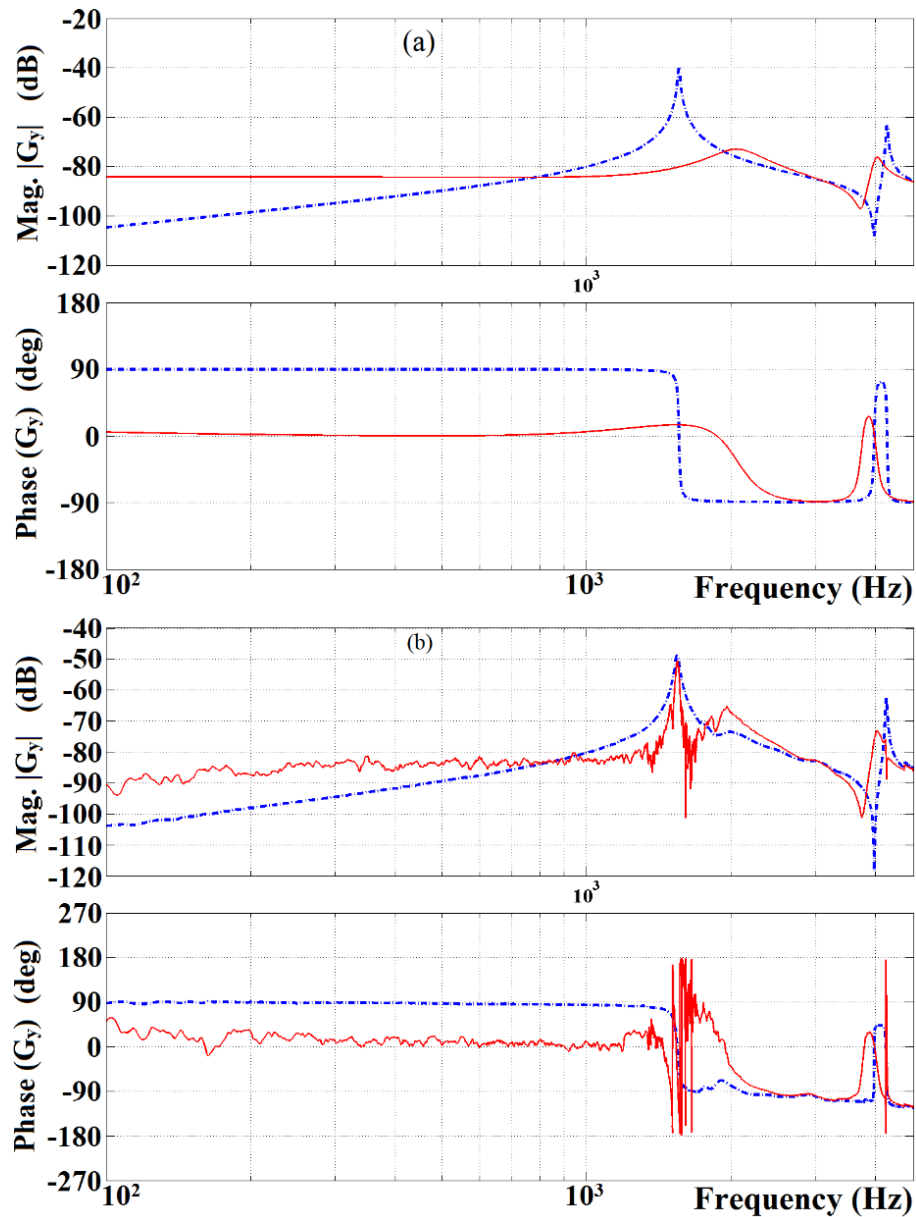


Figure 5-21: Simulated (a) and measured (b) frequency responses of the output signal  $y$  from the sensor per unit sensor's frame velocity with internal open (dashed blue lines) and closed (solid red lines) feedback loops.

With regard to the measured FRFs, Figure 5-21(b) shows that the open-loop response (dashed blue line) based on the measured data is very similar to that predicted from the theoretical data. However, the closed-loop response derived from the measured data appears to be highly affected by noise. Nevertheless, it shows the principal characteristic

found using the theoretical data. As indicated in section 5.5, the FRF of  $G_{X,Fs}$  is saturated by noise within frequencies below 500 Hz. This problem also affects the closed-loop response. The presence of the first resonance peak is due to the fact that the off-line closed-loop simulation is very sensitive to the physical variations in the sensors when the four dynamic measurements ( $G_{Y,Acc}$ ,  $G_{Z,Acc}$ ,  $G_{Y,Fs}$  and  $G_{Z,Fs}$ ) are considered in the simulation. This behaviour could be solved when the full system is operated online, thus, the four dynamic response function will include any physical variation.

## **5.8 Design Issues of the First Prototype Sensor**

The first prototype of the 2-DoF capacitive MEMS velocity sensor presented in this chapter with the lumped parameters listed in Table 5-1 suffers from several problems that degrade the prototype's performance as a velocity sensor.

**First**, the second resonance of the 2-DoF sensor is characterised by the natural frequency of the secondary sensor. The analysis demonstrates that the second resonance has a high peak, hence, very low gain margin of the control loop is obtained. To resolve this problem, a second-order low pass filter was incorporated into the sensor to increase the gain margin. The peak amplitude of the second resonance can be suppressed by introducing more viscous air damping to the secondary sensor or by shifting the resonance frequency to a higher frequency.

**Second**, the relative displacement of secondary proof mass  $x$  was indirectly obtained by using an electronic subtraction circuit, and because the pickoff circuit output of each sensor always has an offset caused by the mismatch between the capacitive transducer and the charge integrator, the offset from each pickoff is fed to the subtraction circuit. Thus, the electronically obtained secondary proof mass displacement  $x$  contains an offset that may reduce the stability of the control loop. Furthermore, given the mismatch between the sense capacitance of the principal and secondary sensors, the pickoff circuit gains are difficult to match.

**Third**, the capacitive actuator attached to the principal sensor is of differential lateral comb design. Although this type of capacitor presents benefits from linear electrostatic force response when fed with an excitation voltage, it requires a high voltage to produce sufficient force to move the proof mass. This issue is the main cause of the noisy response

of the control open-loop transfer function. A similar linear electrostatic force with better performance can be achieved with a parallel plate capacitor and low excitation voltage.

**Fourth**, the 2-DoF sensor is very sensitive to out-of-plane movements, which present obstacles in measuring acceleration with a shaker table. The sensor requires direct placement onto the shaker and connection to the board with fine wires.

**Finally**, the principal and secondary sensors are equipped with sense capacitors with a nominal capacitance of  $640 \times 10^{-15}$  F and  $428 \times 10^{-15}$  F, and the associated parasitic capacitance is around  $30 \times 10^{-12}$  F, which is very large compared with the sense capacitance. Therefore, the noisy open-loop control transfer function is due to the contribution of the relatively small sense capacitor and the low-performing capacitive actuator.

A second prototype of the 2-DoF capacitive MEMS velocity sensor, which is aimed at solving the problems encountered with the first prototype will be presented in the next chapter.

## **5.9 Summary**

This chapter presents the design, microfabrication and experimental work for the first prototype capacitive MEMS velocity sensor. The sensor was fabricated on an SOI wafer with two masks: one for the device layer and another for the handle layer. The process required a carrier wafer to support the fragile SOI wafer during DRIE. The mechanical structures composed of two mass–spring–damper mechanical systems that are connected in series are called the principal and secondary systems. The two systems are equipped with parallel plate sense capacitors, and the principal system is equipped with an interdigitated lateral comb capacitor actuator. The output signal from the secondary system is fed back to this actuator, so that in the frequency range of interest, the output signal from the principal system becomes proportional to the base velocity of the sensor. Moreover, the typical resonance peak that characterises the response of 2-DoF sensors flattens. Finally, at high frequencies above the fundamental resonance frequency of the sensor, the output signal is characterised by a  $-90^\circ$  phase lag rather than the typical  $-180^\circ$  lag that is typical accelerometer sensors. All these properties are of substantial importance

## ***Chapter 5: Implementation and Measurements for the First Prototype Capacitive MEMS Velocity Sensor***

---

in the implementation of stable velocity feedback loops for vibration control with piezoelectric patch actuators.

The sensor interface and the controller are installed on a PCB. The design of the control loop is carried out off-line by using measured frequency response functions for the displacements of the two proof masses with respect to (i) the base acceleration and (ii) the voltage signal that drives the electrostatic actuator. The sensor shows that the measured dynamic responses of the 2-DoF MEMS sensor agree well with those predicted in the simulation. Moreover, with a low-pass filter compensator, the internal feedback loop can implement the stable feedback gains necessary to obtain the desired velocity output signal.

The current design is affected by external noise problems because of the low sensitivity of the capacitive transducers and the electronic circuits used to implement the internal feedback loop.

## Chapter 6: Mechanically Coupled and Electrically Isolated Two-Degree-of-Freedom Capacitive MEMS Velocity Sensor

### 6.1 Introduction

The first prototype 2-DoF velocity sensor exhibits several technical problems that degrade the final output of the sensor. These problems are discussed in section 5.8. In this chapter, a novel design and fabrication process for the second prototype are presented. The design of the sensor is based on an innovative method for directly measuring the relative displacement between the two proof masses. Such measurement is conducted with a capacitive transducer. The method also entails mechanically coupling and electrically isolating the two mass–spring–damper systems, thereby enabling the direct measurement of secondary proof mass deflection by mechanical subtraction. The sensor was fabricated using SOI wafer technology, for which the process requires only three masks. The interface and control electronic circuit were modified to accommodate the new sensor. Therefore, the circuit is briefly discussed. The theoretical and experimental measurements of dynamic response functions, feedback loop stability and closed loop are also presented.

### 6.2 Operation Concept

The block diagram of the 2-DoF velocity sensor is schematically depicted in Figure 6-1. Similar to the sensing element of the first prototype sensor, that of the second prototype consists of two mass–spring–damper systems that are mechanically connected in series. The bottom principal system has a proof mass  $m_p$  anchored onto the sensor frame via a spring  $k_p$ . The top secondary system has a proof mass  $m_s$  anchored onto the mass of the principal system via a spring  $k_s$ . The squeeze film damping effects are modelled using two dashpot elements with damping coefficients  $b_p$  and  $b_s$  for the principal and secondary sensors, respectively. In contrast to the first prototype velocity sensor, the secondary sensor of the second prototype does not interact with the sensor frame. Therefore, the model does not include damping coefficient  $b_{s2}$ , which is incorporated into the model of the first prototype sensor. Furthermore, the relative displacement  $x$  of the secondary proof



on both sides and two double-folded beams ( $K_{7,8}$ ) at the top and bottom of the sensor. The displacement of principal proof mass  $y$  is measured using differential capacitors  $C_{ps\_top}$  and  $C_{ps\_bot}$ . The principal sensor is also equipped with differential parallel plate actuators  $C_{pa\_top}$  and  $C_{pa\_bot}$ , so that the required electrostatic feedback control signal is obtained with less voltage than that derived with the first prototype velocity sensor, which used a lateral comb actuator (see section 5.8).

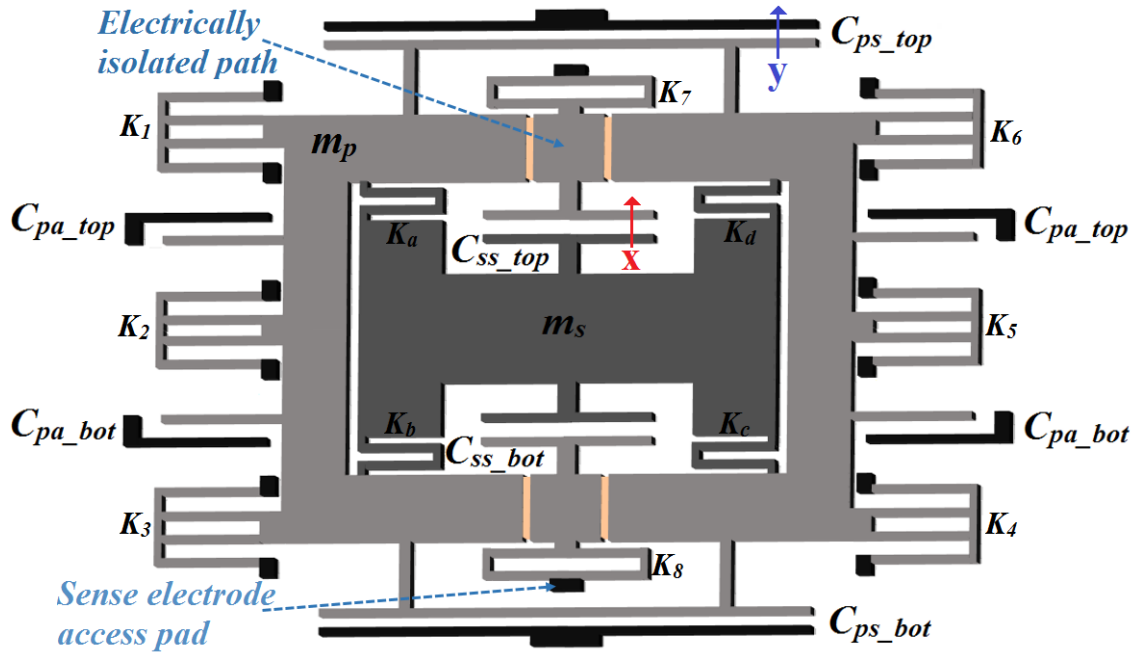


Figure 6-2: Simplified mechanical design of the 2-DoF capacitive MEMS sensor showing the electric isolation trenches, the principal sensor with a proof mass  $m_p$ , top and bottom sense capacitor  $C_{ps\_top,bot}$  for measuring the displacement  $y$  of proof mass  $m_p$ , the secondary sensor with a proof mass  $m_s$  and top and bottom sense capacitor  $C_{ss\_top,bot}$  for measuring displacement  $x$ .

The secondary proof mass  $m_s$  is suspended within the principal proof mass with four folded beams  $K_{a-d}$ . The innovative design of the sensor employs mechanical subtraction between the principal and secondary proof masses. This approach enables the direct capacitive measurement of the relative displacement  $x$  of the secondary sensor. This displacement is measured using sense capacitors  $C_{ss\_top}$  and  $C_{ss\_bot}$ , which are electrically isolated from the principal proof mass and are accessible through the electrode access pads via folded beam springs  $K_{7,8}$ .

**Chapter 6: Mechanically Coupled and Electrically Isolated 2-DoF Capacitive MEMS Velocity Sensor**

Figure 6-3 shows the physical dimensions of the different springs employed in the sensor, and Table 6-1 lists the physical dimensions of the proof masses, sense and actuator capacitors.

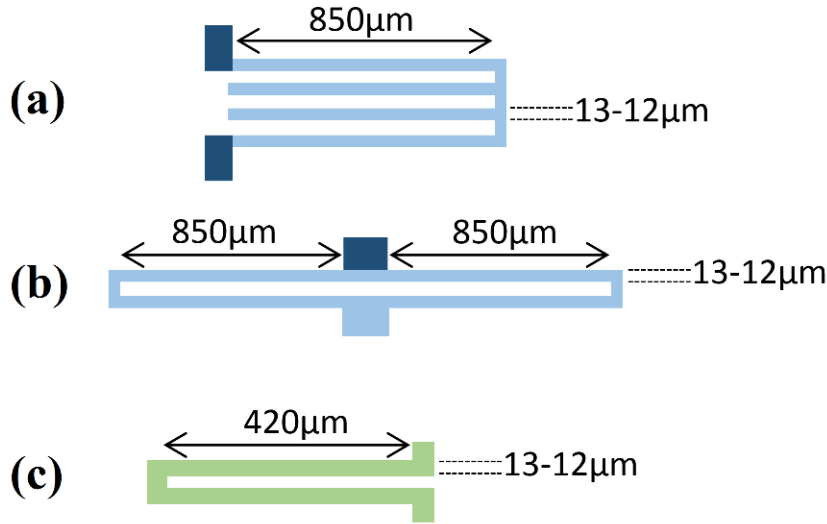


Figure 6-3: Geometries of the (a) folded-flexure beam of the principal sensor, (b) double-folded beam of the principal sensor, and (c) folded beam of the secondary sensor.

	<b>Parameter</b>	<b>Value</b>
<b>Principal sensor</b>	Device layer proof mass area	$4.3596 \times 10^{-6} \text{ m}^2$
	Handle layer support structure area	$1.2972 \times 10^{-6} \text{ m}^2$
	Electrode length of the sense capacitor	$55 \times 10^{-6} \text{ m}$
	Number of sense electrodes top/bottom side	896
	Electrode length of the actuator capacitor	$400 \times 10^{-6} \text{ m}$
	Number of actuator electrodes top/bottom side	48
<b>Secondary sensor</b>	Device layer proof mass area	$0.8781 \times 10^{-6} \text{ m}^2$
	Handle layer support structure area	$0.3662 \times 10^{-6} \text{ m}^2$
	Electrode length of the sense capacitor	$55 \times 10^{-6} \text{ m}$
	Number of sense electrodes top/bottom side	992
	Release hole diameter	$20 \times 10^{-6} \text{ m}$
	Device layer thickness	$100 \times 10^{-6} \text{ m}$
	Handle layer support structure average thickness around	$250 \times 10^{-6} \text{ m}$
	Spring beam average width around	$13 \times 10^{-6} \text{ m}$

Table 6-1: Physical geometries of the principal and secondary proof masses, and sense and actuator capacitor electrode taken from the mask layout.

Table 6-2 shows the lumped model parameters of the second prototype velocity sensor. The proof mass is calculated on the basis of mask geometries. The damping in the 2-DoF sensor is caused primarily by the squeeze-film damping effect between the capacitor

electrodes. This damping is theoretically estimated using equation 2-30 and using the sense and actuator capacitor electrode dimensions in Table 6-1. The spring constant of the double-folded beam is derived according to equation 2-41 and using the dimensions in Figure 6-3. Although, the folded-flexure beam is complex in term of the design, its spring constant equation is similar to the spring constant of the single beam in equation 2-37. However, this complex structure provides the system extra immunity to the out-of-plane movement [30]. The sense and actuator capacitors are calculated using the equation 2-23 and the associated dimensions in Table 6-1.

	<b>Parameter</b>		<b>Value</b>
<b>Principal sensor</b>	Proof mass	$m_p$	$7.71 \times 10^{-6}$ kg
	Damping coefficient	$b_p$	$4 \times 10^{-3}$ N.s/m
	Spring constant	$k_p$	480 N/m
	Natural frequency	$f_{np}$	1250 Hz
	Sense capacitor	$C_{ps}$	$7.27 \times 10^{-12}$ F
	Actuation capacitor	$C_{pa}$	$2.8 \times 10^{-12}$ F
<b>Secondary sensor</b>	Proof mass	$m_s$	$1.85 \times 10^{-6}$ kg
	Damping coefficient	$b_s$	$3.5 \times 10^{-3}$ N.s/m
	Spring constant	$k_s$	800 N/m
	Natural frequency	$f_{ns}$	3310 Hz
	Sense capacitor	$C_{ss}$	$8.05 \times 10^{-12}$ F
Nominal gap between capacitor electrodes		$d_0$	$6 \times 10^{-6}$ m
First 2-DoF resonance frequency		$f_1$	1110 Hz
Second 2-DoF resonance frequency		$f_2$	3730 Hz

Table 6-2: Physical and electronic parameters of the 2-DoF capacitive MEMS velocity sensor.

## 6.4 Finite Element Analysis

The design optimization process was carried out using CoventorWare for the finite element method (FEM) analysis. The FEM analysis of the 2-DOF sensing element is illustrated in Figure 6-4. As would be expected with a 2-DoF inertial system, when the base of the system is excited, the principal and secondary proof masses are deflected in-phase at the first mode (Figure 6-4-a) and out-phase at the second mode (Figure 6-4-b). The handle layer support structure modifies the symmetrical shape of the sensor; therefore, the out-of-plane and buckling modes can disturb the operation of the sensor. To alleviate this problem, the design includes six folded-flexure beam springs that anchor

the principal system to the frame. These springs reduce axial force and result in linear proof mass deflection [47] [109]. As shown in Figure 6-4-c and d, the out-of-plane mode at 6.7 kHz and the buckling mode at 10.7 kHz shift to frequency ranges well above the natural frequency of the second mode.

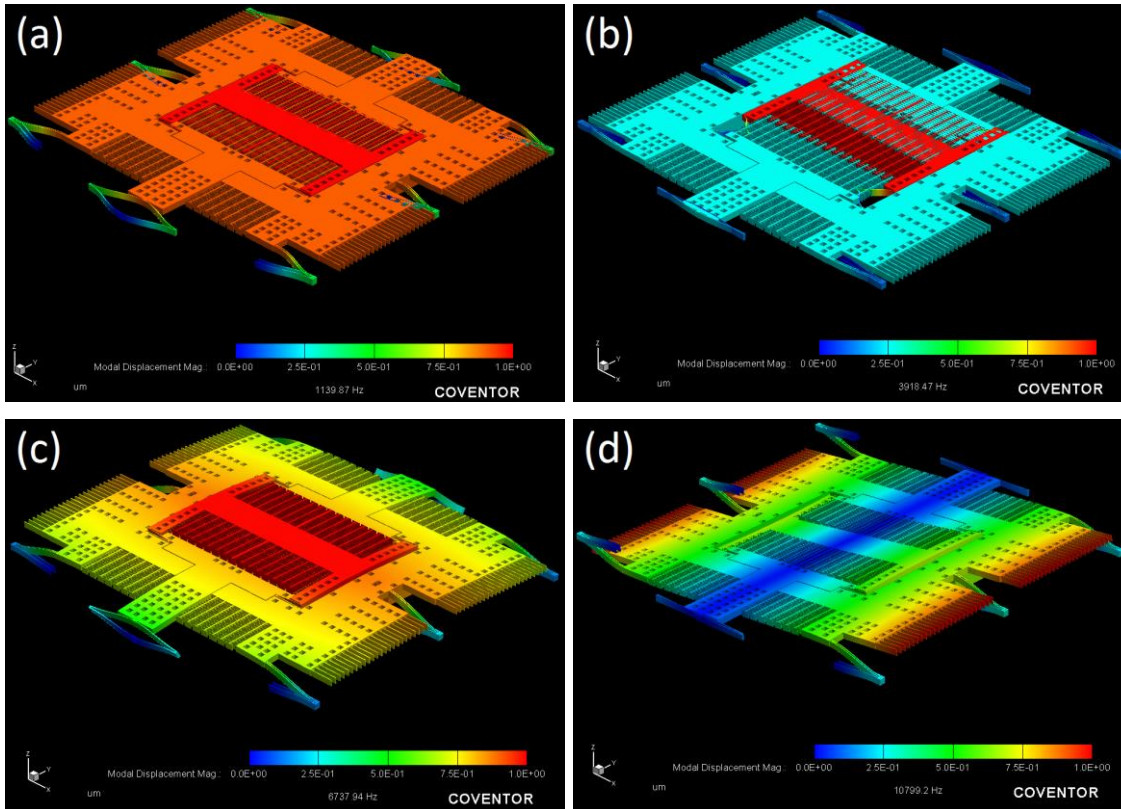


Figure 6-4: Finite element analysis of the 2-DoF sensing element using CoventorWare. It shows that the (a) 1st mode or first resonance frequency is at 1.2 kHz, the (b) 2nd mode or resonance frequency is at 3.9 kHz, the (c) 3rd mode is at 6.74 kHz and the (d) 4th mode is at 10.8 kHz.

## 6.5 Fabrication

A dicing-free SOI fabrication process described in section 3.4.2 was adopted and developed further in this work. The microfabrication steps for the proposed 2-DoF capacitive MEMS velocity sensor are shown in Figure 6-5. The sensor was fabricated using SOI wafer that has a device layer of 100  $\mu\text{m}$  thickness, a 2  $\mu\text{m}$  BOX layer and a 525  $\mu\text{m}$  handle layer. The novel construction of the mechanically coupled and electrically isolated 2-DoF sensor with the handle layer support structure required three masks. The first mask was used for the device layer and the other two for the handle layer.

The handle layer was processed by DRIE, in which a soft mask was used to reach a depth of around 300  $\mu\text{m}$ . The soft mask of the handle layer was stripped and then the exposed silicon area was deep etched using a hard mask on the handle layer. These process steps enabled the trenches to reach the BOX layer before the handle layer support structure was completely etched. The thickness of the support structure was approximately 200-300  $\mu\text{m}$ .

The device and handle layers of the SOI wafer were defined by hard and soft masks, as shown in Figure 6-5(a). Initially, the device and handle layers were processed using the plasma-enhanced chemical vapour deposition (PECVD) process to apply a coat of SiO<sub>2</sub> layer. The hard masks then defined by the inductively coupled plasma (ICP) oxide etching. The handle layer soft mask was then processed with AZ9260 photoresist. At this stage, the SOI wafer was ready for DRIE. For the fabrication parameters, refer to lithography process in appendix C.1, SiO<sub>2</sub> layer coating using PECVD in appendix C.2, and ICP in appendix C.3.

With the soft mask of the handle layer as shown in Figure 6-5(b), DRIE was used to etch 40  $\mu\text{m}$  wide trenches. The average depth of the trenches across the wafer was around 300  $\mu\text{m}$  (refer to appendix C.5 for DRIE process parameter). Then, the soft mask was removed using a plasma asher. Another DRIE process was performed to etch the 100  $\mu\text{m}$  device layer by using the device layer hard mask as shown in Figure 6-5(c), (refer to appendix C.4 for DRIE process parameter). The last DRIE procedure was carried out with the use of the handle layer hard mask (Figure 6-5 (d)), in which the large area of silicon (which defines the handle layer support structure) was etched, and in parallel, the etching of the trenches was continued of step (b) in Figure 6-5, (refer to appendix C.6 for DRIE process parameter). The etch rate of the large area of silicon was about three times faster than that of the already etched trenches. This phenomenon is attributed to the higher activity of the fluorine ion etching agent in the relatively near-large area of exposed silicon than at the bottom of the deep trenches. Therefore, the polymer material has a considerable chance of accumulating in these deep trenches, which generates narrow trenches and may terminate the etching state [110] [111]; apart from this phenomenon, grassing occurs on the sidewall and bottom of the trench (Figure 6-6). This problem was solved by enhancing the polymer etching step within the full DRIE cycle, wherein the

**Chapter 6: Mechanically Coupled and Electrically Isolated 2-DoF Capacitive MEMS Velocity Sensor**

low-frequency bias power was exponentially increased during the DRIE process for the handle layer [112] [113].

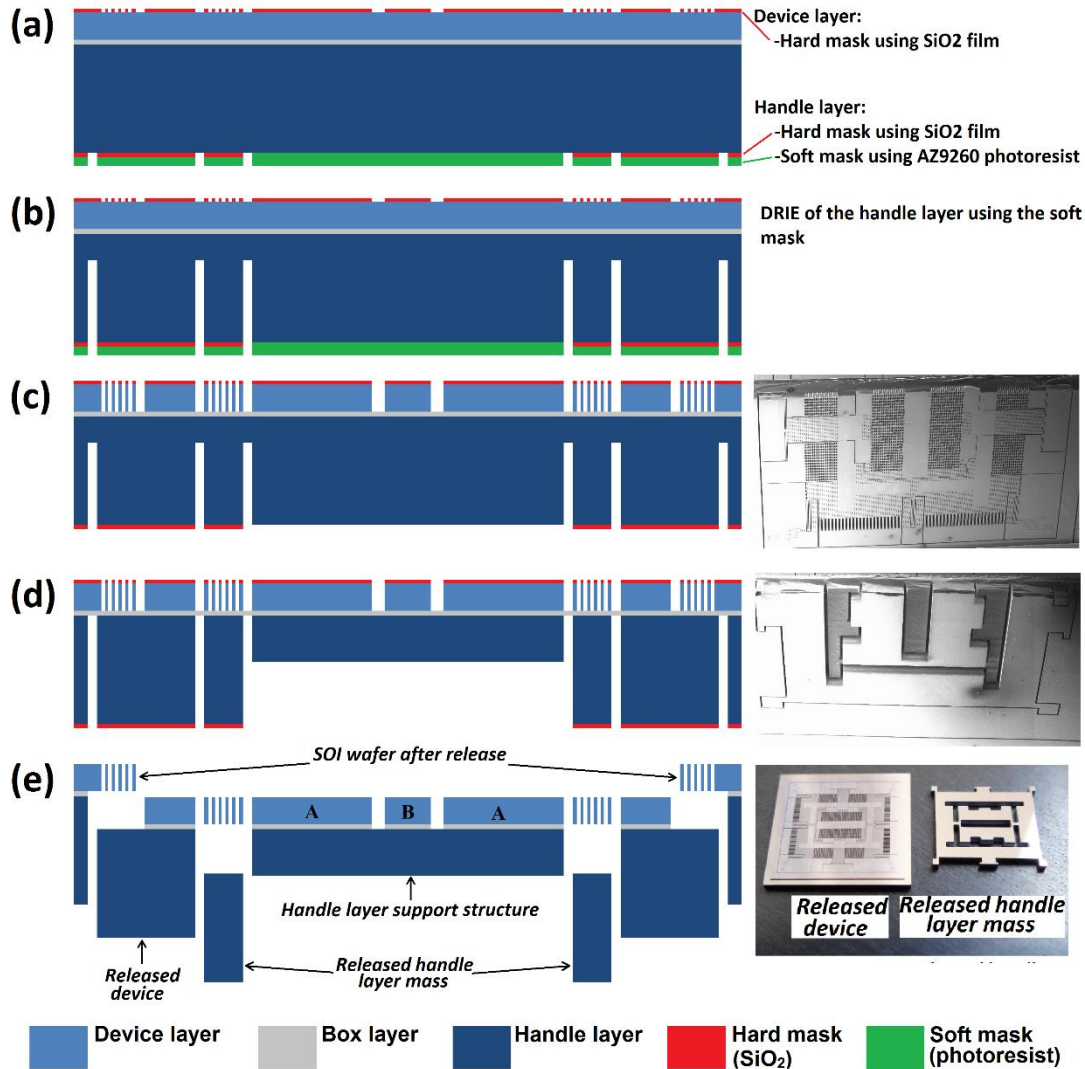


Figure 6-5: SOI microfabrication steps for the proposed 2-DoF velocity sensor. (a) Device and handle layer hard and soft masks, (b) DRIE handle layer using a soft mask, (c) DRIE device layer using a hard mask (d) DRIE handle layer using hard mask, (e) dry-release step using an HF vapour phase etcher. The areas A and B of the proof masses are electrically isolated. The handle layer support structure holds the fragmented proof mass.

The final step (Figure 6-5 (e)) was the dry-release step. The wafer was processed in the HF vapour phase etcher [104]. The device layer was designed with release holes and trenches, which allow the HF to etch the BOX. The oxide etching time was carefully established on the basis of trench and hole spacing, so that the piece of unwanted handle

## Chapter 6: Mechanically Coupled and Electrically Isolated 2-DoF Capacitive MEMS Velocity Sensor

layer mass is released first and then the entire sensor block is separated from the wafer. Figure 6-7 shows the end product of the fabrication process, after around 50 min of dry etch process, about 90 % of the sensors were successfully released from SOI wafer. The remaining sensors (10 %) were unreleased due to the uncompleted handle layer etch.

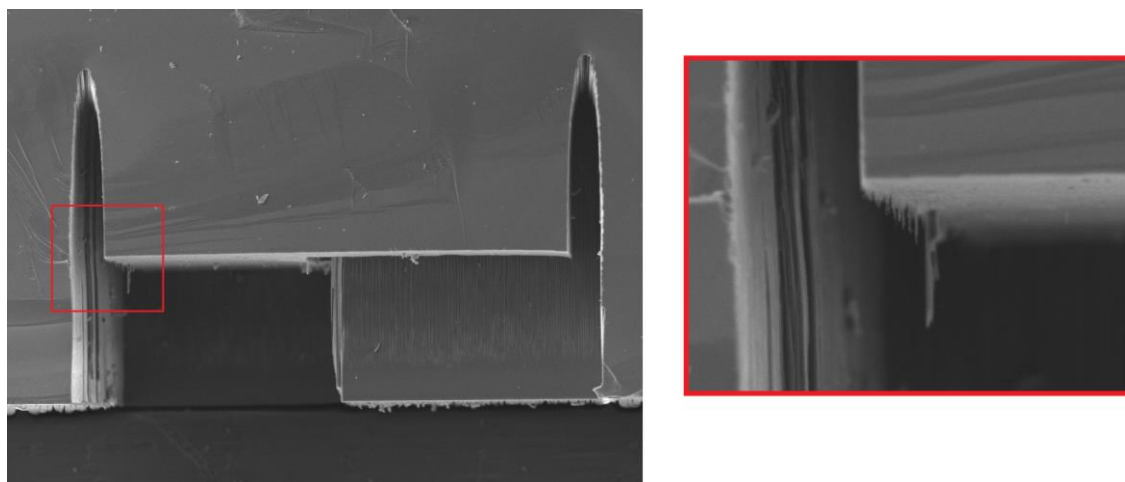


Figure 6-6: SEM image of a development wafer for the two DRIE processes for the handle layer.

Given the insufficient fluorine ion etching agents, the trenches narrow at the end and the grass effect occurs. The grassing occurs at the bottom of the trench and on the edges of the support structure.

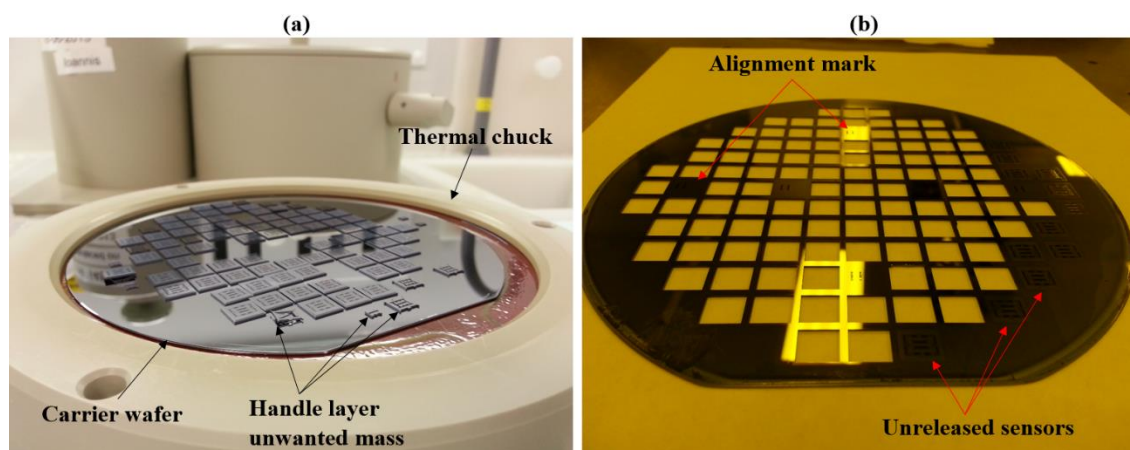


Figure 6-7: HF vapour phase etch step of the first successful fabrication batch, (a) shows the thermal chuck that carries the released devices on the carrier wafer with some released unwanted handle layer pieces, (b) the SOI wafer after the release process, it shows some of the unreleased devices because of the handle layer was not completely processed, and it also shows the alignment marks used during the lithography processes.

**Chapter 6: Mechanically Coupled and Electrically Isolated 2-DoF Capacitive MEMS Velocity Sensor**

The silicon blocks A and B in the end product as indicated in Figure 6-5(e) are electrically isolated by the trenches and the BOX layer underneath. Thus, the change in capacitance of the secondary sensor can be measured via the block B with no electric interference from the block A. Figure 6-8 shows the front view of the sensor, where the sense capacitors of the principal and secondary proof mass are electrically isolated. Figure 6-9 shows the handle layer support structure that is used to join the two blocks of A and B to construct the principal proof mass.

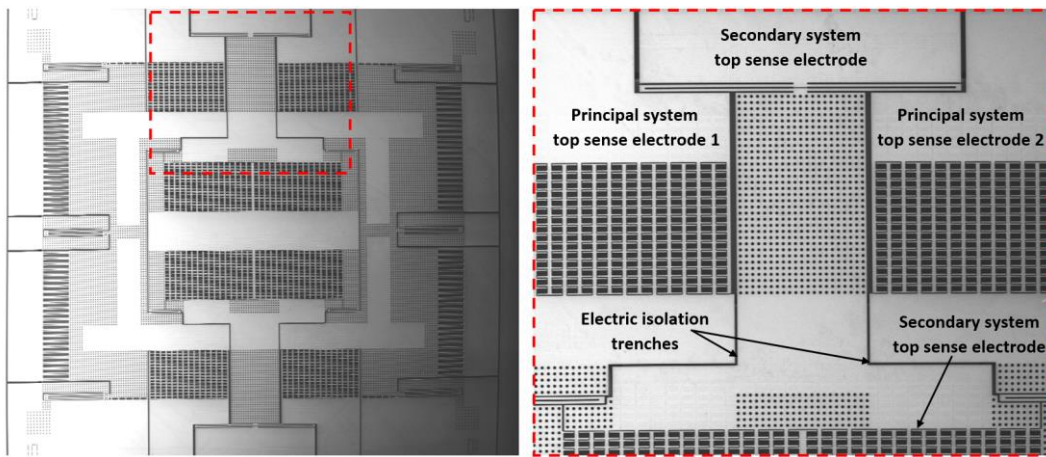


Figure 6-8: Front-side SEM images of the 2-DoF sensing element; (left) full view of the sensor showing the secondary proof mass anchored onto the principal proof mass and the principal proof mass anchored onto the frame; (right) close view of the sensor showing the electric isolation trenches and the principal and secondary top sense electrodes.

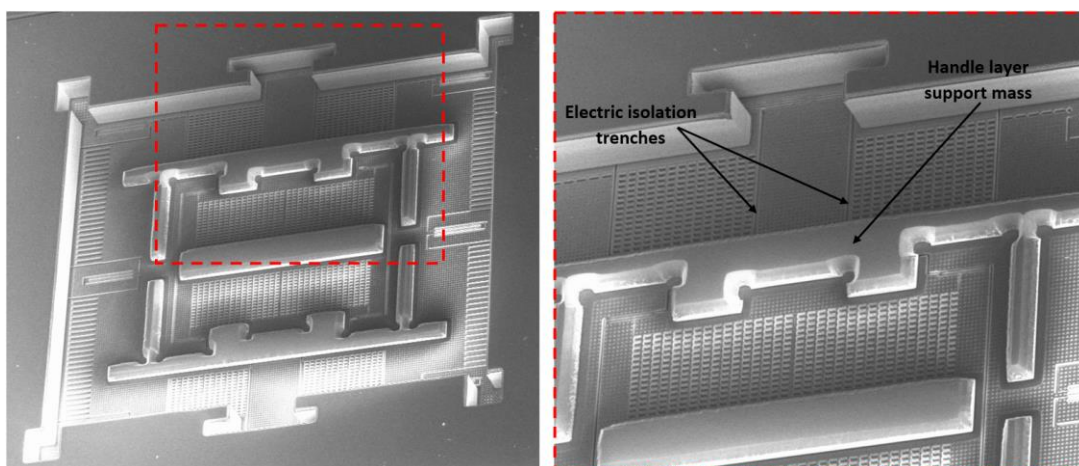


Figure 6-9: Back-side SEM images of the 2-DoF sensing element; (left) full view of the sensor showing the handle layer support structure under the principal and secondary proof masses; (right) close view of the sensor showing the electric isolation trenches and the handle layer support structure.

## 6.6 Interface and Control Circuit

The interface and control circuit of the new sensor is designed with a structure similar to that used in the electronic circuit of the first prototype sensor (discussed in section 5.4). The electronic subtraction circuit is removed because the output signal of secondary proof mass  $x$  is directly obtained by mechanical subtraction. The block diagram of the electronic interface and control circuit is shown in Figure 6-10. The design uses a differential line scheme for the interface electronic circuit, so that common mode noise is eliminated. The principal and secondary sensors are interfaced to a capacitance-to-voltage circuit, which consists of a charge integrator, an amplitude demodulator, a low-pass filter and an instrumentation amplifier. The relative displacement of the proof masses produces a change in the parallel plate capacitance. The charge integrator converts the change in capacitance to a proportional amplitude modulated signal, which is then demodulated with a diode rectifier circuit. The low-pass filter removes the high frequency component. Finally, the instrumentation amplifier combines the differential lines and outputs these into a single line voltage signal that is proportional to the mass displacements. For the detailed schematic circuit, refer to appendix B.2.

The capacitive actuator  $C_{pa}$  of the principal sensor is connected to the feedback control circuit that comprises an integrator amplifier, a gain amplifier and an adder-subtractor amplifier. The secondary sensor feeds the integrator amplifier with the acceleration measurement of the principal sensor. Therefore, the outputs of the integration circuit become proportional to the velocity of the principal sensor. A negative feedback signal is then realised by the adder-subtractor circuit, which generates two out-of-phase voltage signals to drive capacitive actuators  $C_{pa\_top}$  and  $C_{pa\_bot}$ . The interface and control electronic circuit of the second prototype sensor is shown in Figure 6-11.

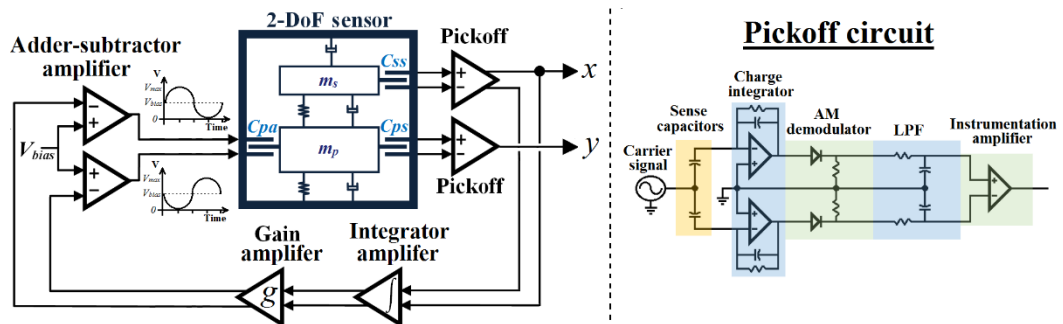


Figure 6-10: Block diagram of the interface and control electronic circuit of the second prototype velocity sensor.

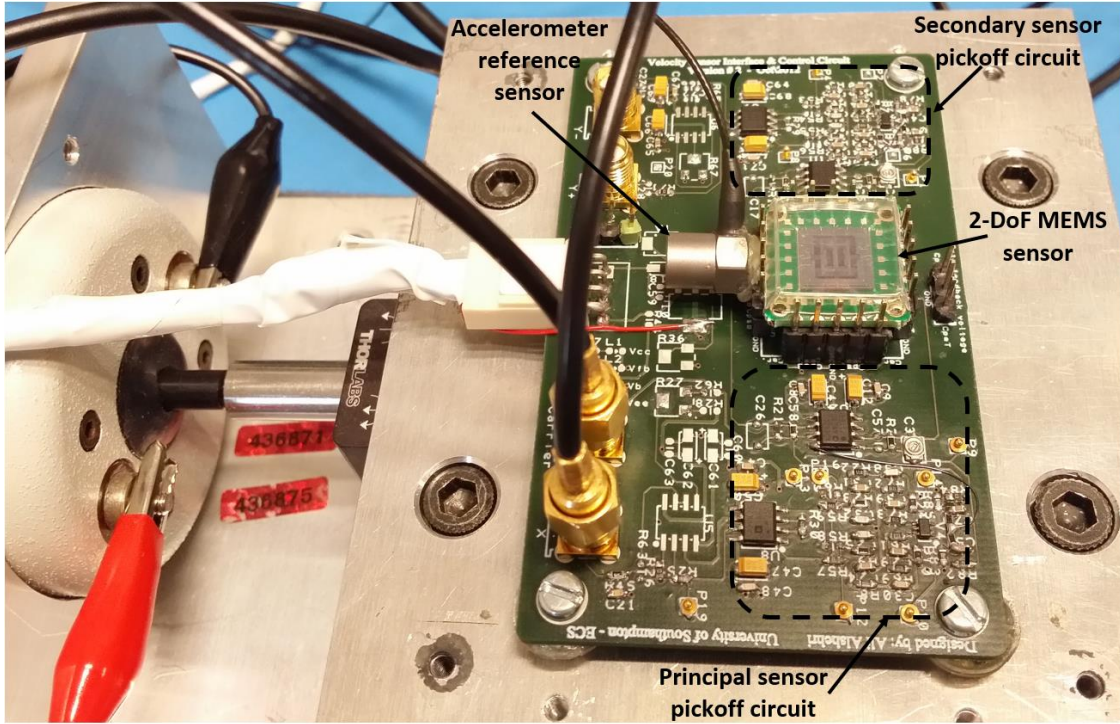


Figure 6-11: Interface and control circuit of the second prototype velocity sensor under test. The accelerometer reference sensor is closely aligned to 2-DoF MEMS sensing element during the acceleration response measurement using shaker table.

## 6.7 Dynamic Response Functions

The dynamic response functions of the 2-DoF sensing element are theoretically presented using the acceleration response functions  $G_{Y,Acc}$  and  $G_{X,Acc}$  derived in equations 4-5(a) and 4-9(a), respectively, and the electrostatic force response functions  $G_{Y,Fs}$  and  $G_{X,Fs}$  derived in equations 4-5(b) and 4-9(b), respectively, and they take following form:

$$G_{Y,Acc} = \left. \frac{Y}{Acc} \right|_{Fs=0} = \frac{-m_p B_2 - m_s B_1}{A_1 B_2 - A_2 B_1} \quad (a)$$

6-1

$$G_{X,Acc} = \left. \frac{X}{Acc} \right|_{Fs=0} = \frac{(B_1 - A_1)m_s + (B_2 - A_2)m_p}{A_1 B_2 - A_2 B_1} \quad (b)$$

$$G_{Y,Fs} = \left. \frac{Y}{Fs} \right|_{Acc=0} = \frac{B_2}{A_1 B_2 - A_2 B_1} \quad (a)$$

6-2

$$G_{X,Fs} = \left. \frac{X}{Fs} \right|_{Acc=0} = \frac{A_2 - B_2}{A_1 B_2 - A_2 B_1}$$

where  $A_1 = m_p s^2 + (b_p + b_s)s + (k_p + k_s)$ ,  $A_2 = B_1 = b_s s + k_s$

$B_2 = m_s s^2 + b_s s + k_s$ .

Experimental measurement were obtained using the same setup discussed in section 5.5. Figure 6-12 (a) and (b) shows the acceleration response functions  $G_{Y,Acc}$  and  $G_{X,Acc}$ , respectively. While, Figure 6-13 (a) and (b) shows the electrostatic force response functions  $G_{Y,Fs}$  and  $G_{X,Fs}$ , respectively, (refer to appendix A.1 for Matlab codeA.2). The blue/dashed line represents the theoretical results and the red/solid line represents the experimental measurements. All four FRFs are characterised by two resonances at 1.1 and 3.7 kHz. The FRFs of  $G_{Y,Acc}$  and  $G_{Y,Fs}$  are also characterised by an antiresonance between the two resonances, which is a typical characteristic of a transfer function given by ratios of physically collocated functions. In contrast, the FRFs of  $G_{X,Acc}$  and  $G_{X,Fs}$  do not show this antiresonance effect. This is also a typical feature of the FRFs given by ratios of physically non-collocated functions.

The  $G_{Y,Acc}$  and  $G_{X,Acc}$  FRFs in Figure 6-12(a,b) were obtained by mounting the 2-DoF sensor on a shaker table operated in such a way to produce a white noise acceleration signal, and observing the output of the pickoff circuits along with the accelerometer reference sensor. The acceleration experimental measurements show close agreement to the simulated one. The FRFs in Figure 6-13 were obtained by driving the capacitive actuator of the principal sensor with a white noise voltage signal and observing the pickoff output signals. The principal sensor measurement  $G_{Y,Fs}$  shows close agreement to the simulated response. The secondary sensor measurement  $G_{X,Fs}$  shows a flat magnitude response below 300 Hz, while the simulated response shows an increase by 40 dB/decade with frequency. Since at low frequencies the output signal is very low values, it is likely that the observed flat response is due to a saturation effect in the pickoff circuit thermal noise [114], which will be discussed in the next section.

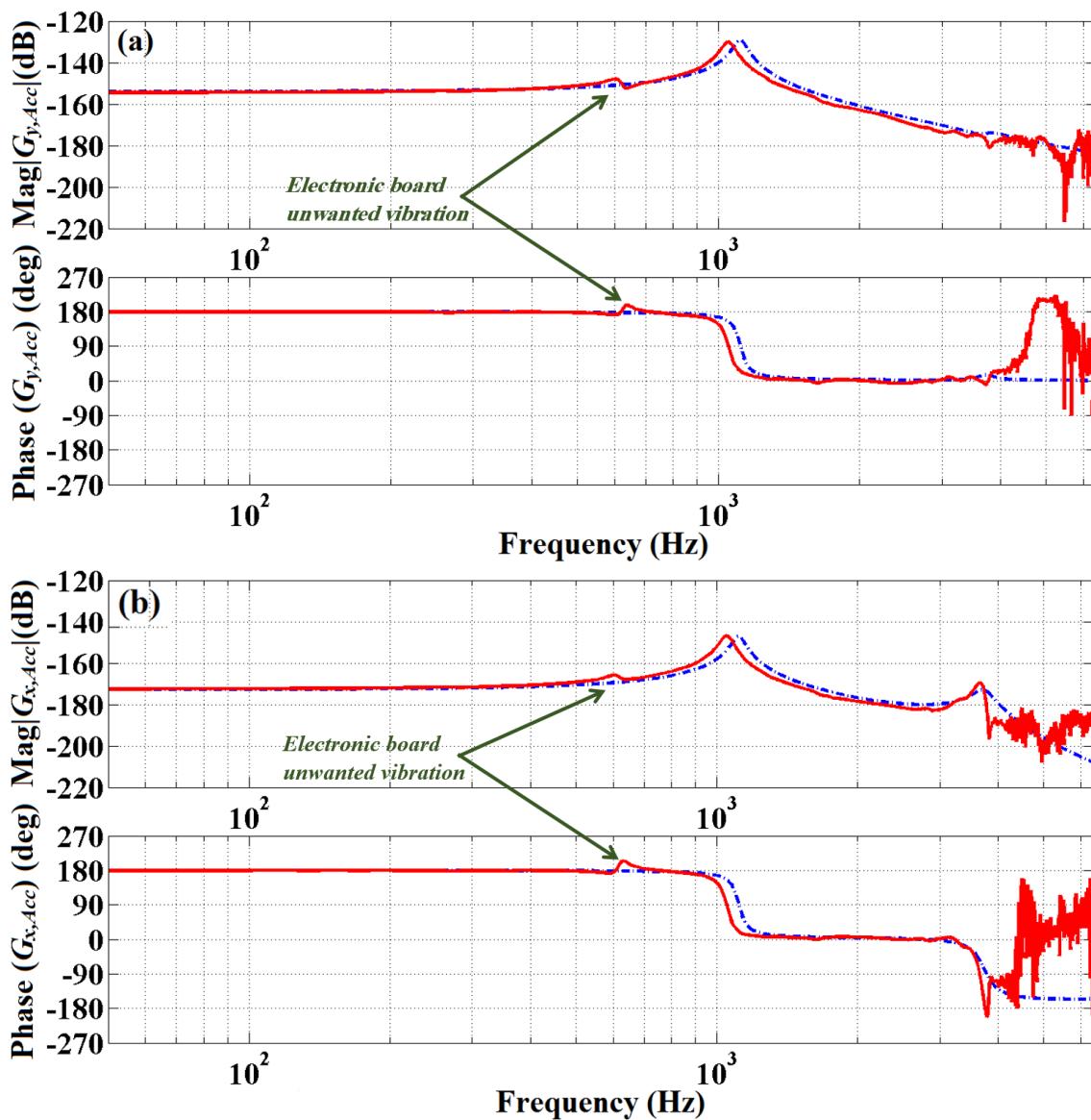


Figure 6-12: Simulated (blue/dashed line) and measured (red/solid line) FRFs of the acceleration input (a)  $G_{Y,Acc}$  and (b)  $G_{X,Acc}$ .

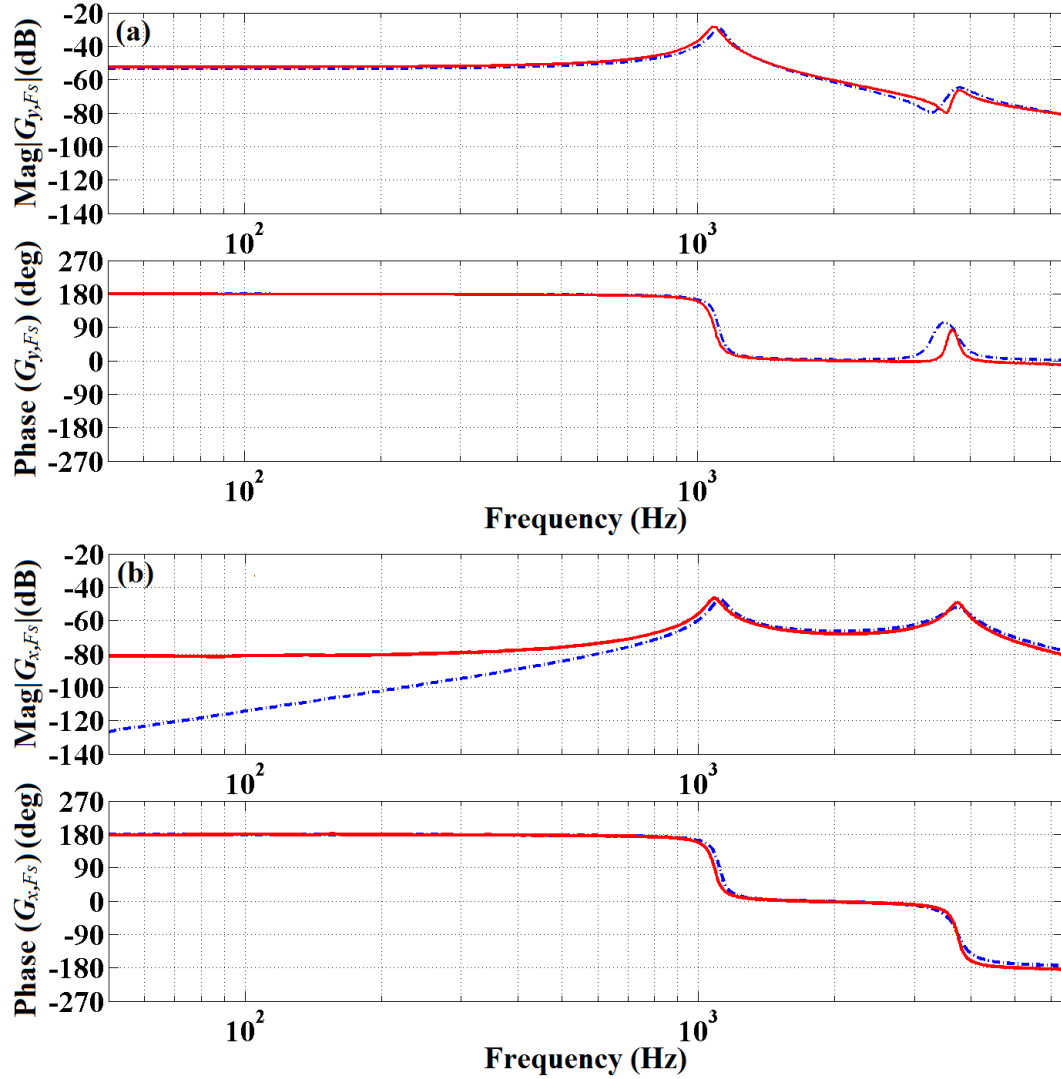


Figure 6-13: Simulated (blue/dashed line) and measured (red/solid line) FRFs of the electrostatic force input applied to the principal sensor (a)  $G_{y,F_s}$  and (b)  $G_{x,F_s}$ .

To examine the effect of the electronic noise of the secondary sensor pickoff, a simulation analysis was carried out. The Simulink model in Figure 6-14 was constructed according to the equations of motion discussed in section 4.4:

$$\begin{aligned} m_p \ddot{w}_1 &= -m_p \ddot{y} - b_p \dot{y} - k_p y + f_s + b_s \dot{x} + k_s x \\ m_s \ddot{w}_1 &= -m_s \ddot{y} - m_s \ddot{x} - c_s \dot{x} - k_s x \end{aligned} \quad 6-3$$

The model includes the measured electronic noise of the secondary sensor, i.e.  $150 \mu\text{V}/\sqrt{\text{Hz}}$ , and the principal and secondary pickoff circuit gains  $K_{pp}$  and  $K_{ps}$ , respectively. The noise measurements and the pickoff gains will be discussed in the next section. The model was excited only by electrostatic force  $F_s$  (i.e. no acceleration input

**Chapter 6: Mechanically Coupled and Electrically Isolated 2-DoF Capacitive MEMS Velocity Sensor**

Acc=0 was applied). The conversion of the voltage signal ( $V_{top\_elec}$  and  $V_{bot\_elec}$ ) to an electrostatic force was included in the model using equation 2-26.

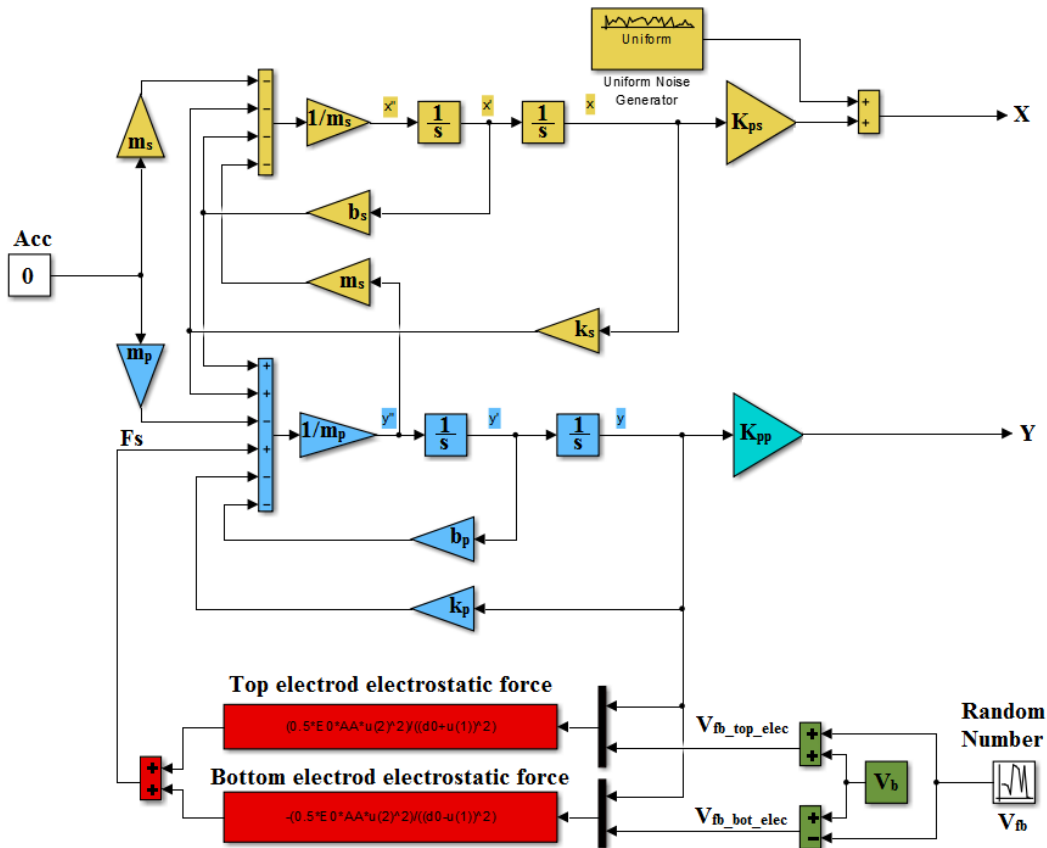


Figure 6-14: Simulink model of the second prototype 2-DoF velocity sensor for the analysis of the pickoff noise generated by the secondary sensor.

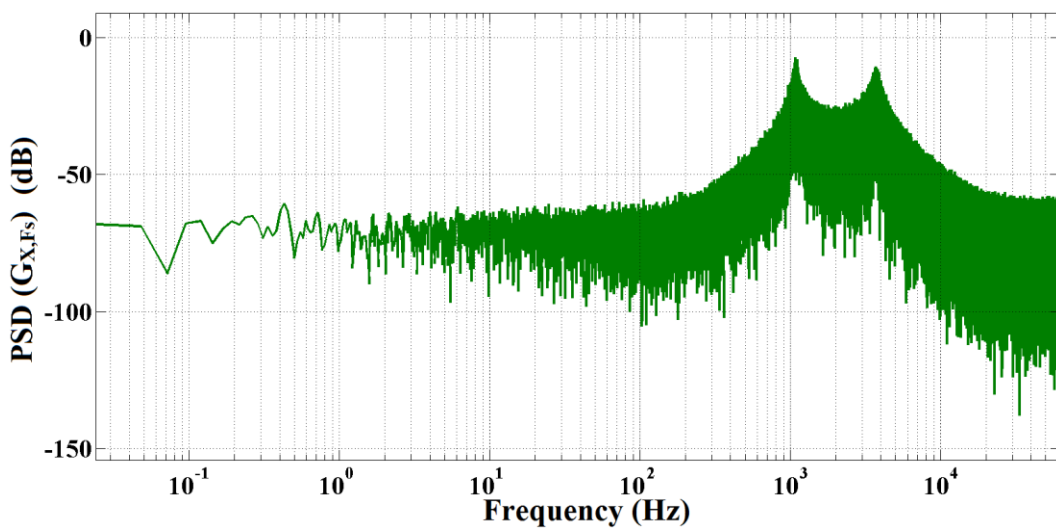


Figure 6-15: Simulated power spectral density of the secondary sensor transfer function  $G_{X,Fs}$  including pickoff noise.

The simulated power spectral density (PSD) of the secondary sensor pickoff at output  $X$  was obtained, as shown in Figure 6-15. The spectrum behaves in a similar manner as the measured one; that is, it exhibits a flat response below 300 Hz. This result indicates that the displacement of secondary proof mass  $X$  is dominated by electronic noise.

## 6.8 Measurement of Pickoff Circuit Gain

As discussed in the previous section, the electrostatic force response of the secondary sensor  $G_{X,Fs}(s)$  is insignificant in the frequency band below 300 Hz because of the dominant pickoff electronic noise. An experiment was carried out to measure the pickoff electronic noise using the Agilent 35670A signal analyser. Figure 6-16 shows that above 300 Hz the secondary pickoff circuit has a noise floor of around  $150 \mu\text{V}/\sqrt{\text{Hz}}$ . However, below 300 Hz, the circuit is affected by flicker noise behaviour, this is due to the instrumentation amplifier at the last stage of the pickoff circuit as the charge integrator at the first stage operates at high frequency (1 MHz) which avoids the flicker noise region [106] [115].

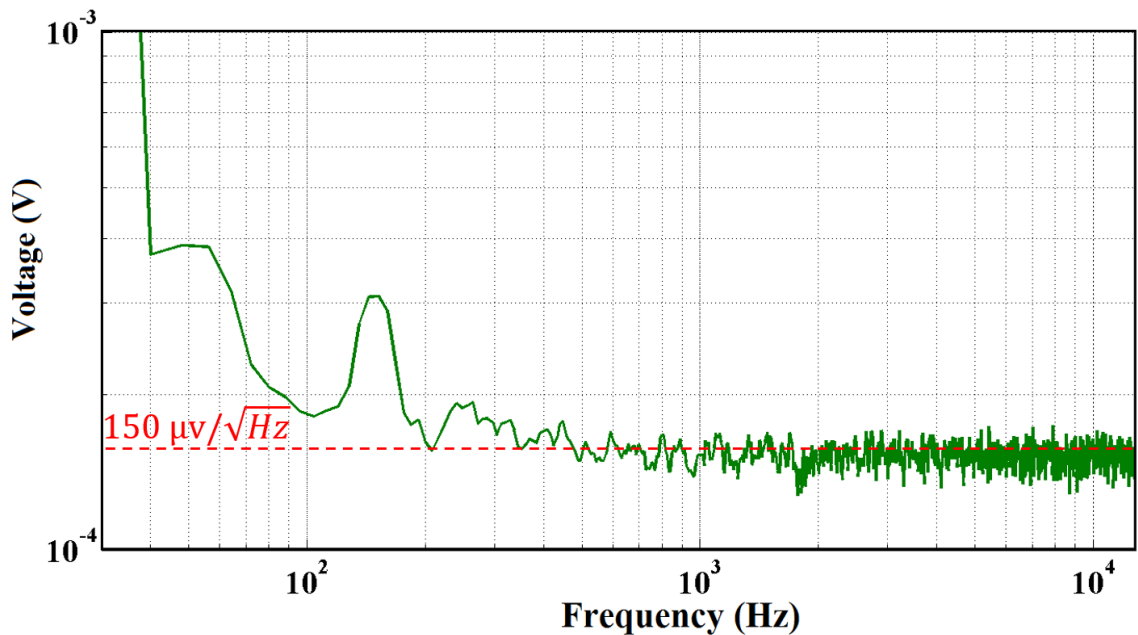


Figure 6-16: Experimental measurement of power spectral density for the electronic noise of the secondary sensor pickoff circuit. The measurement was conducted using Agilent 35670A signal analyser. The electronic noise is around  $150 \mu\text{V}/\sqrt{\text{Hz}}$  for the bandwidth below the first resonance frequency of the 2-DoF.

## Chapter 6: Mechanically Coupled and Electrically Isolated 2-DoF Capacitive MEMS Velocity Sensor

---

The pickoff gains of the principal and secondary sensors were experimentally measured, in which a voltage signal was applied to the principal sensor actuator, so that both proof masses will experience displacement. Displacements  $y$  and  $x$  were then optically measured using the Polytec micro system analyser (MSA400) [116]. The principal sensor was excited with an electrostatic force at the first resonance (1.1 kHz). Figure 6-17(a) shows that the measured output voltage of the pickoff circuit is 4.63 V<sub>pp</sub>, and Figure 6-11(b) indicates that the proof mass displacement is 2.85 μm. Therefore, the pickoff gain of principal sensor  $K_{pp}$  is equal to:

$$K_{pp} = \frac{4.63 V_{pp}}{2.85 \times 10^{-6} m} = 1.6246 \times 10^6 \quad [\text{V/m}] \quad 6-4$$

The secondary pickoff was measured in accordance with the procedure explained above. The MSA400 requires a fixed reference structure (e.g. a sensor frame, pad or anchor) for it to calculate proof mass displacement with reference to the fixed structure. The optical objective of the MSA400 can cover only the secondary and principal proof masses whilst the fixed structures are out of view. At the second resonance frequency, however, the two proof masses move out of phase, and the principal proof mass moves to a minimal extent compared with that achieved using the secondary sensor. Therefore, the MSA400 was set to measure the secondary proof mass with reference to the semi-stationary principal proof mass. Figure 6-18 illustrates the secondary sensor measurement at the second resonance frequency, where (a) shows that the output voltage of the pickoff circuit is 7.1 V<sub>pp</sub>, and (b) indicates that the displacement of the secondary sensor is 2.17 μm. Therefore, the pickoff gain of secondary sensor  $K_{ps}$  is equal to

$$K_{ps} = \frac{7.1 V_{pp}}{2.17 \times 10^{-6} m} = 3.2719 \times 10^6 \quad [\text{V/m}] \quad 6-5$$

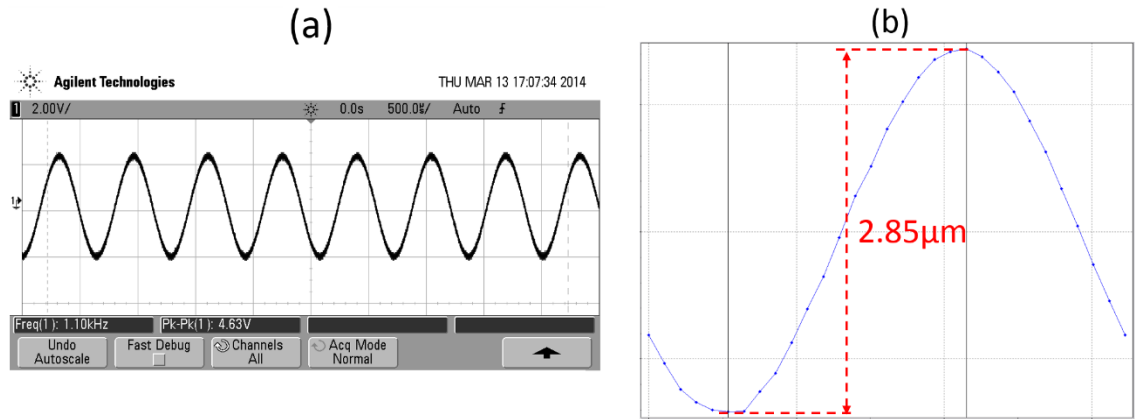


Figure 6-17: Experimental measurements of the pickoff circuit of the principal sensor; (a) the output voltage of the pickoff is 4.63 Vpp and (b) the peak-to-peak MSA400 optical measurement of the principal proof mass displacement is 2.85 µm.

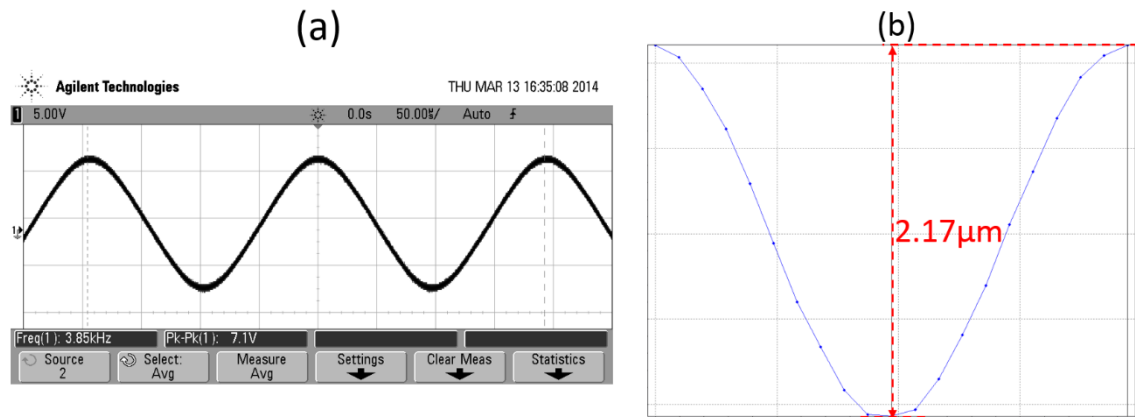


Figure 6-18: Experimental measurements of the pickoff circuit of the secondary sensor; (a) the output voltage of the pickoff is 7.1 Vpp and (b) the peak-to-peak MSA400 optical measurement of the secondary proof mass displacement 2.17 µm.

Another test was performed by using a tilt table to fix the board at a 90° angle. At this angle, the output measurement of the pickoff circuits represents the response due to a static acceleration of 9.81 m/s<sup>2</sup> (i.e. 1 g). The principal and secondary pickoff circuits generate the following measurements:

***Principal sensor pickoff: 1 g → 145 mV***

***Secondary sensor pickoff: 1 g → 38 mV***

The results in equations 6-5 and 6-6 demonstrate that as the sensor is exposed to a static 1 g input, the principal sensor exhibits a displacement of around  $90 \times 10^{-9}$  m resulting in a change in the sense differential capacitance of  $218.1 \times 10^{-15}$  F/g, whereas the secondary sensor shows a displacement of around  $11 \times 10^{-9}$  m, which indicates a change in the differential capacitance of  $29.51 \times 10^{-15}$  F/g. This finding confirms that the secondary sensor has lower sensitivity, which is due to the high spring constant and small proof mass.

In order to theoretically observe the electrostatic force response of the sensor, the Simulink model in Figure 6-14 can be examined. When the feedback voltage  $V_{fb}$  and the bias voltage  $V_b$  are set to 15 V. Thus, the top and bottom electrodes are energised by two out-of-phase sine wave voltage signals, thus, a signal of 30 V peak-to-peak is generated, and when the excitation voltage is set at 50 Hz, the output signal of the secondary pickoff circuit will be around 65  $\mu$ V, and the principal pickoff will be around 300 mV. This indicates that the output voltage of the secondary sensor is below the noise floor of the pickoff circuit and will be demolished. A practical solution that increases the output response of the secondary proof mass is to increase feedback voltage to around 40 Vpp. Nevertheless, the output of the pickoff circuit is attenuated by the cross-coupling of feedback voltage. Therefore, a feedback voltage of 30 Vpp is the value that exerts a low effect on such cross-coupling.

## **6.9 Design of the Internal Velocity Feedback Loop**

The design of the internal feedback loop is presented in this section with reference to the simulated frequency response functions that characterize the sensor. Using the usual assumption to linearize the model when the proof mass displacement is very small relative to the nominal gap [28] [30] [103], the nonlinear behaviour accompanying the parallel electrode sense and actuator capacitors, the squeeze film damping within the capacitors, and the spring constants of the folded-beam can be negligible. Furthermore, when the balanced parallel capacitive actuator is employed, the net electrostatic force applied on the proof mass can be considered linear with relation to the applied voltage [30] [39]. Using the same principle of superposition discussed in section 4.4, the closed loop transfer function  $G_{Y,CL}(s)$  of the displacement  $y$  per unit velocity of the sensor's frame takes the following form:

$$G_{y,CL}(s) = G_{Y,Vel}(s) + G_{Y,Fs}(s)G_{X,Vel}(s) \left( \frac{H(s)}{1 - G_{X,Fs}(s)H(s)} \right) \quad 6-7$$

where  $G_{Y,Vel}$  and  $G_{X,Vel}$  are the displacement  $y$  and  $x$  per unit velocity of the sensor's frame obtained from the measured  $G_{Y,Acc}$  and  $G_{X,Acc}$  FRF as discussed with equation 4-15.

As discussed in section 4.4, to construct a negative velocity feedback loop that generates the desired damping force effect, it is necessary to obtain the velocity measurement of the principal proof mass, therefore, the feedback loop control function  $H(s)$  is given by:

$$H(s) = \frac{Fs(s)}{X(s)} = -g \frac{K_{int}}{1 + \tau s} \quad 6-8$$

Considering the same conditions discussed in section 4.5, where the control gain  $g$  must be set to maintain the stability of velocity feedback loop, and to eliminate the imaginary part of the closed loop transfer function  $G_{Y,CL}(s)$  such that, in the frequency bandwidth of interest, the frequency response of  $G_{Y,CL}(j\omega)$  becomes proportional to the velocity of the sensor's frame.

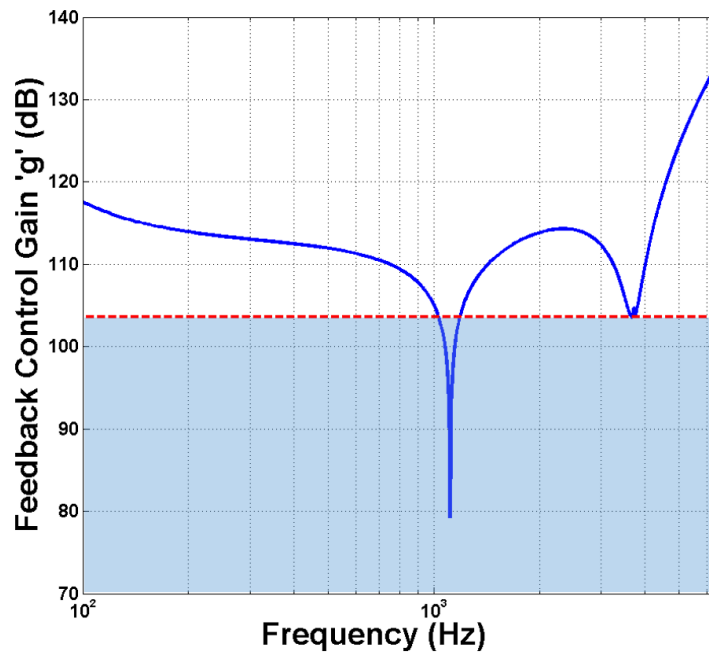


Figure 6-19: Simulated frequency-dependent control gain values (blue/solid line). For stable feedback loop, only  $g$  values under 103 dB are valid for applying the required damping force on the principal sensor.

**Chapter 6: Mechanically Coupled and Electrically Isolated 2-DoF Capacitive MEMS Velocity Sensor**

Figure 6-19, shows the evaluation of the frequency-dependant control gain  $g(\omega)$  in equation 4-20 with the use of the feedback loop functions  $H(s)$  in equation 6-8, (refer to appendix A.2 for Matlab codeA.2)..

The stability analysis of the system can be considered by using the open loop control transfer function given by:

$$G_{ol,X,Fs}(s) = H(s) G_{X,Fs}(s) \tag{6-9}$$

By assuming the control function  $H(s)$  in equation 6-8 has a unity  $K_{int}$  DC gain, a time constant  $\tau = 1$  sec and unity control gain  $g$ , equation 6-9 can be examined as shown in Figure 6-20, (refer to appendix A.4 for Matlab codeA.2). As can be seen, the maximum gain that guarantees stability is about 103 dB. Thus, as highlighted by the dashed red line in Figure 6-19, feedback gains within the shaded area only can be implemented in practice. Accordingly, the 2-DoF velocity sensor with the current  $H(s)$  cannot be stable within the band of interest, below the first resonance.

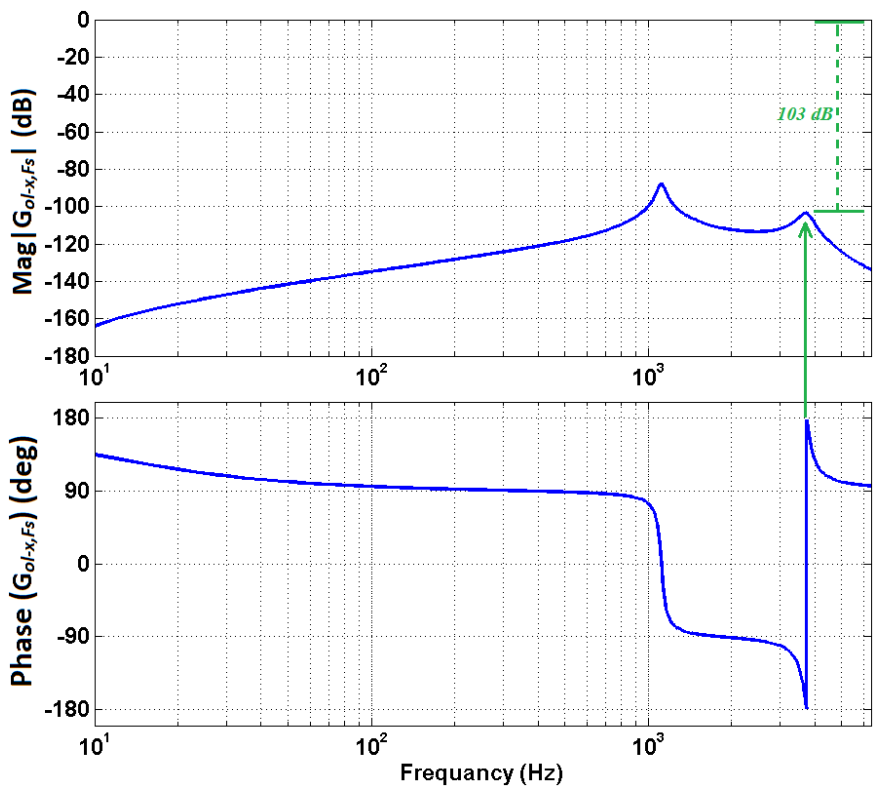


Figure 6-20: Simulated control open loop transfer function  $G_{ol-X-Fs}$  shows the  $-180^\circ$  phase crossover at the second resonance, which determines the maximum stable control gain of 103 dB.

**Chapter 6: Mechanically Coupled and Electrically Isolated 2-DoF Capacitive MEMS Velocity Sensor**

As discussed in section 4.5, to improve the stability limit, a second order low pass control filter with a corner frequency at 2 kHz just above the first resonance frequency of the system can be implemented. In this case, the feedback loop control function  $H(s)$  is given by:

$$H(s) = \frac{Fs(s)}{X(s)} = -g * \frac{K_{int}}{1 + \tau s} * \frac{w_c^2}{s^2 + \frac{w_c}{Q} s + w_c^2} \quad 6-10$$

As shown in Figure 6-21 the maximum control gain that would guarantee stability is about 112 dB. Figure 6-22, shows the frequency dependent gain that would guarantee the desired velocity output signal of the sensor when the low pass filter is included with the feedback loop (refer to appendix A.3 for Matlab codeA.2). The spectrum of the gain function is similar to that found for the uncompensated loop. However, in this case, the dashed line that limits the maximum gain that guarantees stability intersects the desired gain function, and a fixed value of the control gain  $g$  within the shaded can be used.

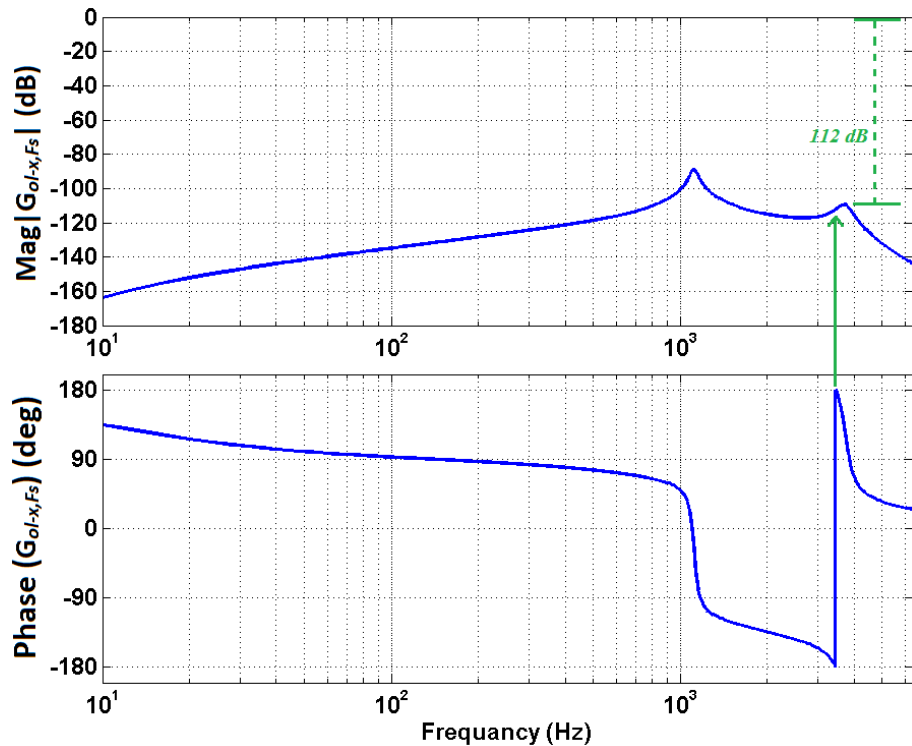


Figure 6-21: Simulated bode plots of control open loop transfer function  $G_{ol-X-Fs}$  with low-pass filter addition; the image shows the  $-180^\circ$  phase crossover at the second resonance, which determines the maximum stable control gain of 112 dB.

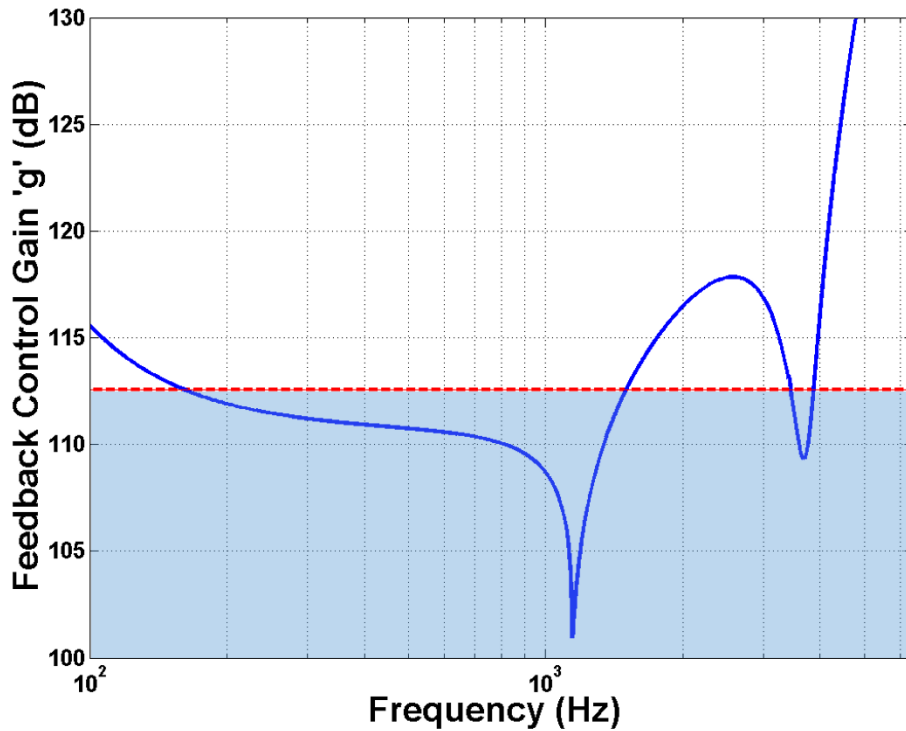


Figure 6-22: Simulated frequency-dependent control gain values (blue/solid line) with the low-pass. Dashed/red line is the maximum gain is 112 dB.

## 6.10 Closed Loop Measurement

The open and closed loop frequency response functions of the sensor output  $Y(s)$  per unit of the velocity of the sensor's frame ( $Vel$ ) are derived by using equation 6-1 along with the feedback control function 6-10, and using the measured dynamic response function  $G_{Y,Acc}$ ,  $G_{X,Acc}$ ,  $G_{Y,Fs}$  and  $G_{X,Fs}$  FRFs presented in the previous section 6.7. The open and closed loop frequency response functions are shown in Figure 6-23 for the simulated result, and in Figure 6-24 for the experimental measurement (refer to appendix A.5 for Matlab codeA.2). The experimental measured open loop response in Figure 6-24 with the blue/dashed line, shows the typical response of an accelerometer with reference to the base velocity, which also closely agree with the simulated open-loop response in Figure 6-23 with the blue/solid line. With regards to Figure 6-24, when the sensor internal loop is closed with a control gain of about  $g = 110.37$  dB, between 300 Hz and 1 kHz, the response of the sensor is proportional to the base velocity. Also the first resonance peak flattens. Finally, at frequencies higher than the first resonance frequency, the amplitude monotonically decreases and is characterised by a  $-90^\circ$  phase lag. These three

observations prove the concept of the velocity sensor with the novel idea of the mechanically coupled and electrically isolated 2-DoF MEMS sensor.

The experimental measured closed loop response of the sensor shown in Figure 6-24 (red/solid line), indicates that the velocity measurement starts after 300 Hz up to the first resonance frequency. This is due to the fact that below 300 Hz, the electrostatic force response function  $G_{X,F_s}$  of the secondary sensor is demolished by the electronic noise as described above in section 6.7, hence, the loop does not produce the required control signal below 300 Hz.

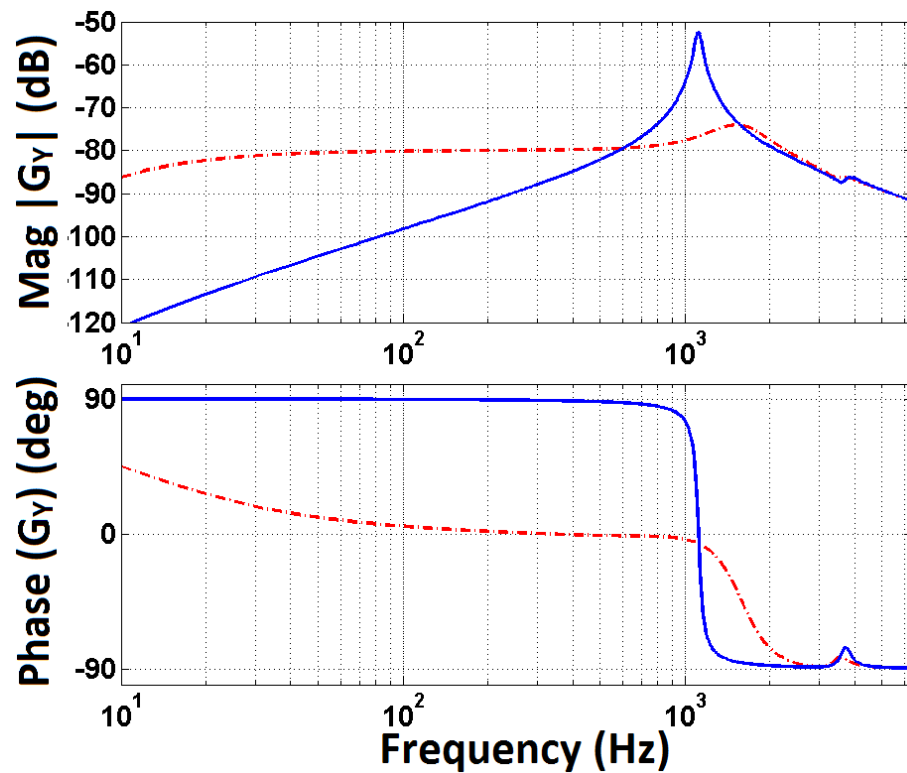


Figure 6-23: Simulated open-loop (solid/blue line) and closed-loop (dashed/red line) Bode plots using transfer function  $G_Y(s)$ , where the open loop response of the sensor using  $g=0$ , and closed loop response using  $g=110.37$  dB at 500 Hz.

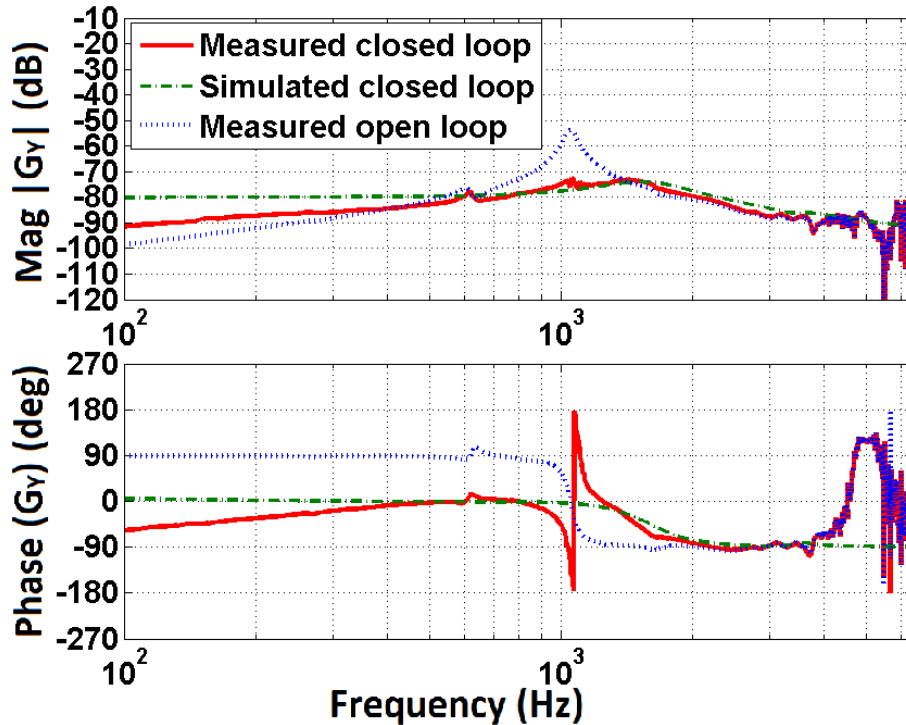


Figure 6-24: Open and closed loop measurement of the velocity sensor output Y per unit of the velocity of the sensor’s frame. The blue/dotted line is the measured open loop response, red/solid line is the measured closed loop response, and green/dashed line is the simulated closed loop response.

### 6.11 Electrostatic Spring Softening Effect in Closed Loop Measurement

The off-line closed loop measurement is very sensitive to the physical variation of the sensor when the four dynamic measurements  $G_{Y,Acc}$ ,  $G_{X,Acc}$ ,  $G_{Y,Fs}$  and  $G_{X,Fs}$  are taken. Around the first resonance frequency, the closed-loop response of the measured sensor shows slight ripples in magnitude and a phase change from  $-180^\circ$  to  $180^\circ$ . The capacitive actuator is designed with a parallel plate type, and during the electrostatic force excitation, the spring softening effect has an influence on the sensor and reduces the mechanical spring constant [117-121]. A theoretical investigation was carried out to study this effect.

The principal sensor is equipped with an electrostatic force actuator; therefore, only the spring constant of the principal sensor is affected by spring softening, while the spring constant of the secondary proof mass is unaffected. The actuator electrodes were connected to two out-of-phase voltage signals, with a maximum amplitude of 30 V. By

**Chapter 6: Mechanically Coupled and Electrically Isolated 2-DoF Capacitive MEMS Velocity Sensor**

recalling the spring softening equation (2-28) and using the dimensions in Table 6-1, the estimated spring softening is given by:

$$k_e = \varepsilon_0 A \frac{V_{fb}}{d_0^3} \tag{6-11}$$

$$= \frac{8.854 \times 10^{-12} * 400 \times 10^{-6} * 100 \times 10^{-6} * 48 * 30}{(6 \times 10^{-6})^3}$$

$$= 2.4 \text{ N/m}$$

The mechanical spring constant of the principal sensor is 480 N/m, but the effective spring constant is 477.6 N/m. This loss in the spring constant lowers the first resonance frequency of  $G_{Y,FS}$  by around 50 Hz, which introduces a mismatch with the first resonance frequency of the other FRFs  $G_{Y,Acc}$ ,  $G_{X,Acc}$ , and  $G_{X,FS}$ .

The closed loop response function (equation 6-12) can then be examined by including the spring softening effect on the electrostatic force response function of the principal sensor  $\hat{G}_{Y,FS}(s)$ .

$$G_{y,CL}(s) = \frac{Y(s)}{S^2 W_1} = G_{Y,Acc}(s) + \hat{G}_{Y,FS}(s) G_{X,Acc}(s) \left( \frac{H(s)}{1 - G_{X,FS}(s) H(s)} \right) \tag{6-12}$$

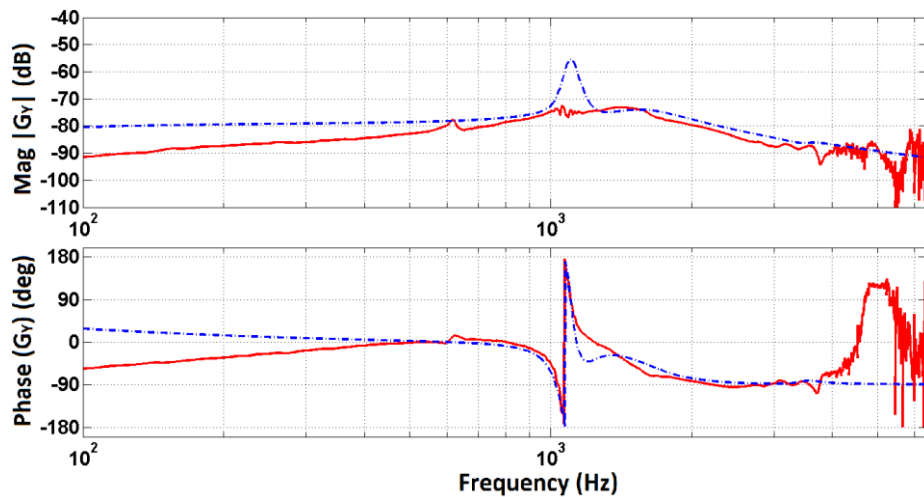


Figure 6-25: Simulated (blue/dashed line) and experimental (red/solid line) closed loop measurement of the velocity sensor output Y per unit of the velocity of the sensor's frame. The simulation measurement includes the spring softening effect; for both measurements, the phase around the resonant frequency shows a change from -180° to 180°.

Figure 6-25 shows a measured (red/solid line) and a simulated (blue/dashed line) closed-loop frequency response. It can be seen that the simulation results reproduced a very close phase shift response around the resonant frequency. This finding supports the assumption of the spring softening effect. This problem can be eliminated if an on-line implementation is considered, where this phenomenon will be included in all the FRFs and the first resonance frequency will be matched in all measurements.

## **6.12 Design Issues of the Second Prototype Sensor**

The second prototype velocity sensor aimed to solve some of the problems encountered with the first one. However, this development brought another area of challenges that degraded the overall performance:

**First**, the electrostatic force response of the secondary sensor was very hard to measure, especially in the frequency band below 300 Hz. The low frequency measurement was demolished by the electronic noise induced by the pickoff circuit. Several solutions can be considered:

- 1- A pickoff circuit with low electronic noise.
- 2- The sensitivity of the secondary sensor can be increased by redesigning the 2-DoF velocity sensor with softer springs and/or a heavier proof mass.
- 3- Increase the sense capacitance of the secondary sensor.

**Second**, a low pass filter was required to make the velocity feedback loop stable, despite the increased number of sense electrodes between the two proof masses, which was aimed to introduce a greater squeeze film damping effect.

**Third**, the use of the parallel plate actuator helped to reduce the required voltage to control the sensor, hence, no voltage amplifier was used during the experimental measurement. However, such actuator comes across nonlinear electrostatic force behaviour for large proof mass deflection.

**Fourth**, even though the concept of the new sensor design was proved using the off-line closed-loop measurement, the closed-loop frequency response showed a phase shift around the resonant frequency, which was due to the spring softening effect included in  $G_{Y,Fs}$ , but was not included in  $G_{Y,Acc}$ ,  $G_{X,Acc}$  and  $G_{X,Fs}$ . To include the spring softening

effect in all FRFs, an online run of the closed-loop sensor could help produce all four FRFs with the same sensor parameters (such as proof mass, damping coefficient and spring constant).

### **6.13 Summary**

The design, micro-fabrication and experimental tests of a novel 2-DoF MEMS sensor are presented. The sensor is formed by two mass-spring-damper systems connected in series and by an internal velocity feedback loop. The study showed that when the control gain of the feedback loop is properly tuned, such that the imaginary part of the closed loop transfer function is eliminated and the feedback loop control is stable, the sensor output becomes proportional to the velocity of the base at low frequencies between about 300 Hz and 1 kHz. The first resonance frequency is flattened. Also the sensor response function is characterised by a declining amplitude with  $-90^\circ$  phase lag around the first resonance frequency. These three features provided by the proposed sensor are of great importance for the construction of a stable velocity feedback loop control system for active vibration control of distributed flexible structures.

The innovative design and microfabrication process of the 2-DoF sensing element enables the mechanical coupling and electrical isolation of two mass-spring-damper systems. This feature allows the sensor to obtain the displacement between the two proof masses by means of a mechanical subtraction. Therefore, the complexity of the electronic circuit that was involved in the first prototype (discussed in chapter 5) is eliminated.

The tests carried out have shown that the proposed design reproduce the expected dynamic response of the MEMS sensor. However, at frequencies below 300 Hz, the electrostatic force frequency response function of the relative displacement between the two masses was very small and jeopardized by pickoff electronic noise. This compromises the quality of the sensor function and affects the internal feedback loop below 300 Hz.



## **Chapter 7: Conclusion and Future Work**

### **7.1 Conclusion**

The research presented the design and implementation of a 2-DoF capacitive MEMS velocity sensor. It is realised for application in a particular concept of smart panels, in which sensors and actuators are embedded on thin plates or shells to enable the implementation of an active vibration control system for velocity feedback loops.

Two prototypes of a 2-DoF velocity sensor were designed in this research. Both prototypes comprise two mass-spring-damper sensors: the principal sensor and the secondary sensor. The function of the principal sensor is to provide the velocity output signal. The function of the secondary sensor is to implement a negative velocity feedback loop on the proof mass of the principal sensor causing a damping force. The damping force exerts three important features on the frequency response function of the sensors: (a) in the frequency range below the first resonance frequency, the response becomes proportional to the base velocity rather than to the base acceleration; (b) it smoothens the first resonance frequency peak; and (c) after the first resonance frequency, the phase lag decreases to  $-90^\circ$ . With these features, the sensor can prevent the instability and control spillover encountered with a velocity feedback loop that employs an accelerometer sensor.

The stability of the internal velocity feedback loop is determined by the second resonance peak of the open-loop control function. The maximum feedback loop gain is proportional to the inverse of the amplitude of the second resonance peak. As the resonance frequency increases, the resonance peak decreases and the gain margin increases. The second resonance peak can be attenuated by increasing the damping coefficient of the secondary sensor. Alternatively, a simple low-pass filter can be included in the feedback loop to reduce the peak, hence the gain margin increases.

For both prototypes, the four FRFs that characterise the dynamics of the 2-DoF sensor with reference to the base acceleration and to electrostatic force were measured and compared with the simulation results on the basis of a simplified lumped mass model. The tests show that the design of the two prototypes reproduces the expected theoretical dynamic response of a 2-DoF MEMS sensor.

The first prototype sensor was fabricated using SOI technology with two masks. In order to close the internal loop of the velocity sensor, the relative displacement of the secondary sensor, with respect to the principal sensor, was obtained by applying electronic subtraction. The closed-loop measurement of the sensor proved the concept of the 2-DoF capacitive MEMS velocity sensor. The output signal was proportional to the base velocity in the frequency range between 600 Hz and 1 kHz, and the phase lag after the first resonance was  $-90^\circ$ .

The first prototype of the 2-DoF capacitive MEMS velocity sensor came across some problems as follows: First, the relative displacement of secondary proof mass was indirectly obtained using an electronic subtraction circuit, and because the pickoff circuit output of each sensor (principal and secondary) always has an offset caused by the mismatch between the capacitive transducer and the charge integrator, the offset from each pickoff is fed to the subtraction circuit. Thus, the electronically-obtained secondary proof mass displacement contains an offset that may reduce the stability of the control loop. Furthermore, given the mismatch between the sense capacitance of the principal and control sensors, the pickoff circuit gains are difficult to match. Second, the sensor was designed with a capacitive actuator based on a lateral comb drive. Although this type of actuator produces linear electrostatic force, it requires a higher voltage than that needed for parallel electrode actuators. Third, the sensor was very sensitive to the wanted out-of-plane movements, which present obstacles in measuring acceleration with a shaker table. Finally, the principal and secondary sensors were designed with sense capacitors of  $640 \times 10^{-15}$  F and  $428 \times 10^{-15}$  F, respectively, and the associated parasitic capacitance was around  $30 \times 10^{-12}$  F, which was very large compared with the sense capacitance.

The design of the second prototype 2-DoF capacitive MEMS velocity sensor aimed to solve the aforementioned problems associated with the first prototype sensor. It was designed based on an innovative method for directly measuring the relative displacement between the two proof masses. The method entails the mechanical coupling and electrical isolation of the two mass-spring-damper systems, which enables the direct measurement of the secondary sensor deflection by means of mechanical subtraction. Furthermore, the sensor was designed with elastic beams that are compliant along the in-plane direction, while stiff in the out-plane direction. Additionally, the principal and secondary parallel plate sense capacitors were increased to  $7 \times 10^{-12}$  F and  $8 \times 10^{-12}$  F, respectively. The principal sensor actuator was designed with parallel plate capacitor, which requires less

excitation voltage when compared with the lateral comb capacitor of the first prototype. The sensor is fabricated using SOI wafer technology, for which the process requires only three masks. The closed-loop experimental measurement showed that the second prototype sensor output has wider velocity measurement bandwidth, when compared with the first prototype. The velocity measurement covers the frequency range between 300 Hz and 1 kHz and the phase lag after the first resonance was  $-90^\circ$ .

To increase the velocity measurement to a lower limit, i.e. below 300 Hz, a pickoff circuit with higher sensitivity and lower electronic noise can be used. The design of the sensor can also be adjusted, so that the sensitivity of the secondary sensor increases. These two topics will be discussed in the next section.

## **7.2 Future Work**

In the succeeding sub-sections, the possible areas for improving the performance of the capacitive MEMS velocity sensors are discussed.

### **7.2.1 Enhancing the Pickoff Circuit Performance**

The second prototype of the 2-DoF capacitive MEMS velocity sensor presented in this research operates in the bandwidth from 300 Hz to the first resonant frequency at 1 kHz, as the pickoff circuit noise constrains the performance of the velocity sensor at a frequency band below 300 Hz. To increase the effective bandwidth below 300 Hz, it is necessary to employ a pickoff circuit with low electronic noise, such that the electrostatic force response of the secondary sensor can be detected in the low frequency band below 300 Hz.

The continuous-time capacitive-to-voltage-converter pickoff circuit employed in this research was constructed using discrete component. The measured electronic noise level was around  $150 \mu\text{V}/\sqrt{\text{Hz}}$ . Also, the flicker noise was noticeable in the low-frequency range. The velocity sensor performance can be improved by considering a low noise and high performance continuous-time (CT) pickoff circuit. Such a circuit has been implemented in an application-specific integrated circuit (ASIC) technology with a noise floor down to  $17\text{-}150 \text{ nV}/\sqrt{\text{Hz}}$  [122-125].

The switched-capacitor (SC) pickoff circuits are other pickoff circuit techniques. However, they generally show higher noise floor when compared with the continuous-time pickoff [115] due to switching noise. Both techniques offer considerable low noise and high sensitivity performance, and both are suitable to be employed with the 2-DoF capacitive MEMS velocity sensor. However, when an ASIC design is considered, the SC pickoff circuits are preferred for their simple implementation and robust performance [105].

SC pickoff circuits that can measure changes in capacitance whilst inducing very low electronic noise in the range of hundreds of nano  $V/\sqrt{\text{Hz}}$  are reported [126-129]. A high-precision capacitive pickoff circuit in [126] comprises a SC pickoff, which employs correlated double sampling (CDS) to cancel  $1/f$  noise, amplifier offset, and compensated finite amplifier gain. This pickoff circuit also consists of a chopper stabiliser that cancels the offset because of switch mismatch [130].  $kT/C$  noise can also be cancelled, as reported in [131] [132], by sampling and by subtracting it from the pickoff output. The low noise SC pickoff circuit for capacitive MEMS sensor in [133] can also be used, as it provides a resolution of  $50\text{zF}/\sqrt{\text{Hz}}$ .

The capacitive MEMS velocity sensor can be integrated with an ASIC that consists of a pickoff circuit and a feedback control circuit. This approach enables the sensor to be secured with an interface and control circuit nearby. Hence, enhanced shielding reduces electromagnetic field interference (EMI) and other external noises.

### **7.2.2 Design Consideration of the Sensing Element**

To enable the sensor to measure low frequency velocity (below 300 Hz), the design of the sensor can be adjusted, so that the sensitivity of the secondary sensor increases. This can be done by shifting the first and second resonance frequencies to a lower frequency range. For example, the first resonance frequency can be shifted to below 1 kHz, and the second resonance can be shifted to around 1.5 kHz. This can be achieved by decreasing the spring constant and/or by increasing the proof mass. Nevertheless, although these procedures increase the sensitivity of the secondary sensor, the improvement comes at the expense of velocity sensor upper bandwidth limit.

As shown in Figure 7-1, the  $-180^\circ$  phase cross occurs at the second resonance frequency. Hence, the maximum feedback loop gain is proportional to the inverse of the amplitude

of the second resonance peak (as discussed in Section 4.6). Therefore, the stability of the feedback loop can be treated in a fashion similar to that applied in the two prototypes sensors, that is, by designing a low-pass filter that suppresses the peak of the second resonance.

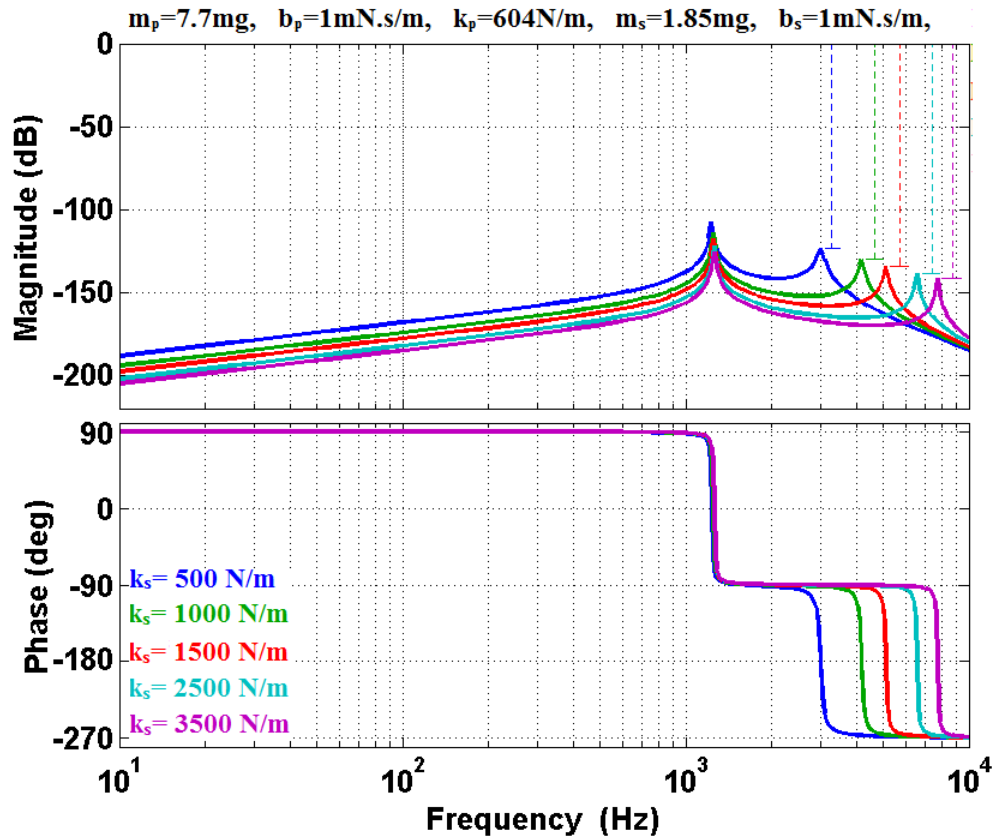


Figure 7-1: Simulated frequency response of the open-loop control function obtained by equation 4-22 and with different secondary spring values. The maximum feedback loop gain is determined by the second resonance frequency.

The detection of secondary proof mass displacement can also be improved by increasing the number of sense capacitors. However, such increase should be carefully studied by FEM analysis to avoid including unwanted modes, such as out-plane modes and buckling within the operational region.

The capacitive actuator of the principal sensor can be enhanced by increasing the overlap area of the capacitors, either with parallel plates or lateral comb plates. For this purpose, low excitation voltage is necessary to achieve the required damping force with low voltage. Given that the interface and control electronic circuit operates with a voltage of

## *Chapter 7: Conclusion and Future Work*

---

12 to 15 V, a preferable approach is to design a capacitive actuator that has an excitation voltage of the same range as system power.

As a result of redesigning the 2-DoF sensor, taking into account the above design parameters together with the enhanced pickoff circuit, the sensor is expected to operate from as low as the cut-off frequency of the real integrator (that is used in the internal feedback loop, for example 10 Hz) up to the first resonance frequency, i.e. 900 Hz.

# Appendices

## Appendix A

### A.1 Frequency Response Functions of the Input Acceleration and Electrostatic Force

```
% FRFs plot

clear all
clc

%Principal Sensor parameters
mp=1.103e-6;           %proof mass
bp=186.51e-6;         %damping coefficient
kp=188;                %spring constant
%Secondary Sensor parameters
ms=0.69807e-6;        %proof mass
bs1=3.3049e-9;        %damping coefficient
bs2=0.12418e-3;      %damping coefficient
ks=261;                %spring constant

MMp=mp;
MMs=ms;
AA1=tf([mp (bp+bs1) (kp+ks)], 1);
AA2=tf([bs1 ks], 1);
BB1=AA2;
BB2=tf([ms (bs1+bs2) ks], 1);

%%%%%%%%%%%% Acceleration FRFs %%%%%%%%%%%%%
%Principal sensor acceleration FRF (Gyacc), relative to
%base
Gyacc= minreal((MMp*BB2-MMs*BB1)/(AA1*BB2-AA2*BB1));

%Secondary sensor acceleration FRF (Gzacc), relative to
%base
Gzacc= minreal((MMs*AA1-MMp*AA2)/(AA1*BB2-AA2*BB1));

%Secondary sensor acceleration FRF (Gxacc), relative to
%principal proof mass
Gxacc=Gzacc-Gyacc;

%%%%%%%%%%%% Electrostatic force FRFs %%%%%%%%%%%%%
%Principal sensor Electrostatic force FRF (Gyacc), relative
%to base
Gyfele= minreal((BB2)/(AA1*BB2-AA2*BB1));

%Secondary sensor Electrostatic force FRF (Gzacc), relative
%to base
Gzfele= minreal((AA2)/(AA1*BB2-AA2*BB1));

%Secondary sensor Electrostatic force FRF (Gzacc), relative
%to principal proof mass
```

```
Gxfele=(Gzfele - Gyfele);
```

```
% FRFs Bode plot command  
P = bodeoptions;  
P.grid = 'on';  
P.XLim = [10 1e4];  
P.FreqUnits = 'Hz';  
P.PhaseUnits = 'deg';  
figure(10)  
bode(Gyfele, 'b', Gzfele, 'r', Gxfele, '-g', P)  
figure(20)  
bode(Gyacc, 'b', Gzacc, 'r', Gxacc, '-g', P)
```

## A.2 MATLAB Code of the Control Gain $g$ With Real Integrator

```

%% Control gain g Matlab code with real integrator
% Load lumped model parameter (mp, bp, kp, ms, bs1, bs2 and ks)
% from the corresponding sensor's parameters table. For sensor
% prototype-2, bs=bs1 and bs2=0

fc=10*2*pi; %Integrator cut-off frequency
Tau=1/fc; %Integrator time constant
Kint=1; %Integrator gain constant
Int_Real=tf(Kint,[Tau 1]); %Integrator transfer function

% Control gain g implementation
Fn4=(-mp*ms*Tau);
Fn3=(-mp*ms-mp*(bs1+bs2)*Tau-ms*bs1*Tau);
Fn2=(-mp*(bs1+bs2)-ms*bs1-mp*ks*Tau-ms*ks*Tau);

Fd5=(mp*ms*Tau);
Fd4=(mp*ms+ms*bs1*Tau+mp*(bs1+bs2)*Tau+bp*ms*Tau);
Fd3=(ms*bs1+mp*(bs1+bs2)+bp*ms+ms*ks*Tau+bs1*bs2*Tau+mp*ks*Tau+
p*(bs1+bs2)*Tau+ka*ms*Tau);
Fd0=ka*ks;

Fr1=ms*ks+bs1*bs2+mp*ks+bp*(bs1+bs2)+ka*ms+bs2*ks*Tau+bp*ks*Tau+
ka*(bs1+bs2)*Tau;
Fr2=-mp*ks-ms*ks;
Fr3=bs2*ks+bp*ks+ka*(bs1+bs2)+ka*ks*Tau;

index=0;

% Control gain g implementation from Start_freq (3000 Hz) down
% to End_freq (50 Hz)
Start_freq=3000;
End_freq=50;

% Loop function
for FREQ=Start_freq:-2:End_freq,
    w=2*pi*FREQ; % convert frequency into rad/sec

    % from equation 4-20, AA=a, BB=b and CC=c
    AA=(ms*Kint)^2*(w^2);
    BB=(Fn3*ms*Kint-ms*Kint*Fd4-Fn4*bs2*Kint)*(w^4)+(-
    Fr2*ms*Kint+Fr1*ms*Kint+Fn2*bs2*Kint)*(w^2)-(ms*Kint*Fd0);
    CC=-((Fn4*Fd5)*w^8+(Fn3*Fd4-Fn4*Fd3-Fn2*Fd5)*w^6+(Fn2*Fd3-
    Fn3*Fr1-Fr2*Fd4+Fn4*Fr3)*w^4+(Fn3*Fd0+Fr2*Fr1-
    Fn2*Fr3)*w^2+(Fr2*Fd0));
    % Solution of the quadratic formula in equation 4-21
    g_1=(-BB+sqrt(BB^2-4*AA*CC))/(2*AA);
    g_2=(-BB-sqrt(BB^2-4*AA*CC))/(2*AA);

    index=index+1;
    result(index, :) = [FREQ g_1 g_2];
end

```

```

% Control gain g plot
figure(2);
semilogx(result(:,1), result(:,2), result(:,1), result(:,3))
xlim([End_freq Start_freq])
hold on

% Extracting the maximum stable control gain, equation 4-22
MMp=mp;
MMS=ms;
AA1=tf([mp (bp+bs1) (kp+ks)], 1);
AA2=tf([bs1 ks], 1);
BB1=AA2;
BB2=tf([ms (bs1+bs2) ks], 1);

%%%%%%%%%% Electrostatic force FRFs %%%%%%%%%%%
%Principal sensor Electrostatic force FRF (Gyacc), relative
%to base
Gyfele= minreal((BB2)/(AA1*BB2-AA2*BB1));

%Secondary sensor Electrostatic force FRF (Gzacc), relative
%to base
Gzfele= minreal((AA2)/(AA1*BB2-AA2*BB1));

%Secondary sensor Electrostatic force FRF (Gzacc), relative
%to principal proof mass
Gxfele=(Gzfele - Gyfele);

% Open-loop control function with real integrator only
Gxfele_ol=minreal(Int_Real* Gxfele);
[Gm2, Pm2, Wcg2, Wcp2] = margin(Gxfele_ol);

% Maximum stable control gain plot
figure(2);
plot([End_freq Start_freq], [Gm2 Gm2], '-r');

```

### A.3 MATLAB Code of the Control Gain $g$ With Real Integrator and 2<sup>nd</sup> Order Low Pass Filter (LPF)

```

% Control gain g Matlab code with LPF2 and real integrator %%%
% Load lumped model parameter (mp, bp, kp, ms, bs1, bs2 and ks)
% from the corresponding sensor's parameters table. For sensor
% prototype-2, bs=bs1 and bs2=0

% Integrator transfer function
fc=10*2*pi; %Integrator cut-off frequency
Tau=1/fc; %Integrator time constant
Kint=1; %Integrator gain constant
Int_Real=tf(Kint, [Tau 1]); %Integrator transfer function

% LPF2 transfer function using resistor and capacitor value
R_LPF2=51e3; % resistor
C_LPF2=1e-9; % capacitor
P=R_LPF2*C_LPF2;
LPF2=tf(1, [P^2 2*P 1]); % LPF2 - 2nd order transfer function

% Control function
II= Int_Real* LPF2;

% Control gain g implementation
f4n=(-mp*ms*Tau);
f3n=(-mp*ms-mp*(bs1+bs2)*Tau-ms*bs1*Tau);
f2n=(-mp*(bs1+bs2)-ms*bs1-mp*ks*Tau-ms*ks*Tau);
f1na=(-mp*ks-ms*ks);
f1nb=(-ms*Kint*gs);

f5d=(mp*ms*Tau);
f4d=(mp*ms+ms*bs1*Tau+mp*(bs1+bs2)*Tau+bp*ms*Tau);
f3d=(ms*bs1+mp*(bs1+bs2)+bp*ms+ms*ks*Tau+bs1*bs2*Tau+mp*ks*Tau+
p*(bs1+bs2)*Tau+kp*ms*Tau);
f2da=(ms*ks+bs1*bs2+mp*ks+bp*(bs1+bs2)+kp*ms+bs2*ks*Tau+bp*ks*Ta
u+kp*(bs1+bs2)*Tau);
f2db=(ms*Kint*gs);
f1da=(bs2*ks+bp*ks+kp*(bs1+bs2)+kp*ks*Tau);
f1db=(bs2*Kint*gs);
f0d=kp*ks;

T2=f2da+2*f1da*P+f0d*P^2;
T1=f1da+2*f0d*P;

n6=f4n*P^2;
n5=2*f4n*P+f3n*P^2;
n4=f4n+2*f3n*P+f2n*P^2;
n3=f3n+2*f2n*P+f1na*P^2;
n2=f2n+2*f1na*P;
n1=f1na+f1nb;

d7=f5d*P^2;
d6=2*f5d*P+f4d*P^2;
d5=f5d+2*f4d*P+f3d*P^2;
d4=f4d+2*f3d*P+f2da*P^2;

```

```

d3=f3d+2*f2da*P+f1da*P^2;
d2=f2da+f2db+2*f1da*P+f0d*P^2;
d1=f1da+f1db+2*f0d*P;
d0=f0d;

% Control gain g implementation from Start_freq (2000 Hz) down
% to End_freq (50 Hz)
index=0;
Start_freq=2000;
End_freq=50;

% Loop function
for FREQ=Start_freq:-2:End_freq,
    w=2*pi*FREQ;          % convert frequency into rad/sec

    % from equation 4-20 with LPF2, AA=a, BB=b and CC=c
    AA=(ms*Kint)^2*(w^3);

    BB=n6*bs2*Kint*w^7-
    n5*ms*Kint*w^7+d6*ms*Kint*w^7+n3*ms*Kint*w^5-d4*ms*Kint*w^5-
    n4*bs2*Kint*w^5+n2*bs2*Kint*w^3-
    flna*ms*Kint*w^3+T2*ms*Kint*w^3-d0*ms*Kint*w;

    CC=(-n6*d7)*w^13+(n6*d5+n4*d7-n5*d6)*w^11+(n5*d4+n3*d6-
    n6*d3-n4*d5-n2*d7)*w^9+(n6*T1-n5*T2-d6*flna+n4*d3+n2*d5-
    n3*d4)*w^7+(n5*d0+n3*T2+d4*flna-n4*T1-n2*d3)*w^5+(n2*T1-
    n3*d0-flna*T2)*w^3+(d0*flna)*w;

    % Solution of the quadratic formula in equation 4-21
    g_1=(-BB+sqrt(BB^2-4*AA*CC))/(2*AA);
    g_2=(-BB-sqrt(BB^2-4*AA*CC))/(2*AA);

    index=index+1;
    result(index, :) = [FREQ g_1 g_2];
end

% Control gain g plot
figure(33);
plot(result(:,1), result(:,2),result(:,1), result(:,3))
hold on

% Extracting the maximum stable control gain, equation 4-22 with
% LPF2
MMp=mp;
MMs=ms;
AA1=tf([mp (bp+bs1) (kp+ks)], 1);
AA2=tf([bs1 ks], 1);
BB1=AA2;
BB2=tf([ms (bs1+bs2) ks], 1);

%%%%%%%%%%%% Electrostatic force FRFs %%%%%%%%%%%%%%
%Principal sensor Electrostatic force FRF (Gyacc), relative
%to base
Gyfele= minreal((BB2)/(AA1*BB2-AA2*BB1));

%Secondary sensor Electrostatic force FRF (Gzacc), relative

```

```

%to base
Gzfele= minreal((AA2)/(AA1*BB2-AA2*BB1));

%Secondary sensor Electrostatic force FRF (Gzacc), relative
%to principal proof mass
Gxfele=(Gzfele - Gyfele);

% Open-loop control function with real integrator and LPF2
Gxfele_ol=minreal(II* Gxfele);
[Gm2,Pm2,Wcg2,Wcp2] = margin(Gxfele_ol);

% Maximum stable control gain plot
xx=[0,Start_freq]; yy=[Gm,Gm];
figure(33)
plot (xx,yy, 'r')
text_handle = text(100,-result(index/2,2), sprintf('Gain margin
= %3.3E ',Gm));
hold off

```

## A.4 Open Loop Control Transfer Function Using Simulated and Measured FRF

```

% Open loop control function simulated and measured FRFs

clear all
clc

%%%%%%%%%%%%%%%%%%%%%%%%%%%%%%%%%%%%%%%%%%%%%%%%%%%%%%%%%%%%%%%%%%%%%%%%
load 'Measured_FRFs.mat';
% Each measured or theoretical data are arranged in an array as
% follows:
% Frequency (HZ) Magnitude (dB) Phase (deg) Complex (r+j.img)
% 1 Gxefm(1,2) Gxefm(1,3) Gxefm(1,4)
% 2 Gxefm(2,2) Gxefm(2,3) Gxefm(2,4)
% . . . .
% . . . .
% fmax Gxefm(fmax,1) Gxefm(fmax,3) Gxefm(fmax,4)
%%%%%%%%%%%%%%%%%%%%%%%%%%%%%%%%%%%%%%%%%%%%%%%%%%%%%%%%%%%%%%%%%%%%%%%%

% Load lumped model parameter (mp, bp, kp, ms, bs1, bs2 and ks)
% from the corresponding sensor's parameters table. For sensor
% prototype-2, bs=bs1 and bs2=0

%%%%%%%%%%%%%%%%%%%%%%%%%%%%%%%%%%%%%%%%%%%%%%%%%%%%%%%%%%%%%%%%%%%%%%%% control loop parameters %%%%%%%%%
% Integrator transfer function
fc=10*2*pi; %Integrator cut-off frequency
Tau=1/fc; %Integrator time constant
Kint=1; %Integrator gain constant
Int_Real=tf(Kint,[Tau 1]); %Integrator transfer function

% LPF2 transfer function using resistor and capacitor value
R_LPF2=51e3; % resistor
C_LPF2=1e-9; % capacitor
P=R_LPF2*C_LPF2;
LPF2=tf(1,[P^2 2*P 1]); % LPF2 - 2nd order transfer function

% Control loop function
II= Int_Real* LPF2;

%%%%%%%%%%%%%%%%%%%%%%%%%%%%%%%%%%%%%%%%%%%%%%%%%%%%%%%%%%%%%%%%%%%%%%%% Theoretical electrostatic force FRFs %%%%%%%%%
%Principal sensor Electrostatic force FRF (Gyacc), relative
%to base
Gyfele= minreal((BB2)/(AA1*BB2-AA2*BB1));

%Secondary sensor Electrostatic force FRF (Gzacc), relative
%to base
Gzfele= minreal((AA2)/(AA1*BB2-AA2*BB1));

%Secondary sensor Electrostatic force FRF (Gzacc), relative
%to principal proof mass
Gxfele=(Gzfele - Gyfele);

```

```

% Open-loop control function with real integrator and LPF2
Gxfele_ol=minreal(II* Gxfele);

%%%%%%%%%%%%%%%%%%%%%%%%%%%%%%%%%%%%%%%%%%%%%%%%%%%%%%%%%%%%%%%%%%%%%%%%
fmin=1;           % start frequency of measured data
fmax=4401;       % end frequency of measured data
ff=1:fmax;      % frequency array in Hz
ww=2*pi*ff;     % frequency array in rad/sec

%%%%%%%%%%%%%%%%%%%%%%%%%%%%%%%%%%%%%%%%%%%%%%%%%%%%%%%%%%%%%%%%%%%%%%%%
%%% Electrostatic force FRFs %%%%%%%%%
% Measured data are in Polar form (magnitude and phase), the
% following function extracts the equivalent Cartesian (real and
% imaginary)

% Secondary sensor theoretical (Gxeft) FRF Polar → Cartesian
[temp1,temp2]=bode(Gxfele,ww);
GxEft(:,1)=ff;           % Frequency array
GxEft(:,2)=20*log10(temp1(1,:)); % Magnitude array
GxEft(:,3)=temp2(1,:); % Phase array
for freq=1: fmax
    % extracting the Cartesian (real and imaginary) part
    [RL,IMG]= pol2cart(GxEft(freq,3)*pi/180,
        10^(GxEft(freq,2)/20));
    % Cartesian array (real + imaginary)
    GxEft(freq,4)=(RL+1j*IMG);
end

% Secondary sensor measured (Gxefm) FRF Polar → Cartesian
for freq=1: fmax
    % extracting the Cartesian (real and imaginary) part
    [RL,IMG]= pol2cart(GxEfm(freq,3)*pi/180,
        10^(GxEfm(freq,2)/20));
    % Cartesian array (real + imaginary)
    GxEfm(freq,4)=(RL+1j*IMG);
end

%%%%%%%%%%%%%%%%%%%%%%%%%%%%%%%%%%%%%%%%%%%%%%%%%%%%%%%%%%%%%%%%%%%%%%%%
%%%%%%%%%%%%%%%%%%%%%%%%%%%%%%%%%%%%%%%%%%%%%%%%%%%%%%%%%%%%%%%%%%%%%%%%
Open loop control function %%%%%%%%%
%%%%%%%%%%%%%%%%%%%%%%%%%%%%%%%%%%%%%%%%%%%%%%%%%%%%%%%%%%%%%%%%%%%%%%%%
%%%%%%%%%%%%%%%%%%%%%%%%%%%%%%%%%%%%%%%%%%%%%%%%%%%%%%%%%%%%%%%%%%%%%%%%

for freq=1:fmax
    % Frequency from Hz to rad/sec
    w=2*pi*freq;

    % Second order low pass filter
    LPF2_w=1/((1j*w*P)^2+(1j*w*2*P)+(1));

    % feedback control function= LPF2*Real_integrator
    Hctrl(freq)=LPF2_w*(Kint/(1+1j*w* Tau));

    %Measured open loop transfer function with no lowpass filter
    % and with an ideal integrator
    GyEFm_ol0(freq,4)=(1/(j*w))*GyEFm(freq,4);

```

```

%Theoretical open loop transfer function with no lowpass
% filter and with an ideal integrator
GyEFt_ol0(freq,4)=(1/(j*w))*GyEFt(freq,4);
%Measured open loop transfer function with no lowpass
% filter and with real integrator
GyEFm_ol1(freq,4)=(Kint/(1+1j*w*Tau))*GyEFm(freq,4);

%Theoretical open loop transfer function with no lowpass
% filter and with real integrator
GyEFt_ol1(freq,4)=(Kint/(1+1j*w*Tau))*GyEFt(freq,4);

%Measured open loop transfer function with LPF2
% and real integrator
GyEFm_ol2(freq,4)= Hctrl(freq)*GyEFm(freq,4);

% Theoretical open loop transfer function with LPF2
% and real integrator
GyEFt_ol2(freq,4)= Hctrl(freq)*GyEFt(freq,4);

%Measured open loop transfer function with no lowpass filter
%and with an ideal integrator
GyEFm_ol0(freq,1)= freq;
% Cartesian → Polar
[theta,rho]= cart2pol(real(GyEFm_ol0(freq,4)),
    imag(GyEFm_ol0(freq,4)));
GyEFm_ol0(freq,2)= 20*log10(rho);           % Magnitude
GyEFm_ol0(freq,3)= (theta*180/pi);        % Phase

%Theoretical open loop transfer function with no lowpass
% filter and with an ideal integrator
GyEFt_ol0(freq,1)= freq;
% Cartesian → Polar
[theta,rho]= cart2pol(real(GyEFt_ol0(freq,4)),
    imag(GyEFt_ol0(freq,4)));
GyEFt_ol0(freq,2)= 20*log10(rho);           % Magnitude
GyEFt_ol0(freq,3)= (theta*180/pi);        % Phase

%Measured open loop transfer function with no lowpass filter
%and with real integrator
GyEFm_ol1(freq,1)= freq;
% Cartesian → Polar
[theta,rho]= cart2pol(real(GyEFm_ol1(freq,4)),
    imag(GyEFm_ol1(freq,4)));
GyEFm_ol1(freq,2)= 20*log10(rho);           % Magnitude
GyEFm_ol1(freq,3)= (theta*180/pi);        % Phase

% Theoretical open loop transfer function with no lowpass
% filter and with real integrator
GyEFt_ol1(freq,1)= freq;
% Cartesian → Polar
[theta,rho]= cart2pol(real(GyEFt_ol1(freq,4)),
    imag(GyEFt_ol1(freq,4)));
GyEFt_ol1(freq,2)= 20*log10(rho);           % Magnitude
GyEFt_ol1(freq,3)= (theta*180/pi);        % Phase

```

```

    %Measured open loop transfer function with LPF2
    %and real integrator
    GyEFm_ol2(freq,1)= freq;
    % Cartesian → Polar
    [theta,rho]= cart2pol(real(GyEFm_ol2(freq,4)),
        imag(GyEFm_ol2(freq,4)));
    GyEFm_ol2(freq,2)= 20*log10(rho);        % Magnitude
    GyEFm_ol2(freq,3)= (theta*180/pi);      % Phase

    %Theoretical open loop transfer function with LPF2
    %and real integrator
    GyEft_ol2(freq,1)= freq;
    % Cartesian → Polar
    [theta,rho]= cart2pol(real(GyEft_ol2(freq,4)),
        imag(GyEft_ol2(freq,4)));
    GyEft_ol2(freq,2)= 20*log10(rho);        % Magnitude
    GyEft_ol2(freq,3)= (theta*180/pi);      % Phase
end

%%% Measured and theoretical open loop transfer function with
%%% ideal integrator only
figure(1);
subplot(2,1,2)
semilogx(GyEFm_ol0(:,1), GyEFm_ol0(:,2),'r','LineWidth',2);
grid on
hold on
subplot(2,1,2)
semilogx(GyEFm_ol0(:,1), GyEFm_ol0(:,3),'r','LineWidth',2);
grid on
hold on

subplot(2,1,1)
semilogx(GyEft_ol0(:,1), GyEft_ol0(:,2),'-b','LineWidth',2);
set(gca,'FontSize',14,'FontWeight','bold');
title('Open loop sensor-actuator transfer function ideal
    integrator');
ylabel('Mag (dB)')
grid on

subplot(2,1,2)
semilogx(GyEft_ol0(:,1),GyEft_ol0(:,3),'-b','LineWidth',2);
set(gca,'YTick',[-180:90:180],'FontSize',14,
    'FontWeight','bold');
legend('Measured','Simulated','Location','SouthWest');
ylabel('Phase (deg)')
xlabel('Frequency (Hz)')
grid on

%%% Measured and theoretical open loop transfer function with
%%% real integrator only
figure(2);
subplot(2,1,2)
semilogx(GyEFm_ol1(:,1), GyEFm_ol1(:,2),'r','LineWidth',2);
grid on
hold on
subplot(2,1,2)

```

```

semilogx(GyEFm_ol1(:,1), GyEFm_ol1(:,3), 'r', 'LineWidth', 2);
grid on
hold on

subplot(2,1,1)
semilogx(GyEFt_ol1(:,1), GyEFt_ol1(:,2), '-.b', 'LineWidth', 2);
set(gca, 'FontSize', 14, 'FontWeight', 'bold');
title('Open loop sensor-actuator transfer function with Real
      Integrator');
ylabel('Mag (dB)')
grid on

subplot(2,1,2)
semilogx(GyEFt_ol1(:,1), GyEFt_ol1(:,3), '-.b', 'LineWidth', 2);
set(gca, 'YTick', [-180:90:180], 'FontSize', 14,
      'FontWeight', 'bold');
legend('Measured', 'Simulated', 'Location', 'SouthWest');
ylabel('Phase (deg)')
xlabel('Frequency (Hz)')
grid on

%%% Measured and theoretical open loop transfer function with
%%% LPF2 and real integrator
figure(3);
subplot(2,1,2)
semilogx(GyEFm_ol2(:,1), GyEFm_ol2(:,2), 'r', 'LineWidth', 2);
grid on
hold on
subplot(2,1,2)
semilogx(GyEFm_ol2(:,1), GyEFm_ol2(:,3), 'r', 'LineWidth', 2);
grid on
hold on

subplot(2,1,1)
semilogx(GyEFt_ol2(:,1), GyEFt_ol1(:,2), '-.b', 'LineWidth', 2);
set(gca, 'FontSize', 14, 'FontWeight', 'bold');
title('Open loop sensor-actuator transfer function with Real
      Integrator and LPF2');
ylabel('Mag (dB)')
grid on

subplot(2,1,2)
semilogx(GyEFt_ol2(:,1), GyEFt_ol2(:,3), '-.b', 'LineWidth', 2);
set(gca, 'YTick', [-180:90:180], 'FontSize', 14,
      'FontWeight', 'bold');
legend('Measured', 'Simulated', 'Location', 'SouthWest');
ylabel('Phase (deg)')
xlabel('Frequency (Hz)')
grid on

```

## A.5 Post Process for Closed Loop Prediction Using Simulated and Measured FRF

```

% Velocity sensor open- and closed-loop offline simulated and
% measured results

clear all
clc

%%%%%%%%%%%%%%%%%%%%%%%%%%%%%%%%%%%%%%%%%%%%%%%%%%%%%%%%%%%%%%%%%%%%%%%%
% Load measurement file
load 'Measured_FRFs.mat';
% Each measured or theoretical data are arranged in an array as
% follows:
% Frequency (HZ) Magnitude (dB) Phase (deg) Complex (r+j.img)
% 1 Gxefm(1,2) Gxefm(1,3) Gxefm(1,4)
% 2 Gxefm(2,2) Gxefm(2,3) Gxefm(2,4)
% . . . .
% . . . .
% fmax Gxefm(fmax,1) Gxefm(fmax,3) Gxefm(fmax,4)
%%%%%%%%%%%%%%%%%%%%%%%%%%%%%%%%%%%%%%%%%%%%%%%%%%%%%%%%%%%%%%%%%%%%%%%%

% Load lumped model parameter (mp, bp, kp, ms, bs1, bs2 and ks)
% from the corresponding sensor's parameters table. For sensor
% prototype-2, bs=bs1 and bs2=0

% Start and end frequency range

fmin=1;
fmax=6400;
ff=1:fmax;
ww=2*pi*ff;

%%%%%%%% Control gain g %%%%
g=32.22e3; % control gain for theoretical simulation
gm=g; % Control gain for experimental simulation

%%%%%%%%%%%%%%%%%%%%%%%%%%%%%%%%%%%%%%%%%%%%%%%%%%%%%%%%%%%%%%%%%%%%%%%% Theoretical FRFs %%%%%%%%%
AA1=tf([mp (bp+bs) (kp+ks)], 1);
AA2=tf([bs ks], 1);
BB1=tf([bs ks], 1);
BB2=tf([ms bs ks], 1);

%%%%%%%%%%%%%%%%%%%%%%%%%%%%%%%%%%%%%%%%%%%%%%%%%%%%%%%%%%%%%%%%%%%%%%%% Acceleration FRFs %%%%%%%%%
%Principal sensor acceleration FRF (Gyacc), relative to
%base
Gyacc= minreal((MMp*BB2-MMs*BB1)/(AA1*BB2-AA2*BB1));

%Secondary sensor acceleration FRF (Gzacc), relative to
%base
Gzacc= minreal((MMs*AA1-MMp*AA2)/(AA1*BB2-AA2*BB1));

```

```

%Secondary sensor acceleration FRF (Gxacc), relative to
%principal proof mass
Gxacc=Gzacc-Gyacc;

%%%%%%%%%% Electrostatic force FRFs %%%%%%%%%%%
%Principal sensor Electrostatic force FRF (Gyacc), relative
%to base
Gyfele= minreal((BB2)/(AA1*BB2-AA2*BB1));

%Secondary sensor Electrostatic force FRF (Gzacc), relative
%to base
Gzfele= minreal((AA2)/(AA1*BB2-AA2*BB1));

%Secondary sensor Electrostatic force FRF (Gzacc), relative
%to principal proof mass
Gxfele=(Gzfele - Gyfele);

%%%%%%%%%%%%%%%%%%%%%%%%%%%%%%%%%%%%%%%%%%%%%%%%%%%%%%%%%%%%%%%%%%%%%%%%
% Theoretical Gxfs Polar → Cartesian
[temp1,temp2]=bode(Gxfele,ww);
GxEft(:,1)=ff;
GxEft(:,2)=20*log10(temp1(1,:));
GxEft(:,3)=temp2(1,:);
for freq=1:fmax
    [RL,IMG]=
pol2cart(GxEft(freq,3)*pi/180,10^(GxEft(freq,2)/20));
    GxEft(freq,4)=(RL+1j*IMG);
end

%%%%%%%%%%%%%%%%%%%%%%%%%%%%%%%%%%%%%%%%%%%%%%%%%%%%%%%%%%%%%%%%%%%%%%%%
% Theoretical Gyfs Polar → Cartesian
[temp1,temp2]=bode(Gyfele,ww);
GyEft(:,1)=ff;
GyEft(:,2)=20*log10(temp1(1,:));
GyEft(:,3)=temp2(1,:);
for freq=1:fmax
    [RL,IMG]= pol2cart(GyEft(freq,3)*pi/180,
    10^(GyEft(freq,2)/20));
    GyEft(freq,4)=(RL+1j*IMG);
end

%%%%%%%%%%%%%%%%%%%%%%%%%%%%%%%%%%%%%%%%%%%%%%%%%%%%%%%%%%%%%%%%%%%%%%%%
% Theoretical Gzfs Polar → Cartesian
[temp1,temp2]=bode(Gzfele,ww);
GzEft(:,1)=ff;
GzEft(:,2)=20*log10(temp1(1,:));
GzEft(:,3)=temp2(1,:);
for freq=1:fmax
    [RL,IMG]= pol2cart(GzEft(freq,3)*pi/180,
    10^(GzEft(freq,2)/20));
    GzEft(freq,4)=(RL+1j*IMG);
end

%%%%%%%%%%%%%%%%%%%%%%%%%%%%%%%%%%%%%%%%%%%%%%%%%%%%%%%%%%%%%%%%%%%%%%%%
% Theoretical Gxacc Polar → Cartesian
[temp1,temp2]=bode(Gxaccl,ww);

```

```

GxAcct(:,1)=ff;
GxAcct(:,2)=20*log10(temp1(1,:));
GxAcct(:,3)=temp2(1,:);
for freq=1:fmax
    [RL, IMG]= pol2cart(GxAcct(freq,3)*pi/180,
        10^(GxAcct(freq,2)/20));
    GxAcct(freq,4)=(RL+1j*IMG);
end

%%%%%%%%%%%%%%%%%%%%%%%%%%%%%%%%%%%%%%%%%%%%%%%%%%%%%%%%%%%%%%%%%%%%%%%%
% Theoretical Gyacc Polar → Cartesian
[temp1,temp2]=bode(Gyaccl,ww);
GyAcct(:,1)=ff;
GyAcct(:,2)=20*log10(temp1(1,:));
GyAcct(:,3)=temp2(1,:);
for freq=1:fmax
    [RL, IMG]= pol2cart(GyAcct(freq,3)*pi/180,
        10^(GyAcct(freq,2)/20));
    GyAcct(freq,4)=(RL+1j*IMG);
end

%%%%%%%%%%%%%%%%%%%%%%%%%%%%%%%%%%%%%%%%%%%%%%%%%%%%%%%%%%%%%%%%%%%%%%%%
% Theoretical Gzacc Polar → Cartesian
[temp1,temp2]=bode(Gzaccl,ww);
GzAcct(:,1)=ff;
GzAcct(:,2)=20*log10(temp1(1,:));
GzAcct(:,3)=temp2(1,:);
for freq=1:fmax
    [RL, IMG]= pol2cart(GzAcct(freq,3)*pi/180,
        10^(GzAcct(freq,2)/20));
    GzAcct(freq,4)=(RL+1j*IMG);
end

%%%%%%%%%%%%%%%%%%%%%%%%%%%%%%%%%%%%%%%%%%%%%%%%%%%%%%%%%%%%%%%%%%%%%%%%
% Measured GxEF Polar → Cartesian
for freq=1:fmax
    [RL, IMG]= pol2cart(GxEFm(freq,3)*pi/180,
        10^(GxEFm(freq,2)/20));
    GxEFm(freq,4)=(RL+1j*IMG);
End

%%%%%%%%%%%%%%%%%%%%%%%%%%%%%%%%%%%%%%%%%%%%%%%%%%%%%%%%%%%%%%%%%%%%%%%%
% Measured GyEF Polar → Cartesian
for freq=1:fmax
    [RL, IMG]= pol2cart(GyEFm(freq,3)*pi/180,
        10^(GyEFm(freq,2)/20));
    GyEFm(freq,4)=(RL+1j*IMG);
end

%%%%%%%%%%%%%%%%%%%%%%%%%%%%%%%%%%%%%%%%%%%%%%%%%%%%%%%%%%%%%%%%%%%%%%%%
% Measured GxAcc Polar → Cartesian
for freq=1:fmax
    [RL, IMG]= pol2cart(GxAccm(freq,3)*pi/180,
        10^(GxAccm(freq,2)/20));

```

```

GxAccm(freq,4)=(RL+1j*IMG);

%%%%%%%%%%%%%%%%%%%%%%%%%%%%%%%%%%%%%%%%%%%%%%%%%%%%%%%%%%%%%%%%%%%%%%%%
% Measured GyAcc Polar → Cartesian
[RL,IMG]= pol2cart(GyAccm(freq,3)*pi/180,
10^(GyAccm(freq,2)/20));
GyAccm(freq,4)=(RL+1j*IMG);
end

% Differentiation in time domain is (d/dt), in Laplace multiply
% by s and in frequency domain multiply by jww=jf*2*pi

def=1j*ww'; %Differentiation array

GxVelm=GxAccm(:,4).* def; %Measured velocity of the
%secondary sensor GxAcc*diff=GxVel

GxVelt=GxAcct(:,4).* def; ; %Theoretical velocity of the
%secondary sensor GxAcc*diff=GxVel

GyVelm=GyAccm(:,4).* def; ; %Measured velocity of the
%principal sensor GyAcc*diff=GyVel

GyVelt=GyAcct(:,4).* def; ; %Theoretical velocity of the
%principal sensor GyAcc*diff=GyVel

%%%%%%%%%%%%%%%%%%%%%%%%%%%%%%%%%%%%%%%%%%%%%%%%%%%%%%%%%%%%%%%%%%%%%%%%
%%%%%%%%%%%%%%%%%%%%%%%%%%%%%%%%%%%%%%%%%%%%%%%%%%%%%%%%%%%%%%%%%%%%%%%%
Offline open- and closed loop simulation %%%%%%%%%
using simulated and experimental measurement %%%%%%%%%
%%%%%%%%%%%%%%%%%%%%%%%%%%%%%%%%%%%%%%%%%%%%%%%%%%%%%%%%%%%%%%%%%%%%%%%%
%%%%%%%%%%%%%%%%%%%%%%%%%%%%%%%%%%%%%%%%%%%%%%%%%%%%%%%%%%%%%%%%%%%%%%%%
control loop parameters %%%%%%%%%
% Integrator transfer function
fc=10*2*pi; %Integrator cut-off frequency
Tau=1/fc; %Integrator time constant
Kint=1; %Integrator gain constant
Int=tf(Kint,[Tau 1]); %Integrator transfer function

% LPF2 transfer function using resistor and capacitor value
R_LPF2=51e3; % resistor
C_LPF2=1e-9; % capacitor
Pp=R_LPF2*C_LPF2;
LPF2=tf(1,[Pp^2 2*Pp 1]); %2nd order LPF transfer function

% Control loop function
II= Int* LPF2;

% Start of the offline data post process
%%%%%%%%%%%%%%%%%%%%%%%%%%%%%%%%%%%%%%%%%%%%%%%%%%%%%%%%%%%%%%%%%%%%%%%%
for freq=1:fmax
%Frequency from Hz to rad/sec
w=2*pi*freq;

% Second order low pass filter
LPF2_w=1/((1j*w*Pp)^2+(1j*w*2*Pp)+(1));

```

```

% feedback control function= LPF2*Real_integrator
Hctrl(freq)=LPF2_w*(Kint/(1+1j*w*Tau));

% Offline post process with experimental measurement
%%%%%%%%%%%%%%%%%%%%%%%%%%%%%%%%%%%%%%%%%%%%%%%%%%%%%%%%%%%%%%%%%%%%%%%%
% Velocity sensor equation 4-16 (right part only)
Gy_wclm_1(freq,1)=(gm*Hctrl(freq)*GxVelm(freq))/
                (1-gm*Hctrl(freq)*GxEFm(freq,4));

% Velocity sensor equation 4-16 (full)
Gy_wclm(freq,4)= GyVelm(freq)+GyEFm(freq,4)*
                Gy_wclm_1(freq,1);

% save frequency in the function array
Gy_wclm(freq,1)= freq;

% Cartesian → Polar
[theta,rho]= cart2pol(real(Gy_wclm(freq,4)),
                    imag(Gy_wclm(freq,4)));
Gy_wclm(freq,2)= 20*log10(rho);
Gy_wclm(freq,3)= (theta*180/pi);

% Offline post process with theoretical measurement
%%%%%%%%%%%%%%%%%%%%%%%%%%%%%%%%%%%%%%%%%%%%%%%%%%%%%%%%%%%%%%%%%%%%%%%%
% Velocity sensor equation 4-16 (right part only)
Gy_wclt_1(freq,1)=(g*Hctrl(freq)*GxVelt(freq))/
                (1-g*Hctrl(freq)*GxEft(freq,4));

% Velocity sensor equation 4-16 (full)
Gy_wclt(freq,4)= GyVelt(freq)+GyEft(freq,4)*
                Gy_wclt_1(freq,1);

% save frequency in the function array
Gy_wclt(freq,1)= freq;

% Cartesian → Polar
[theta,rho]= cart2pol(real(Gy_wclt(freq,4)),
                    imag(Gy_wclt(freq,4)));
Gy_wclt(freq,2)= 20*log10(rho);
Gy_wclt(freq,3)= (theta*180/pi);

end

%%%%%%%%%%%%%%%%%%%%%%%%%%%%%%%%%%%%%%%%%%%%%%%%%%%%%%%%%%%%%%%%%%%%%%%% Plotting Gxwcl and Gxfs %%%%%%%%%
figure(501);
clf
subplot(2,1,1)
semilogx(Gy_wclm(:,1), Gy_wclm(:,2), 'r', 'LineWidth',2);
set(gca, 'FontSize',14, 'FontWeight', 'bold');
hold on;
title('Closed loop velocity sensor response ----> g=32.22k')
xlim([100 4000])
hold on;
subplot(2,1,1)
semilogx(Gy_wclt(:,1), Gy_wclt(:,2), '-.b', 'LineWidth',2);
ylim([-110 -40])
set(gca, 'YTick', [-130:10:-40], 'FontSize',18,

```

```
'FontWeight','bold');
grid on

subplot(2,1,2)
semilogx(Gy_wclm(:,1),Gy_wclm(:,3),'r','LineWidth',2);
xlim([100 4000])
hold on;
subplot(2,1,2)
semilogx(Gy_wclt(:,1),Gy_wclt(:,3),'-b','LineWidth',2);
hold on;
set(gca,'YTick',[-180:90:180],'FontSize',18,
'FontWeight','bold');
grid on
```

## **Appendix B**

### **B.1 First Prototype PCB**



## **B.2 Second Prototype PCB**



# Appendix C

## C.1 Lithography

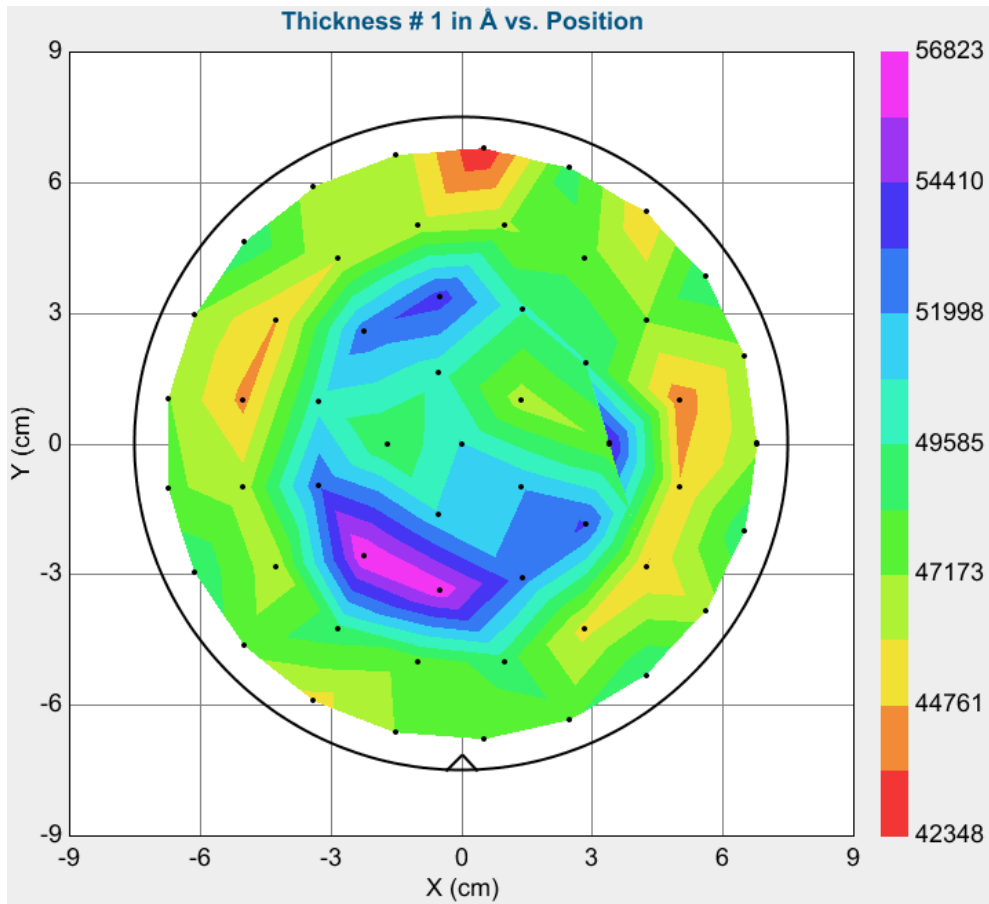
The lithography process used with the Si test wafers and the SOI wafer was developed by the Southampton Nanofabrication Centre [134]. It was adopted and further developed in this fabrication process. The lithography steps are as follows:

- 1- The wafer was first cleaned by immersing it in Nitric acid for 5 min, to ensure no organic contamination left. Then, the wafer was rinsed with DI water and spin dried.
- 2- The wafer was then dipped in buffered HF (20:1) for around 1 min to remove any SiO<sub>2</sub> formed layer on the silicon surface. Then, the wafer was rinsed with DI water and spin dried.
- 3- Before applying the photoresist (PR), the wafer was dehydrated in a hot oven at 120°C for 30 min.
- 4- Spin coat and bake a TI-Prime to enhance PR adhesion, as follows:
  - a. Spine with a speed at 3000 rpm for 20 sec, and then 100 rpm for 1 sec.
  - b. Soft bake at 120°C for 2 min.
- 5- The AZ9260 photoresist was immediately applied to the wafer as follows:
  - a. The target thickness of the PR was about 5µm, therefore the spinning speed was set as follows:

	<i>Start up</i>	<i>Main</i>	<i>Slow down</i>	<i>Stop</i>
<i>Spinning speed (rpm)</i>	400	4000	400	0
<i>Acceleration (m/sec<sup>2</sup>)</i>	200	1200	1200	200
<i>Rise time (sec)</i>	2	3	2	2
<i>Spin time (sec)</i>	7	30	2	0

Table C-1: Spinning speed of the AZ9260 photoresist.

- b. Soft bake the PR at 110°C for 2 min and 30 sec.
- c. Rehydrate the PR for 30 min before exposure.
- d. The PR thickness was measured using the Woolham M-2000 spectroscopic ellipsometer [135]. The average thickness of the PR was 4.9µm, as shown in the below figure.



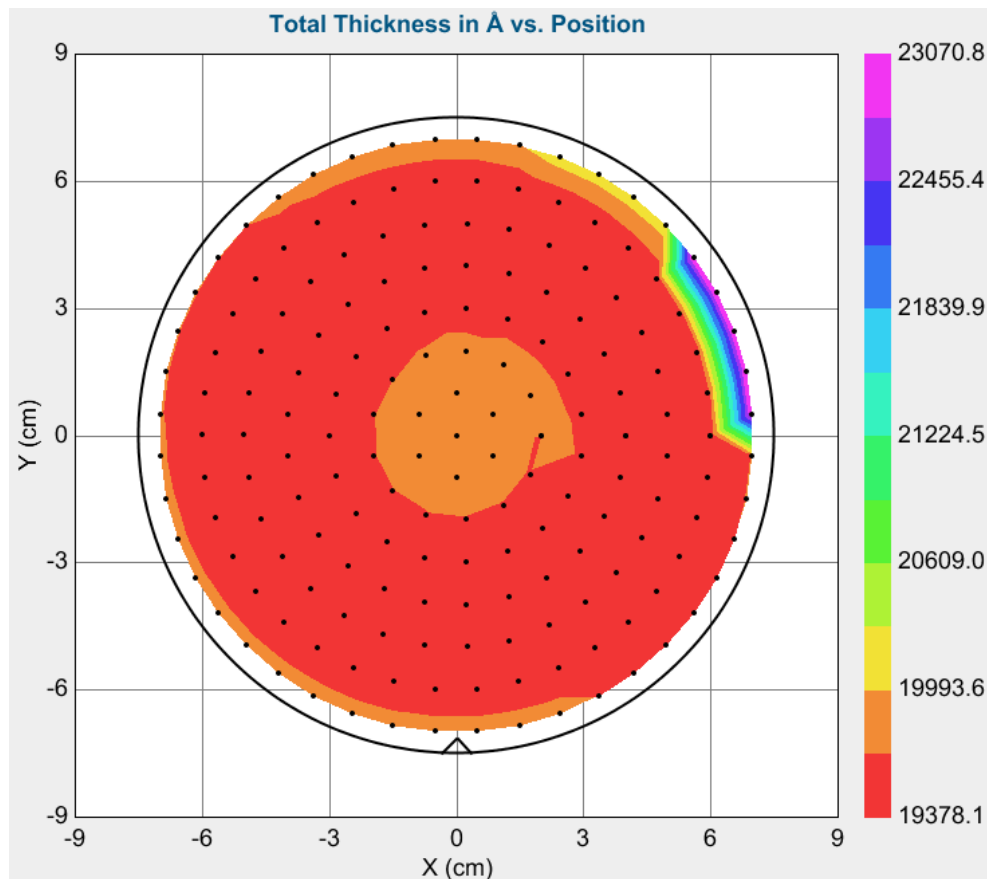
- e. The PR exposure was performed using the EVG 620TB double sided mask aligner [136] with no I-line filter. The PR of the hard masks was exposed to 8.5 sec, while the soft mask of the handle layer was exposed to 13 sec.
- f. The PR is then developed in AZ400K (1:4) for 4:30-5:00 minutes.

## C.2 SiO<sub>2</sub> Layer Coating Using PECVD

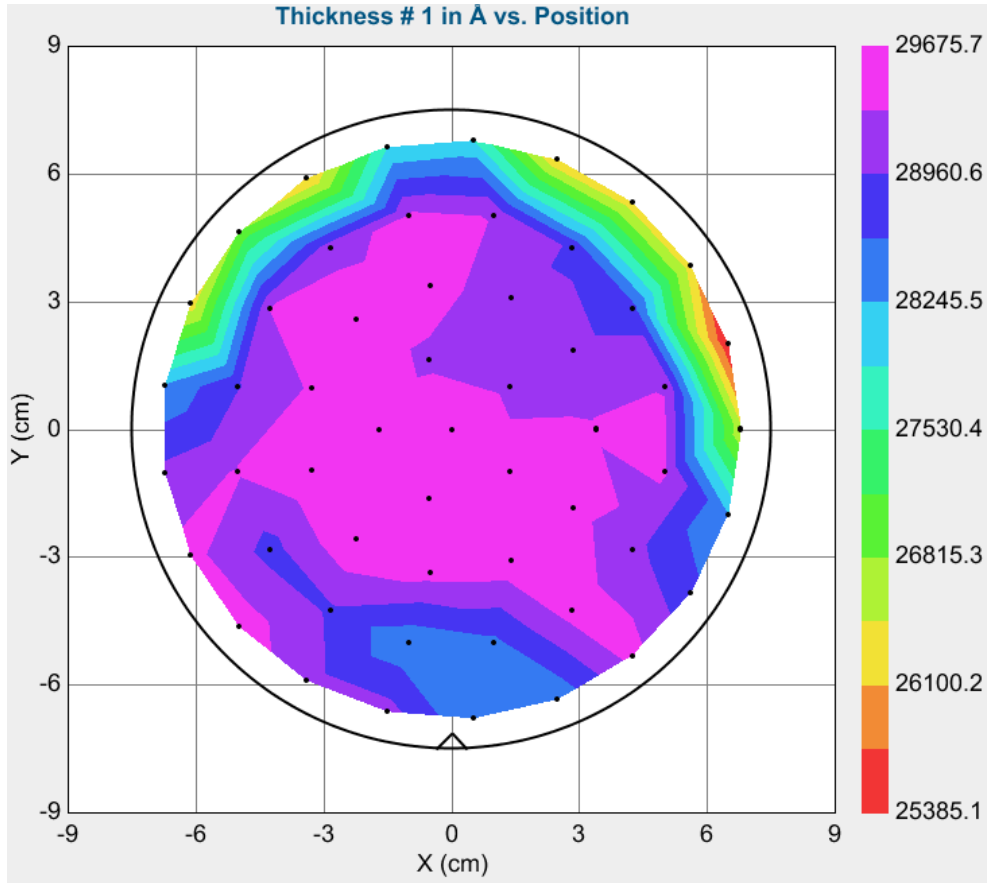
The oxford instruments plasmalab system 100 for PECVD [137] was used to produce a SiO<sub>2</sub> layer on the device layer (~2μm) and handle layer (~3μm) of the SOI. The PECVD system was set as follows:

<i>Parameter</i>	<i>Value</i>	<i>unit</i>
<i>Table temperature</i>	350	°C
<i>Chamber pressure</i>	1000	mTorr
<i>RF Power</i>	20	Watt
<i>SiH<sub>4</sub></i>	4.2	sccm
<i>N<sub>2</sub>O</i>	350	sccm
<i>N<sub>2</sub></i>	80	sccm

In order to form a layer around 2μm thickness on the device layer, the PECVD process performed for 33 min and 16 sec. The SiO<sub>2</sub> thickness was measured as shown below.



While the PECVD performed for 50 min to form a layer around  $3\mu\text{m}$  on the handle layer of the SOI wafer. The  $\text{SiO}_2$  thickness was measured as shown below.

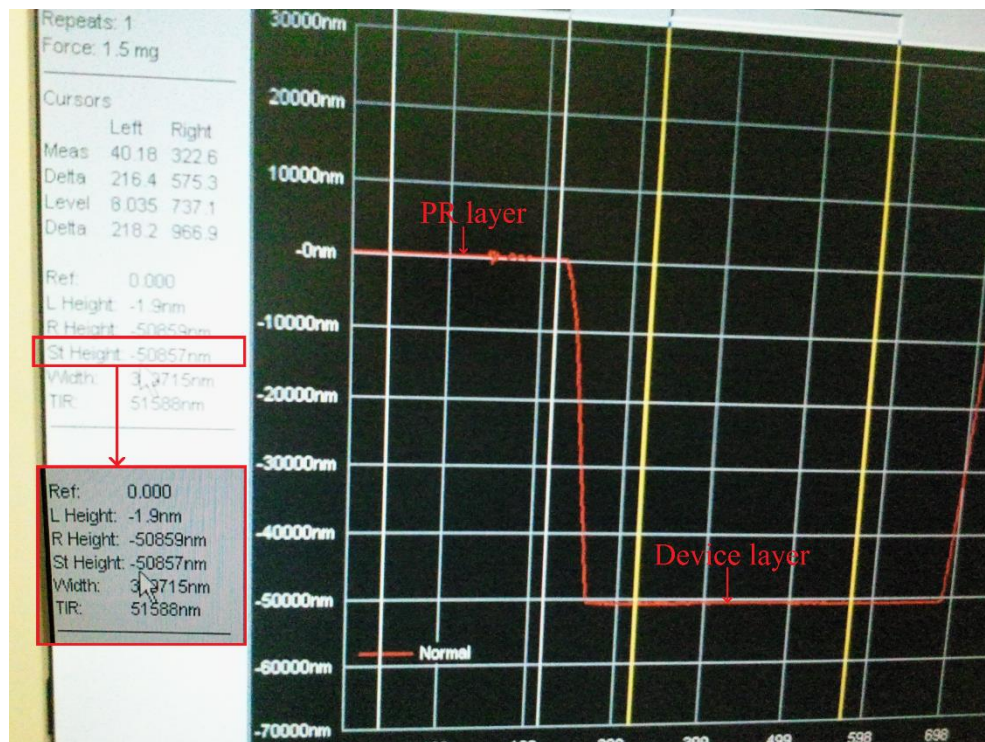


### C.3 Hard Mask SiO<sub>2</sub> Etch Using ICP Etching

The dielectric ICP etch tool OPIT SYS380 [138] was used to etch the SiO<sub>2</sub> layer on the device and handle layer to obtain the hard mask. The ICP system was set as follows:

<i>Parameter</i>	<i>Value</i>	<i>unit</i>
<i>Temperature</i>	15	°C
<i>Chamber pressure</i>	7	mTorr
<i>RF power</i>	100	Watt
<i>ICP power</i>	1500	Watt
<i>C4F8</i>	32	scm
<i>O2</i>	8.5	scm
<i>CHF3</i>	37.4	scm

The etch time required for 2 $\mu$ m SiO<sub>2</sub> layer was 10 min and 30 sec, while for the 3 $\mu$ m was about 16 min. After a complete etch of the handle layer hard mask, the profilometer tool was used to measure the feature thickness. The PR was etched during the ICP process and around 2 $\mu$ m was remaining on top of the 3 $\mu$ m SiO<sub>2</sub> layer, as shown in the figure below the total layer above the device layer is 5.08 $\mu$ m.



## C.4 DRIE of the Device Layer

The DRIE process for the SOI wafer was performed using the Plasma-Therm's VERSALINE tool [139]. The tool performs the time-multiplexed DRIE Bosch process, which is accomplished by repeating three steps [84] [140]:

- 1- Deposition: a passivation layer is deposited to protect the sidewalls from lateral Si etch.
- 2- Etch – A: this step to remove the passivation layer accumulated at the bottom of the trench.
- 3- Etch – B: this step to etch the exposed area of silicon.

The device layer DRIE run time was 55 min. The parameter of the DRIE process were set as follows:

	<i>Deposition</i>	<i>Etch – A</i>	<i>Etch – B</i>
<i>Time (sec)</i>	2	1.5	2
<i>Pressure (mTorr)</i>	25	40	40
<i>C4F8 (sccm)</i>	150	150	150
<i>SF6 (sccm)</i>	150	150	150
<i>Ar (sccm)</i>	30	30	30
<i>LF Bias (V)</i>	10	350-550 (0.8)	10
<i>ICP (Watt)</i>	2000	2000	25000
<i>Temperature (°C)</i>	15	15	15

## C.5 DRIE of the Handle Layer Using Soft Mask

The Handle layer DRIE run time was 77 min. The parameter of the DRIE process were set as follows:

	<i>Deposition</i>	<i>Etch – A</i>	<i>Etch – B</i>
<i>Time (sec)</i>	2	1.5	2
<i>Pressure (mTorr)</i>	25	40	80
<i>C4F8 (sccm)</i>	150	150	150
<i>SF6 (sccm)</i>	150	150	350
<i>Ar (sccm)</i>	30	30	30
<i>LF Bias (V)</i>	10	250-450 (0.1)	10
<i>ICP (Watt)</i>	2000	2000	25000
<i>Temperature (°C)</i>	15	15	15

## C.6 DRIE of the Handle Layer Using Hard Mask

The Handle layer last DRIE run time was 45 min. The parameter of the DRIE process were set as follows:

	<i>Deposition</i>	<i>Etch – A</i>	<i>Etch – B</i>
<i>Time (sec)</i>	2	1.5	2
<i>Pressure (mTorr)</i>	25	40	80
<i>C4F8 (sccm)</i>	150	150	150
<i>SF6 (sccm)</i>	150	150	350
<i>Ar (sccm)</i>	30	30	30
<i>LF Bias (V)</i>	10	500-950 (0.1)	10
<i>ICP (Watt)</i>	2000	2000	25000
<i>Temperature (°C)</i>	15	15	15

---

## List of References

- [1] Khoshnoud, F., de Silva, C.W., “Recent advances in MEMS sensor technology – mechanical applications,” *IEEE Instrumentation & Measurement Magazine*, vol. 15, no. 2, pp. 14-24, February 2012.
- [2] Perlmutter, M., Robin, L., “High-performance, low cost inertial MEMS: A market in motion!,” *IEEE/ION Position Location and Navigation Symposium (PLANS)*, pp. 225-229, 23-26 April 2012.
- [3] Stauffer, J. -M, Dietrich, O., Dutoit, B., “RS9000, a novel MEMS accelerometer family for Mil/Aerospace and safety critical applications,” *Position Location and Navigation Symposium (PLANS), 2010 IEEE/ION*, pp. 1-5, 4-6 May 2010.
- [4] Tadigadapa, S., Mateti, K., “Piezoelectric MEMS sensors: State-of-the-art and perspectives,” *Measurement Science and Technology*, vol. 20, no. 9, p. 30, Sept. 2009.
- [5] Bogue, R., “Recent developments in MEMS sensors: A review of applications, markets and technologies,” *Sensor Review*, vol. 33, no. 4, pp. 300-304, 2013.
- [6] Bryzek, J., Roundy, S., Bircumshaw, B., Chung, C., Castellino, K., Stetter, J. R., Vestel, M., “Marvelous MEMS,” *IEEE Circuits and Devices Magazine*, vol. 22, no. 2, pp. 8-28, March March-April 2006.
- [7] Sutton, T.J., Elliott, S.J., McDonald, A.M., Saunders, T.J., “Active control of road noise inside vehicles,” *Noise Control Engineering Journal*, vol. 42, no. 4, pp. 137-146, July-Aug. 1994.
- [8] Oh, S., Kim, H., Park, Y., “Active control of road booming noise in automotive interiors,” *Journal of the Acoustical Society of America*, vol. 111, no. 1, pp. 180-188, Jan. 2002.

- [9] Duan, J., Li, M., Lim, T., Lee, M., Vanhaaften, W., Cheng, M., Abe, T., “Active control of vehicle transient power train noise using a twin- FXLMS algorithm,” *Journal of Dynamic Systems, Measurement and Control*, vol. 133, pp. 034501-(1-4), May 2011.
- [10] Duan, J., Li, M., Lim, T., Lee, M., Cheng, M., Vahaaften, W., Abe, T., “Combined feedforward–feedback active control of road noise inside a vehicle cabin,” *Journal of Vibration and Acoustics*, vol. 136, pp. 041020-(1-8), Aug. 2014.
- [11] Fuller, C.R., Elliott, S.J., Nelson, P.A., *Active control of vibration*, London: Academic Press, 1996.
- [12] Gardonio, P., “Review of active techniques for aerospace vibro-acoustic control,” *Journal of Aircraft*, vol. 39, no. 2, pp. 206-214, March-April 2002.
- [13] Elliott, S., “A review of active noise and vibration control in road vehicles,” Technical Memorandum No 981, Southampton - United Kingdom, Dec. 2008.
- [14] Preumont, A., *Vibration control of active structures*, London: Kluwer Academic, 2002.
- [15] Jayachandran, V., Sun, J.Q., “Unconditional stability domains of structural control systems using dual actuator-sensor pairs,” *Journal of Sound and Vibration*, vol. 208, no. 1, pp. 159-166, Nov. 1997.
- [16] Balas, M. J., “Feedback control of flexible systems,” *IEEE Transactions on Automatic Control*, vol. 23, no. 4, p. 673–679, Aug 1978.
- [17] Gavagni, M., Garadonio, P., Elliott, S., “Theoretical study of a velometer sensor piezoelectric patch actuator pair for direct velocity feedback control systems,” Technical Report No 303, University of Southampton, Southampton - United Kingdom, July 2004.

- 
- [18] Gardonio, P., Bianchi, E., Elliott, S.J., “Smart panel with multiple decentralized units for the control of sound transmission. Part II: design of the decentralized control units,” *Journal of Sound and Vibration*, vol. 274, p. 193–213, July 2004.
- [19] Aoki, Y., Gardonio, P., Gavagni, M., Galassi, C., Elliott, S., “Parametric study of a piezoceramic patch actuator for proportional velocity feedback control loop,” *Journal of Vibration and Acoustics*, vol. 132, pp. 061007-(1-10), 2010.
- [20] Elliott, S. J., Gardonio, P., Sors, T. J., Brennan, M. J., “Active vibroacoustic control with multiple local feedback loops,” *Journal of the Acoustical Society of America*, vol. 11, no. 2, pp. 908-915, 2002.
- [21] Bianchi, E., Gardonio, P., Elliott, S., “Smart panel with multiple decentralized units for the control of sound transmission. Part III: control system implementation,” *Journal of Sound and Vibration*, vol. 274, p. 215–232, July 2004.
- [22] Gardonio, P., Aoki Y. and Elliott S.J., “Smart panel with active damping wedges along the perimeter,” *Journal of Smart Materials and Structures*, vol. 19, no. 6, pp. 1-15, 2010.
- [23] Clark R. L., Saunders W. R., Gibbs G.P., *Adaptive Structures*, New York: John Wiley & Sons, Inc., 1998.
- [24] Fahy, F., Gardonio, P., *Sound and structural vibration: Radiation, transmission and response*, Second edition ed., London, UK: Academic Press, 2007.
- [25] Gardonio, P., Bianchi, E., Elliott, S.J., “Smart panel with multiple decentralized units for the control of sound transmission. Part I: Theoretical predictions,” *Journal of Sound and Vibration*, vol. 274, no. 1-2, pp. 163-192, July 2004.

- [26] Gardonio, P., Gavagni, M., Bagolini, A., “Seismic velocity sensor with an internal sky-hook damping feedback loop,” *IEEE Sensors Journal*, vol. 8, no. 11, pp. 1776-1784, Nov. 2008.
- [27] Gavagni, M., Gardonio, P., “Design and fabrication of a micro-velocity sensor for direct velocity feedback control systems,” *Proceedings of the Sixth International Symposium on Active Noise and Vibration Control, ACTIVE 2006*, pp. 1-16, 19-20 Sept. 19-20 Sept. 2006.
- [28] Beeby, S., Ensell, G., Kraft, M., White, N, MEMS mechanical sensors, London: Artech House, 2004.
- [29] Yazdi, N., Ayazi, F., Najafi, K., “Micromachined inertial sensors,” *Proceedings of the IEEE*, vol. 86, no. 8, pp. 1640-1659, Aug. 1998.
- [30] Acar, C., Shkel, A., MEMS vibratory gyroscopes: Structural approaches to improve robustness, New York: Springer Science+Business Media, LLC, 2009.
- [31] Alshehri, A., Kraft, M., Gardonio, P., “Two-degree-of-freedom capacitive MEMS velocity sensor: Initial test measurements,” *21st Micromechanics and Micro Systems Europe Workshop (MME 2010)*, pp. 269-272, 26-29 Sept. 2010.
- [32] Alshehri, A., Gardonio, P., Elliott, S., Zilletti, M., Kraft, M., “Experimental evaluation of a two degree of freedom capacitive MEMS sensor for velocity measurements,” *Procedia Engineering*, vol. 25, p. 619–622, 4-7 Sept. 2011.
- [33] Alshehri, A., Kraft, M., Gardonio, P., Elliott, S., Zilletti, M., “Two-mass MEMS velocity sensor feedback control loop design,” *IEEE Sensors 2011*, pp. 153-156, 28-31 Oct. 2011.
- [34] Alshehri, A., Kraft, M., Gardonio, P., “Two-mass MEMS velocity sensor: Internal feedback loop design,” *IEEE Sensors Journal*, vol. 13, no. 3, pp. 1003-1011, March 2013.

- 
- [35] Alshehri, A., Almutairi, B., Gardonio, P., Kraft, M., “Two-degree of freedom capacitive MEMS velocity sensor with two coupled electrically isolated mass-spring-damper systems,” *IEEE Sensors 2014*, (accepted).
- [36] Merovitch, L., *Fundamentals of vibrations*, New York: McGraw-Hill, 2001.
- [37] Gatti, P., Ferrari, V., *Applied structural and mechanical vibrations*, London: Taylor & Francis Group LLC, 2003.
- [38] Rao, S. S., *Mechanical Vibrations*, New York: Addison-Welsey Publishing Company, 1995.
- [39] Fargas-Marques, A., Casals-Terre, J., and Shkel, A.M., “Resonant pull-in condition in parallel-plate electrostatic actuators,” *Journal of Microelectromechanical Systems*, vol. 16, no. 5, pp. 1044-1053, Oct. 2007.
- [40] Chuang, W., Lee, H., Chang, P., Hu, Y., “Review on the Modeling of Electrostatic MEMS,” *Sensors 2010*, vol. 10, no. 6, pp. 6149-6171, June 2010.
- [41] Han, C., Choi, D., Yoon, J., “Parallel-plate MEMS variable capacitor with superior linearity and large tuning ratio using a levering structure,” *Journal of Microelectromechanical Systems*, vol. 20, no. 6, pp. 1345-1354, Dec. 2011.
- [42] Kempe, V., *Inertial MEMS: principles and practice*, Cambridge: Cambridge University Press, 2011.
- [43] Bao, M., Yang, H., “Squeeze film air damping in MEMS,” *Sensors and Actuators A: Physical*, vol. 136, no. 1, pp. 3-27, May 2007.
- [44] Sumali, H., “Squeeze-film damping in the free molecular regime: model validation and measurement on a MEMS,” *Journal Micromechanics and Microengineering*, vol. 17, pp. 2231-2240, 2007.

- [45] Lobontiu, N., Garcia, E., *Mechanics of microelectromechanical systems*, Boston: Kluwer Academic Publishers, 2005.
- [46] Bao, M., *Micro mechanical transducers: Pressure sensors, accelerometers and gyroscopes*, Amsterdam, The Netherlands: Elsevier B. V., 2000.
- [47] Legtenberg, R., Groeneveld, A.W., Elwenspoek, M., “Comb-drive actuators for large displacements,” *Journal of Micromechanics and Microengineering*, vol. 6, pp. 320-329, 1996.
- [48] Beards, C. F., *Engineering vibration analysis with application to control systems*, London: Edward Arnold, a division of Hodder Headline PLC, 1995.
- [49] Bies, D. A., Hansen, C., *Engineering noise control: Theory and practice*, London: E and FN Spon Press, 2003.
- [50] Ver, I. L., Beranek, L. L., *Noise and vibration control engineering: Principles and applications*, Hoboken, New Jersey: John Wiley & Sons, Inc., 2006.
- [51] Dorf, R. C., Bishop, R. H., *Modern control systems*, Ninth edition ed., New Jersey: Prentice-Hall, 2001.
- [52] Sun, J. Q., “Some observations on physical duality and collocation of structural control sensor and actuators,” *Journal of Sound and Vibration*, vol. 194, pp. 765-770, 1996.
- [53] Rohlfing, J., Gardonio, P., “Ventilation duct with concurrent acoustic feed-forward and decentralised structural feedback active control,” *Journal of Sound and Vibration*, vol. 333, no. 3, p. 630–645, Feb. 2014.
- [54] Gardonio, P., Alujević, N., “Double panel with skyhook active damping control units for control of sound radiation,” *Journal of Acoustical Society of America*, vol. 128, no. 3, pp. 1108-1117, Sept. 2010.

- 
- [55] Kim, S. M., Pietrzko, S., Brennan, M., “Active vibration isolation using an electrical damper or an electrical dynamic absorber,” *IEEE Transactions on Control Systems Technology*, vol. 16, no. 2, pp. 245-254, March 2008.
- [56] Gatti, G., Brennan, M., Gardonio, P., “Active damping of a beam using a physically collocated accelerometer and piezoelectric patch actuator,” *Journal of Sound and Vibration*, vol. 303, no. 3-5, p. 798–813, June 2007.
- [57] Gardonio, P., Aoki, Y., Elliott, S. J., “A smart panel with active damping wedges along the perimeter,” *Smart Materials and Structures*, vol. 19, no. 6, p. 15, May 2010.
- [58] Aoki, Y., Gardonio, P., Elliott, S., “Rectangular plate with velocity feedback loops using triangularly shaped piezoceramic actuators: Experimental control performance,” *The Journal of Acoustical Society of America*, vol. 123, no. 3, p. 1421–1426, March 2008.
- [59] Diaz, C., Paulitsch, C., Gardonio, P., “Smart panel with active damping units: Implementation of decentralized control,” *Acoustical Society of America Journal*, vol. 124, no. 2, p. 898–910, 2008.
- [60] Gardonio, P., Gavagni, M., Elliott, S.J., “Velocity sensor with an internal feedback control loop,” *Smart Materials and Structures*, vol. 14, no. 6, p. 1517–1525, Nov. 2005.
- [61] Hoover, G. M., O'Brien, J. T., “The influence of the planted geophone on seismic land data,” *Geophysics*, vol. 45, no. 8, pp. 1239-1253, Aug. 1980.
- [62] Krohn, C. E., “Geophone ground coupling,” *Geophysics*, vol. 49, no. 6, pp. 722-731, June 1984.

- [63] Roset, X., del Rio, J., Manuel, A., Palomera-Garcia, R., "Contributions to model characterization of geophone sensor," *IMTC - Instrumentation and Measurement Technology Conference*, pp. 1896-1899, 18-20 May 2004.
- [64] Sujatha, C., *Vibration and acoustics: Measurement and signal analysis*, New Delhi, India: Tata McGraw Hill Education Private Limited, 2010.
- [65] Geospace Sensors, "GS-20DX Geophone," [Online]. Available: <http://www.geospace.com/geophones-gs-20dx/>. [Accessed 10 Jan 2014].
- [66] Goldberg, H., Gannon, J., Marsh, J., Reichert, B., Zavaleta, M., "An extremely low-noise MST accelerometer using custom ASIC circuitry," *Proceedings Sensors Expo, Anaheim, CA, USA*, pp. 479-482, 2000.
- [67] Aizawa, T., Kimura, T., Matsuoka, T., Takeda, T., Asano, Y., "Application of MEMS accelerometer to geophysics," *International Journal of the JCRM*, vol. 4, no. 2, pp. 33-36, Dec. 2008.
- [68] Speller, K. E., Yu, D., "A low-noise MEMS accelerometer for unattended ground sensor applications," *Proceedings of SPIE - The International Society for Optical Engineering (Proceedings of SPIE )*, vol. 5417, pp. 63-72, 2004.
- [69] Rohlfing, J., Gardonio, P., Thompson, D. J., "Comparison of decentralized velocity feedback control for thin homogeneous and stiff sandwich panels using electrodynamic proof-mass actuators," *Journal of Sound and Vibration*, vol. 330, no. 5, pp. 843-867, Feb. 2011.
- [70] Shkel, A. M., "Type I and type II micromachined vibratory gyroscopes," *Position, Location, And Navigation Symposium, 2006 IEEE/ION*, pp. 586-593, 25-27 April 2006.

- 
- [71] Acar, C., Shkel, A., “Four degrees-of-freedom micromachined gyroscopes,” *Journal of Modeling and Simulation of Microsystems*, vol. 2, no. 1, pp. 71-82, 2001.
- [72] Acar, C., Shkel, A., “Nonresonant micromachined gyroscopes with structural mode-decoupling,” *IEEE Sensors Journal*, vol. 3, no. 4, pp. 497-506, Aug. 2003.
- [73] Acar, C., Painter, C., Schofield, A., Shkel, A., “Robust micromachined gyroscopes for automotive applications,” *NSTI - Nanotech 2005 Conference*, vol. 3, pp. 375-378, 2005.
- [74] Joen, S., Lee, J., Jung, H., Chang, H., Kim, Y., “Two-mass system with wide bandwidth for SiOG (silicon on glass) vibratory gyroscopes,” *The 13th International Conference on Solid-state Sensors, Actuators and Microsystems*, vol. 1, pp. 539-542, 5-9 June 2005.
- [75] Acar, C., Shkel, A., “Inherently robust micromachined gyroscopes with 2-DOF sense-mode oscillator,” *Journal of Microelectromechanical Systems*, vol. 15, no. 2, pp. 380-387, April 2006.
- [76] Schofield, A., Trusov, A., Shkel, A., “Multi-degree of freedom tuning fork gyroscope demonstrating shock rejection,” *IEEE Sensors, 2007*, pp. 120-123, 28-31 Oct. 2007.
- [77] Schofield, A., Trusov, A., Shkel, A., “Effects of operational frequency scaling in multi-degree of freedom MEMS gyroscopes,” *IEEE Sensors Journal*, vol. 8, no. 10, pp. 1672-1680, Oct. 2008.
- [78] Beeby, S., Tudor, M., White, N., “Energy harvesting vibration sources for microsystems applications,” *Measurement Science and Technology*, vol. 17, p. R175–R195, 2006.
- [79] Wong, Z., Yan, J., Soga, K., Seshia, A., “A multi-degree-of-freedom electrostatic MEMS power harvester,” *Proceedings of the International Workshops on Micro*

*and Nanotechnology for Power Generation and Energy Conversion Applications - Power MEMS*, pp. 300-303, 1-4 December 1-4 Dec. 2009.

- [80] Bartsch, U., Gaspar, J., Paul, O., “A 2D electret-based resonant micro energy harvester,” *IEEE 22nd International Conference on Micro Electro Mechanical Systems, MEMS 2009.*, pp. 1043-1046, 25-29 Jan. 25-29 Jan. 2009.
- [81] Zhu, Y., Moheimani, S., Yuce, M., “A 2-DOF MEMS ultrasonic energy harvester,” *IEEE Sensors Journal*, vol. 11, no. 1, pp. 155-161, Jan. 2011.
- [82] Tang, X., Zuo, L., “Enhanced vibration energy harvesting using dual-mass systems,” *Journal of Sound and Vibration*, vol. 330, no. 21, p. 5199–5209, Oct. 2011.
- [83] Sari, I., Zeimpekis, I., Kraft, M., “A full wafer dicing free dry release process for MEMS devices,” *Procedia Engineering*, vol. 5, pp. 850-853, 5-8 Sept. 2010.
- [84] Madou, M. J., *Fundamentals of microfabrication: The science of miniaturization*, Boca Raton, Florida: CRC PRESS, 2002.
- [85] Witvrouw, A., Du Bois, B., De Moor, P., Verbist, A., Van Hoof C., Bender, H., Baert, K., “A comparison between wet HF etching and vapor HF etching for sacrificial oxide removal,” *Proceedings of SPIE, Micromachining and Microfabrication Proces Technology VI*, vol. 4174, pp. 130-141, 2000.
- [86] Buhler, J., Steiner, F.P., Baltes, H., “Silicon dioxide sacrificial layer etching in surface micromachining,” *Journal of Micromechanics and Microengineering*, vol. 7, p. R1–R13, Jan. 1997.
- [87] Amini, B. V., Ayazi, F., “Micro-gravity capacitive silicon-on-insulator accelerometers,” *Journal of Micromechanics and Microengineering*, vol. 15, no. 11, p. 2113–2120, Sept. 2005.

- [88] Sari, I., Zeimpekis, I., Kraft, M., "A dicing free SOI process for MEMS devices," *Microelectronic Engineering*, vol. 95, pp. 121-129, 2012.
- [89] Amini, B. V., Abdolvand, R., Ayazi, F., "Sub-micro-gravity capacitive SOI microaccelerometers," *The 13th International Conference on Solid-State Sensors, Actuators and Microsystems, TRANSDUCERS'05*, vol. 1, pp. 515-518, 5-9 June 5-9 June 2005.
- [90] Bai, Y., Yeow, J., Wilson, B., "Design, fabrication, and characteristics of a MEMS micromirror with sidewall electrodes," *Journal of Microelectromechanical Systems*, vol. 19, no. 3, pp. 619-631, June 2010.
- [91] Chunbo, Z., Najafi, K., "Fabrication of thick silicon dioxide layers for thermal isolation," *Journal of Micromechanics and Microengineering*, vol. 14, no. 6, p. 769-774, April 2004.
- [92] Barillaro, G., Diligenti, A., Nannini, A., Pennelli, G., "A thick silicon dioxide fabrication process based on electrochemical trenching of silicon," *Sensors and Actuators A: Physical*, vol. 107, no. 3, pp. 279-284, November Nov. 2003.
- [93] Jiang, H., Yoo, K., Yeh, J., Li, Z., Tien, N., "Fabrication of thick silicon dioxide sacrificial and isolation blocks in a silicon substrate," *Journal of Micromechanics and Microengineering*, vol. 12, no. 1, pp. 87-95, Jan. 2002.
- [94] Kanda, K., Mitsuyama, K., Nakamura, J., Fujita, T., "Silicon dioxide as mechanical structure realized by using trench-etching and oxidation process," *Procedia Engineering*, vol. 25, pp. 843-846, September 2011.
- [95] Lorenz, H., Despont, M., Fahrni, N., LaBianca, N., Renaud, P., Vettiger, P., "SU-8: a low-cost negative resist for MEMS," *Journal of Micromechanics and Microengineering*, vol. 7, pp. 121-124, 1997.

- [96] Conradie, E. H., Moore, D.F., “SU-8 thick photoresist processing as a functional material for MEMS applications,” *Journal of Micromechanics and Microengineering*, vol. 12, p. 368–374, 2002.
- [97] Abgrall, P., Conedera, V., Camon, H., Gue, A., Nguyen, N., “SU-8 as a structural material for labs-on-chips and microelectromechanical systems,” *Electrophoresis Journal*, vol. 28, p. 4539–4551, 2007.
- [98] Rouabah, H., Park, B., Zaouk, R., Morgan, H., Madou, M., Green, N., “Design and fabrication of an ac-electro-osmosis micropump with 3D high-aspect-ratio electrodes using only SU-8,” *Journal of Micromechanics and Microengineering*, vol. 21, no. 3, p. 35018, Feb. 2011.
- [99] “SU-8 2000 Permanent Epoxy Resists,” MicroChem, [Online]. Available: <http://www.microchem.com/Prod-SU82000.htm>. [Accessed September 2011].
- [100] Zhang, J., Tan, K., Gong, H., “Characterization of the polymerization of SU-8 photoresist and its applications in micro-electro-mechanical systems (MEMS),” *Polymer Testing*, vol. 20, no. 6, p. 693–701, 2001.
- [101] Rouabah, H., Design and fabrication of a new 3D AC-electroosmotic micropump, PhD thesis: School of Electronics and Computer Science, UNIVERSITY OF SOUTHAMPTON, 2010.
- [102] Hwang, K., Park, C., Kim, J., Suh, K., Cho, E., Huh, N., “The effects of adhesion energy on the fabrication of high-aspect-ratio SU-8 microstructures,” *Journal of Micromechanics and Microengineering*, vol. 20, no. 11, pp. 117001-(1-7), Nov. 2010.
- [103] Gaura, E., Newman, R., Kraft, M., Flewitt, A., Monteiro, D., Smart MEMS and sensor systems, London: Imperial College Press, 2006.

- [104] Idonus Sarl, "Products: HF Vapor Phase Etcher - Product Description," June 2014. [Online]. Available: <http://www.idonus.com/>.
- [105] Choudhary, V., Iniewsk, K., MEMS: Fundamental technology and applications, Boca Raton, FL: CRC Press, 2013.
- [106] Lotters, J.C., Olthuis, W., Veltink, P.H., Bergveld, P., "A sensitive differential capacitance to voltage converter for sensor applications," *IEEE Transactions on Instrumentation and Measurement*, vol. 48, no. 1, pp. 89-96, Feb. 1999.
- [107] Texas Instruments, "THS4131 high-speed, low-noise, fully-differential I/O amplifiers," May 2011. [Online]. Available: <http://www.ti.com.cn/cn/lit/ds/symlink/th4131.pdf>.
- [108] Sedra, A., Smith, K., Microelectronic circuits, New York: Oxford University Press, 2010.
- [109] Liu, R., Paden, B., Turner, K., "MEMS resonators that are robust to process-induced feature width variations," *Journal of Microelectromechanical systems*, vol. 11, no. 5, pp. 505-511, Oct. 2002.
- [110] Yeom, J., Wu, Y., Selby, J. C., and Shannon, M. A., "Maximum achievable aspect ratio in deep reactive ion etching of silicon due to aspect ratio dependent transport and the microloading effect," *Journal of Vacuum Science & Technology B*, vol. 23, pp. 2319-2329, 2005.
- [111] Wu, B., Kumar, A., Pamarthy, S., "High aspect ratio silicon etch: A review," *Journal of Applied Physics*, vol. 108, pp. 051101(1-20), 2010.
- [112] Jansen, H. V., de Boer, M. J., Unnikrishnan, S., and Louwse, M. C., "Black silicon method X: a review on high speed and selective plasma etching of silicon with profile control: an in-depth comparison between Bosch and cryostat DRIE

- processes as a roadmap to next generation equipment,” *Journal of Micromechanics and Microengineering*, vol. 19, pp. 033001-(1-41), Feb. 2009.
- [113] Owen, K. J., VanDerElzen, B., Peterson, R.L., Najafi, K., “High aspect ratio deep silicon etching,” *Micro Electro Mechanical Systems (MEMS), 2012 IEEE 25th International Conference on*, pp. 251-254, 29/Jan - 02/Feb 29/Jan-2/Feb 2012.
- [114] Kulah, H., Chae, J., Yazdi, N., and Najafi, K., “Noise analysis and characterization of a sigma-delta capacitive microaccelerometer,” *IEEE Journal of Solid-State Circuit*, vol. 41, no. 2, pp. 352-361, Feb. 2006.
- [115] Wu, J., Fedder, G.K., Carley, L.R., “A low-noise low-offset capacitive sensing amplifier for a 50- $\mu\text{g}/\sqrt{\text{Hz}}$  monolithic CMOS MEMS accelerometer,” *IEEE Journal of Solid-State Circuits*, vol. 39, no. 5, pp. 722 - 730, May 2004.
- [116] Polytec GmbH Waldbronn, “Microsystem & MEMS Analyzers,” [Online]. Available: [www.polytec.com/int/microsystems](http://www.polytec.com/int/microsystems). [Accessed 20 Jan 2014].
- [117] Bae, S. Y., Haywroth, K. J., Yee, K. Y., Shcheglove, K., Wiberg, D. V., “High performance MEMS micro-gyroscope,” *Proc. SPIE 4755, Design, Test, Integration, and Packaging of MEMS/MOEMS 2002*, vol. 4755, pp. 316-324, April 2002.
- [118] Droogendijk, H., Bruinink, C. M., Sanders, R., Dagamseh, A., Wiegerink, R., Krijnen, G., “Improving the performance of biomimetic hair-flow sensors by electrostatic spring softening,” *Journal of Micromechanics and Microengineering*, vol. 22, pp. 065026 (1-9), May 2012.
- [119] Torun, H., Sarangapani, K., Degertekin, F., “Spring constant tuning of active atomic force microscope probes using electrostatic spring softening effect,” *Applied Physics Letters*, vol. 91, pp. 253113(1-4), Dec. 2007.
- [120] Elshurafa, A., Khirallah, K., Tawfik, H., Emira, A., Abdel Aziz, K., Sedky, S. , “Nonlinear dynamics of spring softening and hardening in folded-MEMS comb

- drive resonators,” *Journal of Microelectromechanical Systems*, vol. 20, no. 4, pp. 943-958, Aug. 2001.
- [121] Ghatnekar-Nilsson, S., Forsen, E., Abadal, G., Verd, J., Campabadal, F., Perez-Murano, F., Esteve, J., Barniol, N., Boisen, A., Montelius, L., “Resonators with integrated CMOS circuitry for mass sensing applications, fabricated by electron beam lithography,” *Nanotechnology*, vol. 16, no. 1, pp. 98-102, Jan. 2005.
- [122] Sharma, A., Zaman, M.F., Ayazi, F., “A 104-dB dynamic range transimpedance-based CMOS ASIC for tuning fork microgyroscopes,” *IEEE Journal of Solid-State Circuits*, vol. 42, no. 8, pp. 1790-1802, Aug. 2007.
- [123] Sun, H., Jia, K., Liu, X., Yan, G., Hsu, Y., Fox, R., Xie, H., “A CMOS-MEMS gyroscope interface circuit design with high gain and low temperature dependence,” *IEEE Sensors Journal*, vol. 11, no. 11, pp. 2740-2748, Nov. 2011.
- [124] Salvia, J., Lajevardi, P., Hekmat, M., Murmann, B., “A 56M $\Omega$  CMOS TIA for MEMS applications,” *Custom Integrated Circuits Conference, 2009. CICC '09. IEEE*, pp. 199-202, 13-16 Sept. 2009.
- [125] Aaltonen, L., Halonen, K., “Continuous-time interface for a micromachined capacitive accelerometer with NEA of 4  $\mu$ g and bandwidth of 300 Hz,” *Sensors and Actuators A: Physical*, vol. 154, pp. 46-56, July 2009.
- [126] Yazdi, N., Kulah, H., Najafi, K., , “Precision readout circuits for capacitive microaccelerometers,” *Proceedings of IEEE Sensors*, vol. 1, pp. 28-31, 24-27 Oct. 2004.
- [127] Ye, Z., Yang, H., Yin, T., Huang, G., Liu, F., “High-Performance Closed-Loop Interface Circuit for High-Q Capacitive Microaccelerometers,” *IEEE Sensors Journal*, vol. 13, no. 5, pp. 1425,1433, May 2013.

- [128] Petkov, V.P., Balachandran, G.K., Beintner, J., “A Fully Differential Charge-Balanced Accelerometer for Electronic Stability Control,” *IEEE Journal of Solid-State Circuits*, vol. 49, no. 1, pp. 262,270, Jan. 2014.
- [129] Shiah, J., Mirabbasi, S., , “A 5-V 290-  $\mu$ W Low-Noise Chopper-Stabilized Capacitive-Sensor Readout Circuit in 0.8-  $\mu$ m CMOS Using a Correlated-Level-Shifting Technique,” *Circuits and Systems II: Express Briefs, IEEE Transactions on*, vol. 61, no. 4, pp. 254-258, April 2014.
- [130] Yazdi, N., Najafi, K., “An interface IC for a capacitive silicon  $\mu$ g accelerometer,” *IEEE International Solid-State Circuits Conference, Digest of Technical Papers. ISSCC*, pp. 132-133, 17-17 Feb. 1999.
- [131] Wongkomet, N., Boser, B.E., , “Correlated double sampling in capacitive position sensing circuits for micromachined applications,” *The IEEE Asia-Pacific Conference on Circuits and Systems, IEEE APCCAS*, pp. 723-726, 24-27 Nov 1998.
- [132] Lemkin, M., Boser, B.E., , “A three-axis micromachined accelerometer with a CMOS position-sense interface and digital offset-trim electronics,” *IEEE Journal of Solid-State Circuits*, vol. 34, no. 4, pp. 456-468, Apr 1999.
- [133] Si-Ware systems, “Configurable high performance interface ASIC for MEMS inertial sensors (SWS1110),” Si-Ware Egypt, [Online]. Available: <http://www.si-ware.com/sws1110/>. [Accessed 5 Sept 2014].
- [134] Sari, I., “SOI based accelerometer fabricatoin process note,” Release 5.0, Electronics and Computer Science - University of Southampton, Spet-Oct 2011.
- [135] J.A. WOOLLAM CO. INC., “M-2000 Ellipsometer,” [Online]. Available: [http://www.jawoollam.com/m2000\\_home.html](http://www.jawoollam.com/m2000_home.html). [Accessed 20 Jan 2014].

- [136] EV Group, “EVG620 Double Side Mask Aligner,” [Online]. Available: [https://www.evgshop.com/epages/EVGroup.sf/en\\_IE/?ObjectPath=/Shops/EVGroup/Products/EVG620TB](https://www.evgshop.com/epages/EVGroup.sf/en_IE/?ObjectPath=/Shops/EVGroup/Products/EVG620TB). [Accessed 02 Dec 2013].
- [137] Oxford Instruments, “Plasmalab System 100 for RIE, PECVD and ICP,” [Online]. Available: <http://www.oxfordplasma.de/systems/100ll.htm>. [Accessed 14 June 2014].
- [138] Oxford Instruments, “Plasmalab System 400,” [Online]. Available: <http://www.oxfordplasma.de/systems/plab400.htm>. [Accessed 10 June 2014].
- [139] Plasma-Therm, “Plasma-Therm’s VERSALINE,” [Online]. Available: <http://www.plasmatherm.com/versaline.html>. [Accessed 24 March 2014].
- [140] Abdolvand, R., Ayazi, F., “An advanced reactive ion etching process for very high aspect-ratio sub-micron wide trenches in silicon,” *Sensors and Actuators A: Physical*, vol. 144, no. 1, pp. 109-116, May 2008.



